UNIVERSITY OF STRATHCLYDE

Modelling of tides, waves and currents in coastal waters: hydrodynamics of the Firth of Clyde and of the east coast of Scotland.

Alessandro Sabatino

A thesis submitted in partial fulfillment for the
degree of Doctor of Philosophy

in the
Faculty of Science
Department of Mathematics and Statistics

April 2017

Copyright declaration

Signed:

Date:

“Para além do porto
Ha só o ampio mar
Mar eterno absorto
No seu murmurar

Que amargo o estar
Aqui, meu amor
Olho o mar a ondear
E um ligeiro pavor

Toma em mim a cor
De desejar ter
Qualquer cousa melhor
Que quanto é viver ”.

Fernando Pessoa

“El mar
sonríe a lo lejos.
Dientes de espuma,
labios de cielo.”.

Federico Garcia Lorca

Supervisors: Michael Heath and Douglas Speirs

UNIVERSITY OF STRATHCLYDE

Abstract

Faculty of Science

Department of Mathematics and Statistics

Doctor of Philosophy

by Alessandro Sabatino

The thesis here presented is based on three main parts. The first part of the thesis is based on modelling the water circulation of the Clyde Sea, in order to understand the dynamics of the dispersion of the *Neprophs* larvae. Previous researches in this area of Scotland highlighted the importance of the temperature- and saline-driven circulation in the Clyde Sea. However, few researches were focused on the surge dynamics, that are governing the dynamics of the water level in winter.

A three-dimensional finite-volume model was used to simulate the surge propagation, while a historical re-analysis was applied to understand the pattern and the propagation of the surge wave in the Clyde.

The results highlighted that the largest storms that hit the Clyde in the past 30 years were mostly generated in the North Atlantic. Most interestingly, the results also suggest that severe surges are not only caused by extreme surge events, but also by the coupling of spring high tides with moderate surges.

In the second part the coupled dynamics of waves, tides and wind-driven circulation in the east coast of Scotland are studied. Wave-Current Interactions (WCI) are particularly relevant close to the coastline, where the effect of the spectral dispersion and wave breaking are more important and where the currents are stronger.

The results showed that the coupling of strong currents with large waves travelling in opposite direction could enhance in east coast of Scotland the significant wave height (H_s) up to 3 m, threatening potentially infrastructures and ships near the coastline.

The last part of the thesis was dedicated to an experimental study of rogue waves in crossing sea. Crossing sea is one of the most common state in world seas, and occurs when a wind-generated wave train interact with another train of waves, that can be swell waves or another wind-generated wave train, maybe caused by a rapidly turning wind direction. Some numerical studies showed that this interaction can lead to the mechanism of modulation instability and, consequently, to the formation of rogue waves. A water tank experiment was carried out to confirm this theory. The results shows that the angle of the interaction is a fundamental variable that can decrease

or increase the instability of the wave train. However, most interestingly, in the same conditions, the monochromatic sea state was showing a larger number of rogue waves than the crossing sea.

Acknowledgements

I would probably should have an entire thesis just for the acknowledgement list, to thank all the people that is some way helped me in these years here in Scotland. First I need to say thanks to my girlfriend, Alessandra Romanò for her patience and for her presence, even if more than 2,000 km were between us. Everything that is in that thesis or in my papers would have been impossible without her. Without her constant encouragement, I would have probably been still in my BSc.

Many thanks also to my parents, that were supporting me from Italy and to my grandmother, and to the parents of my girlfriend, that are for me a second family.

I'm deeply grateful to my supervisors Prof. Mike Heath and Dr. Douglas Speirs for giving me the opportunity of live this magic adventure in the real science. I need to thank them also because they gave me a certain degree of freedom to wonder into the world of science.

Thank also to Ian Thurlbeck, for helping me with all my IT technical problems and for the help with the lagrangian runs from the FVCOM simulations. I shared an office for three years with Vanessa Trijoulet, Aidan Hunter and with little less than 3 years with Jackie McLean, Trevor Slaughter and Ian Gardiner. I need to thank them for the patience for having me wandering around the room and writing strange formula on the blackboard. Just two doors close there were Alan McDonald, Robert Wilson and Andisheh Bahshi, in which I was also working for a little period of time on the workstation for the east coast model, and in which I was using the espresso machine for drinking some good coffee.

Many thanks to dr. Chris McCaig, that worked with me on the TeraWatt project and that was a very good company during our travel to Orkneys for TeraWatt meetings. Thanks also to everyone involved in the TeraWatt project, for the priceless moments passed in Orkneys, in particular Arne Vögler for having us on his ship, Venki Venugopal for the food that he cooked that night on the ship, to Jon Side, Susana Baston and

Simon Waldman for hosting us in their university and to Michela De Dominicis for the opportunity to speak italian also in Scotland.

I'm extremely grateful also to Ken Brink, that two days before my 26th birthday suddenly and unexpectly appeared in my office, helping me to go out from the dark wood as Virgil with Dante with his suggestions.

I'm also grateful to all my co-authors: Rory O'Hara Murray and Alan Hills, that helped me a lot expecially during the first year of my Ph.D., giving me advices on how FVCOM was working and about the oceanography of the Clyde Sea and the North Sea; Sophie Elliott for helping me to develop and improve the Clyde Sea model for her studies near Arran Island; Gianluca Miglio and his group in the Department of Pharmacology in the University of Turin, for letting me wonder again in another field of Science, extremely interesting; to Pierre Cazenave for having shared with me his codes for the FVCOM models.

An expecial thanks goes to Marina Serio and Miguel Onorato, for having me encouraged to take this opportunity of the Ph.D. and to do research, and also for their precious collaboration, that took a chapter of this thesis, one published paper, one submitted paper and one drafted paper. Another expecial thank goes to the staff of Qua Restaurant for giving me the opportunity to taste the italian pizza also here in Scotland.

Contents

List of Figures

List of Tables

Abbreviations

ABBREVIATIONS	
FVCOM	Finite-Volume Community Ocean Model
UMassD	University of Massachusetts Dartmouth
SWAN	Simulating WAves Nearshore
DHI	Danish Hydraulic Institute
MIKE 3 FM	MIKE 3 Flow Model
MIKE 21 SW	MIKE 3 Spectral Waves
WCI	Wave-Currents Interactions
JONSWAP	JOint North Sea WAve Project
ECMWF	European Centre for Medium-Range Weather Forecasts
ERA	ECMWF Re-Analysis
NCEP	National Centers for Environmental Prediction
NCAR	National Center for Atmospheric Research
BGS	British Geological Survey
CEFAS	Centre for Environment, Fisheries and Aquaculture Science
BODC	British Oceanographic Data Center
GEBCO	General Bathymetric Chart of the Oceans
GSHHG	Global Self-consistent, Hierarchical, High-resolution Geography Database
OTPS	OSU Tidal Prediction Software
OSU	Oregon State University
SEPA	Scottish Environmental Protection Agency
MSS	Marine Scotland Science

RCM	Rotor Current Meter
CTD	Conductivity Temperature Depth
ERS2	European Remote-Sensing Satellite 2
JAS1	Jason-1 NASA Satellite
SMS	Surface-water Modelling System by Acquaveo
SST	Sea Surface Temperature
SEMA	SEmi-MAjor Axis
SEMI	SEmi-MInor Axis
RMSE	Root-Mean Square Error
NRMSE	Normalized Root-Mean Square Error
SI	Scatter Index
R^2	Pearson Correlation Coefficient

Preface

Not all those who wander are lost.

John Ronald Reuel Tolkien, *The Fellowship of the Ring*

My initial Ph.D. project was about Modelling the larvae dispersal in the Clyde Sea. However, seems that the destiny at the end had other plans for my Ph.D.: from December 2012 I was involved in the TeraWatt project with Chris McCaig and prof. Mike Heath, while few months later, an Easter vacation and a casual visit to my MSc supervisor - prof. Marina Serio - was fundamental for the rogue wave paper. I was like a little boy in rapture in front of a showcase full of toys, with trains that were wandering around and all the other stuff.

Then, a cold morning of May 2014, Ken Brink materialized himself in my office, suggesting me to force the hydrodynamic model of the Clyde Sea with residuals from the boundaries, in order to study the propagation of the surge in the Clyde and in the surrounding areas. Was really a major breaktrough.

Few months later the MSc supervisor of my girlfriend - prof. Gianluca Miglio - was in need of a mathematician for a pharmacology problem. I offered myself as a volunteer. I spent part of my Summer holidays of 2014 on working on applications of mathematics to biochemistry, in particular to some mechanism that occur in proteins that are present in human body. For me it was like going in the middle of nowhere, in a deep and dense forest without any chart or idea where I was. I felt this sensation many times, when I

was young and I was wandering around the mountains in Italy, or when I was with my bicycle, finding a new climb and I like it.
Curiosity, the love for science and for the adventure was and is the main reason of why I'm here

"Consider well the seed that gave you birth:
You were not made to live as brutes,
But to follow virtue and knowledge"
(Dante Alighieri,Divina Commedia, Inferno XXVI, 118-120)

But why all of these projects?
From a scientific point of view, each of these project had a sound motivation. The shellfish larvae was important from a ecosystem point of view, in order to protect the larvae of these animals from fishing and also for studying the places in which these larvae were going. The TeraWatt project had a really ambitious but extremely important goal: to understand the impact of the marine renewables, such as tidal and wave farm, on the surrounding environment, in particular on the current dynamics and on sediment dynamics. On the other hand the two hydrodynamic model that I've built were used also for understanding the surge dynamics in the Clyde, that would be very important for the flood forecasting, and for understanding the wave dynamics and the thin link between windsea waves, swell and currents and their mutual interactions and the importance of these interactions both in storms and in the sediment dynamics.
The Clyde Sea model was also used by Sophie Elliott to model the environment (in particular the seabed habitat and the species prevalence) in the Clyde Sea.
The crossing sea state study was carried out to understand better the mechanism of the rogue wave formation in the crossing sea compared to the monochromatic sea. The obvious reason for studying this is to improve the understanding of rogue waves and to prevent accidents like the Louis Majesty in 2011 or similar.

Finally, the modelling of the succination mechanism in proteins (that is not reported in this Ph.D. thesis, since it was very difficult to squeeze inside it, in particular for the project itself, that is very far from the others) was important because it helped to model a modification in proteins - the succination - which importance is not fully understood. While was seen that causes irreversible inactivation of *glyceraldehyde-3-phosphate dehydrogenase* (GAPDH) in vitro and could be related to diabetes and autoimmune desorders in the humans.

Part I

Publications

Publications

Peer-reviewed publications published:

1. **A.D. Sabatino** and M. Serio. Experimental investigation on statistical properties of wave heights and crests in crossing sea conditions. *Ocean Dynamics* 65(5): 707-720, 2015.

2. **A.D. Sabatino**, C. McCaig, R.B. O'Hara Murray, and M.R. Heath. Modelling wave-current interactions off the east coast of Scotland. *Ocean Science* 12 (4): 861-873, 2016.

3. **A.D. Sabatino**, R.B. O'Hara Murray, A. Hills, D.C. Speirs, and M.R. Heath. Modelling surges in the Clyde Sea. *Natural Hazards*: 1-23, 2016.

4. M.R. Heath, **A.D. Sabatino**, N.Serpetti, C. McCaig, and R.B. O'Hara Murray. Modelling the sensitivity of suspended sediment profiles to tidal current and wave conditions. *in press in Ocean and Coastal Management*: 2016.

5. A. Gallego, J. Side, S. Baston, S. Waldman, M. Bell, M. James, I. Davies, R. O'Hara Murray, M. Heath, **A. Sabatino**, D. McKee, C. McCaig, H. Karunarathna, I. Fairley, A. Chatzirodou, V. Venugopal, R. Nemalidinne, T.Z. Yung, A. Vogler, R. MacIver, M. Burrows. Large scale three-dimensional modelling for wave and tidal energy resource and environmental impact: Methodologies for quantifying acceptable

thresholds for sustainable exploitation. *in press in Ocean and Coastal Management*: 2016.

Publications submitted in peer-review journals:

1. **A.D. Sabatino** and M. Serio. Statistical properties of mechanically generated wave trains in crossing and unidirectional sea conditions. *submitted to Ocean Engineering*.

Position papers:

1. M.R. Heath, **A.D. Sabatino**, N.Serpetti, and R.B. O'Hara Murray. Scoping the impact tidal and wave energy extraction on suspended sediment concentrations and underwater light climate. *Terawatt Position Papers*, 2015.
2. **A.D. Sabatino**, R. Clement, M.R. Heath and D. McKee. Use of ocean colour remote sensing to monitor sea surface suspended sediments. *Terawatt Position Papers*, 2015.

Presentations at national/international conferences/meetings:

1. **A.D. Sabatino**, C. McCaig, R. Nemaliddine, V. Vengupal, R.B. O'Hara Murray and M.R. Heath. Simulating Tides and Waves in the East Coast of Scotland. *MASTS ASM*, Edinburgh 2014.
2. **A.D. Sabatino**, M.R. Heath, D. Speirs, A. Hills and R.B. O'Hara Murray. Study of the Clyde Sea Tidal Circulation using FVCOM. *MASTS ASM*, Edinburgh 2013.

Other outputs at national/international conferences/meetings:

1. M.R. Heath, **A.D. Sabatino**, N.Serpetti, and R.B. O'Hara Murray. Scoping the impact tidal and wave energy extraction on suspended sediment concentrations and underwater light climate. *MASTS ASM*, Glasgow 2015.

2. S.A.M. Elliott, **A.D. Sabatino**, M.R. Heath, W.R. Turrell, and D.M. Bailey. Predictive substratum modelling for juvenile gadoid distribution and abundance. *ICES Conference*, Copenhagen 2015.

3. C. McCaig, **A.D. Sabatino**, and M.R. Heath. Statistical modelling of suspended sediments off Stonehaven. *MASTS ASM*, Edinburgh 2013.

Part II

Introduction

Chapter 1

Introduction

The sea, once it casts its spell, holds one in its net of wonder forever

Jacques-Yves Cousteau

This thesis presents the results of research on currents and waves in the ocean. The research was carried out using hydrodynamic models implemented in the Firth of Clyde and in the east coast of Scotland, and by analysis of data from wave-tank experiment.

1.1 The hydrodynamic modelling

The physical processes that affect the motion of the water in the sea are strongly and intimately related to the ecology. However, our ability to describe these processes is dependent on many different equations that, after more than 200 years of research, have no analytical solution: the Navier-Stokes equations. In 2000 these became one of the Millennium Problems for the Clay Institute (Fefferman, 2000).

This is the main reason why scientists studying fluid dynamics problems uses numerical methods to 'solve' the Navier-Stokes equations, in order to have some knowledge of the

behavior of fluids.

The history of hydrodynamic modelling is quite young: the first numerical 'simulation' of Navier-Stokes equation dates back to the First World War (Richardson, 2007). The attempt was made by Lewis Fry Richardson, one of the greatest scientist of the last century, who at that time was serving with the Quaker Ambulance in Northern France attached to the 16th French Infantry Division (Körner, 1996). No computer. No cluster. Just papers and hand (Lynch, 2008; Gold, 1954).

The first numerical simulation - based on the weather conditions on the 10 May 1910 -, ultimately, failed (Lynch, 2006).

But Richardson did not gave up: in 1950 he replicate his attempt. This time with the first modern computer, ENIAC. To simulate the global weather for 24 hours, the simulation took 24 hours (Lynch, 2008). After this first attempt years and years passed, and with the development of computers and high performance clusters, the Richardson's dream was finally realized: simulating the behavior of the fluids using hydrodynamic models is now largely diffuse and the precision of the prediction is extremely high.

The simulation using CFD is now widely used not only in research but also in industry, in particular for automotive and aerospace. In this thesis fluid dynamics numerical simulations were applied to two sea areas in Scotland: the east coast of Scotland and the Clyde Sea.

1.2 Waves

In the thesis two kind of ocean waves are studied: the wind waves, with a period less than 20 s are the most familiar waves in the ocean, while the other waves, the planetary waves have a far longer period: the tidal waves, for example, have a period of about 12 hours. The waves are the main 'natural' solution to the hydrodynamic equations: the nature 'solves' the Navier-Stokes equation every time a fluid moves and often this movement is harmonic. Since the impossibility, as we seen in the previous section, to

solve analitically the N-S equations, another useful way to study physical phenomena is the harmonic analysis. Physical oceanography owes very much to one man, Jean Baptiste Joseph Fourier, who in 1807, after having escaped the 'Great Terror', when he was imprisoned in 1795 and was at risk of being guillottined, published a book that revolutioned Mathematics and Physics: *Memoire sur la propagation de la chaleur dans les corps solides*. It contained the theory of the Fourier transform, that was fundamental for studying oscillatory phenomena.

The Fourier transform, in fact, allowed the scientist to change completely the way of seeing waves: it allows the transition from the time domain to the frequency domain. Long series of oscillations now could be transformed to peaks on a frequency-amplitude diagram and the dominant frequencies can be connected to the physical phenomena that caused the oscillations. This was an exceptional and remarkable revolution made by one of the greatest mind of all the time, which caused a dramatic change of perspective in physics. The study of the tide in the 20th century was not possible without the Fourier transform, as well as the spectral theory of windsea waves. All the theory of the evolution of waves, and also the formation of the waves is all based on changes in the frequency spectrum components. Even the numerical hydrodynamic models (in particular, the wave models) would not have been possible without the Fourier transform. No Fourier transform would have meant no possibility of predicting tidal motion, and no possibility to study the evolution of a train of waves during its propagation.

This is the immense contribution that Fourier gave to physical oceanography, even if the Fourier transform was not designed specifically for the ocean, but was used to solve another fundamental problem in physics: the propagation of heat in bodies.

1.3 Motivation for the research

The three researches in this thesis have different motivation. In the Clyde Sea no in depth studies were carried out for the understanding of storm patterns and storm

surge propagation. Clyde Sea is affected periodically by severe surge events. The understanding of the mechanism of how storm surge propagates in the Clyde would be extremely useful for predicting such events and understanding which areas are more sensible to water level surges.

On the other side, the North Sea is well known to be one of the most perilious seas for waves. Occurrence of rogue waves is very well documented as well as severe storm waves causing damages along the east coast of Great Britain. Altough many studies in the last years on waves and tides were focusing in the British coast, no high resolution wave models were developed for the east coast of Scotland. High resolution wave models are a relatively young science, but are extremely helpful for the understanding of coastal phenomena, such as wave-currents interactions. These interactions can have a huge effect on the enhancement of the wave heights of the waves, in particular when approaching the coast.

In addition there are few high resolution model for the coastline of the Scotland, despite this documented long history of coastal damages. Furthermore, the availability of long term sediment data (Serpetti et al., 2011, 2012; Serpetti, 2012) gave us the unique opportunity to statistically studying the relationship between bed composition, tidal signal and wave characteristics.

Another important phenomena that can be studied with the aid of those models are the wave-wave interactions. These occur usually when a trains of waves generated in the far-field (swell waves) interact with locally generated waves (also called windsea waves). This interaction could cause a significant enhancement of the wave heights such as the wave-currents interaction, but the wave-wave interaction is more effective in deep waters rather than near the coastline.

Wave-wave interactions are also involved in the rogue wave formation in deep water.

1.4 The choice of the models

Two different models were used to simulate the water dynamics in the Clyde Sea and in the east coast of Scotland. In the first case, in the Clyde Sea, the FVCOM model was used (Chen et al., 2003). The Finite-Volume Community Ocean Model (FVCOM) is an open-source unstructured-grid, finite-volume, primitive equation 3-D hydrodynamic model developed by a team from the University of Massachussets-Darmouth and from the Woods Hole Oceanographic Institute (WHOI). The reason of choosing this model was because is one of the newest model in physical oceanography, giving a large degree of flexibility in the choice of equation closure and on the physical phenomena to consider during the simulation.

This flexibility become fundamental when studying an area with complex coastline and rapidly changing bathymetry such as the Clyde Sea, with different forcing interacting all together.

On the other side, for the east coast of Scotland was used a commercial model: MIKE 3 and MIKE 21. The reason was that MIKE by DHI is one of the few models that is feasible for the wave modelling and the tide and currents modelling with an unstructured grid solution. FVCOM, for example, at the beginning of my Ph.D. did not have a module for the simulation of the wave propagation, and still does not have possibility for a complete coupled wave and currents simulation. Other models that does have some of the features present in MIKE 3 and 21 were based on the structured-grid approach. Having squares instead of triangles for the elements of the grid have one disadvantage: the difficulty of modelling properly the land boundaries, and, consequently, losing details on the flow and on the wave propagation.

Some alternatives were also considered during the initial stage of the study: ROMS was also initially evaluated as alternative to FVCOM, but FVCOM was more promising for its module of lagrangian tracking that was extensively used by other oceanographers in UK. Also the fact that there is a large group of FVCOM user in UK, in which there is a

sharing of pre-processing and post-processing tool was very important for this choice.

1.5 Chapter organization

The organization of the Chapters was one of the most difficult task in this thesis: it was extremely difficult to decide which was the best rational configuration for all the research.

In the next chapter - Chapter 2 - there will be a very brief review of the main concepts of physical oceanography. It will be more in-depth for waves rather than tides or wind-driven circulation, since the largest part of it is more recent, in particular the rogue wave part. In Chapter 3 there will be a review of the previous studies about the physical oceanography in the Clyde Sea. Chapter 4 reports the methodologies adopted for the Clyde Sea model. The results of the model simulations with the main findings are reported in Chapters 5. The following 3 chapters are on the East coast of Scotland model, and the division follows the previous adopted for the Clyde. From Chapter 9 to Chapter 10, the rogue waves in crossing sea is studied, while in the last chapter (Chapter 11) conclusive remarks are given.

Chapter 2

Physical processes

In this chapter there will be a brief review of the physical phenomena that are studied in this thesis.

2.1 The tidal motion

Tides are the movement of large masses of water driven by the gravitational interactions between the Moon, the Sun, and the Earth (Boon, 2013). Every day in every part of the Earth usually there are two high and two low tides, one sublunar high and one antipodal high (high tide when the Moon is on the opposite side of the Earth) (Pugh, 1996), however there are some particular places in which the high tide occurs only once every day.

Mathematically, it is possible to see the astronomical tidal elevation as a linear superposition of harmonic functions, since the phenomena that cause tides are periodic, due to the rotational motion of the Earth around its axis and the movement of the Earth or of the Moon around the Sun. From the Fourier's harmonic analysis theory, it is possible

to write the sealevel elevation as:

$$H_n = \sum_{n=1}^{N} A_n cos(\omega_n t - g_n) \tag{2.1}$$

where A_n is the amplitude of the n-th harmonic tidal component, ω_n is the angular speed associated to each component and g_n is the phase lag on the so-called Equilibrium tide at Greenwich. The modern harmonic analysis tidal theory is based on the studies of Darwin (1880); Doodson (1921); Cartwright and Tayler (1971); Cartwright and Edden (1973); Foreman (1979). In particular Doodson (1921), Schureman (1958) and Cartwright and Edden (1973) compiled an extensive and exaustive catalogue of the harmonic components in the ocean. In the Table 2.1 are reported some of the main harmonic components that will be cited throughout the thesis.

Name	**Period (h)**	**Description**
M_2	12.4206	Principal Lunar Component
S_2	12.0000	Principal Solar Component
N_2	12.6583	Larger Elliptical Lunar
K_1	23.9345	Lunar Diurnal
N_1	25.8193	Lunar Diurnal
P_1	24.0659	Principal Solar
Q_1	26.8683	Larger Elliptical Lunar
M_4	6.2103	Shallow Water Overtides of Principal Lunar
M_6	4.1402	Shallow Water Overtides of Principal Lunar
MN_4	6.2692	Shallow Water Quarterdiurnal
MS_4	6.1033	Shallow Water Quarterdiurnal

TABLE 2.1: Main harmonic tidal components (Doodson, 1921; Schureman, 1958; Cartwright and Edden, 1973; Pugh, 1996)

It is also possible to represent this tidal wave graphically in the ocean through a so-called cotidal chart, in which the amplitude and the phase lag of each component separately are shown graphically on a chart.

From these charts it can be seen that the tidal wave in the ocean has a point in which the amplitude is zero. This point is called an amphidrome. The amplitude of the

tidal wave component grows with the distance from the amphidrome, while the phase lines rotates with the asimmetrical angle from the amphidromic point. Spatially, each harmonic component of the astronomical tide can be seen as a standing wave oscillation on a rotating earth: this means that away from the land boundaries, where reflections and interaction with shallow waters deform the wave, the tidal wave can be seen as two Kelvin or Poincaré waves travelling in opposite directions (Proudman, 1944) and the wave rotates around the amphidrome (Taylor, 1922). The amphidrome can be also virtual or degenerate. That occur when the amphidrome is not in the ocean but is on land.

The interaction of the tidal wave with shallow water causes multiple reflections which gives origin to higher harmonics in the tide, that are tidal waves with a period that is a multiple of the wave that generated it (*phase-locked*): this distortion can cause double high water or double low water events (Doodson and Warburg, 1941). The condition for the formation of double high waters due to overtides is:

$$\frac{Bn^2}{A} > 1 \tag{2.2}$$

where B is the amplitude of the overtide, A is the amplitude of the semi-diurnal harmonic tide, and n is ratio between the frequency of the overtide with the frequency of the semi-diurnal tide.

Recently an alternative mechanism for the formation of double high water was proposed by Bowers et al. (2013) based on the tide-generated *seiches*.

Connected to the tidal motion of high and low water, are the tidal currents. Tidal currents are a good approximation of the current motion in areas where the tidal circulation is strong and the stratification is very low. However, when a strong baroclinic circulation is present or in presence of strong winds, the tidal currents alone cannot explain the circulation of the sea in the considered region.

2.2 Wind-driven circulation

The wind-driven circulation, as the tidal-driven circulation, is a barotropic circulation, in which the difference of the density in the water column does not effect the water circulation. This circulation was first explored by the Swedish scientist Vagn Wafrid Ekman, who discovered that the net transport due to the wind action is shifted of 90° with the direction of the wind (Ekman, 1902). He discovered also that on the surface of the sea the direction of the resulting current forms an angle of 45° with the direction of the wind due to the balance between the Coriolis force and the wind stress. The direction of the current changes with the depth: in particular Ekman found that the expression for the current in presence of a wind in the y-direction (in the northern emisphere):

$$u_E = V_0 \cos\left(\frac{\pi}{4} + \frac{\pi}{D_E}z\right) \exp\left(\frac{\pi}{D_E}z\right) \tag{2.3}$$

$$v_E = V_0 \sin\left(\frac{\pi}{4} + \frac{\pi}{D_E}z\right) \exp\left(\frac{\pi}{D_E}z\right) \tag{2.4}$$

Where V_0 is the current at surface caused by the wind, that can be written as:

$$V_0 = \frac{\sqrt{2}\pi\tau_w}{D_E \rho f} \tag{2.5}$$

where ρ is density of the sea water, τ_w is the wind stress, f is the Coriolis force and D_E is the depth of the so-called Ekman layer:

$$D_E = \pi \left(\frac{2A_z}{f}\right)^{1/2} \tag{2.6}$$

where A_z is the vertical eddy viscosity of the sea. From expression 2.3 and 2.4, the resulting profile of the velocity with the depth is a spiral (called Ekman spiral) in which

the vector of the velocity rotates clockwise in the Northern hemisphere and anticlockwise in the Southern hemisphere (in the equation 2.3 in the Southern hemisphere there is a minus instead of the plus in front of the expression). In addition, the vector of the velocity decreases exponentially with the depth. The depth of the Ekman layer (D_E) is the point in which this spiral dissipates.

The Ekman theory is an approximation of the wind-driven circulation: in the real ocean the effect of the stratification and the interaction with tidally-driven currents changes and deform the spiral, or masks the effect of the wind-driven circulation. Due to this, it is very difficult to observe the Ekman spiral. However the Ekman spiral was observed in the oceans (Roach et al., 2015; Lenn and Chereskin, 2009; Price et al., 1987). Some years after Ekman's discoveries, Sverdrup (1947) applied the Ekman discoveries to the real ocean, in particular to the eastern Pacific current, finding that the currents, and the related transport in the Pacific are directly related to the curl of the wind stress. However, his results could be only applied to the eastern boundary, while for the western boundary the problem remained open. Studying the wind-driven currents in the North Atlantic Ocean, Stommel (1948), solved the Sverdrup problem for the western boundary, adding a term of bottom friction to balance the pressure and the Coriolis term. This balance explained why in the North Atlantic basin (and in the Pacific), the wind-driven circulation is stronger at the western boundary (the so-called western boundary intensification) and the gyre of the circulation is deformed compared to a non-rotating wind-driven gyre, with the center shifted to the west. The ocean wind-driven circulation theory was then completed by the study of Munk (1950), who added the lateral friction at the boundary, giving a more realistic approach to the ocean wind-driven circulation.

2.3 Storm surges

Storm surges are abnormal enhancements of the sea water level not caused by the tidal motion, but caused by low-pressure weather systems: the low pressure causes a bulge of water in the sea. Also the wind can cause storm surges. The worst atmospheric situation for low-lying coastal communities is when spring high tides coincide with severe storm surge (Lamb, 1980; Murty, 1984). The Great Britain is particularly prone to surge events: the largest storm surge hitting UK was the 1953 surge, also called 'The North Sea Flood', that caused about 1800 deaths in The Netherlands (Gerritsen, 2005) and more than 300 deaths in England and Scotland (Baxter, 2005). This event was caused by a low pressure system on the southern North Sea, near the Dutch coastline (Heaps, 1983), bringing extremely strong winds in shallow coastal water (Flather, 1984). The resulting surge wave was exceeding 3 m in some locations and the significant wave height was more than 12 m (Wolf and Flather, 2005).

One of the most important mechanism for the surge formation is the Ekman transport by winds parallel to the coast transports water toward the coast causing a rise in sea level (Ekman, 1902). In addition winds blowing toward the coast push water directly toward the coast. The low pressure inside the storm raises sea level by one centimeter for each millibar decrease in pressure through the inverted-barometer effect. Finally, the storm surge adds to the tides, and high tides can change a relative weak surge into a much more dangerous one. A part from the pressure effect, using an approximation, wind blowing over shallow water causes a slope in the sea surface proportional to wind stress (Ekman, 1902):

$$\frac{\partial \zeta}{\partial x} = \frac{\tau_0}{\rho g H} \tag{2.7}$$

where ζ is sea level, x is horizontal distance, H is water depth, τ_0 is wind stress at the sea surface, ρ is water density; and g is gravitational acceleration.

2.4 Baroclinic circulation: stratification in the ocean

Stratification occurs when water masses with very different properties (density, temperature and/or salinity) form distint layers with little or no mixing between them. This because the water mass above is less dense than the ocean below and the buoyancy forces are much stronger then the mixing forces. Vertical mixing, instead, occurs if there is enough energy to dissipate the stratification. This energy is normally due to strong tidal currents or to strong wind-driven currents. Based on this idea, Simpson and Hunter (1974), studying the Irish Sea, introduced a criterion for the condition of stratification in different regions of the ocean. The Simpson-Hunter number is defined as:

$$\frac{u_B^3}{h} \geq S_{HS} \tag{2.8}$$

where u_B is the current in the area, h is the depth and S_{HS} is the threshold for the breaking of the stratification, and is defined as:

$$S_{HS} = \frac{g}{2}\frac{\alpha H}{C_p}\frac{1}{\delta_s \rho C_D} \tag{2.9}$$

where α is the thermal expansion coefficient ($\sim 10^{-4}$, for temperature and salinity conditions; T = 10°C and s = 30 PSU, $\alpha = 1.562 \times 10^{-4}$ (McDougall, 1987)), H is the stratifying buoyancy flux, C_p is the specific heat capacity of the seawater at constant pressure, ρ is the water density, C_D is the drag coefficient and δ_s is the fraction of the work due to the current stress that is used to mix the water column. If the rate of heating is constant, S_{HS} is a constant. For the North Sea and for the shelf seas near Scotland and England, Pingree et al. (1978) found that the Simpson-Hunter criteria was:

$$\frac{h}{u_B^3} = 350 m^{-2} s^3 \tag{2.10}$$

In the Irish Sea, for example, the criterion for the tidal current necessary to mix the water column is $u \geq 0.75 m/s$ (Simpson and Hunter, 1974; Pingree et al., 1978).

2.5 Wind Waves

Surface waves or wind waves are water level oscillations in the ocean with a very short period (generally less than 20 s (Adcock and Taylor, 2014)) caused by the wind.

2.5.1 Main wave features

Before considering the processes that are studied in this thesis, it is important to introduce some basic concepts about the waves and, most importantly, the sea state. Sea state is fundamental for both the rogue waves statistics and the wave modelling. However, characterizing the condition of the waves in the sea in a determined time is not easy, because the possible presence of other wavetrain (crossing sea state), because the wind that can give extra energy to the waves and because of the currents (wave-current interactions). Normally windsea waves are described by those four parameters (Adcock and Taylor, 2014):

- The wave spectrum.
- The significant wave height (H_s), that was originally defined as the mean of the highest third of the waves, is defined as $H_s = 4\sqrt{m_0}$ (Holthuijsen, 2007), where m_0 is the zero-th moment of the power spectrum.
- The peak frequency or the peak wavenumber.

- The mean direction and directional spreading.

When wind blows over the ocean for a period of time the energy is transmitted from the atmosphere to the ocean. However, this energy is not monochromatic, but is distributed over many frequencies depending on the characteristics of the wind and of the geographic region (such as the sea surface in which the wind can blow). One of the first attempts of describing theoretically the spectrum of waves in the sea was made by Pierson and Moskowitz (1963). They introduced in their work the concept of fully developed sea: if the wind will blow over a large area for a long time, the wave field generated by this wind will be in equilibrium with the wind itself. In the fully developed sea, the wind cannot transfer more energy to the wave field. The resulting wave spectrum of a fully developed sea assumes the following form (Pierson and Moskowitz, 1963; Moskowitz, 1964; Pierson, 1964):

$$S(\omega) = \frac{\alpha g^2}{\omega^5} exp\left(-\beta\left(\frac{\omega_0}{\omega}\right)^4\right) \tag{2.11}$$

where $\omega = 2\pi f$ is the angular frequency of the spectrum, f is the frequency, α and β are two normalization coefficients that assumes respectively the value of $\alpha = 8.1\times10^{-3}$ and $\beta = 0.74$, $\omega_0 = g/U_{19.5}$, where $g = 9.81 m/s^2$ is the gravity acceleration of Earth, and $U_{19.5}$ is the wind at 19.5 m above the sea surface, that is the height of the anemometers that were used by Pierson and Moskowitz (1963) on the weather ship. This can be related to the standard wind at 10 m to the sea surface $U_{19.5} \approx 1.026 U_{10}$.
Having defined the spectrum, it is possible to relate the spectrum and the main features of the spectrum to both the peak frequency and the H_s. The peak angular frequency ω_p can be found from the spectrum solving the differential equation $dS/d\omega = 0$, that gives:

$$\omega_p = \frac{0.877 g}{U_{19.5}} \tag{2.12}$$

While from the definition above, the significant wave height is 4 times the m_0 of the spectrum:

$$H_s = 4\int_0^\infty S(\omega)d\omega \approx 0.22\frac{(U_{10})^2}{g} \approx \frac{0.16}{g\omega_p^2} \tag{2.13}$$

However, the Pierson-Moskowitz spectrum required the fully developed sea condition, that is not a common/frequent condition on the sea. Quite often in the real ocean the wind can change of magnitude or in direction in very small time or can suddenly stop blowing. Komen et al. (1984), for example, found that quasi-stationary solutions in the sea (a weaker concept of fully developed sea) could exist and the one-dimensional spectrum is close to the Pierson-Moskowitz, however this is not true when considering the angular spreading.

Hasselmann et al. (1973) proposed a new spectral form, based on the results from an intensive measurement campaign carried out in the North Sea. In their field measurements they found that the sea state was never fully-developed: non-linear wave-wave interactions constantly changes the shape of the spectrum, such as the energy dissipation. Given those results, they propose a spectrum, called JONSWAP spectrum, that is a modified Pierson-Moskowitz spectrum, with a new term called the peak enhancement factor (γ^r). The resulting spectrum is defined as:

$$S(\omega) = \frac{\alpha g^2}{\omega^5} exp\left(-\frac{5}{4}\left(\frac{\omega_p}{\omega}\right)^4\right)\gamma^r \tag{2.14}$$

$$r = exp\left[-\frac{(\omega-\omega_p)^2}{2\sigma^2\omega_p^2}\right] \tag{2.15}$$

In which the term α in the equation is no longer a constant, but is determined experimentally as (Hasselmann et al., 1973):

$$\alpha = 0.076\left(\frac{U_{10}^2}{Fg}\right)^{0.22} \tag{2.16}$$

While the peak angular frequency is:

$$\omega_p = 22 \left(\frac{g^2}{U_{10} F} \right)^{1/3} \tag{2.17}$$

In those equation appear a new term, F, that is called fetch or fetch length and is defined as the length of water over which the wind that generated the wavetrain has blown. The other two parameters that are in the JONSWAP spectrum are γ that is called peak enhancement factor and is in average 3.3, but can be normally between 1 and 6 (depending on the 'age' of the wavetrain) and σ that is a constant that is 0.07 when $\omega \leq \omega_p$ and is 0.09 when $\omega > \omega_p$.

Those two spectral forms are the most used in the physical oceanography. From those two spectra, given the strengh of the wind and the features of the wind itself, it is possible to know the peak frequency and the significant wave height of the wave train. The last variable that is important for a complete sea state description is the direction and directional spreading of the spectra. It indicates how the energy is distributed spatially and this distribution is normally a function of the angle. The description of this variable, however is of fundamental importance in both rogue waves description (Onorato et al., 2002b, 2009) and in the propagation of the wavetrain (Donelan et al., 1985; Benjamin, 1967).

Experimental work (Mitsuyasu et al., 1975; Ewans, 1998; Donelan et al., 1985) showed that the directional spreading is not only a function of the angle, but depends on the frequency of the wavetrain itself.

2.5.2 Wave propagation

Wave propagation is fundamental for both modelling and understanding the physics behind rogue waves. For the wave propagation usually the governing equation of all the spectral wave models is the wave action conservation equation (Andrews and McIntyre,

1978). The wave action (N) is defined as:

$$N(\sigma, \theta) = \frac{E(\sigma, \theta)}{\sigma} \tag{2.18}$$

Where E is the energy density of the wavetrain, that is calculated from the spectra and σ is the relative angular frequency, that coincide with the absolute angular frequency ω in absence of an external current. The wave action conservation equation is usually written as:

$$\frac{\partial N}{\partial t} + \nabla \cdot (cN) = \frac{S}{\sigma} \tag{2.19}$$

where c is the phase speed, while S is the energy source term, that account for the modification of energy due to linear and nonlinear interactions. Those interactions are the transfer of the wind energy to the wave field, the dissipation due to depth induced wave breaking, the wave-wave interaction, the dissipation due to bottom friction and the dissipation caused by the white-capping:

$$S = S_{in} + S_{nl} + S_{ds} + S_{bot} + S_{surf} \tag{2.20}$$

Considering a wavetrain propagating without wind input, after a certain time it will decay and become a swell train, with a decrease of the peak frequency and an increase of the directional spreading. Before this stage, however, certain wavetrains have a phase that is called Benjamin-Feir instability. Some studies revealed that the relaxation of the wavetrain begin occurs after 100-1000 T_p after the generation of the wavetrain, leading to the stabilization of the wavetrain due to the broadening of the bandwidth (Eliasson and Shukla, 2010; Dysthe et al., 2003), but before this stage the modulational instability, that usually occur after 30-40 T_p (Onorato et al., 2002a; Janssen, 2003), lead to the narrowing of the bandwidth and to the focusing of the spectra. This focusing (Benjamin-Feir instability), that will be analyzed in the section 2.5.4 is considered to be the main nonlinear mechanism of the rogue wave formation in the ocean.

2.5.3 Rogue waves

Rogue waves (also called freak (Draper, 1966) or monster waves) are waves whose height exceed two times the significant wave height of the ocean in which they were generated. Dysthe et al. (2008) also reported an alternative definition: rogue waves are also waves whose crest height is more than 1.25 the significant wave height.

For many years scientists generally believed that those waves should not exist in the ocean. Very few scientists since 1990 were convinced that these waves were real and not an exotic mathematical result. Mariners, however, were more convinced than scientists. Sitting in a pub near the port it was often possible to hear mariners talking about giant waves smashing into the ship, damaging the keel or throwing someone in the sea.

However, the linear theory of the waves, based on seminal studies of water waves made by Airy (1845) and by Stokes (1847) denied the possibility of such waves. After the second world war, the development of new techniques for observing and analysing the ocean were availables. Longuet-Higgins (1952) showed that the Rayleigh distribution was the most appropriate distribution of waveheight for narrow-banded ocean wind-generated waves. Some years later, Forristall (1978) studied a dataset of 116 hours of recorded hurricane-generated waves in Gulf of Mexico, finding that the Rayleigh distribution overestimated the frequency of highest waves. A similar result was obtained few years before by Haring et al. (1976) studying 376 hours of storm wave records from various locations such as Australia, Gulf of Mexico, North Sea and Gulf of Alaska. Processes of wave energy dissipation such as wave-breaking (Battjes and Janssen, 1978) or white-capping (Hasselmann, 1974) were considered responsible for this overestimation of the waves by Rayleigh distribution (Tayfun, 1980). These two evidences were ruling out the existence of freak waves in the ocean.

However, some strange ship loss, such as the *München* in 1978, that disappeared with 27 men aboard, were unexplained. An early account of rogue waves observation was given by Mallory (1974), that identified a series of abnormally high waves between

1952 and 1973 off the coast of South Africa. This was one of the first account of rogue wave observations in physical oceanography. In '90s freak waves passed from exotic mathematics to reality. Sand et al. (1990) gave the first large scale account of measured rogue waves in the sea. This report contained a timeseries from the Gorm platform in Central North Sea during the 17 November 1984, in which a 11 m wave in a 5 m H_s wave state was recorded (about 2.2 H_s). However, the most convincing evidence of the existence of rogue waves in the ocean occurred on the 1 January 1995 when on the Draupner oil platform a wave with an height of 26 m and a 18.5 m crest in a sea state of H_s of 11.8 m (about 1.5 H_s) was measured (Haver, 2004; Adcock and Taylor, 2014). Haver (2004) estimated that a wave with H = 26-27 m, for the linear theory should occur once every 100 year and the wave crest condition was estimated, with linear theory 1 every 10,000 year.
After the so-called 'New Year Wave', many other measurement lead scientists to study rogue waves and, more in general, the non-linear deviations of the wave theory (Adcock and Taylor, 2014; Kharif and Pelinovsky, 2003; Dysthe et al., 2008; Müller et al., 2005).

2.5.4 The physics of rogue waves

Several conditions were identified throughout the years to explain the appearance of the rogue waves in the oceans (Adcock and Taylor, 2014; Kharif and Pelinovsky, 2003; Dysthe et al., 2008; Müller et al., 2005). All of those conditions are based on the focusing of the wave spectra, and this focusing (that can be linear or non-linear) can be achieved in different ways. The evolution of the waves in the ocean is weakly non-linear: the equations that describe the evolution of a wave in the ocean, expecially in deep water, presents non-linear terms. In deep water the evolution of the waves is often described with the Non-Linear Schrödinger equations. Benjamin and Feir (1967) in 1967 suggested that a wavetrain in deep water is unstable: after the generation of

this wavetrain due to the action of the wind on the sea, the energy, due to nonlinear interactions, is transferred from a wave to another wave inside the wave group: in practice some waves grow inside the wave group stealing energy from the neighbor waves. This mechanism can account for the formation of rogue waves in deep water due to nonlinear interactions. In their seminal study Benjamin and Feir (1967) propose also that after this stage, the wavetrain eventually would disintergrate. They also found that this mechanism would occur if

$$0 \leq \delta \leq \sqrt{2}ka \tag{2.21}$$

where δ is the sideband frequency, k is the dominant wavenumber and a is the amplitude of the wavetrain. In practice, what this relation is telling is that those instabilities will occur in deep water if the spectrum is narrow-banded. It is worth noticing, however, that this relation was found with the approximation of a infinitely deep inviscid liquid: in this formulation, the dissipation due to viscosity is not taken in account, as well as the dissipation due to wave-breaking and white-capping. Results with a inviscid fluid leaded to an indefinite energy transfers and an indefinite growing. The Benjamin-Feir instability (BFI) is considered the main mechanism for the nonlinear focusing of wavetrains leading to the formation of rogue waves in both unimodal (Osborne et al., 2000; Onorato et al., 2001) and in bimodal or crossing sea state (Onorato et al., 2006a) as in the presence of currents (Onorato et al., 2011; Toffoli et al., 2015).

Numerical and experimental studies confirmed that the Benjamin-Feir instability in random waves depends strongly on both the spectral width in the direction of the propagation and to the spectral width perpendicular to the direction of the propation (directional spreading) (Gramstad and Trulsen, 2007; Toffoli et al., 2010). One of the main predictors of this kind of instability is the kurtosis. Janssen (2003) introduced an index to account for the nonlinearities in the wavetrain. This index was named Benjamin-Feir Index (BFI) and can be expressed as a function of the wave steepness

and the narrowness of the spectrum as:

$$BFI = \frac{\sqrt{2}\epsilon_s}{\delta_w} \tag{2.22}$$

Where ϵ_s is the wave steepness, that is the ratio between the amplitude of the wavetrain and its wavelength (or $\epsilon_p = k_p a$, where k_p is the peak wavenumber and a is the amplitude of the wavetrain), and the δ_w is the bandwidth of the spectrum (both in direction of the propagation and perpendicular). The BFI is connected to the kurtosis of the water elevation as following:

$$\lambda_4 = \frac{\pi}{\sqrt{3}} BFI^2 \tag{2.23}$$

This relation - as the Benjamin-Feir index -, however, it is only defined rigorously for a single wavetrain and not for a sea state in which more than one wavetrain is present. However, a similar formulation that relates the narrowness of the bandwidth and the steepness with the instabilities of the wavetrain in crossing sea was found by Onorato et al. (2006a).

2.5.5 Wave-current interactions (WCI)

Wave-current interaction is a well-known mechanism of interaction in the ocean and is due to the spatial focusing of the wave train. In the Chapter 4 of this thesis and in Sabatino et al. (2015) we considered this mechanism for the modification of H_s in the ocean. However, this mechanism could also trigger the appearance of a rogue wave, in particular when a wavetrain is moving on the opposite direction to a strong current (Onorato et al., 2011; Toffoli et al., 2015).

The south-east coast of South Africa is one of the most important region for the formation of rogue waves due to wave-currents interactions. This is due to the presence of a strong current, the Agulhas current, that near the coast has a jetlike structure with a

prevalent south-west direction along the shelf edge, conversely, the wave conditions in this area have often a north-east direction, due to the passage of cold fronts followed by strong winds and waves from the southwest (Irvine and Tilley, 1988; Lavrenov, 1998; Dysthe et al., 2008).

Evidence of this mechanism for the rogue wave generation is very strong. In their review Adcock and Taylor (2014) stated that the physics of the wave-current interaction is well understood, and very strong experimental evidence supports the theory on the generation of rogue waves due to WCI. This theory is also supported by laboratory experiments (Toffoli et al., 2011b, 2013) and by numerical simulations (Hjelmervik and Trulsen, 2009; Onorato et al., 2011).

Currents in opposite directions causes a non-linear focusing of the wavetrain as well as an enhancement of the H_s (Phillips, 1977).

2.5.6 Crossing sea state

Crossing sea is defined as a sea state in which two trains of waves coexist and interact. This sea state is quite common in the ocean: measurements in 1980s and 1990s in the North Sea, for both coastal and deep water, allow us to conclude that the crossing sea state occurs about 25% of the time in the sea (Guedes Soares, 1984, 1991). An increasing amount of evidence pointed out that in crossing sea state there is an increased probability of rogue waves appearance: some ship accidents related to rogue waves were found to be in crossing sea state, such as the Louis Majesty accident (Cavaleri et al., 2012) in the Mediterranean Sea, or the Suwa-Maru accident (Tamura et al., 2009) occurred in the Pacific Ocean (east of Japan).

Onorato et al. (2006a) suggested that the mechanism of the formation of rogue waves in crossing sea is similar to the one in monochromatic sea state: the modulational instability (Benjamin-Feir instability). Stability analysis of the Zakharov equation (the Zakharov equation, as the Non-Linear Schrödinger equations are often used for the

propagation of wavetrains in deep water) for the crossing sea state highlighted that the modulational instability depends on the angle between the two wavetrains (Onorato et al., 2010), in particular with an highest probability of rogue wave appearance with a crossing sea angle β between 10° and 30°. Successive numerical simulations, based on the Euler potential equations, found that the highest probability are between 30° and 60° (Toffoli et al., 2011a). Those results were also supported by the increase of the kurtosis found from a wave tank experiment (Toffoli et al., 2011a): a more in-depth analysis of these data are reported in the Chapter 7 of this thesis.

Another experiment, carried out in the same wave basin, gave similar results (Petrova et al., 2013), finding an enhanced probability of rogue waves even for crossing sea angles of 120°.

Part III

Clyde Sea

Chapter 3

The physical oceanography of the Clyde Sea and the North Channel

3.1 Introduction

The Clyde Sea is semienclosed marginal sea of the Atlantic Ocean of 3,600 km^2 in the south-west of Scotland, that presents fjordic features, called *lochs*. The physical oceanography of these seas is strongly influenced by the North Atlantic Ocean, but also by the local conditions, such as the freshwater input from the river discharge.

3.2 Hydrography of the Clyde Sea and North Channel

The Clyde Sea is a semienclosed tidal sea that includes the estuary of the Clyde, the Firth of Clyde and some other sealochs. The open sea boundary of the Clyde is delimited by the North Channel of the Irish Sea and extends from the Mull of Kintyre to the Corsewall Point (Halliday, 1969).

Water circulation in the Clyde Sea is influenced by different factors. From an oceanographic point of view, it can be divided in two different regions (Matthews et al., 1999): the first region is the so-called inner firth, that encompasses all the fjords (or *lochs*) of the Clyde Sea and the Clyde estuary, this area is mostly influenced by the freshwater input and presents an estuarine circulation; the second area is called the outer firth that is the wide and shallow part that communicates with the North Channel and is more influenced by the tides and ocean climate.

The North Channel (also known as Straits of Moyle) is a narrow but deep channel that separates the island of Great Britain from the island of Ireland. It connects the North Atlantic Ocean with the Irish Sea and is classified by the International Hydrographic Institution as an inner sea off the west coast of Scotland. The deepest part of the North Channel is the Beaufort's Dyke (Kinahan, 1900) that is a very deep sea trench just 3.5 km wide that reaches 312 m of maximum depth (Callaway et al., 2011b). In this area 1 million tons of ordnance were dumped following the Oslo and London conventions in 1972 (Callaway et al., 2011a), as well as phosgene and mustard gas after the Second World War (Harper and Dock, 2007).

The figure 1 shows the bathymetry of the Clyde Sea and the North Channel.

From the figure can be clearly seen the shallow sill area ($< 40m$) that separates the Clyde Sea and the North Channel. The map also shows the deep areas in the SE North Channel (Beaufort's Dyke) and the deep areas in the Clyde Sea, localized near the Isle of Arran (Arran Trench) and at the beginning of the Loch Fyne, where the depth goes below -100 m.

It can be also noticed that the Global Self-consistent, Hierarchical, High-resolution Geography Database (GSHHG) bathymetry (Wessel and Smith, 1996) have some areas in which no data are available for the bathymetry, principally in narrow fjords, becase the resolution of the GSHHG does not allow to cover this area properly. This was also an initial limitation of our model, because the open-source dataset of bathymetry often are too coarse for the Clyde Sea area. We overcome this problem using also some non

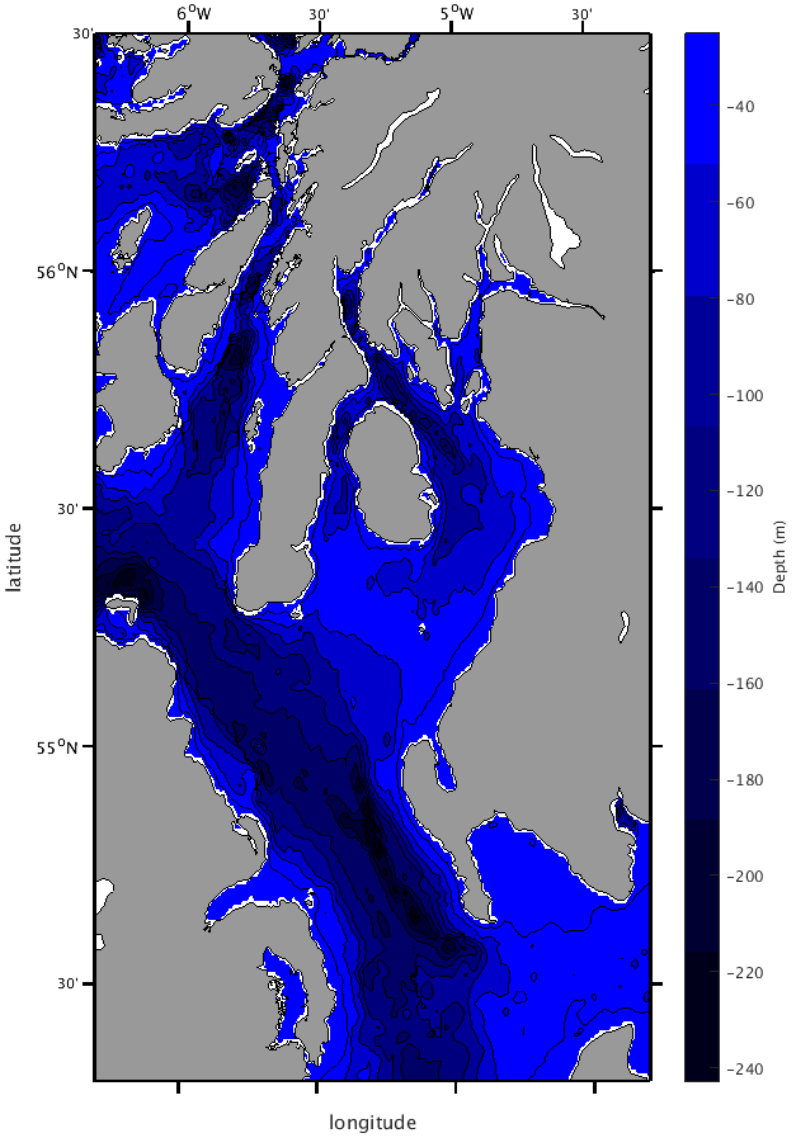

FIGURE 3.1: The bathymetry of the Clyde Sea and the North Channel (bathymetry from Global Self-consistent, Hierarchical, High-resolution Geography Database (GSHHG), for more information see Wessel and Smith (1996))

freely available bathymetry data (SeaZone) in order to cover properly these areas and to model the water circulation.

3.3 Tidal circulation

Tides are one of the most important forcings of the Clyde Sea and the North Channel. The tidal motion in this area is mainly driven by the amphidrome point of the M_2 component, situated north to the Clyde Sea, near the Isle of Mull (Pingree and Griffiths, 1979; Gjevik and Straume, 1989). Close to the M_2 amphidrome, there is also an amphidrome of the S_2 component (Pingree and Griffiths, 1981b) and of the N_2 component (Pingree and Griffiths, 1981a).

Strong differences have been noted between the tidal circulation of the North Channel and Clyde Sea. In the North Channel, in particular at the bottleneck between the Mull of Kintyre and Torr Head, the tidal currents are extremely strong (exceeding 1 m/s), while in the Clyde the currents are weak (in the order of magnitude of 0.1-0.2 m/s) (Dooley, 1979; Davies et al., 2004; Knight and Howarth, 1999).

In order to study the importance of the tidal circulation in the Clyde and in the North Channel, Davies et al. (2004) considered the thickness of the tidal bottom turbulent boundary layer in the two areas. The boundary layer is an extremely important indicator of the physical features in shelf seas (Grant and Madsen, 1986): the thicker the boundary layer, the more difficult it will be for the water to be stratified. The boundary layer thickness was defined in Soulsby (1983) as:

$$\delta = \frac{|R_+|\delta_+}{|R_+| + |R_-|} + \frac{|R_-|\delta_-}{|R_+| + |R_-|} \tag{3.1}$$

in which δ_+ and δ_- are the boundary layer thickness of the anticlockwise and of the clockwise circulation respectively, and defined as:

$$\delta_+ = \frac{CU_*}{\omega + f} \tag{3.2}$$

$$\delta_- = \frac{CU_*}{\omega - f} \tag{3.3}$$

in which ω is the frequency of the current, in the approximation that the current components u and v can be represented as a sinusoidal oscillation, f is the Coriolis parameter, U_* is the bed friction velocity and C is a coefficient, that ranges between 0.1-0.4 (Soulsby, 1983; Stigebrandt, 1988; Garrett et al., 1978; Loder and Greenberg, 1986; Werner et al., 2003). $|R_+|$ and $|R_-|$ are the rotary components of the tidal velocity (anticlockwise and clockwise respectively) in the approximation that the tidal wave could be represented as a Sverdrup pressure wave defined as:

$$P^{\pm} = -i(f \pm \omega)R^{\pm} \tag{3.4}$$

The results of this analysis in the Clyde Sea and in the North Channel have revealed that the boundary layer of the North Channel occupies all the water column: this means that the tidal turbulence keeps the North Channel well mixed, making stratification impossible. On the other hand the boundary layer of the Clyde Sea is much thinner, enabling stratification in the Clyde region (Davies et al., 2004).

Davies et al. (2004) highlighted also that the tidal energy flux is confined to the North Channel and very little flux is transmitted to the Clyde Sea.

The M_4 constituent was studied by Davies and Hall (1998). The M_4 is a tidal constituent caused by a non-linear distortion of the main semidiurnal lunar component M_2 in shallow water. The harmonic components that originate from this interaction are often called over-tides (Andersen, 2004, 1999). In the Clyde Sea the effect of this component was only significant when the advection term of the moment was significant, so only in a few areas along the coastline of the Clyde, while in the North Channel this

constituent was negligible.

3.4 Wind- and pressure-driven circulation

The wind is another major player in the area: large storm events driven by wind and pressure systems are common in the Clyde Sea and in the North Channel. Later in the chapters dedicated, there will be an extensive description of surge events and surge propagation in the Clyde Sea and in the North Channel, in particular in the fjordic areas. Davies et al. (2001a), studying the region with a structured low-resolution grid, found that the North Channel is more influenced by shelf-wide wind events, while the Clyde Sea is more affected by local wind. The wind also affected the transport between the Clyde Sea and the North Channel. Davies and Hall (2000) found that this transport depends strongly on the direction of the wind. In particular when the wind is across the North Channel, there is a significant exchange between the Clyde Sea and the North Channel, but when the flow is through the western, southern or eastern open boundaries (far-field wind events), the exchange between North Channel and Clyde was small and the ocean flow was contained through the topographic boundary.

The Clyde Sea is one of the areas in Scotland more exposed to disastrous surge events (Ball et al., 2014). This coastal hazards is likely to be extremely dangerous in the future: sea level rise will increase the probability of severe events hitting the coast of the Clyde Sea. Recent projections based on different IPCC scenarios estimated that the sea-level change in the Clyde Sea area will be of + 0.815 to + 1.78 m (1990-2000 average compared with 2090-2099 projection) (Nicholls et al., 2014; Hinkel et al., 2015; Howard et al., 2014).

One of the first attempts at surge modelling was carried out by Townson and Collar (1986) who simulated the exceptional 1972 and 1979 storm surges that affected the Clyde Sea using two structured grid models of 5 km and 3 km resolution, respectively.

The main limit was the model resolution, that was too coarse for many of the fjordic areas of the Clyde Sea. In addition, the difference between predicted and recorded sea level was not satisfactory. Some years later, on the 5th January 1991, a large storm surge hit the city of Glasgow, causing damage exceeding £10.5 million. This event highlighted a need for an early warning system for flooding.

In 1999 the Scottish Environment Protection Agency (SEPA) developed a hydrodynamic model for this purpose, that improved the forecasting capabilities in the area (Kaya et al., 2005). However the model had some limitations for the surge forecasting: first of all the area covered by the model was quite limited and the model was constructed from in particular in the fjordic area was still low (about 500 m).

Conversely, considering the combined effect of surge and wind stress on the surface, Flather (1987) estimated that the maximum depth-averaged storm surge currents are weak on a 50 year period are quite weak both in the Clyde Sea and in the North Channel, not exceeding 0.4 m/s in the North Channel and in the southern Clyde, and 0.2 m/s in the northern areas of the Clyde Sea.

3.5 Temperature and salinity and associated circulation

The temperature and salinity conditions in the Clyde Sea and in the North Channel are mainly affected by the solar heating, that is the main forcing for the stratification cycle in the european shelf. As seen in the subsection 2.2.1, the boundary layer due to turbulence in the North Channel occupies all the water column due to the strong tidal current in the area, making it impossible for stratification to develop in the channel (Edwards et al., 1986). Conversely, the low tidal currents in the Clyde and the topography cause persistent stratification of the Clyde Sea (Davies et al., 2004). Another factor that promotes the stratification and the stability of the water column in the Clyde Sea area is the freshwater input (quantified as $\sim$ 350 m^3/s), that mainly comes from the Clyde River (Poodle, 1986).

A front of density separates the well mixed North Channel with the stratified Clyde Sea that is situated on the Great Plateau, the shallow area that separates the North Channel from the Clyde Sea (Kasai et al., 1999).

Some studies suggest that the stratification of the Clyde Sea follows an annual cycle, with a strong and persisting stratification in summer months by a combination of thermal and freshwater inflow, and a weaker stratification in winter. In between these two states, usually in November, stratification is eroded and a complete vertical mixing of the water is possible (Simpson and Rippeth, 1993). In addition, a two-box model proposed by Rippeth and Simpson (1996) to explain the episodes of vertical mixing, found that during the transition between these two states, the North Channel water may replace the deep water in the Clyde Sea in winter.

Some hypotheses were made for explaining the cycle of stratification and the vertical mixing episodes. Inall and Rippeth (2002) hypotized that a large part of the vertical mixing is due to the dissipation of the internal tide. To test this hypothesis they placed 2 ADCPs in the Clyde Sea. They found that the dissipation rate of turbulent kinetic energy (TKE) was in agreement with the rate of dissipation of the internal tide, while they found that the mixing process needed other external sources of energy.

In 2004 Cottier et al. (2004) discover that the autumnal vertical mixing of the water column was due to local convective processes that destroys the thermocline and causes a reduction in the overall KE density. KE density that was found to be constant throughout the year without any seasonality.

The circulation induced by the stratification is a two-layer circulation, typically observed throughout the year, where surface flow forms an anticyclonic circulation near the Isle of Arran, and the lower water column consists of an opposing circulation (Midgley et al., 2001).

Large internal waves have also been discovered in the Clyde Sea (Jackson and Elliott, 2002). Internal wave are a particular kind of waves that does not occur in the interface

between atmosphere and sea (such as wind-sea waves), but occur inside the sea, normally in stratification conditions. A stratified sea can be modelled as a two-layer fluid, with low density water overtopping more dense water, with an interface between the two called pycnocline. If the stratification is mainly due to temperature, the pycnocline is usually called thermocline (Munk and Anderson, 1948). Internal waves are perturbation, driven normally by external factors, such as tides, that propagate and intensify on the pycnocline or on the thermocline (Garrett and Munk, 1975; Benjamin, 1967; Garrett and Munk, 1972; Kao et al., 1985). Mathematically these perturbations can be seen as solitary waves propagating on the interface of two fluids (Davis and Acrivos, 1967). Osborne and Burch (1980) were the first to successfully identify internal waves in the world ocean in the Andaman Sea. These waves were fitting perfectly the shape of solitary waves.

Jackson and Elliott (2002) found that in the Clyde Sea the vertical displacement of the observed internal waves could exceed 3 m, with energy levels according to the Garrett-Munk spectrum (Garrett and Munk, 1972, 1975).

Chapter 4

Clyde Sea model: Materials and Methods

4.1 Introduction

In order to model the water circulation of the Clyde Sea, the Finite-Volume Community Ocean Model (FVCOM) model was chosen. FVCOM is the state-of-the-art open-source hydrodynamic model, that has been successfully applied to many different areas of the world, in particular for estuaries and areas with complex topography as well for surge forecast, such as Rego and Li (2009b,a, 2010a,b); Weisberg and Zheng (2008).

4.2 FVCOM model description

The Finite-Volume Community Ocean Model (FVCOM) is an open-source unstructured-grid, finite-volume, primitive equation 3-D hydrodynamic model developed by Chen et al. (2003, 2006a). Governing equations are solved on Cartesian or spherical coordinates by the computation of the flow and the different fluxes between non-overlapping

triangular cells. The code is written on FORTRAN 90/95 and was optimized for the running in a High-Performance Computing Cluster. The parallelization of the FVCOM code was made by Cowles (2008), and consist in the partition of the domain in different subdomains that are simulated from each node of the cluster: for example if the simulation run on 4 nodes, the FVCOM code authomatically the domain into four different subdomains.

In the absence of oceanic ice or snow precipitation, the FVCOM governing conservation equations assume, in Cartesian coordinates, the following formulation (Chen et al., 2006b):

$$\frac{\partial u}{\partial t} + u\frac{\partial u}{\partial x} + v\frac{\partial u}{\partial y} + w\frac{\partial u}{\partial z} - fv = -\frac{1}{\rho}\frac{\partial(p_H + p_a)}{\partial x} - \frac{1}{\rho}\frac{\partial q}{\partial x} + \frac{\partial}{\partial z}(K_m\frac{\partial u}{\partial z}) + F_u \quad (4.1)$$

$$\frac{\partial v}{\partial t} + u\frac{\partial v}{\partial x} + v\frac{\partial v}{\partial y} + w\frac{\partial v}{\partial z} + fu = -\frac{1}{\rho}\frac{\partial(p_H + p_a)}{\partial y} - \frac{1}{\rho}\frac{\partial q}{\partial y} + \frac{\partial}{\partial z}(K_m\frac{\partial v}{\partial z}) + F_v \quad (4.2)$$

$$\frac{\partial w}{\partial t} + u\frac{\partial w}{\partial x} + v\frac{\partial w}{\partial y} + w\frac{\partial w}{\partial z} = -\frac{1}{\rho}\frac{\partial q}{\partial z} + \frac{\partial}{\partial z}(K_m\frac{\partial w}{\partial z}) + F_w \quad (4.3)$$

$$\frac{\partial u}{\partial x} + \frac{\partial v}{\partial y} + \frac{\partial w}{\partial z} = 0 \quad (4.4)$$

$$\frac{\partial T}{\partial t} + u\frac{\partial T}{\partial x} + v\frac{\partial T}{\partial y} + w\frac{\partial T}{\partial z} = \frac{\partial}{\partial z}(K_h\frac{\partial T}{\partial z}) + F_T \quad (4.5)$$

$$\frac{\partial S}{\partial t} + u\frac{\partial S}{\partial x} + v\frac{\partial S}{\partial y} + w\frac{\partial S}{\partial z} = \frac{\partial}{\partial z}(K_h\frac{\partial S}{\partial z}) + F_S \quad (4.6)$$

$$\rho = \rho(T, S, p) \quad (4.7)$$

where equations 4.1, 4.2 and 4.3 are the Navier-Stokes equations in Cartesian coordinates under the assumption of incompressible flow (4.4), and equations 4.5 and 4.6 are the convection-diffusion equations for temperature and salinity respectively. The different terms of the equations above are: x, y, z are the Cartesian coordinates; t is the time; u, v, w are the x, y, z components of the current respectively; f is the Coriolis parameter; g is the gravitational acceleration; K_m and K_h are the vertical eddy viscosity coefficient

for momentum and the thermal vertical eddy viscosity coefficient respectively; F_u, F_v, F_w, F_T and F_S are the horizontal (u and v), vertical, thermal and salt diffusion terms. Total pressure in the model is given by the sum of the three pressure terms p_a, q and p_H, where the hydrostatic pressure p_H satisfies the following equation:

$$\frac{\partial p_H}{\partial z} = -\rho g \tag{4.8}$$

The non-hydrostatic term is non-zero only if the non-hydrostatic condition in the model is selected.

The model solves the equation at specified levels fixed by the user in the water column. A more innovative approach is also implemented in FVCOM, in which the governing equations are expressed in a coordinate system that is not depth-fixed but follows the seabed. Defining $\hat{g} = \hat{g}(x, y, r, t)$ as the new coordinate system (generalized terrain-following coordinate system) and r as the new vertical axis varying from -1 to 0; the governing equations assumes the following formulation (Chen et al., 2003):

$$\begin{aligned}\frac{\partial uJ}{\partial t} + \frac{\partial u^2 J}{\partial x} + \frac{\partial uvJ}{\partial y} + \frac{\partial u\omega}{\partial r} - fvJ = -gJ\frac{\partial \zeta}{\partial x} - \frac{J}{\rho_0}\frac{\partial p_a}{\partial x} - \\ \frac{gJ}{\rho_0}[\int_r^0 J(\frac{\partial \rho}{\partial} + \frac{\partial \rho}{\partial r'}\frac{\partial r'}{\partial x})\,\mathrm{d}r'] - \frac{1}{\rho_0}(\frac{\partial qJ}{\partial} + \frac{\partial qA_1}{\partial r}) + \frac{\partial}{\partial r}(\frac{K_m}{J}\frac{\partial u}{\partial r}) + JF_u\end{aligned} \tag{4.9}$$

$$\begin{aligned}\frac{\partial vJ}{\partial t} + \frac{\partial uvJ}{\partial x} + \frac{\partial v^2 J}{\partial y} + \frac{\partial v\omega}{\partial r} + fuJ = -gJ\frac{\partial \zeta}{\partial y} - \frac{J}{\rho_0}\frac{\partial p_a}{\partial y} - \\ \frac{gJ}{\rho_0}[\int_r^0 J(\frac{\partial \rho}{\partial y} + \frac{\partial \rho}{\partial r'}\frac{\partial r'}{\partial y})\,\mathrm{d}r'] - \frac{1}{\rho_0}(\frac{\partial qJ}{\partial y} + \frac{\partial qA_2}{\partial r}) + \frac{\partial}{\partial r}(\frac{K_m}{J}\frac{\partial v}{\partial r}) + JF_v\end{aligned} \tag{4.10}$$

$$\frac{\partial wJ}{\partial t} + \frac{\partial uwJ}{\partial x} + \frac{\partial vwJ}{\partial y} + \frac{\partial w\omega}{\partial r} = -\frac{1}{\rho}\frac{\partial q}{\partial r} + \frac{\partial}{\partial r}(\frac{K_m}{J}\frac{\partial w}{\partial r}) + JF_w \tag{4.11}$$

$$\frac{\partial uJ}{\partial x} + \frac{\partial vJ}{\partial y} + \frac{\partial uA_1}{\partial r} + \frac{\partial vA_2}{\partial r} + \frac{\partial w}{\partial r} = 0 \tag{4.12}$$

$$\frac{\partial TJ}{\partial t} + \frac{\partial TuJ}{\partial x} + \frac{\partial TvJ}{\partial y} + \frac{\partial T\omega}{\partial r} = \frac{\partial}{\partial r}(\frac{K_h}{J}\frac{\partial T}{\partial r}) + +J\hat{H} + JF_T \tag{4.13}$$

$$\frac{\partial SJ}{\partial t} + \frac{\partial SuJ}{\partial x} + \frac{\partial SvJ}{\partial y} + \frac{\partial S\omega}{\partial r} = \frac{\partial}{\partial r}(\frac{K_h}{J}\frac{\partial S}{\partial r}) + JF_S \tag{4.14}$$

$$\rho = \rho(T, S, p) \tag{4.15}$$

where J is defined as $J = \partial z/\partial r$, A_1 and A_2 are coordinate transformation coefficients ($A_1 = J\partial r/\partial x$, $A_2 = J\partial r/\partial y$) and ω is:

$$\omega = \frac{1}{J}(w - \frac{\partial \hat{g}}{\partial t} - \vec{v} \cdot \nabla \hat{g}) \tag{4.16}$$

A longer description of the FVCOM and more details about the model and the different equations can be found in (Chen et al., 2006b). The equations above are closed in FVCOM with different formulations for the momentum diffusion. The horizontal diffusion in FVCOM can be closed choosing between a constant value or the Smagorinsky eddy parametrization method (Smagorinsky, 1963). The Smagorinsky eddy parametrization, defines the horizontal diffusion coefficient as:

$$A_m = 0.5C\Omega^u \sqrt{\left(\frac{\partial u}{\partial x}\right)^2 + 0.5\left(\frac{\partial v}{\partial x}\frac{\partial u}{\partial y}\right) + \left(\frac{\partial v}{\partial y}\right)^2} \tag{4.17}$$

Where C is the Smagorinsky constant and Ω^u is the the area of the individual momentum control element. A similar formulation is applied for the temperature diffusion:

$$A_m = \frac{0.5C\Omega^\zeta}{Pr} \sqrt{\left(\frac{\partial u}{\partial x}\right)^2 + 0.5\left(\frac{\partial v}{\partial x}\frac{\partial u}{\partial y}\right) + \left(\frac{\partial v}{\partial y}\right)^2} \tag{4.18}$$

Where Pr is the Prandtl number. The vertical diffusion in the model is parametrized using the Mellor and Yamada level 2.5 approach for both the vertical eddy viscosity and for the vertical thermal diffusion (Mellor and Yamada, 1982), including the upper and lower limits of the stability function (Galperin et al., 1988), the wind-driven surface wave breaking-induced turbulent energy (Mellor and Blumberg, 2004); and an improved parameterization of pressure-strain covariance and shear instability-induced

mixing that is very important in strongly stratified region, such as the Clyde Sea (Kantha and Clayson, 1994). The Mellor and Yamada (1982) is implemented in FVCOM as a function of the turbulent kinetic energy (TKE) q^2:

$$\frac{\partial q^2}{\partial t} + u\frac{\partial q^2}{\partial x} + v\frac{\partial q^2}{\partial y} + w\frac{\partial q^2}{\partial z} = 2\left(P_s + P_b - \epsilon\right) + \frac{\partial}{\partial z}\left(K_q\frac{\partial q^2}{\partial z}\right) + F_q \tag{4.19}$$

$$\frac{\partial q^2 l}{\partial t} + u\frac{\partial q^2 l}{\partial x} + v\frac{\partial q^2 l}{\partial y} + w\frac{\partial q^2 l}{\partial z} = lE_1\left(P_s + P_b - \frac{\tilde{W}}{E_1}\right) + \frac{\partial}{\partial z}\left(K_q\frac{\partial q^2 l}{\partial z}\right) + F_l \tag{4.20}$$

where $q^2 = (u'^2 + v'^2)/2$ is the TKE, l is the turbulent macroscale, K_q is the vertical eddy diffusion coefficient, F_q and F_l are the horizontal diffusion of the TKE and the macroscale respectively, P_s and P_b are the shear and the buoyancy terms respectively of the turbulent kinetic energy, while ϵ is the dissipation rate of the turbulent kinetic energy, and $\tilde{W}$ is the wall proximity function that depends on the von Karman constant.

The unstructured grid approach, used in FVCOM is a relatively new approach in geophysics computational fluid dynamics (Ferziger and Perić, 2002). The advantage of this approach is that an unstructured grid can represent complex coastlines better than a regular grid and have therefore a realistically simulation of the flow, enabling the geography of the coastline to effect the propagation of tidal and surface waves in a realistic manner. The computational grid for the present work was generated using SMS, a commercial software by Aquaveo, that is used for generating complex grids and also for preprocessing and postprocessing geophysical data. This software was used because FVCOM has some quality requirements for the computational grid, that are mandatory in order to run the model correctly, that are specified in the user manual (Chen et al., 2006b). In particular the computational grid should have these features:

- Minimum interior angle of each element: 30°
- Maximum interior angle of each element: 120°

- Maximum slope: 0.1
- Element area change: 0.5
- Connecting elements: should be less than 8 for each node

The grid was generated with the boundaries far away from the area in study. This in order to avoid that boundary noise would influence the circulation in the area in study and preventing the Clyde Sea from unphysical speeds or water elevations.

4.2.1 Atmosphere heating

The FVCOM model has two ways of implementing the radiation from the atmosphere as input to the model. The first is the $heating\_on$, in which the user specifies directly in the model the radiation fluxes: the net shortwave radiation, the net longwave radiation, the total net radiation, the sensible and the latent heat fluxes. The model uses these fluxes, togheter with the advection of temperature and salinity from the boundaries and the evaporation/precipitation flux to compute the temperature and the salinity in each point of the model. This approach is very useful when a Weather Research and Forecasting (WRF) Model of the region in study is available, since all the information can be transferred from one model to another.
The WRF is a next-generation mesoscale numerical weather prediction model designed for both operational research and for numerical prediction of the atmospheric circulation. Another possibility is the $heating\_calculated\_on$ approach, in which the model itself calculated the net radiation fluxes and the sensible/latent heat flux. This approach is very useful when only coarse data of the net radiation are available. The input in this case are: the Solar shortwave radiation flux, the Solar longwave radiation flow, the atmospheric temperature above the sea (usually the 2 m temperature), the mean sea level pressure, the relative humidity (in %) and the evaporation/precipitation flux.

4.2.2 FVCOM particle tracking

There are two ways of simulating the trajectories of the particles in the flow using FVCOM. First, there is an online (the particle tracking is run at the same time as the model) module, that simulate the path of particles in the area at the same time that the model is running. The obvious problem of this module is that it slows down the simulation, in particular when a particle passes from a subdomain to another. The offline code, instead, runs separately from the FVCOM simulation: it uses the NetCDF files generated by FVCOM to simulate the trajectories of the particles.
In both cases, the Lagrangian particle tracking module in FVCOM consists of solving a nonlinear system of ordinary differential equations (ODE):

$$\frac{d\overrightarrow{x}}{dt} = \overrightarrow{v}\left(\overrightarrow{x}(t), t\right) \tag{4.21}$$

where $\overrightarrow{x}$ is the position of the particle at the time t, $d\overrightarrow{x}/dt$ is the rate of change of the position in time, and $\overrightarrow{v}$ is the current velocity field generated by the model. The ODEs are solved by the FVCOM particle tracking using an explicit Runge-Kutta (ERK) multi-step method. In addition, this module can also account for the sub-grid scale turbulence using a random-walk type process.

4.3 Datasets description

4.3.1 Model Forcing

The model forcing data, are summarized here in tables. Table 4.1 lists the sources for the Clyde Sea. Rivers data provided by SEPA are reported in Table 4.2, while in the following table (Table 4.3) the features of those rivers, such as catchment, is given. Tide gauges used for evaluating residuals for the Clyde Sea model are described in

Table 4.4.

In the next section will be described the procedure used for the set-up of the model using these input data.

Variable	Source	Time res.	Spat. res.	Reference
Bathymetry	GEBCO	N/A	30" x 30"	Fisher et al. (1982)
Bathymetry	SeaZone	N/A	$< 100m$	N/A
Coastline	GSHHG	N/A	$< 1km$	Wessel and Smith (1996)
Tides	OTPS	15 min	2' x 2'	Egbert et al. (2010)
Wind	ERA-Interim ECMWF	3 hs	1/8° x 1/8°	Dee et al. (2011)
Pressure	ERA-Interim ECMWF	3 hs	1/8° x 1/8°	Dee et al. (2011)
Rivers	SEPA	Tab. 4.3-4.4	Tab. 4.3-4.4	N/A
Residuals	BODC	Tab. 4.5	Tab. 4.5	N/A
Precipitation	ERA-Interim ECMWF	3 hs	1/8° x 1/8°	Dee et al. (2011)
Evaporation	ERA-Interim ECMWF	3 hs	1/8° x 1/8°	Dee et al. (2011)
Solar Radiation	NCEP/NCAR	6 hs	1° x 1°	Kalnay et al. (1996)
Latent Heat	NCEP/NCAR	6 hs	1° x 1°	Kalnay et al. (1996)
Sensible Heat	NCEP/NCAR	6 hs	1° x 1°	Kalnay et al. (1996)
Air Temperature	NCEP/NCAR	6 hs	1° x 1°	Kalnay et al. (1996)
Relative Humidity	NCEP/NCAR	6 hs	1° x 1°	Kalnay et al. (1996)
SST	ERA-Interim ECMWF	3 hs	1/8° x 1/8°	Dee et al. (2011)

TABLE 4.1: Clyde model initial conditions and forcings

Name	Station	Temporal res.	Latitude (°)	Longitude (°)
Doon	Auchendrane	15 min	55.410	-4.627
Stinchar	Balnowlart	15 min	55.107	-4.968
Clyde	Daldowie	15 min	55.830	-4.122
Little Eichaig	Dalinlongart	15 min	55.995	-4.980
Carradale	Dippen	15 min	55.583	-5.497
Ayr	Mainholm	15 min	55.461	-4.593
Girvan	Robstone	15 min	55.259	-4.808
Irvine	Shewalton	15 min	55.597	-4.628

TABLE 4.2: Location of the river data provided by Scottish Environmental Protection Agency (SEPA) for the Clyde model

Name	**Catchment** (km^2)	**Mean Flow** (m^3/s)	**Max Flow** (m^3/s)	**Period** *(years)*
Doon	323.8	7.641	-	1974-
Stinchar	341	10.713	177	1973-
Clyde	1903.1	48.192	464.81	1964-
Little Eichaig	30.8	1.789	13.04	1968-2008
Carradale	58.5	2.476	-	1995-
Ayr	574	15.943	231.08	1976-
Girvan	245.5	6.788	63.592	1963-
Irvine	380.7	9.689	324.43	1972-2011

TABLE 4.3: Flow data for the rivers in Table 3.3. The informations are from the National River Flow Archive (NRFA) for the Clyde model

Tide Gauge	**Latitude (°)**	**Longitude (°)**
Southern boundary		
Holyhead	53.308	-4.631
Workington	54.651	-3.568
Llandudno	53.332	-3.825
Port Erin*	54.09	-4.77
Northern boundary		
Tobemory	56.623	-6.064
Port Rush*	55.206	-6.657
Port Ellen*	55.63	-6.19

TABLE 4.4: List of tide gauges used for calculating the residuals. * those tide gauges are inside the model boundary and were also used for the validation of the model

4.3.2 Model set-up

This section describes how the model was set-up using the forcing data reported in the previous section. For the Clyde Sea, after the grid generation using SMS, a bathymetry file was generated from the interpolation of the GEBCO and SeaZone bathymetry with the grid. The resulting file contained the information of the interpolated bathymetry at each node of the grid. The interpolation was made with a triangular based interpolation. Using SMS the points of the grid corresponding to the open boundary of the model were also identified. This is fundamental because at the open boundaries tidal as well as surge and temperature/salinity information were provided in order to simulate the Clyde Sea and the North Channel hydrodynamic circulation.

Tidal boundary conditions were provided by OSU (Oregon State University) Tidal Prediction Software (OTPS), that is a free software developed by Egbert et al. (2010). The tidal predictions are based on water elevations recorded by TOPEX/Poseidon and Jason satellites, adjusted with tidal gauges from ports around the world. For the Clyde Sea model, the water elevations were extracted from OTPS with a timestep of 15 minutes. In order to account for the surges coming from the open boundaries, we used tide gauges reported in the Table 3.5: we extracted the residuals from these tide gauges and we added the residuals to the predicted tidal elevations for the boundaries. Temperature and salinity fields were also added at the boundaries using model outputs from a large scale model and from ECMWF sea surface temperature, while the salinity at the boundary was set from a monthly mean from a 10-years period simulation in POLCOMS from the ERSEM model for the UK shelf (Edwards et al., 2012). The initial conditions of the temperature model were set using a combination of ECWMF and the ERSEM model along with CTD observations.

4.3.3 Validation and calibration datasets

Table 4.5 reports the locations used for the water level validation for the Clyde Sea, in Table 4.6 are reported the locations for the validation of the tidal currents, in Table 4.7 are reported the temperature measurements in the Clyde for validating the run for 1986.

Tide Gauge	Tide Gauge Name	Latitude	Longitude	Provided by
A	Rothesay	55.84	-5.05	SEPA
B	Girvan	55.24	-4.87	SEPA
C	Tarbert	55.86	-5.41	SEPA
D	Portrush	55.21	-6.66	BODC
E	Port Erin	54.09	-4.77	BODC
F	Port Ellen	55.63	-6.19	BODC
G	Portpatrick	54.84	-5.12	BODC
H	Bangor	54.66	-5.67	BODC
I	Millport	55.75	-4.91	BODC
J	Campbeltown	55.43	-5.60	SEPA

TABLE 4.5: Position of the tide gauges used for the validation of the Clyde Sea model

4.3.4 Validation methods

For the tidal validation, the harmonic components were extracted from the recorded and modelled water level for the tide gauges reported in table 4.5. Tides can be expressed as a linear superposition of harmonic functions, called harmonic tidal constituents. These were firstly discovered by Darwin (1880), and then the theory was later improved by Doodson (1921). From this, later studies discovered that each component could be seen as a Kelvin wave propagating in the ocean (Munk et al., 1970; Miles, 1972).

These harmonic constituents of the tide are due to the combined effect of the gravitational attraction of the Moon and the Sun and the rotation of the Earth. The tidal components extracted from the observations in Table 4.5 and 4.7 were compared with the modelled tidal consituents. These tidal constituents were computed using the Matlab function UTide, developed by Codiga (2011).

For the validating tidal currents in the Clyde Sea were compared tidal ellipses, that are computed from the tidal analysis of the u and v components of the current as following: Given the tidal currents of the harmonic components:

$$u = a_u cos(\omega t - \phi_u) \tag{4.22}$$

No	BODC No	Lat	Lon	Source	σ	Instrument	Days
1	b0567289	55.47	-5.52	BODC	0.71	RCM	54
2	b0060980	55.39	-5.08	BODC	0.94	RCM	93
3	b0060979	55.39	-5.08	BODC	0.41	RCM	93
4	b0060955	55.39	-5.09	BODC	0.95	RCM	39
5	b0060943	55.39	-5.09	BODC	0.46	RCM	39
6	b0060906	55.37	-5.45	BODC	0.68	RCM	87
7	b0061031	55.37	-5.44	BODC	0.70	RCM	77
8	b0061067	55.37	-5.45	BODC	0.71	RCM	79
9	b0061079	55.33	-5.35	BODC	0.84	RCM	79
10	b0061055	55.33	-5.34	BODC	0.37	RCM	50
11	b0061043	55.33	-5.34	BODC	0.84	RCM	50
12	b0060931	55.33	-5.34	BODC	0.84	RCM	41
13	b0060918	55.33	-5.34	BODC	0.36	RCM	41
14	b0567032	55.28	-5.21	BODC	0.45	RCM	38
15	b0058582	55.28	-5.21	BODC	0.49	RCM	170
16	b0567216	55.28	-5.21	BODC	0.47	RCM	77
17	b0567148	55.28	-5.21	BODC	0.79	RCM	92
18	b0567136	55.28	-5.21	BODC	0.41	RCM	92
19	b0567124	55.24	-5.05	BODC	0.79	RCM	93
20	b0567112	55.24	-5.05	BODC	0.52	RCM	93
21	b0058570	55.23	-5.05	BODC	0.77	RCM	91
22	b0058569	55.23	-5.05	BODC	0.50	RCM	91
23	b0567185	55.23	-5.06	BODC	0.77	RCM	37
24	b0567056	55.23	-5.06	BODC	0.53	RCM	37
25	b0567100	55.22	-4.98	BODC	0.70	RCM	94
26	b0567228	55.22	-4.98	BODC	0.69	RCM	54
27	b0507968	55.01	-5.23	BODC	0.90	RCM	32
28	b0507956	55.01	-5.23	BODC	0.68	RCM	36
29	b0507944	55.01	-5.23	BODC	0.37	RCM	36
30	b0577038-b0576999	54.86	-5.22	BODC	0.87	RCM	98
31	b0577026-b0576987	54.86	-5.22	BODC	0.25	RCM	98
32	b0576766	54.79	-5.55	BODC	0.17	RCM	74
33	b0564507	54.75	-5.20	BODC	0.95	RCM	48
34	b0101298	54.73	-5.19	BODC	0.96	RCM	47
35	b0101286	54.73	-5.19	BODC	0.38	RCM	47
36	b0101305	54.71	-5.21	BODC	0.98	RCM	48
37	b0101329	54.69	-5.24	BODC	0.96	RCM	48
38	b0101317	54.69	-5.24	BODC	0.38	RCM	48
39	b0101330	54.66	-5.32	BODC	0.42	RCM	33
40	b0564439	54.55	-5.16	BODC	0.84	RCM	44

TABLE 4.6: Position of the current observations used for the validation of the Clyde Sea model

No	BODC No	Lat	Lon	Source	Date	Time	Instrument
1T	709768	54.26867	-5.35967	BODC	21/03/2005	15:11	CTD
2T	709781	54.01083	-5.26350	BODC	21/03/2005	18:29	CTD
3T	709873	55.98283	-7.33467	BODC	25/03/2005	10:24	CTD
4T	709885	56.18183	-7.39850	BODC	25/03/2005	12:57	CTD
5T	709897	56.44133	-6.68617	BODC	25/03/2005	16:11	CTD
6T	713614	54.54417	-5.19100	BODC	24/11/2005	08:16	CTD
7T	713626	54.33650	-4.95267	BODC	24/11/2005	09:51	CTD
8T	713638	54.02383	-5.20967	BODC	24/11/2005	13:00	CTD
9T	713755	55.43817	-4.85683	BODC	28/11/2005	07:57	CTD
10T	713767	55.28817	-5.18950	BODC	28/11/2005	09:26	CTD
11T	713779	55.41100	-6.74950	BODC	28/11/2005	15:08	CTD
12T	713927	55.93900	-6.68683	BODC	02/12/2005	08:04	CTD
13T	713939	55.99483	-7.21367	BODC	02/12/2005	09:55	CTD
14T	713952	56.36067	-6.84050	BODC	02/12/2005	15:07	CTD
15T	720149	55.95433	-6.63117	BODC	18/03/2005	18:31	CTD
16T	720150	55.46283	-4.82000	BODC	19/03/2005	05:58	CTD
17T	720162	55.30183	-5.18333	BODC	19/03/2005	08:19	CTD
18T	720174	54.72500	-5.69850	BODC	19/03/2005	14:13	CTD
19T	720186	54.51533	-5.21000	BODC	19/03/2005	18:21	CTD
20T	720291	54.27033	-5.00183	BODC	21/03/2005	12:44	CTD

TABLE 4.7: Position of the temperature observations used for the validation of the Clyde Sea model

$$v = a_v cos(\omega t - \phi_v) \tag{4.23}$$

Where a_u and a_v are the harmonic amplitudes of u and v respectively evaluated from the harmonic analysis, ϕ_u and ϕ_v are the harmonic phases, while ω is the tidal angular frequency that depends only on the period of the tidal wave associated to each harmonic components.

We can then define the complex current w as:

$$w = u + iv \tag{4.24}$$

Now, tracing the w on the Argand plane, the result is an ellipse.

$$w = u + iv = a_u cos(\omega t - \phi_u) + i a_v cos(\omega t - \phi_v) \tag{4.25}$$

Then using the Euler's formula:

$$w = \frac{a_u \left(e^{i(\omega t - \phi_u)} + e^{-i(\omega t - \phi_u)}\right)}{2} + i\frac{a_v \left(e^{i(\omega t - \phi_v)} + e^{-i(\omega t - \phi_v)}\right)}{2} \tag{4.26}$$

$$w = \frac{a_u e^{-i\phi_u} + i a_v e^{-i\phi_v}}{2} e^{i\omega t} + \frac{a_u e^{i\phi_u} + i a_v e^{i\phi_v}}{2} e^{-i\omega t} = W_p e^{i(\omega + \theta_p)} + W_m e^{i(\omega + \theta_m)} \tag{4.27}$$

Then it is possible to evaluate the semimajor axis ($SEMA$), the semiminor axis ($SEMI$) and the phase (α):

$$SEMA = W_p + W_m \tag{4.28}$$

$$SEMI = W_p - W_m \tag{4.29}$$

$$\alpha = \frac{\theta_p + \theta_p}{2} \tag{4.30}$$

In order to evaluate the global performance of the model we considered the Root-Mean Square Error based on the difference between model and experimental harmonic components for all the tide gauges, in order to have the Root-Mean Square error for all the components for the model. The Root-Mean Square error (or $RMSE$) is defined as:

$$RMSE = \sqrt{\frac{1}{N}\sum_{i=1}^{N} (x_{o_i} - x_{m_i})^2} \tag{4.31}$$

For the comparison between modelled and recorded total water level, currents and waves we used, other statistical indicators, in order to evaluate the performance of the model against each observation.

$$Bias = \frac{1}{N}\sum_{i=1}^{N}\left(x_{o_i} - x_{m_i}\right) \tag{4.32}$$

$$RMSE = \sqrt{\frac{1}{N}\sum_{i=1}^{N}\left(x_{o_i} - x_{m_i}\right)^2} \tag{4.33}$$

$$R = \frac{\sum_{i=1}^{N}\left(x_{o_i} - \overline{x}_o\right)\left(x_{m_i} - \overline{x}_m\right)}{\sqrt{\sum_{i=1}^{N}\left(x_{o_i} - \overline{x}_o\right)^2\left(x_{m_i} - \overline{x}_m\right)^2}} \tag{4.34}$$

$$SI = \frac{RMSE}{\overline{x}_o} \tag{4.35}$$

$$NRMSE = \frac{RMSE}{max(x) - min(x)} \tag{4.36}$$

Chapter 5

Clyde Sea

5.1 Introduction

This chapter reports the process of validation, calibration, and the results from the FVCOM model of the Clyde Sea. The model was then used for the hindcasting of surge events in the Clyde Sea, in particular the stormy period November-December 2011.

5.2 Calibration and Validation

5.2.1 Grid generation and Calibration

The Clyde Sea model computational grid was generated following the quality requirements reported in the Chapter 4 and in the User FVCOM manual. It is composed of 30644 nodes, 56131 elements and extends from about the Isle of Mull in the North, to the central part of Irish Sea to the South. The spatial resolution in the Clyde and in North Channel is very fine: 1 km for the North Channel area, 600-800 m for the southern part of Clyde Sea, 300-400 m for the central part and about 100 m for the northern

sealochs and the estuary. The resolution at the open boundaries is approximately 7 km (Figure 5.1).

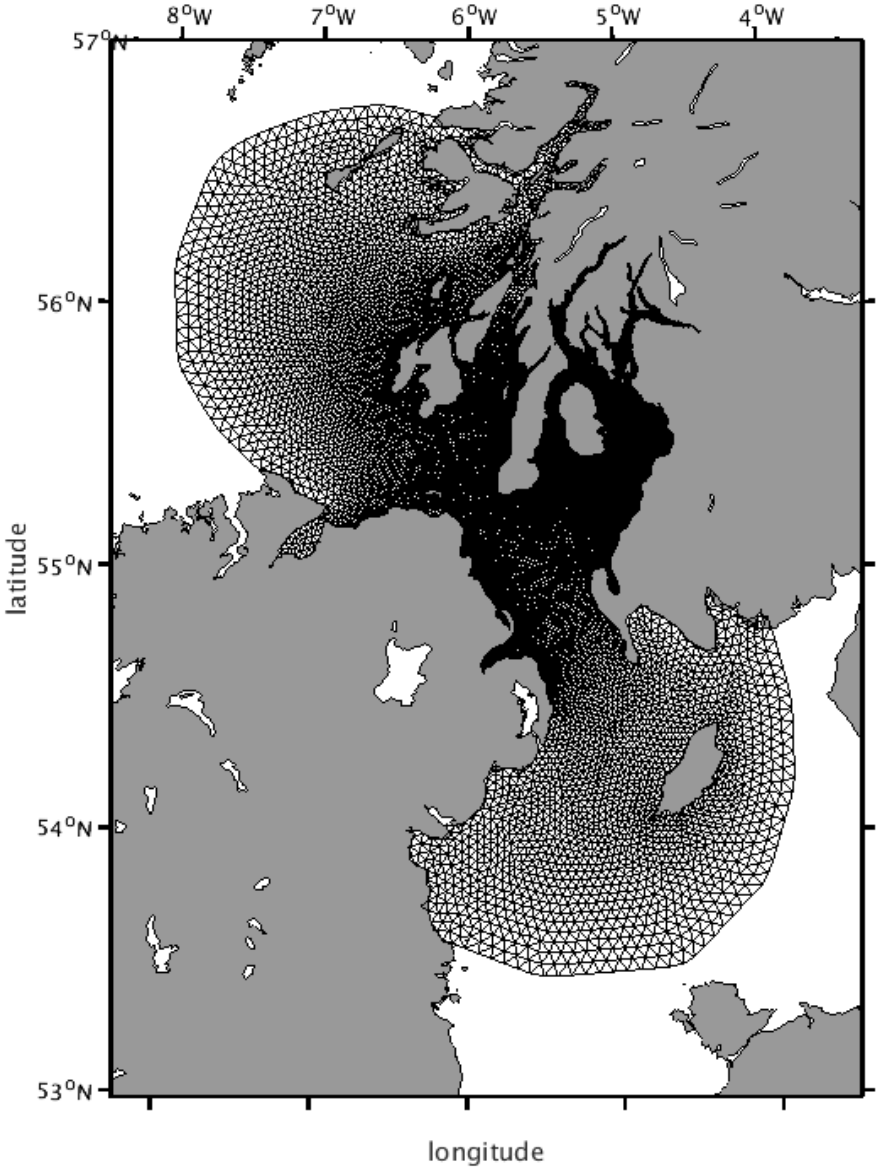

FIGURE 5.1: The computational grid generated with SMS used for the FVCOM Clyde Sea model

The Clyde model was firstly made in the FVCOM version 2.7.1: the calibration of the model was carried out for the year 2002 and was based on the agreement between the modelled and the observed tidal harmonic components in Millport. Initially the first calibration was based on three parameters only (Roughness Length, Sponge Layer extension and damping coefficient). Successively this calibration was extended to other variables for a fine tuning calibration. However, this fine tuning was carried out successively when the model was updated from the version 2.7.1 to the version 3.1.6. In this case, the calibration of the model was repeated and a definitive set of run parameters was chosen. The calibration was carried out with the timestep of 1 s. After the calibration reported here another calibration was made in order to verify if for higher timestep the model was still stable, however unfortunately it was not.

In Table 5.1 we report the initial set of set-up parameters used for the calibration of the model. This set does not include all the set-up parameters that gave a blow-up as a result of the simulation, but only the successful parameters that gave a stable run. The results (Table 5.2) are the difference between the modelled and the observed harmonic components in Millport based on a 7 months run (1 month spin-up and 6 months of run). Based on the differences between the model and the observed components, the set FoCEx 17 was initially chosen, then we decided to update the model to the version 3.

The code name of the model in version 2.7.1 was FoCEx (Firth of Clyde Extended), since the first mesh (FoC) was not extended to boundaries reported in the Figure 5.1, but was only limited to the Firth of Clyde (from Corsewell point to the Mull of Kintyre). The mesh was, then, changed due to unphysical speeds at the boundaries. Successively, the code name of the model changed in FoCN (Firth of Clyde New) when updated in the version 3.1.6 and in FoCNh (Firth of Clyde New heating) for the baroclinic version, where the temperature and salinity and the external radiation were added as input for the model.

Model	Roughness (m)	Sponge Layer (m)	Viscosity
FoCEx 1	0.0026	10000	0.01
FoCEx 2	0.0026	8000	0.01
FoCEx 3	0.0026	9000	0.01
FoCEx 4	0.0026	8500	0.01
FoCEx 5	0.0035	8500	0.01
FoCEx 6	0.0026	8500	0.05
FoCEx 7	0.0026	8500	0.1
FoCEx 8	0.0026	8500	0.02
FoCEx 9	0.0026	8500	0.005
FoCEx 10	0.0050	8500	0.01
FoCEx 11	0.0050	6000	0.01
FoCEx 12	0.0026	7000	0.01
FoCEx 13	0.0026	3000	0.01
FoCEx 14	0.0026	4000	0.01
FoCEx 15	0.0026	4500	0.01
FoCEx 16	0.0026	4500	0.0095
FoCEx 17	0.0026	3500	0.01
FoCEX 18	0.0026	3500	0.0095
FoCEx 19	0.0026	3250	0.009
FoCEx 20	0.0026	3500	0.011
FoCEx 21	0.0026	3750	0.01
FoCEx 22	0.0026	5500	0.01

TABLE 5.1: The set of parameters for the different successful runs done for the calibration of the FoCEx model for the FVCOM version 2.7.1

	1	2	3	4	5	6	7	8	9	10	11	12	13	14	15	16	17	18	19	20	21	22
$M_{2(a)}$	-8	4	-2	-2	1	-60	-77	-26	14	0	9	6	-6	9	14	14	0	0	-5	0	6	12
$M_{2(p)}$	10	9	11	10	11	29	33	20	3	13	8	8	-6	-2	1	0	-6	-6	-7	-6	-4	4
$S_{2(a)}$	4	-1	-2	-1.5	-2	-16	-21	-8	4	-2	3	2	-4	2.4	4	4	-1	-1	-3	-1	0.7	4
$S_{2(p)}$	21	18	19	18	20	35	44	25	13	22	18	15	9	11	12	12	10	12	6	10	13	13
$N_{2(a)}$	-5	-4	-5	-4	-4	-13	-16	-8	-1	-4	-2	-2	-5	-2	-1	-1	-4	-4	-4	-4	-3	1
$N_{2(p)}$	18	14	16	15	16	32	36	23	10	18	16	14	6	7	9	8	3	3	4	3	5	11
$K_{1(a)}$	1.5	2	2	2	2	-4	-7	0.5	1.3	2	1	1	0.7	1	1	1	1	1	1	1	1	1
$K_{1(p)}$	180	16	18	16	17	46	59	27	14	19	18	17	12	11	12	12	10	10	6	10	10	15
$O_{1(a)}$	-0.3	0	-0.1	0	0	-4	-7	-1	0.3	0	0.2	0.1	0.2	0.3	0.3	0.2	0.3	0.3	0.2	0.3	0.3	0.2
$O_{1(p)}$	15	11	13	12	13	44	59	22	5	14	9	9	2	3	4	9	0.8	0.8	0.9	0.9	1.3	7

TABLE 5.2: Difference between the modelled and the observed tidal harmonic component for the Millport tide gauge, for each set of parameter reported in Table 5.1. When no sign is in front of the number means positive deviation of the model compared with the observed value; (a) is referred as the amplitude of the harmonic component (cm), while (p) is for the phase ($^{\circ}$).

The first attempt for the version 3.1.6 for the calibration was made using the same setting of parameter for the version 2.7.1. However, unfortunately, the model had a blow-up, due to unrealistic high speed at the boundaries. Due to this inconvenient, we decided to set a larger sponge layer, with the same damping coefficient: the first attempt was around 7-8 km, the second around 10-11 km. After a similar calibration procedure carried out for the FVCOM 2.7.1, the FVCOM model was calibrated.

Then, a fine tuning calibration based on the other parameters was carried out. The calibration was maintained the same also for the surge model, since the validation of the model based on the harmonic coefficient was the same as the tidal model. A sensitivity analysis on the number of the sigma layers was also carried out: we concluded that small or no changes in the water level harmonic components and in the total water level were present when changing the numbers of the sigma layers.

The model was run on the cluster of the Centre for Numerical Algorithms and Intelligent Software (NAIS), that is a partnership of the Schools of Mathematics and Informatics and the Edinburgh Parallel Computing Centre (EPCC) at the University of Edinburgh, and the Departments of Mathematics at Heriot-Watt and Strathclyde University. A sensitivity analysis based on the number of nodes was made, in order to see which was the fastest solution for running the Clyde Sea model. This analysis was carried out in collaboration with Ian Thurlbeck: we found out that, since the architecture of the cluster, the best solution was to run the model on 16 nodes, since after this value the model was running at a lower speed. For a 1-year simulation, with 11 layers and without temperature and salinity as input for the model, the average time was 7 days.

A new re-calibration of the model was carried out when temperature and salinity were added to the model, in order to simulate the baroclinic circulation of the Clyde Sea.

Both of the two possible solutions in FVCOM for the inclusion of the temperature/salinity/heating in the model were implemented: the $heating\_on$ and the $heating\_calculated\_on$. The first is based on specifying directly the net radiation fluxes from the atmosphere: the net longwave radiation flux, the net shortwave radiation flux, the net radiation flux,

the sensible heat flux and the latent heat flux. This first attempt, after a long calibration procedure based on the change of different parameters such as the mixing coefficients, and - most importantly - the timestep, was unsuccessful, since a pronunced cold bias in shallow areas was present.

Some stable runs for 200 days were made, but with the exclusion from the computation of shallow areas of the Clyde Sea. Since this, we decided to use the second approach for simulating the temperature and salinity in the Clyde Sea. The $heating\_calculated\_on$ approach is based on the calculation of the net fluxes directly from the model: the user have to specify the solar downward radiation fluxes (longwave and shortwave) and the atmospheric conditions (relative humidity, atmosphere temperature, mean sea level pressure, and the evaporation/precipitation fluxes).

The calibration of the model was mostly based on the stability of the model and on the agreement of the model output with temperature measurement in the Clyde Sea for the year 1986.

The final set-up of the model is reported in Table 5.3.

Variable	**Value**
External Timestep[1]	1 s
Internal time split[1]	1
External Timestep[2]	0.2 s
Internal time split[2]	10
Smagorinsky constant	0.2
Horizontal Prandtl number	1.0
Vertical Prandtl number	1.0
Horizontal mixing coefficient	0.4
Vertical mixing coefficient	10^{-6}
Minimum Bottom Roughness	0.0024 m
Roughness length	0.001 m
Sponge layer	11 km
Damping coefficient	0.008
Boundary temperature nudging timescale	0.005
Boundary salinity nudging timescale	0.005

TABLE 5.3: Parameters of the model after the calibration procedure: for the timestep, two values are reported: [1] is for the barotropic Clyde Sea model, with no temperature and salinity included, while [2] is for the baroclinic model

5.2.2 Model validation

After the calibration of the model reported above, the model was then validated. In the Section 4.4.4 the validation procedure is reported and, most importantly, the statistical parameters used in this section are explained.
The model was run for the entire 2007 (1 month spin up time: December 2006) for the initial validation, in barotropic mode, with 10 vertical layers. Three different validation procedures were adopted to validate the barotropic model:

1. The harmonic components (amplitude and phase) were extracted the $UTide$ MatLab script in the model corresponding locations to the tide gauges observations available (Table 4.6), then the modelled and the observed main diurnal and semidiurnal harmonic components were compared (Table 5.4 and 5.5 for the results).

2. The total water level predicted by the model was compared with the observed total water level from the tide gauges in Table 4.6 (Table 5.6).

3. The harmonic components (amplitude and phase) were extracted the $UTide$ MatLab script in the model corresponding locations to the current observations available (Table 4.7), then the semimajor (SEMA), semiminor (SEMI) axes and the phase were estimated for both model and observations and compared (Table 5.8-5.9 for the results).

Table 5.4 and 5.5 shows that the model performs reasonably well against tidal component (both diurnal and semidiurnal). In particular, the main component in the Clyde Sea and in the North Channel is the M_2 component. Considering the results from the ten tide gauges above, the Root-Mean Square Error for the M_2 is 1.19 cm and 7.06 $^\circ$ for the amplitude and the phase respectively.

	M_2				S_2				N_2			
	h_o	g_o	h_m	g_m	h_o	g_o	h_m	g_m	h_o	g_o	h_m	g_m
A	118	342	117	342	31.8	35.3	29.4	38.2	22.2	315	20.8	318
B	108	347	106	338	28.9	40.4	26.4	33.4	20.5	321	18.9	314
C	115	344	115	342	31.2	37.2	28.8	38.5	21.7	317	20.4	318
D	53.1	199	54.1	199	22.7	212	24	211	11.7	176	11.8	171
E	184	322	184	323	56.3	1.55	54.5	5.81	35.7	297	34.1	299
F	15.6	85.7	15.7	65.4	13.9	151	14.6	150	2.23	74.4	2.93	61
G	136	332	137	332	38.4	16.9	37	18.4	25.9	306	25	307
H	118	317	119	317	30.4	0.574	28.4	0.626	22.5	291	21.3	291
I	113	342	115	341	30.5	34.7	28.9	37.7	21.7	317	20.5	317
J	105	344	104	344	28.1	36.7	25.8	41.1	20	317	18.5	320

TABLE 5.4: Comparison of the observed and modelled amplitude and phase for dominant semi-diurnal tidal components h_0 and g_0 are the observed amplitude in cm and the phase degrees respectively and h_m and g_m are the modelled amplitude in cm and the phase degrees

	K_1				O_1			
	h_o	g_o	h_m	g_m	h_o	g_o	h_m	g_m
A	11.4	192	10.9	192	10	45.6	10.2	47.4
B	10.9	195	10.6	190	10.1	46.6	10	45.8
C	11.4	191	10.8	192	10.3	44.6	10.2	47.6
D	9.53	174	9.51	166	8.70	28.2	8.29	28
E	11.2	189	11.8	192	10.3	40.6	10.9	44.9
F	9.44	187	8.66	185	8.56	40.5	8.31	44.6
G	11	190	11.2	191	10	42.9	10.3	45.1
H	10.7	188	11.3	185	10.3	36.3	10.2	40.8
I	11.5	192	10.9	191	10.1	44.1	10.2	47.1
J	11.1	191	10.6	193	9.92	45.8	9.98	48.3

TABLE 5.5: Comparison of the observed and modelled amplitude and phase for dominant diurnal tidal components h_0 and g_0 are the observed amplitude in cm and the phase degrees respectively and h_m and g_m are the modelled amplitude in cm and the phase degrees

Location	**Bias (m)**	**RMSE (m)**	**NRMSE**	R^2
Millport (I)	-0.004	0.164	0.039	0.966
Bangor (H)	-0.003	0.134	0.033	0.978
Portpatrick (G)	-0.003	0.135	0.029	0.983
Port Rush (D)	-0.001	0.112	0.043	0.943
Port Erin (E)	-0.004	0.145	0.024	0.989

TABLE 5.6: Statistical analysis of the surge model performance

We also calculated the performance of the model during the storm period studied in the surge chapter (November-December 2011 - Table 5.7).

Location	Bias (m)	RMSE (m)	NRMSE	R^2
Millport (I)	-0.002	0.148	0.036	0.973
Bangor (H)	-0.003	0.115	0.026	0.984
Portpatrick (G)	0.009	0.127	0.027	0.987
Port Rush (D)	0.003	0.084	0.033	0.970
Port Ellen (F)	-	-	-	-
Port Erin (E)	0.009	0.143	0.025	0.990
Girvan (B)	-0.002	0.123	0.031	0.979
Tarbert (C)	-0.007	0.311	0.062	0.889

TABLE 5.7: Statistical analysis of the surge model performance during November-December 2011. In Port Ellen tide gauge there were no valid data for the comparison

The Root-Mean Square for the total water level does not exceed 20 cm and 5 $\%$ of the total water level. Analyzing the residuals between modelled and recorded water level, it is possible to conclude that the model underestimate the total water level, but this quantity is very close to zero ($< 1cm$ for all the tide gauges considered).

It was also evaluated the performance of the model for currents. In Table 5.8-5.9 are reported the results of the validation of the current based on the performance with estimated tidal ellipses: in 5.8 we report the aggregated results based on the Root-Mean Square Error of the values reported in the Table 5.9.

Component	RMS error		
	SEMA (cm/s)	semi (cm/s)	α (°)
M_2	3.39	0.81	6.77
S_2	2.31	1.34	11.67
N_2	3.19	0.81	10.50

TABLE 5.8: Aggregated tidal ellipse RMS error for main harmonic components, from the data in table 5.9. SEMA is the semimajor axis (cm/s), semi is the semiminor axis (cm/s) and α (°) is the orientation of the semimajor axis

	M_2					S_2					N_2				
No	$Majo$	α_o	$Mino$	$Majm$	α_m	$Minm$	$Majo$	α_o	$Mino$	$Majm$	α_m	$Minm$	$Majo$	α_o	$Mino$	$Majm$	α_m	$Minm$
1	14.15	69.80	0.54	10.80	65.28	0.59	2.56	22.98	-0.12	3.13	65.23	0.10	3.79	15.07	-0.69	1.88	25.31	0.06
2	21.83	54.10	5.70	20.62	47.02	3.91	8.66	51.73	2.13	6.03	39.26	1.29	2.93	63.95	0.12	3.58	40.34	0.20
3	22.82	32.89	0.63	24.67	37.78	0.51	8.25	36.22	0.75	7.25	37.26	0.52	3.68	44.38	0.98	4.41	37.33	0.19
4	21.75	45.03	4.69	17.82	37.26	3.78	3.56	17.60	-0.56	5.20	39.00	1.15	5.13	45.87	-0.31	4.41	37.12	0.28
5	24.08	31.84	0.30	24.16	35.71	0.48	5.02	41.15	0.81	7.11	34.89	0.52	3.78	30.06	0.09	4.31	35.06	0.18
6	40.54	69.99	-1.60	39.02	68.30	-1.43	8.40	70.69	-0.83	11.33	67.92	-0.58	6.81	67.39	-0.25	6.87	66.11	-0.31
7	36.90	71.53	-0.21	37.64	66.32	-0.92	11.20	75.76	0.11	11.04	66.59	-0.42	6.95	78.91	0.07	6.76	74.87	-0.32
8	34.10	66.38	3.50	40.40	64.68	0.50	8.74	67.19	0.21	11.80	62.42	0.17	7.39	72.14	-0.08	7.29	78.33	0.34
9	22.90	20.55	7.75	21.14	33.50	2.86	5.90	26.84	1.12	9.39	31.85	2.08	5.78	18.49	0.59	5.42	24.90	0.72
10	35.60	34.19	-4.03	34.71	32.52	-1.63	10.00	28.39	1.42	10.57	30.26	1.24	6.61	14.32	0.11	6.08	15.00	-1.15
11	24.39	28.95	5.42	28.69	34.47	3.22	5.95	36.27	2.69	8.64	32.86	2.01	4.50	33.15	1.32	5.02	35.18	0.75
12	27.91	29.71	6.09	30.51	30.87	2.87	4.75	24.40	1.81	9.06	29.94	1.91	4.82	23.27	3.37	5.29	32.65	0.59
13	36.19	36.50	-1.86	35.23	29.50	-0.52	6.43	34.09	1.45	10.53	27.70	1.37	8.63	21.03	0.53	6.34	29.28	0.28
14	26.94	23.20	0.47	26.51	18.96	1.44	5.31	28.41	1.39	7.78	9.05	2.13	6.62	144.10	0.09	4.78	150.70	0.48
15	26.14	25.49	1.58	26.29	18.96	1.72	7.76	27.20	1.80	7.72	16.61	2.23	4.88	26.65	0.10	4.73	18.41	0.11
16	26.92	33.34	2.09	26.15	18.34	1.97	5.82	27.45	1.71	7.67	16.19	2.23	6.52	34.80	-0.77	4.73	17.50	0.12
17	22.57	22.70	5.23	23.94	18.75	3.83	8.40	25.30	3.11	7.02	16.93	2.68	3.98	31.00	0.52	4.27	18.99	0.79
18	28.19	22.06	1.46	26.37	18.41	1.68	9.59	23.92	2.47	7.76	16.08	2.26	4.28	20.57	0.60	4.78	17.39	0.52
19	18.22	36.36	3.57	16.28	27.12	4.21	6.55	42.08	1.65	5.20	33.29	2.44	3.56	29.82	0.22	3.08	28.16	0.00
20	15.76	42.23	4.13	17.20	28.27	3.28	6.32	59.96	1.70	5.46	33.69	2.32	2.45	43.72	1.52	3.17	27.67	0.82
21	17.04	33.05	3.70	16.17	26.69	4.23	4.80	36.65	1.41	5.21	32.12	0.47	4.64	38.16	0.16	2.94	27.22	0.31
22	15.31	42.43	3.67	17.16	28.13	3.14	4.77	53.41	1.23	5.48	32.48	2.24	3.16	53.68	1.23	3.18	26.47	0.79
23	17.17	31.92	4.12	16.04	24.95	4.44	3.55	45.60	0.65	5.10	31.50	2.71	3.33	31.01	1.00	2.90	25.85	0.95
24	16.48	35.95	3.03	16.91	26.15	3.47	3.69	47.06	1.03	5.39	32.76	0.46	2.56	46.03	0.59	3.12	48.03	0.82
25	13.71	40.59	1.45	13.78	40.45	2.38	5.83	44.98	0.94	4.55	47.38	1.24	2.23	36.73	0.50	2.47	41.94	0.52
26	12.48	37.33	1.52	13.51	40.35	2.36	3.70	40.48	-0.17	4.39	46.03	1.18	3.29	33.84	0.29	2.41	41.42	0.28
27	52.00	93.20	4.52	45.78	86.10	4.69	22.21	91.87	1.59	19.22	84.03	1.55	9.03	83.40	0.07	9.05	84.40	0.56
28	56.25	86.12	-1.19	52.09	84.38	2.06	23.81	85.31	0.14	22.03	82.38	0.76	9.32	84.29	-0.01	10.37	82.81	0.21
29	57.87	90.33	-2.38	57.09	83.67	-1.45	26.40	89.28	-0.78	24.22	81.51	-0.43	9.79	89.26	-0.03	11.43	81.88	-0.26
30	62.16	120.18	12.46	69.86	116.56	9.36	23.27	122.86	2.48	27.69	117.08	3.13	11.40	119.74	1.98	13.34	117.00	1.31
31	79.02	116.65	0.06	86.40	112.92	0.33	30.00	114.01	0.73	34.95	112.31	0.22	14.62	115.98	-0.10	16.92	112.44	0.15
32	74.72	127.40	-0.50	81.00	125.59	-0.06	27.08	124.67	1.00	31.74	125.89	1.10	11.59	125.09	1.20	15.89	126.70	0.57
33	50.89	122.87	15.01	56.74	121.63	8.23	14.38	122.23	3.42	22.21	122.25	2.81	11.46	116.77	1.43	10.96	122.77	1.33
34	53.18	115.86	9.88	56.35	114.10	6.76	16.78	121.63	3.03	21.77	114.54	2.53	11.23	119.56	1.37	10.76	115.00	1.13
35	76.26	121.40	-7.33	75.15	115.50	-5.15	25.67	118.72	-1.71	29.58	115.15	-0.45	16.11	95.70	1.87	14.89	115.00	-0.27
36	51.09	127.51	15.94	49.69	113.88	10.04	13.72	125.87	4.03	19.33	115.03	3.30	9.60	135.18	-1.27	9.64	114.00	-1.55
37	61.70	114.82	9.17	55.64	113.51	8.52	20.54	114.78	1.07	21.79	113.84	2.95	13.59	103.88	3.69	10.70	115.10	1.36
38	80.90	117.80	-5.85	78.06	112.58	-0.93	26.23	116.09	-1.57	31.36	112.00	-0.27	17.06	95.18	1.29	15.40	112.00	0.14
39	75.95	112.86	-4.95	80.08	111.26	-2.41	27.72	110.93	-1.49	32.20	110.92	-0.96	17.44	107.16	-0.93	15.85	110.46	-0.39
40	56.47	110.61	8.07	52.15	112.26	7.96	15.88	114.98	3.76	21.38	111.82	2.85	11.45	100.27	1.60	10.17	113.13	1.19

TABLE 5.9: Comparison of the modelled ($_m$) and observed ($_o$) computed semimajor, semiminor and phase (equations 4.44-4.46) for the locations reported in Table 4.7. Maj is the Semimajor axes, Min is the semiminor axes and α is the phase

The model, then, was run in baroclinic mode, in order to simulate more realistically the physical oceanography of the Clyde Sea. The model was run for the entire 2005 (January 2005: spin-up time).

The through-flow of the North Channel was given by Knight and Howarth (1999) and is about $(0.077 \pm 0.013)\, x10^6 m^3 s^{-1}$ with a positive residual flow of about 0.03 m/s, leading to a theoretical spin-up time of at least one year. However, before this 2005-2006 simulation, another entire year simulation (1986 year) was run, in order to understand if using a so-called 'hotstart' initial condition (defining the initial condition of the run) could reduce the spin-up time. We notice from the result of this simulation that 1 month spin-up time was a reasonable time for the spin-up of the model. Temperature and salinity were validated using CTD measurements in 2005-2006 in the North Channel and in the Clyde Sea obtained from BODC. Both salinity and temperature were recorded and this allowed us to compare the CTD measurements with the modelled values. The results of this validation are shown in the Table 5.10.

We also compared the predicted water level harmonic components of the baroclinic model with the harmonic components predicted by the barotropic model. The results are showed in Table 5.11.

Observation	**Temperature**			**Salinity**		
	Bias ($°C$)	*RMS* ($°C$)	*SI*	*Bias* (PSU)	*RMS* (PSU)	*SI*
709768	+0.170	0.292	0.038	-0.430	0.431	0.013
709781	-0.163	0.319	0.040	-0.180	0.190	0.006
709873	-1.113	1.210	0.128	-0.666	0.679	0.019
709885	-1.073	1.131	0.121	-0.656	0.664	0.019
709897	-0.136	0.350	0.043	-0.738	0.745	0.021
713614	-1.832	1.835	0.145	-0.223	0.228	0.007
713626	-1.550	1.562	0.124	+0.081	0.087	0.003
713638	-1.249	1.281	0.102	+0.185	0.186	0.006
713755	-1.141	1.184	0.106	-1.371	1.425	0.043
713767	-1.244	1.303	0.119	-1.945	1.963	0.059
713779	-1.422	1.436	0.126	-0.725	0.734	0.021
713927	-0.244	0.771	0.070	-0.206	0.253	0.007
713939	+0.186	0.446	0.040	-0.419	0.446	0.012
713952	-0.956	0.975	0.089	-0.025	0.069	0.002
720149	+0.068	0.125	0.016	-0.696	0.700	0.020
720150	+0.219	0.272	0.037	-1.597	1.602	0.048
720162	+0.140	0.237	0.032	-1.626	1.637	0.049
720174	-0.218	0.232	0.028	-1.061	1.062	0.031
720186	-0.144	0.171	0.022	-0.826	0.832	0.024
720291	+0.019	0.166	0.021	-0.427	0.433	0.013

TABLE 5.10: Performance of the model on temperature and salinity compared with available CTD observations in the area

	M_2				S_2				N_2				K_1				O_1			
	h_1	g_1	h_2	g_2	h_1	g_1	h_2	g_2	h_1	g_1	h_2	g_2	h_1	g_1	h_2	g_2	h_1	g_1	h_2	g_2
A	116	341	117	342	31.5	35.6	29.4	38.2	20.9	318	20.8	318	10.8	189	10.9	192	10.3	47.6	10.2	47.4
B	129	345	106	338	35.1	40.8	26.4	33.4	23.0	323	18.9	314	11.1	191	10.6	190	10.4	49.8	10	45.8
C	126	345	115	342	34.4	41.0	28.8	38.5	22.6	323	20.4	318	11.1	191	10.8	192	10.4	50.0	10.2	47.6
D	43.8	207	54.1	199	19.3	210	24	211	9.72	177	11.8	171	9.79	165	9.51	166	8.53	30.3	8.29	28
E	189	327	184	323	56.9	9.55	54.5	5.81	35.1	303	34.1	299	12.2	192	11.8	192	11.2	47.1	10.9	44.9
F	23.9	47.9	15.7	65.4	15.1	134	14.6	150	4.52	38.1	2.93	61	8.70	185	8.66	185	8.47	48.4	8.31	44.6
G	145	334	137	332	40.8	21.5	37	18.4	26.5	311	25	307	11.4	190	11.2	191	10.6	47.1	10.3	45.1
H	127	321	119	317	32.1	7.09	28.4	0.626	22.7	297	21.3	291	11.7	183	11.3	185	10.4	42.0	10.2	40.8
I	126	344	115	341	34.5	40.0	28.9	37.7	22.6	322	20.5	317	11.1	191	10.9	191	10.4	49.5	10.2	47.1
J	114	347	104	344	30.9	43.2	25.8	41.1	20.5	325	18.5	320	10.8	192	10.6	193	10.2	50.8	9.98	48.3

TABLE 5.11: Comparison of the baroclinic and barotropic modelled amplitude and phase for dominant water level tidal components h_1 and g_1 are the modelled baroclinic amplitude in cm and the phase in degrees respectively and h_2 and g_2 are the modelled barotropic amplitude in cm and the phase in degrees. The model parameters were the same, a part from the timestep

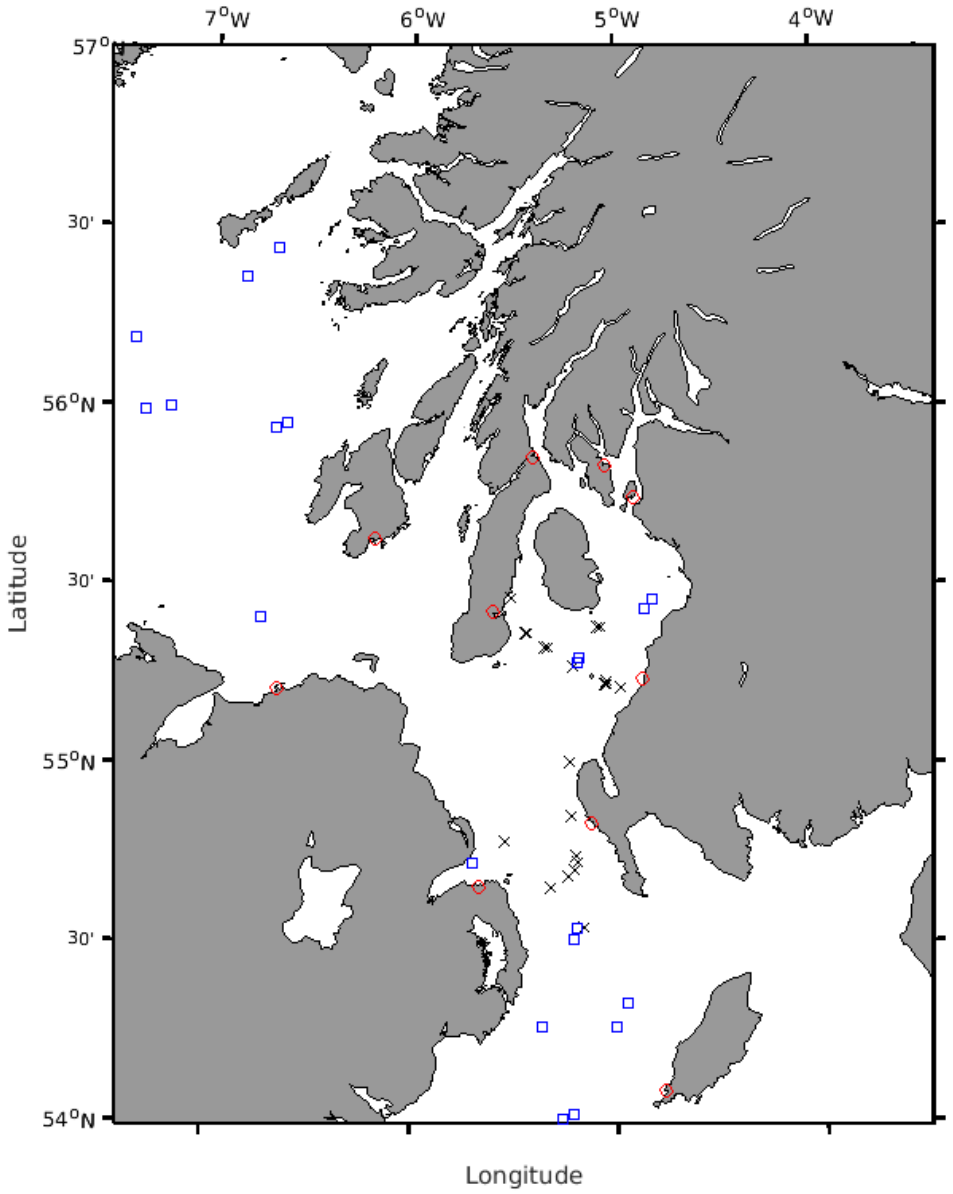

FIGURE 5.2: Position of the devices used for the validation of the model: red circles are tide gauges, black crosses are RCMs and blue squares are CTD

The model shows a discrete performance for both the salinity and the temperature: in particular the difference between modelled and observed salinity is very low, less than 1 PSU for most of the considered observations, while slightly underestimate the salinity in the Clyde Sea (see Figure 5.4). This underestimation is probably due to an overestimation of the river discharge. For the temperature, the model seems to have a strong cold bias (about 1-1.5$^{\circ}C$) compared with the observations in the month of November 2005, while in March the results are better. Table 5.11 shows that there are significant variation in the water level between barotropic and baroclinic model: the baroclinic run tends to have a slightly higher amplitude compared to the barotropic run: the combined effect of the salinity and the temperature changes the tidal wave amplitude and the phase. In the Figure 5.2 are shown all the locations in which the validation was performed and the kind of validation (water level, current or temperature/salinity). The spatial coverage of the observations was good for all the variables, but no observations were available for the *lochs* in the Clyde Sea. In the Figure 5.3 and 5.4, the spatial performances of the model for temperature and salinity respectively are shown.

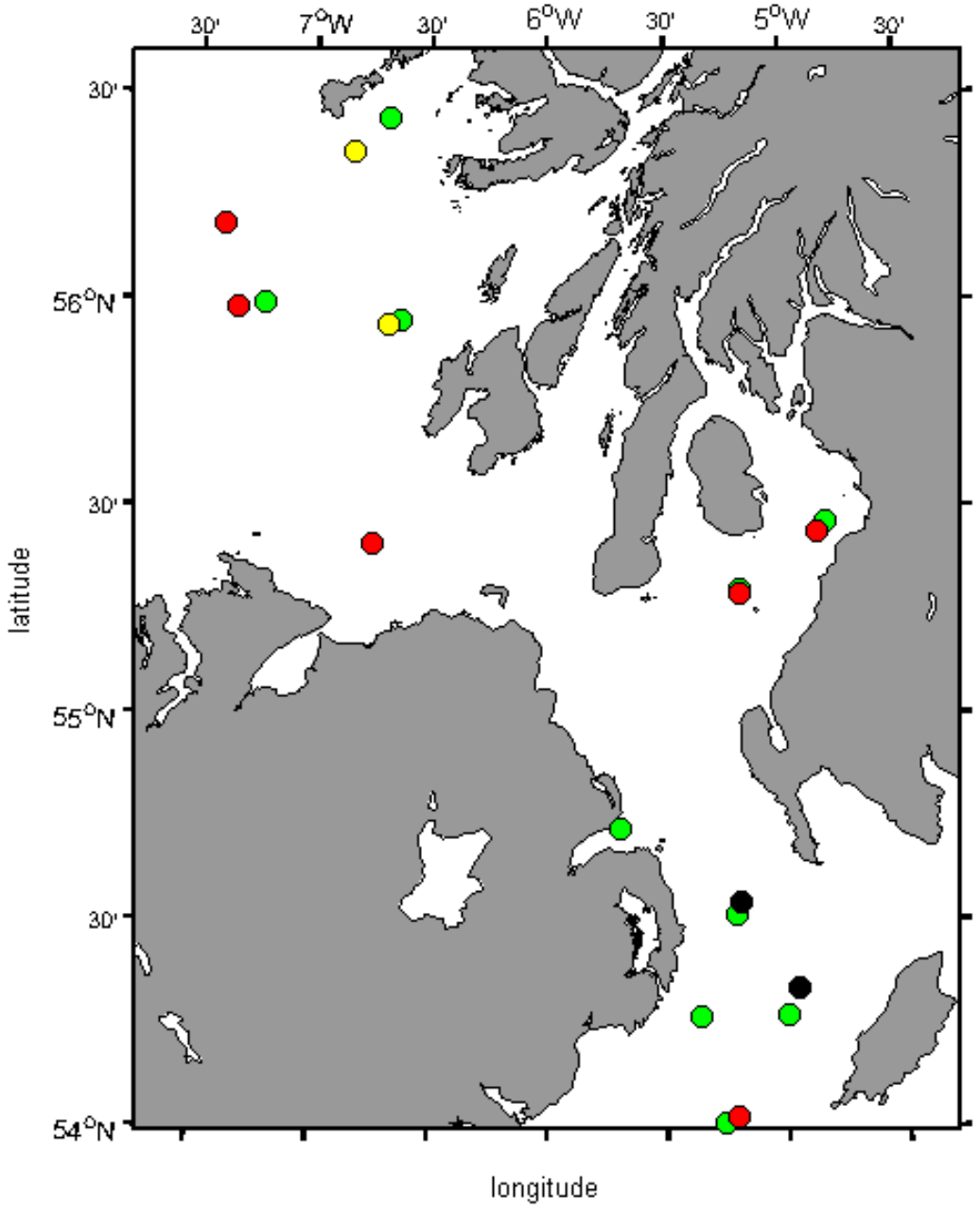

FIGURE 5.3: Performance of the Clyde Sea model in the observations in Figure 5.2 for temperature. Green points are observations with RMSE $< 0.5°C$, yellow points have RMSE between $0.5°C$ and $1°C$, red points have RMSE between $1.0°C$ and $1.5°C$, while black points are observations with RMSE $> 1.5°C$

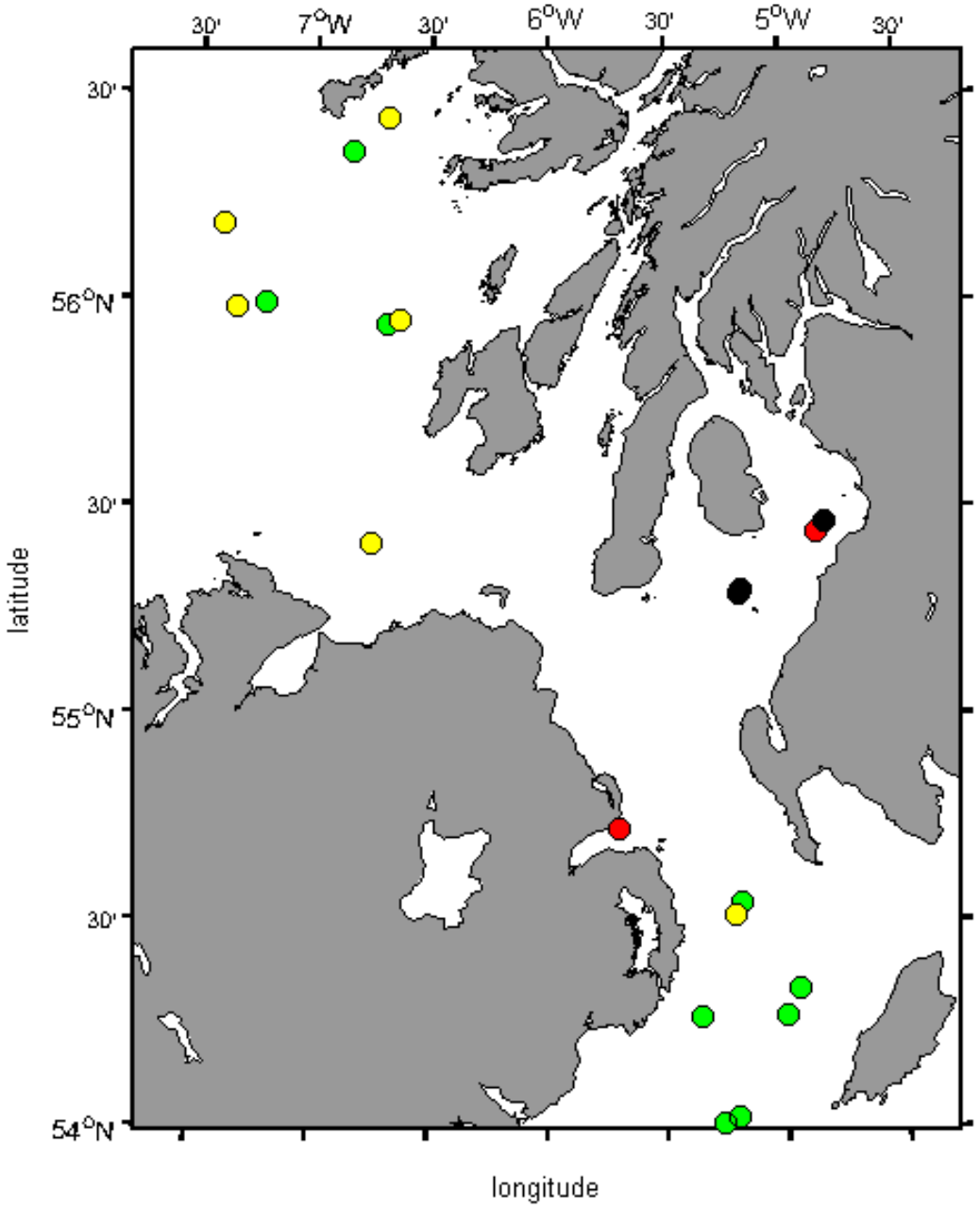

FIGURE 5.4: Performance of the Clyde Sea model in the observations in Figure 5.2 for salinity. Green points are observations with RMSE $< 0.5PSU$, yellow points have RMSE between $0.5PSU$ and $1PSU$, red points have RMSE between $1.0PSU$ and $1.5PSU$, while black points are observations with RMSE $> 1.5PSU$

5.3 Tidal circulation of the Clyde Sea

For understanding the tidal circulation in the Clyde Sea and in the North Channel, cotidal charts were computed. This allowed us to see how the tidal wave behavior in the Clyde Sea, and the effect of the deformation of the Kelvin wave due to the interaction with the coastline and the shallow bathymetry. Co-tidal charts are computed for the Clyde Sea for the main harmonic components (Figure 5.5-5.9). The cotidal charts were computed running the model in barotropic mode.

The Tidal Form parameter (TF) was also computed: this parameter is defined in Boon (2013) as the ratio of the sum of diurnal to semi-diurnal amplitudes.

$$TF = \frac{K_1 + O_1}{M_2 + S_2} \tag{5.1}$$

where K_1 and O_1 are the amplitudes of the two most dominate diurnal tidal components and M_2 and S_2 are the two most dominate semi-diurnal component (lunar and solar respectively). Different values of TF correspond to different tidal behaviors: if $TF < 0.25$ the tide is semi-diurnal, if $0.25 < TF < 1.5$ the tide is mixed semi-diurnal, if $1.5 < TF < 3$ the tide is mixed diurnal, if $TF > 3$ the tide is diurnal. This parameter is used usually to see if there are a part of the area in study which tidal circulation is not semi-diurnal. The figures 5.5-5.9 shows the propagation of the wave in the Clyde and its deformation due to the bathymetry and to the coastline, in particular in the fjordic area, in which the co-phase lines become parallel and no more perpendicular to the co-amplitude lines. Due to the high precision of the model in reproducing the tidal dynamics in the Clyde, the co-tidal charts here are at higher spatial resolution and more detailed than the previous charts, such as Davies et al. (2004) and Davies et al. (2001b).

Co-tidal lines are more dense near the Mull of Kintyre area, where stronger currents are expected, while they are more spaced in the Clyde itself. The tidal motion is one of the

main driver of the Clyde Sea: since this, the tidal motion is fundamental for all the processes linked to the sediment resuspension and to the habitat characterization: swell waves from the North Atlantic Ocean, in fact, does not penetrate further into the Clyde Sea and internally-generated wind sea waves does not exceed 1.2 m (Karunarathna, 2011).

The Tidal Form map (Figure 5.10) shows that in the North Channel the circulation is fully semi-diurnal, with very low values of F. In the northern part of the Irish Sea the tidal circulation is fully semi-diurnal, while north of the Mull of Kintyre the circulation becomes mixed semi-diurnal, and eventually diurnal near the amphidromic point of M_2 and S_2. The reason for this is mainly due to the presence of the amphidromic point for both M_2 and S_2 in this area, which causes higher values for diurnal components rather than the semi-diurnal components.

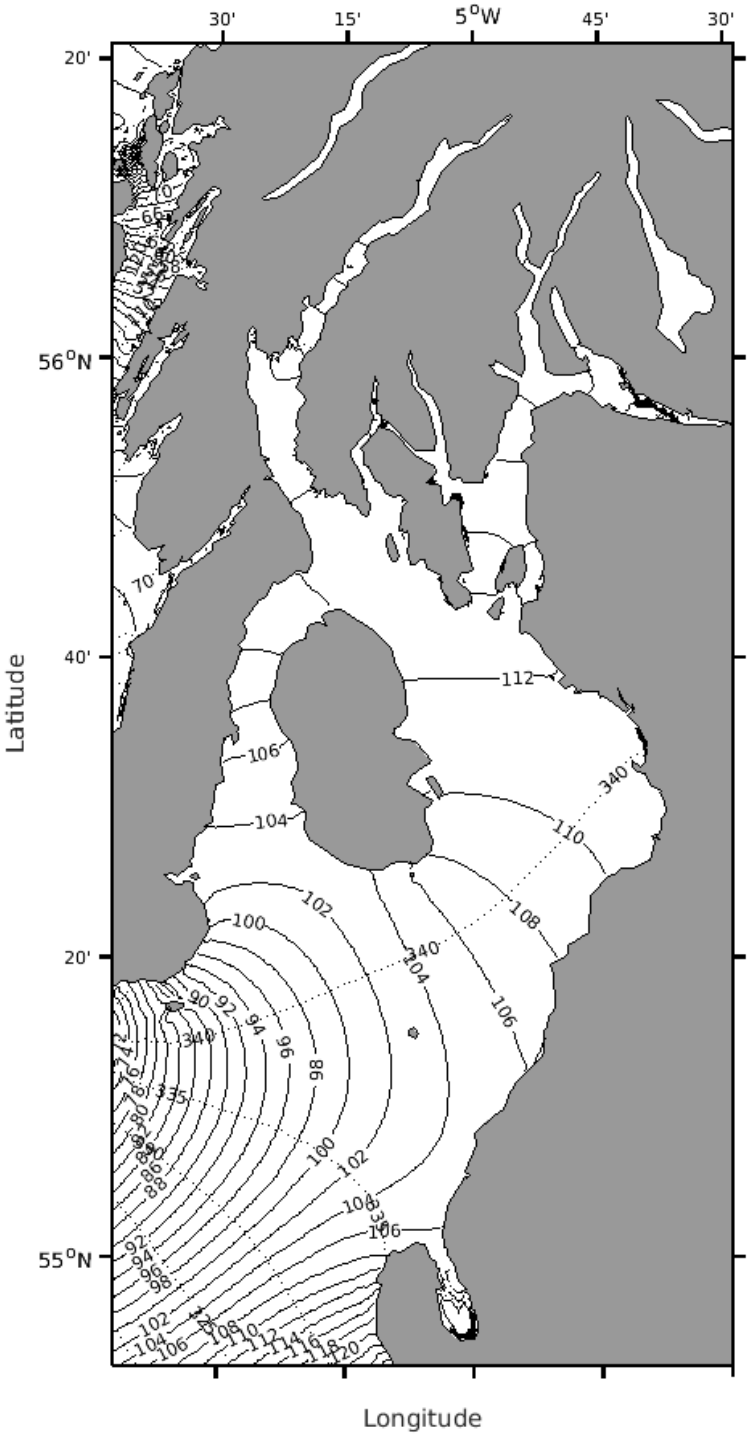

FIGURE 5.5: Cotidal chart for the M_2 harmonic component predicted by the hydrodynamic model. Solid line is the amplitude, dashed line is the phase

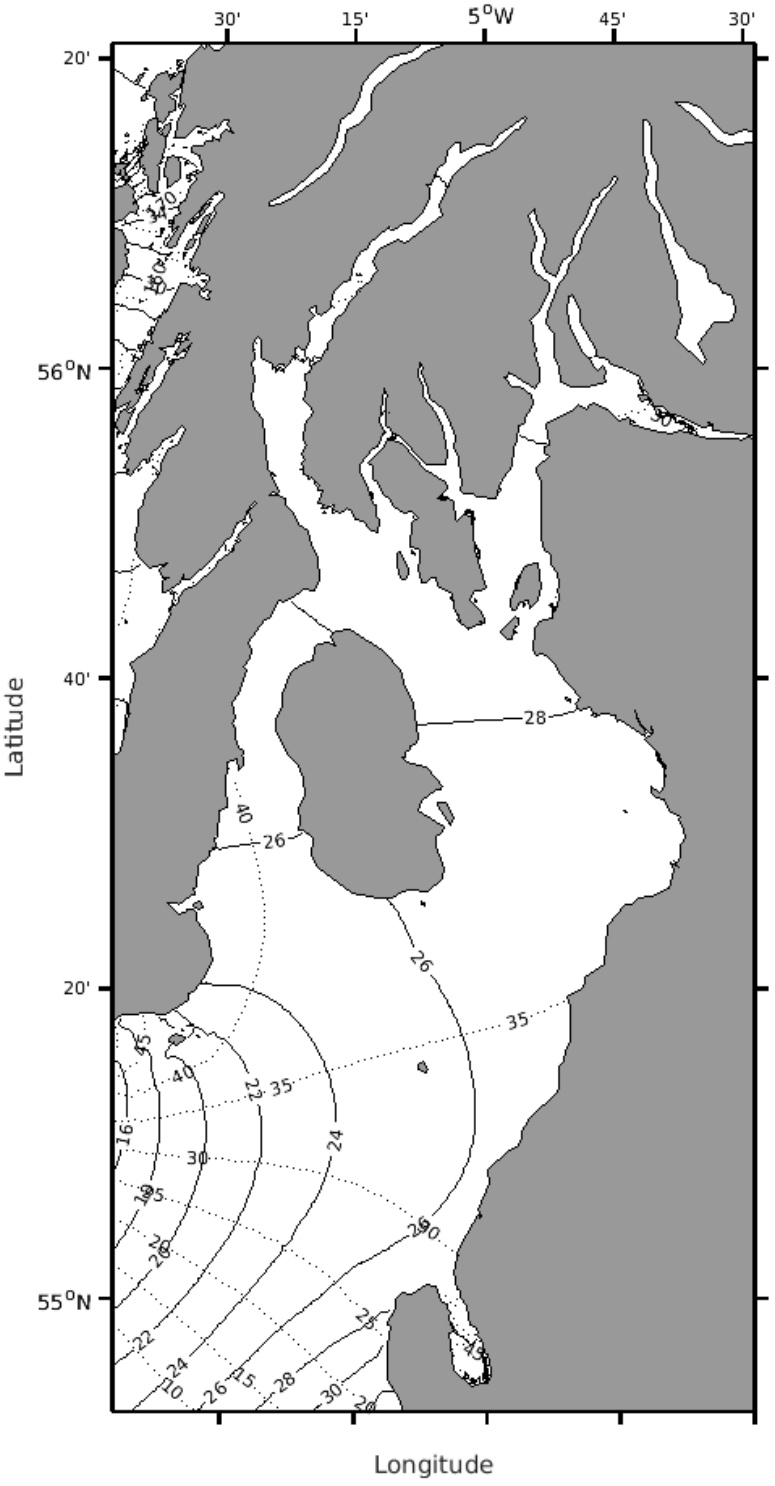

FIGURE 5.6: Cotidal chart for the S_2 harmonic component predicted by the hydrodynamic model. Solid line is the amplitude, dashed line is the phase

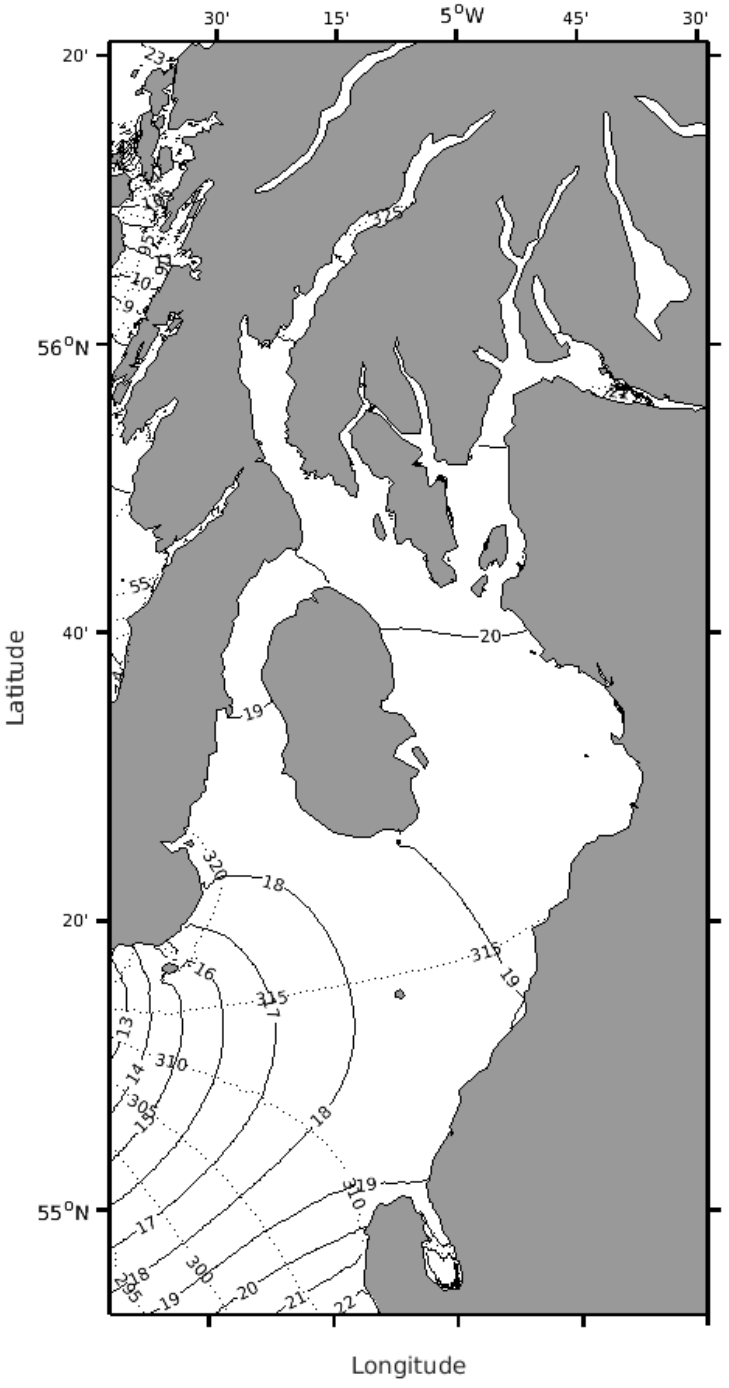

FIGURE 5.7: Cotidal chart for the N_2 harmonic component predicted by the hydrodynamic model. Solid line is the amplitude, dashed line is the phase

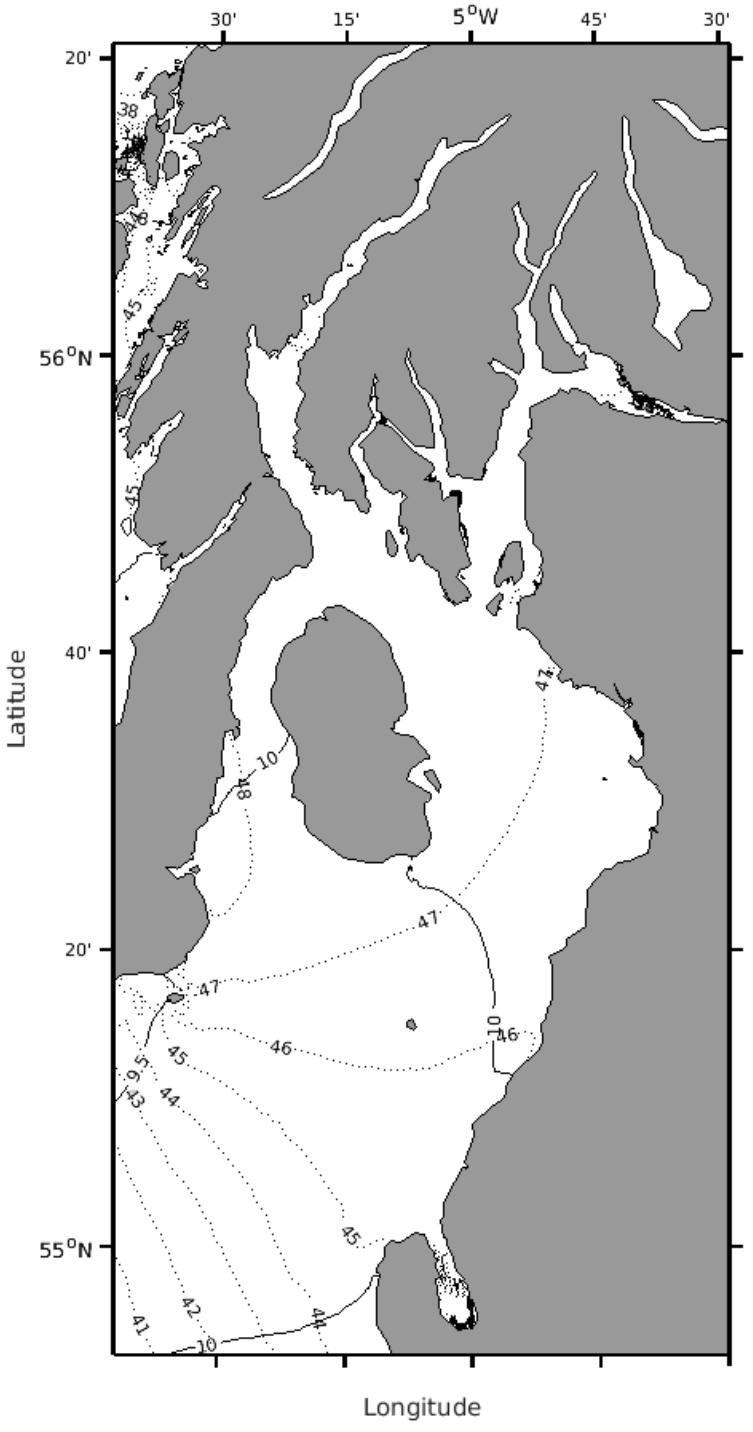

FIGURE 5.8: Cotidal chart for the O_1 harmonic component predicted by the hydrodynamic model. Solid line is the amplitude, dashed line is the phase

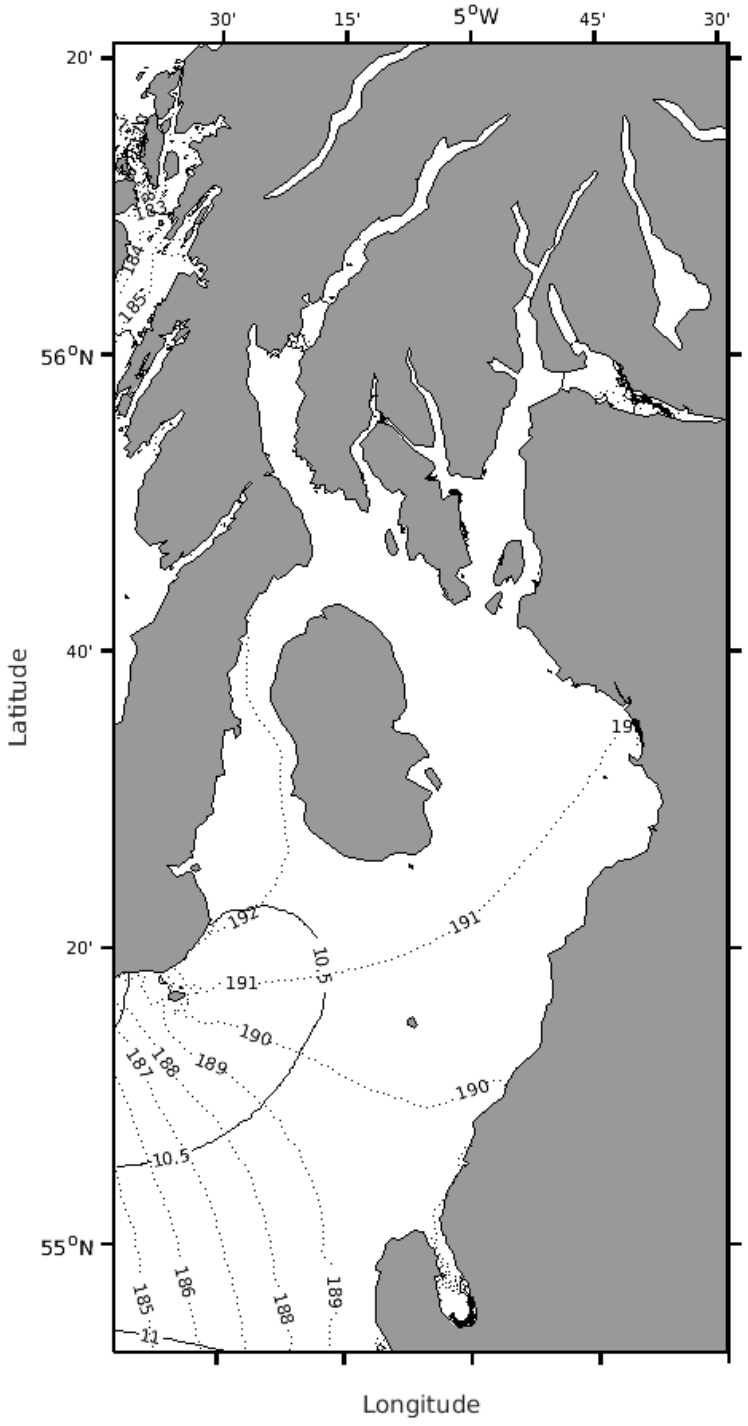

FIGURE 5.9: Cotidal chart for the K_1 harmonic component predicted by the hydrodynamic model. Solid line is the amplitude, dashed line is the phase

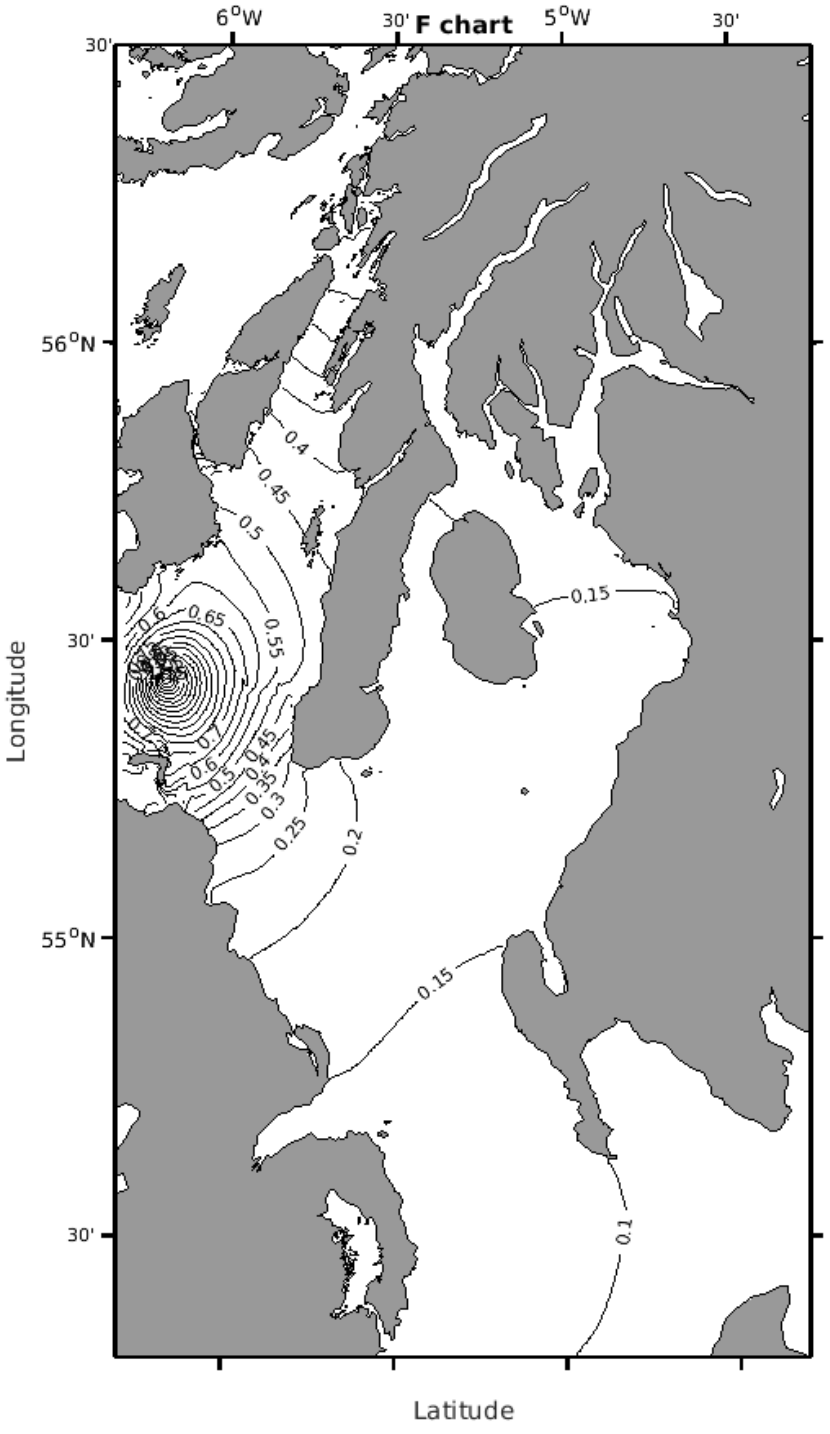

FIGURE 5.10: Computed F-chart for the Clyde Sea

5.4 Currents

If the water level change is more influenced by tides, with some contribution from the baroclinic effect and from the surge events (that are studied in the next section), the currents are more sensible to water stratification or wind-driven circulation in the Clyde: tidal currents, in fact, are very weak in the Clyde Sea (0.2-0.4 m/s in average), while the wind can have a strong effect on modifying these currents (Davies and Hall, 2000).

Using the baroclinic run we estimate the currents in the Clyde Sea and in the North Channel. Maximum current speed were plotted in Figure 5.11 and 5.12 for the bottom and the top layer, while in Figure 5.13-5.14 the average currents are shown for the top and the bottom layer respectively. Strong currents are present in the South of the Mull of Kintyre, with maximum speed exceeding 3 m/s on the surface and 1 m/s on the bottom layer. These high speed are mainly due to the tidal forcing. Those strong tidal currents near the Mull of Kintyre, indicate that it would be possible to extract a significant amount of tidal energy from the flow to generate electricity. The Scottish spatial plan for the tidal energy development is considering, in fact, this area for this scope. Strong currents are recorded in all the North Channel, while between the Clyde Sea and the North Channel the magnitude of the velocity dramaticaly declines to less than 1 m/s, while the average current of the Clyde Sea is 0.2-0.4 m/s. Only a few places in the Clyde show strong currents, such as the initial part of the Loch Fyne and the area of the estuary of the Clyde river. However, these currents does not exceed 1.5 m/s. Currents are also weaker than the North Channel in the Belfast Lough, the bay in front of Belfast, in which the bathymetry suddenly changes from deep water to shallow water.

Other strong currents that the model predicts can be found in the Sound of Jura and in the Sound of Islay, situated North-West to the Clyde Sea and to the North Channel and around the Mull of Galloway, the southernmost part of the Scotland.

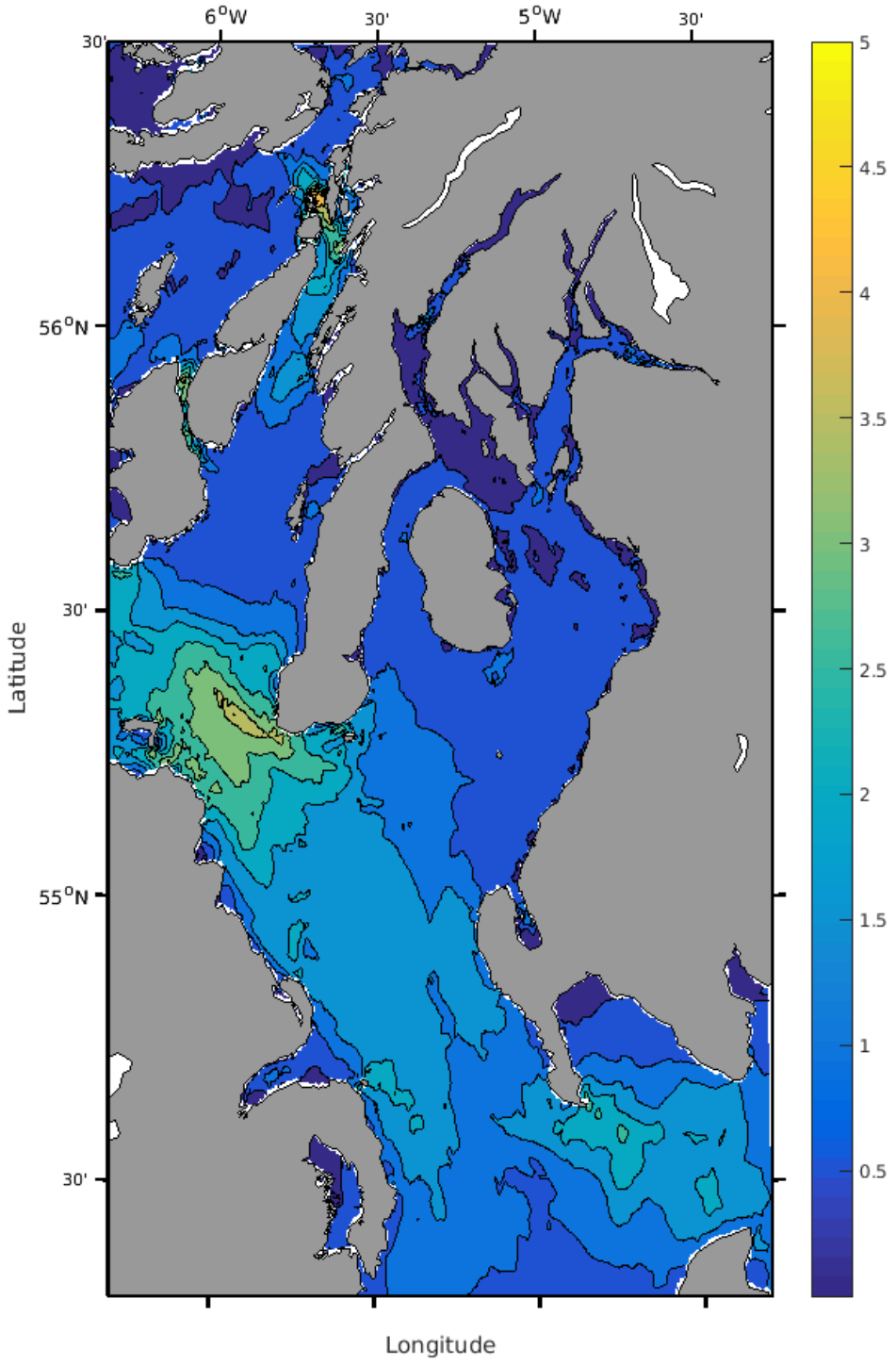

FIGURE 5.11: Maximum surface velocity (m/s) predicted by the hydrodynamic model in the Clyde Sea, in the North Channel and in the surrounding areas

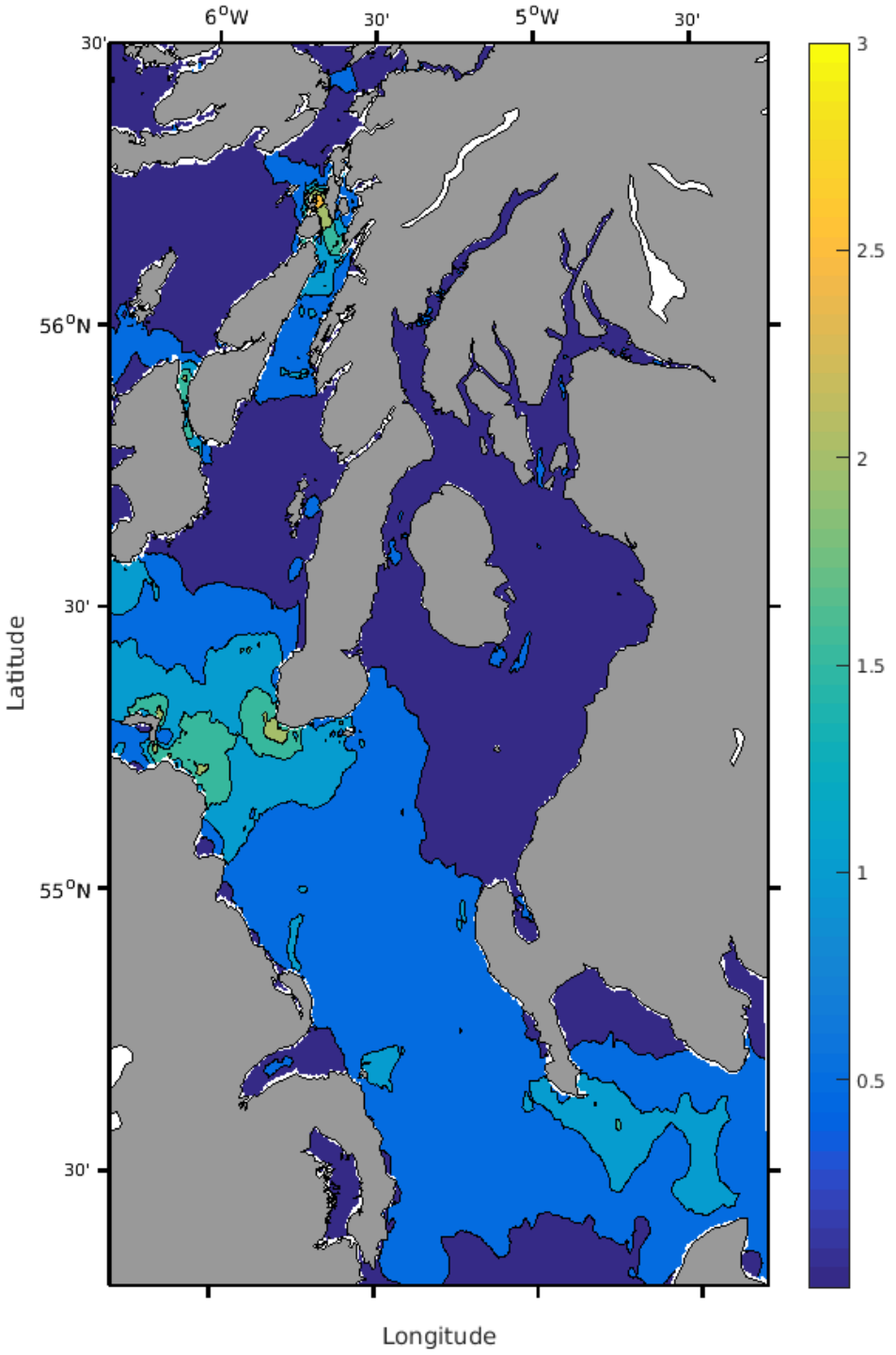

FIGURE 5.12: Maximum bottom velocity (m/s) predicted by the hydrodynamic model in the Clyde Sea, in the North Channel and in the surrounding areas

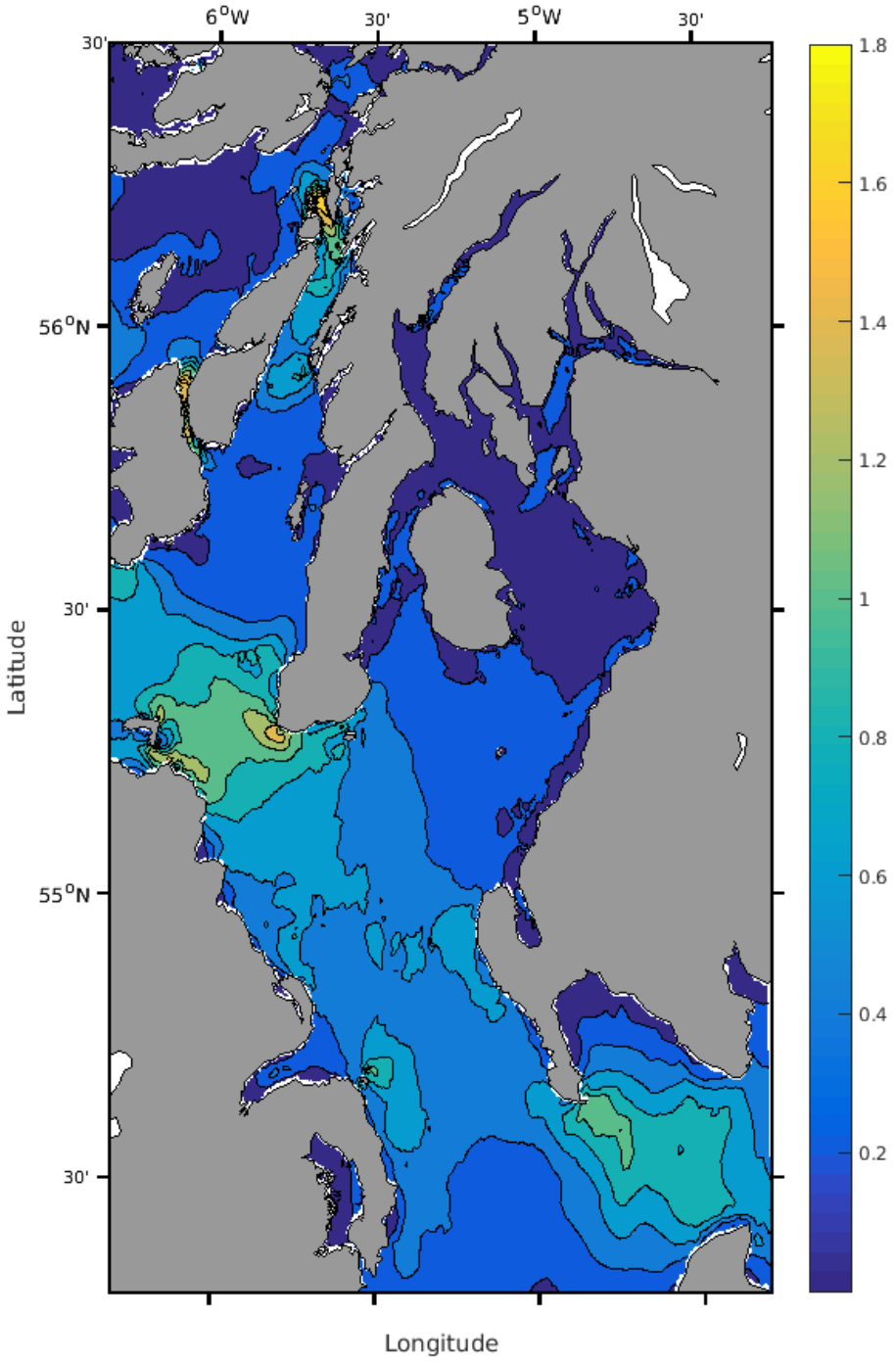

FIGURE 5.13: Average surface velocity (m/s) predicted by the hydrodynamic model in the Clyde Sea, in the North Channel and in the surrounding areas

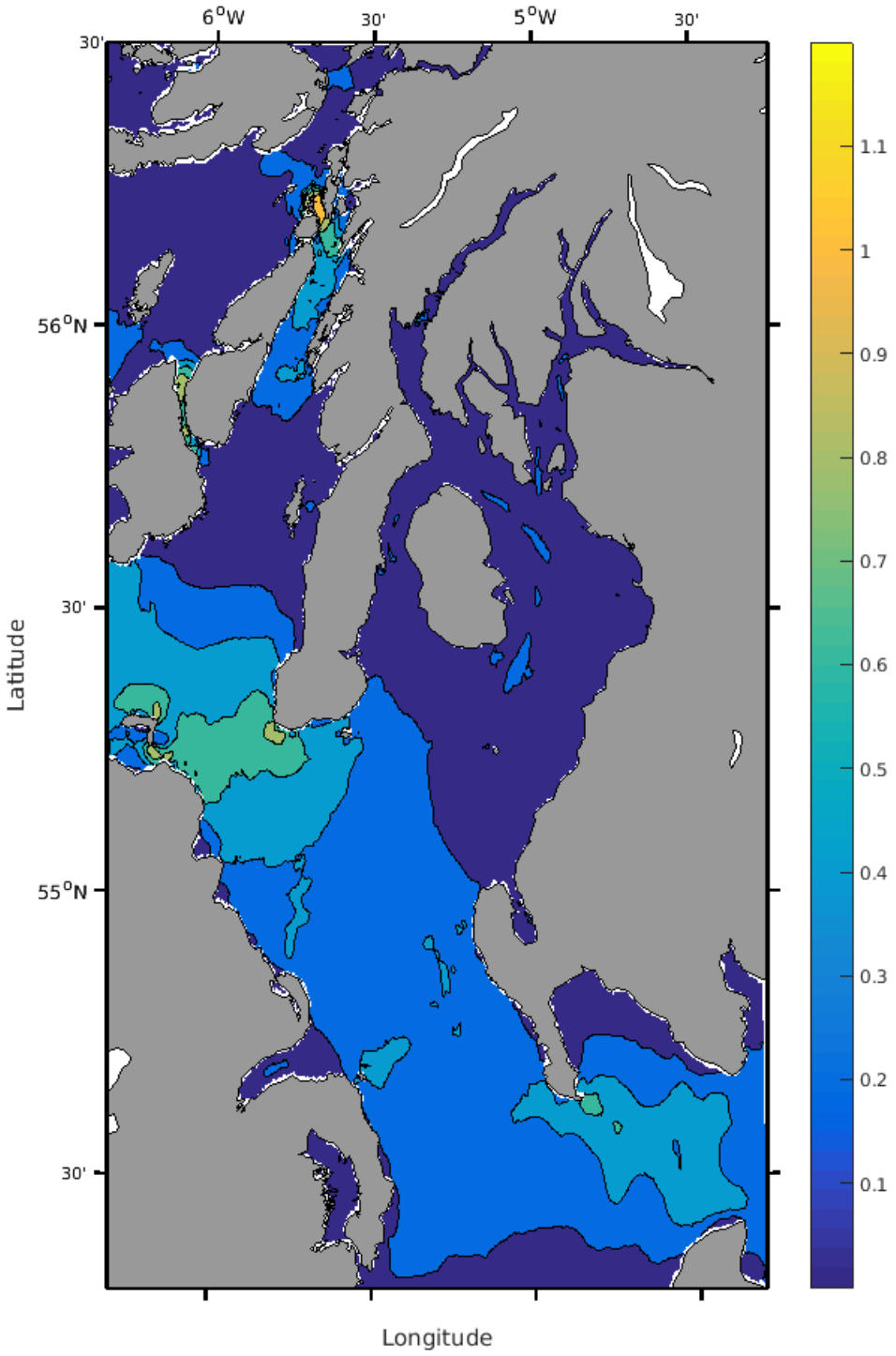

FIGURE 5.14: Average bottom velocity (m/s) predicted by the hydrodynamic model in the Clyde Sea, in the North Channel and in the surrounding areas

5.5 Surges in the Clyde

An extensive analysis of the surges affecting the Clyde was carried out. First, the largest storms in the period 1984-2015 were identified from an analysis on the Millport tide gauge data: the storms with residuals exceeding 1 m were chosen and the sources of those surges were found by an analysis on the meteorological conditions at the time of the surge. Between 1985 and 2014 the Millport tide gauge recorded 92 surge events that exceeded 1 m. Sources of storms were classified in five main categories (Table 5.12), depending on the position of the low baric minimum that caused the storm surge (Table 10.3 of the Appendix provides more details of the 92 storms considered). The most common pattern for a weather system causing a large surge event in the Clyde is a low pressure system moving from the North Atlantic Ocean to generally the Fair Isle Channel (Table 5.12). The storm surge could be generated in this case in the open North Atlantic itself (case 1) or when close to the coastline of Scotland (case 2), depending where the storm reaches its baric minimum. It is also possible that the baric minimum from the North Atlantic Ocean moves over the mainland Scotland (N to the Clyde Sea, between 56 and 60 N) and the storm surge is generated near the Clyde Sea (case 3). Rarely, severe storm surges are internally generated in the Clyde: this is the case of a low pressure system moving from the North Atlantic Ocean to Ireland and to Clyde Sea itself (case 4). In this case the storm surge is caused in response to the local field of wind and pressure. An extremely rare case is when the wind circulation around a low pressure on the North Sea causes a storm surge in the Irish Sea and in the Clyde Sea (case 5). During the period investigated the case 5 happened only once, on the 31 December 2006.

Comparing results in Table 5.12 with the results in Table 1 of Olbert and Hartnett (2010), it is possible to see that both for Irish waters and for the Clyde Sea, most storms come from SW and pass to the N of the Clyde: the same storm events that can

Storm group	Percentage	Location	Description
North of Scotland	34.6 %	Above 60 N	Depression over Orkneys or in the Fair Isle Channel
North Atlantic	28.9 %	West of 10 W	Depression over North Atlantic Ocean
North-West Scotland	25.6 %	Between 55 N and 60 N	Depression over Hebridian Island or North-West Scotland
Scotland South	8.9 %	South of 55 N	Depression over Ireland, North Channel or Clyde Sea
North Sea	1.1 %	East of 2 W	Depression over the North Sea

TABLE 5.12: Classification of depression that caused large storms in the Clyde Sea, compare with Table 1 in Olbert and Hartnett (2010)

cause damages on Irish coastal cities can cause floodings in the Clyde Sea. However, the frequency of storms generated when the barometric minimum is south of 55 N is very rare in the Clyde Sea (with a percentage of about 9 % of the severe storms), but is about 29 % for the more southerly Irish coastline.

Figure 5.15 shows the climate statistics regarding the occurrence of storms based on the month of occurrence. As expected the autumn-winter period (from November to February) is the stormiest period for the Clyde Sea, in which the majority of the large storm surges are recorded in Millport. However some surges exceeding 1 m are recorded also in spring and in summer months.

After this the propagation of the surge wave inside the Clyde Sea was considered. For doing so, three large storm events in 2011 were considered. We choose to consider those storm for the modelling since were all very close in time, and for two of those there were both media description, due to the damages that they caused and also photographic witnessing by Prof. Mike Heath on the last of those three.

Having a direct feedback on the damages caused by those storm and manage to reconstruct the ocean conditions in those periods was very important for the understanding of the threat posed by the storm to the Clyde Sea coastline.

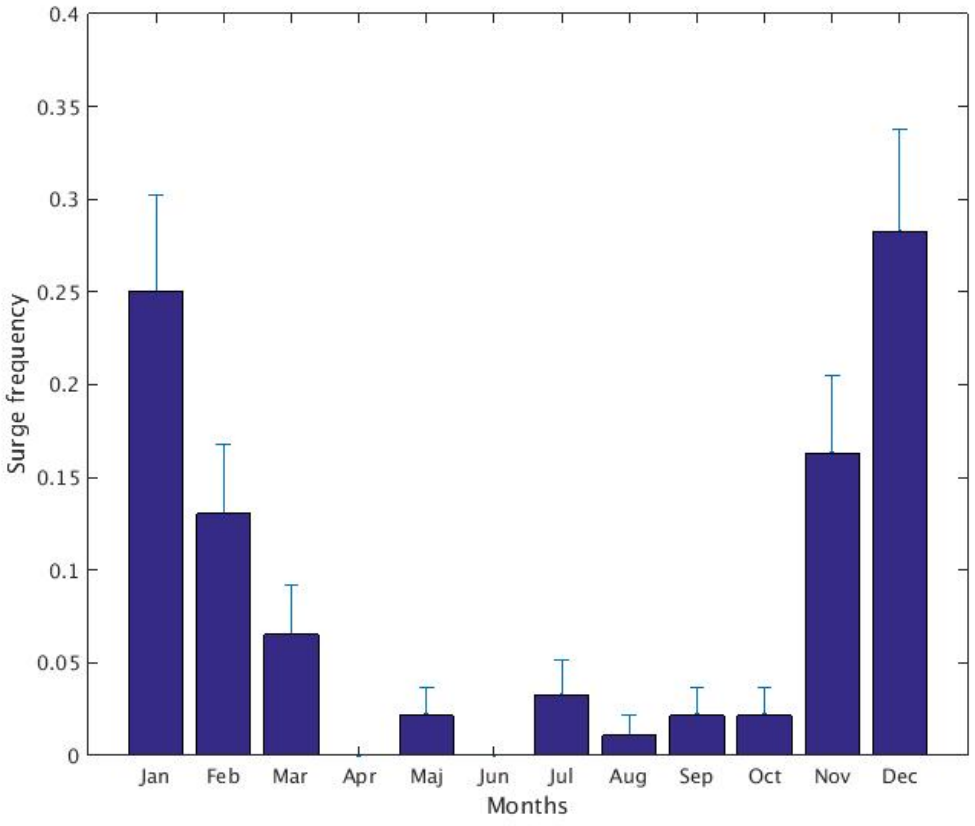

FIGURE 5.15: Monthly frequency of the surges in Millport exceeding 1 m in the period 1985-2014

ERA-Interim datasets were used to hindcast pressure conditions during the three storms occurred in December 2011. Between 8-9 December 2011 Britain experienced an extremely intense extratropical cyclone, with hurricane-force winds hitting Scotland and Northern England. Winds exceeding 150 km/h were reported, causing widespread damage. The extratropical cyclone was nicknamed by the British press Hurricane Bawbag. Figure 5.16 shows the evolution of the storm between 8-9 December 2011 over Great Britain. The storm was formed in the North Atlantic Ocean and moved quickly to Scotland. On the 8 December at 12:00 UTC the pressure minimum was 957 hPa, with maximum sustained wind observed at surface exceeding 170 km/h. In Ayr, a coastal town in the Clyde Sea, wind gusts of 130 km/h were recorded. At the 9 December

at 00:00 UTC the minimum was over the North Sea, passing through Orkney-Fair Isle channel.

A few days later, a strong depression formed over the North Atlantic Ocean, with a pressure minimum less than 945 hPa, that was the lowest recorded pressure in UK since 2000. Figure 5.17 shows the evolution of Cyclone Hergen. The path and the evolution of this cyclone was very similar to the Hurricane Bawbag, generating a very large storm surge with residuals exceeding 1 m in Millport, flooding Helensburgh and other towns in the Clyde Sea. On the Irish coast surface waves exceeding 20 m were recorded.

The last storm considered in this study occurred on the 28 December 2011 and generated a surge wave that in Millport exceeded 0.7 m. The storm followed the same path of the other two previous storms, with the low pressure in the North Atlantic Ocean moving to Orkneys-Fair Isle channel. In this storm, however, the pressure minimum was less intense and the damages were less than the other two (Figure 5.18).

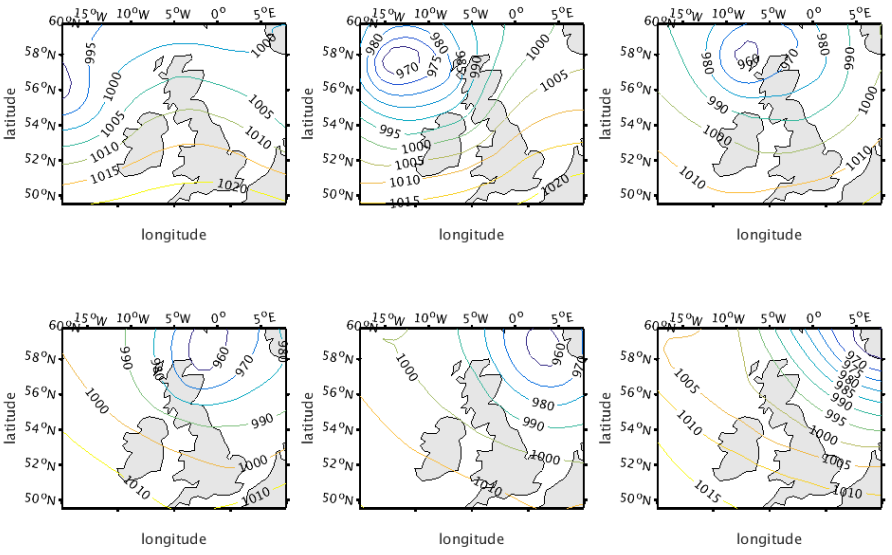

FIGURE 5.16: Evolution of the mean sea level pressure (hPa) during Hurricane Bawbag from 8 December 2011 00:00 UTC. The pressure field is plotted every 6 hours

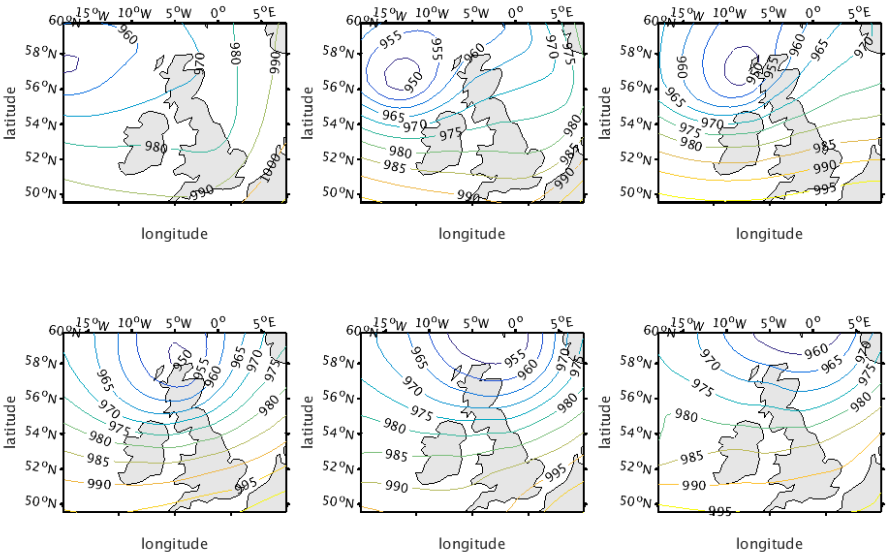

FIGURE 5.17: Evolution of the mean sea level pressure (hPa) during the Cyclone Hergen from 13 December 2011 00:00 UTC. The pressure field is plotted every 6 hours

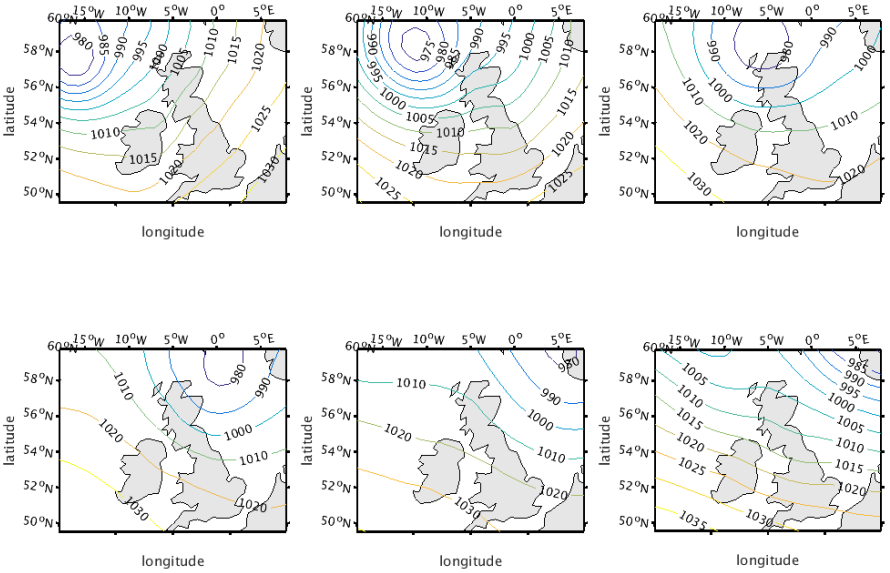

FIGURE 5.18: Evolution of the mean sea level pressure (hPa) during the 28 December storm from 00:00 UTC. The pressure field is plotted every 6 hours

The performance of the model was evaluated during December 2011 (Figure 5.19 and Table 5.7): the model accurately predicted the total water level during this stormy period.

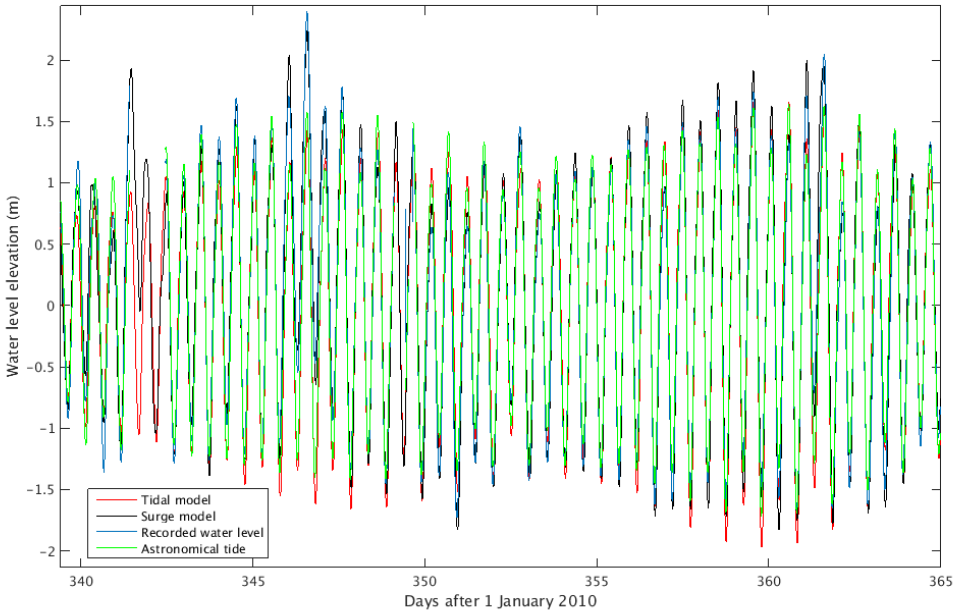

FIGURE 5.19: Comparison between modelled and recorded water level and astronomical tide in Millport tide gauge for November-December 2011

Figure 5.20-5.22 reports the results of the model for the Clyde Sea for the peak of recorded high water for each storm. For the first storm, the peak of the surge wave arrived after the maximum astronomical tide. In fact, the model hindcast shows a very strong enhancement of the water level in coincidence with the subsequent low astronomical tide (Figure 5.20). Due to this lag between the peak storm wave and the high tide, as well as the coincidence with a neap tide period, the maximum total modelled water level did not exceeded 2-2.5 m during the storm, despite a 1-1.5 m surge wave (Figure 5.20b). The surge wave was effectively enhanced by the shallow bathymetry and the coastline of the sea lochs during this surge. The difference in height of the surge wave between the central part of the Clyde and the sealochs was 0.2-0.4 m. Nevertheless, in the northern sea lochs (Loch Fyne and the estuary of the

Clyde in particular) and on the coastline near Ayr, some limited flooding events were reported. Unfortunately, the Millport tide gauge malfunctioned and did not record the peak period of the storm. The hydrodynamic model, in this case, was able to reconstruct the coupling between the surge wave tidal wave, predicting a surge wave exceeding 1 m in the Millport area. Conversely, in the North Channel the surge never exceeded 1 m (Figure 5.20b) and the maximum water level elevation was never $>$ 2 m (Figure 5.20a). The surge caused by Cyclone Hergen (Figure 5.21) occurred at the same time as a spring tide period, so even though the surge wave was less intense than the one caused by Hurricane Bawbag, the total water level was higher, exceeding 2.5 m in the Clyde Sea and more than 3 m southward in the northern Irish Sea (Figure 5.21a). This coupling between strong surge and spring tides caused the flooding in many coastal communities in the Clyde Sea, in particular in Helensburgh. The last storm (Figure 5.23 for the photos of that day, Figure 5.22 for the model results) was less intense than the other two storms analyzed. Nevertheless, many coastal communities were still flooded, and much damage was recorded. The storm surge in the Clyde Sea never exceeded 1 m (Figure 5.22b), but the spring tide conditions caused a high sea level in the sea lochs, in particular in the Clyde estuary similar to the storm caused by the Hergen cyclone. This coupling caused another flood in streets near to the seafront in Helensburgh (Figure 5.23). The last analysis that was carried out on the surge dynamics was to understand which are the most dangerous conditions for surge in the Clyde. The three surges analyzed above highlighted that also a moderate surge wave could cause severe floodings, while large surges could not be so devastating since they occur during a neap tide period or during a low water event.

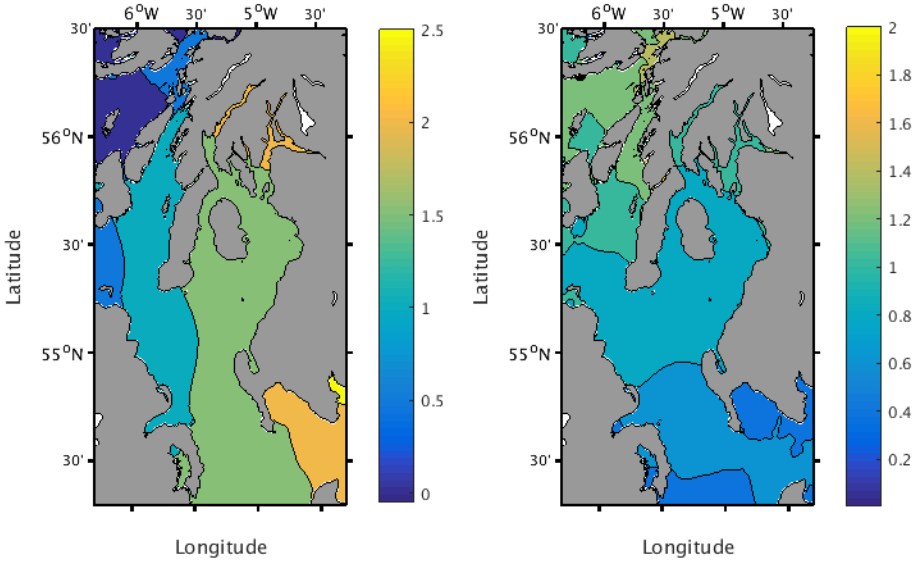

FIGURE 5.20: Water level in the Clyde Sea at high water during Hurricane Bawbag: a) total water level, b) surge contribution

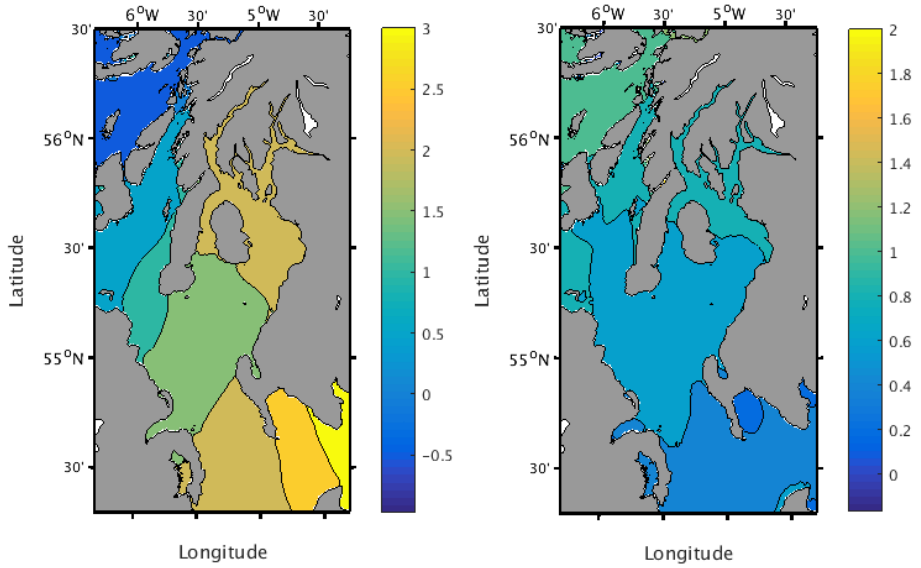

FIGURE 5.21: Water level in the Clyde Sea at high water during Cyclone Hergen: a) total water level, b) surge contribution

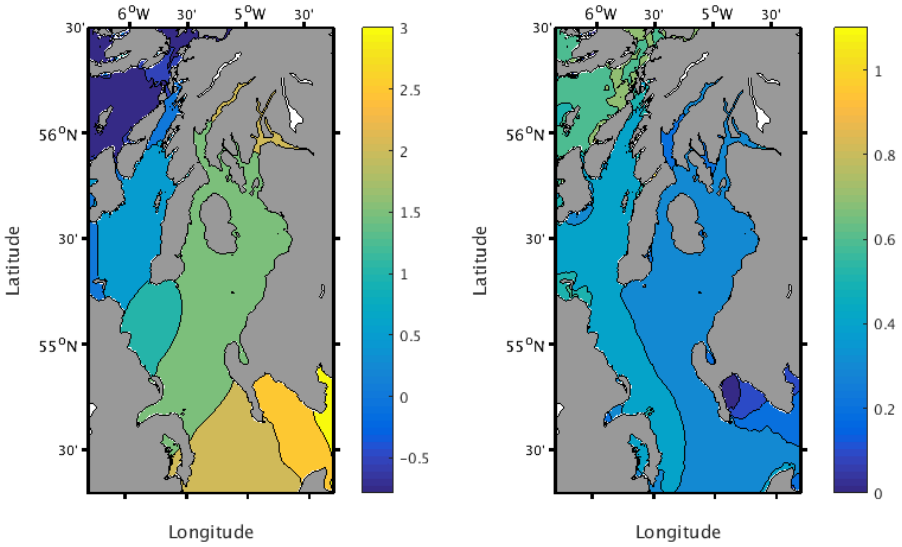

FIGURE 5.22: Water level in the Clyde Sea at high water during the 28 December storm: a) total water level, b) surge contribution

FIGURE 5.23: Images from the 28 December 2011 storm in Helensburgh (Photos Joanna Heath)

To do so, the data from Millport tide gauge were again considered and a statistical analysis based on the total water level was carried out. The standard deviation of the total water elevation was evaluated, then were considered all the points that were above the threshold of $+2\sigma_{wl}$ and $+3\sigma_{wl}$. For all the measurement, then, the tidal signal was separated from the residuals due to surge events and the events over 2 and 3 σ_{wl} were plotted (Figure 5.24), in order to see which are the conditions causing high water level events.

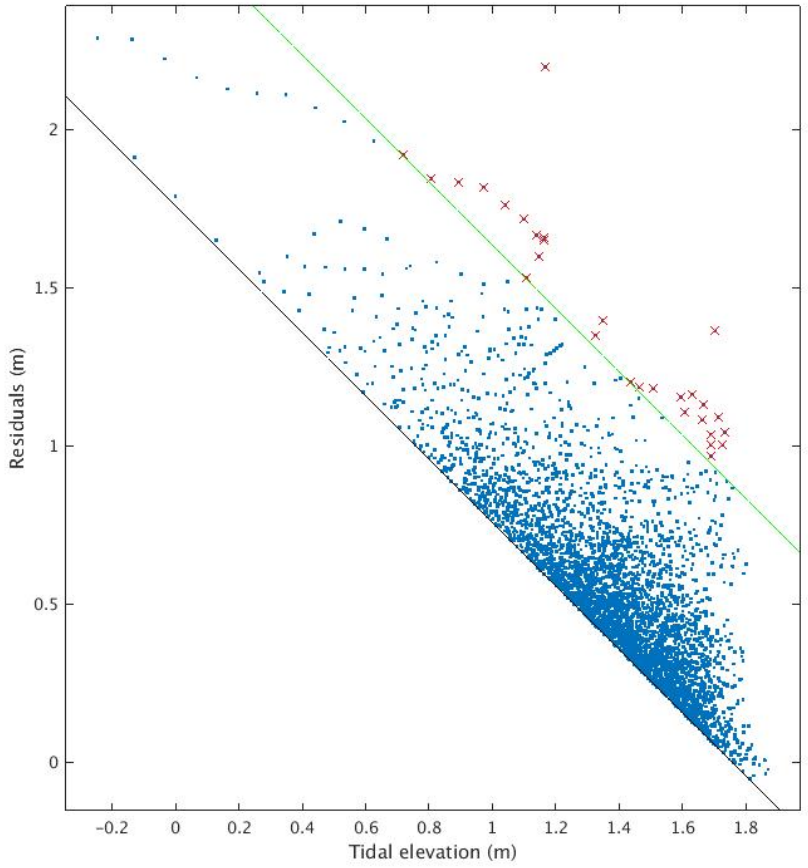

FIGURE 5.24: Surge residuals vs astronomical tidal elevations for large water level events in Millport, blue points are recorded water level exceeding $2\sigma_{wl}$ (1.75 m) in Millport, while red crosses are recorded water level exceeding $3\sigma_{wl}$ (2.63 m). σ_{wl} is the standard deviation of the water level (0.89 m). The black and the green line represent the $2\sigma_{wl}$ and the $3\sigma_{wl}$ respectively

The figure shows that the higher density of point exceeding $+2\sigma_{wl}$ had a large tidal amplitude (spring high water event) coupled with moderate surge (0.5-0.7 m), while less events were showing a strong surge activity coupled with a moderate high water condition (nor spring or neap), while very few events were in neap tide. For the second threshold, very high water events occur only when spring high tides are coupled with severe surge conditions (about 1 m or more).
In the Clyde Sea the main forcing for the water level variability is tides, that during spring tide cycles have a tidal range of more than 3 m. Those spring tide conditions, when exacerbated with also moderate surges caused mainly by storms from outside the Clyde Sea could cause severe damages to properties around the Clyde (see Figure 5.24).

5.5.1 River contribution to surges

The river contribution was evaluated first considering the Root-Mean Square difference between the storm surge model without rivers and with rivers for the entire 2005. The average effect was extremely small for all the rivers: the only river that had an effect $>$ 0.01 m was the Clyde river, but no significant far-field effect was detected. During the November-December 2011 run we studied the contribution of the Clyde river, comparing the results for the surge model without rivers and the surge model with the Clyde river as input (the other rivers in this case were not considered). No far field effect due to the Clyde was detected in any of the three considered storms, but was only limited to the estuary and to neighbour areas. For the first storm (08/12/2011) the maximum contribution of the Clyde to the water level was $<$ 0.02 m. For the second storm (13/12/2011) the maximum contribution was $<$ 0.02 m, while for the last storm the maximum contribution was $<$ 0.01 m.

5.6 Stratification

The stratification is another fundamental factor affecting the Clyde Sea current dynamics. The stratification in the Clyde Sea is mainly due to the fact that the combined tidal, wind-driven and storm-driven circulation does not have enough energy to allow the mixing of the water column in the region. One way to visualize the potential areas that can be affected by this phenomena is to compute the Simpson and Hunter (1974) number. Simpson and Hunter (1974), while studying the position of the fronts in the Irish Sea, introduced this parameter (S_{HS}) for studying the occurrence of the stratification, that is based on the energy budget of the water column: if the combined energy of the barotropic factor is higher than the critical value (that changes from area to area and depends mainly on the radiation input from the atmosphere, the water column is mixed. Pingree and Griffiths (1978) found that for UK water, the critical value is about $h/u^3 \approx 350 s^3/m^2$. In terms of the Simpson-Hunter number, that approximately means that for $S_{SH} > -1$ the water column is well mixed, for $S_{SH} < -2$ is stratified and for values between -1 and -2 the area is transitional. Normally the current u is taken at spring tide. In Figure 5.25 and 5.26 we computed contour plots of the Simpson-Hunter criteria for the Clyde for the months of August and November 2005: in blue are showed the location in which $S_{SH} > -1$, green are the areas in which $-2 < S_{SH} < -1$ and yellow the areas for $S_{SH} < -2$.

Figures 5.25-5.26 of the spatial Simpson-Hunter number are consistent with previous studies carried out for the Irish Sea or for the entire UK shelf, but with a coarser resolution of the Clyde Sea, such as for all the UK waters (Souza et al.; Pingree et al., 1978).

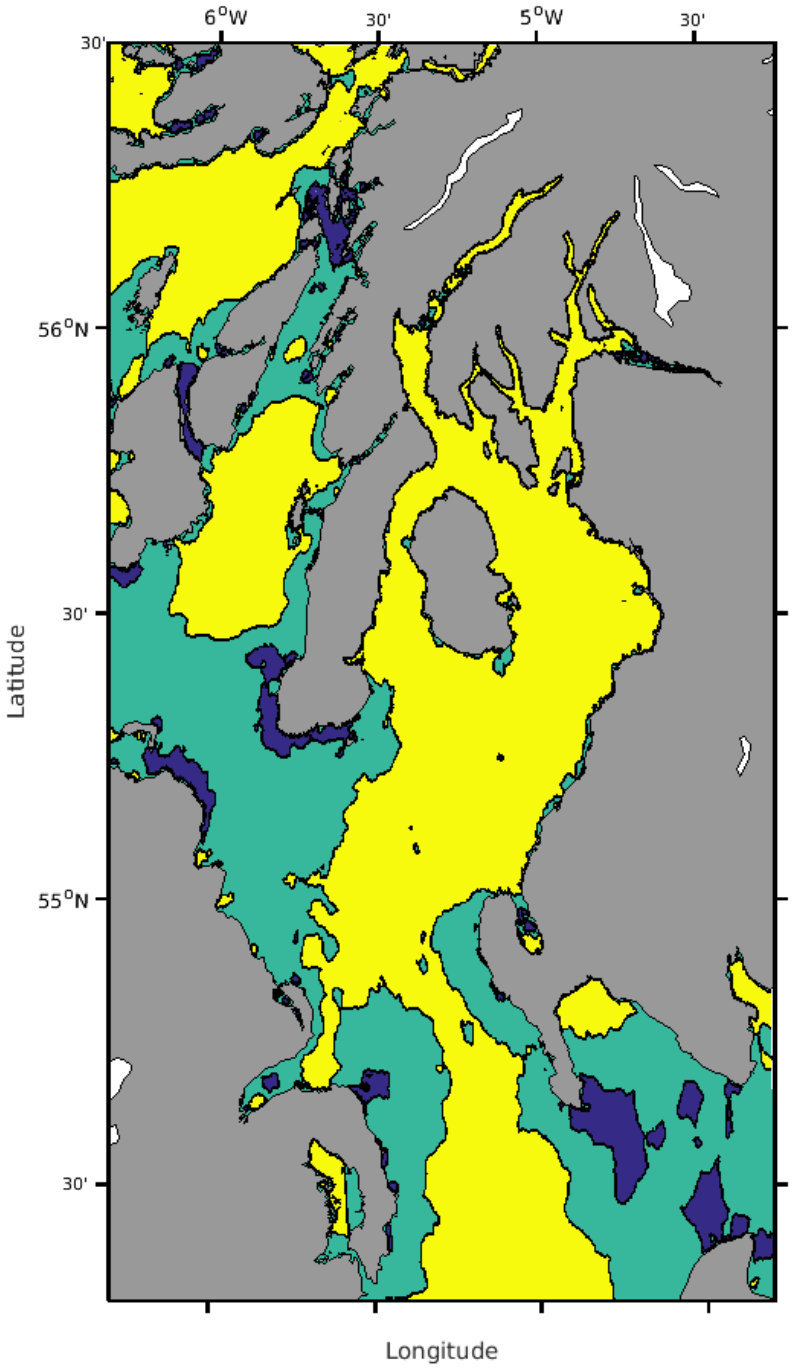

FIGURE 5.25: Computed Simpson-Hunter number $S_{HS} = -\log_{10}(h/u^3)$ for the Clyde Sea and for the North Channel for the month of August 2005, blue is when the value of $S_{SH} > -1$, green areas have an intermediate Simpson-Hunter number between -1 and -2, while yellow areas have values $S_{HS} < -2$

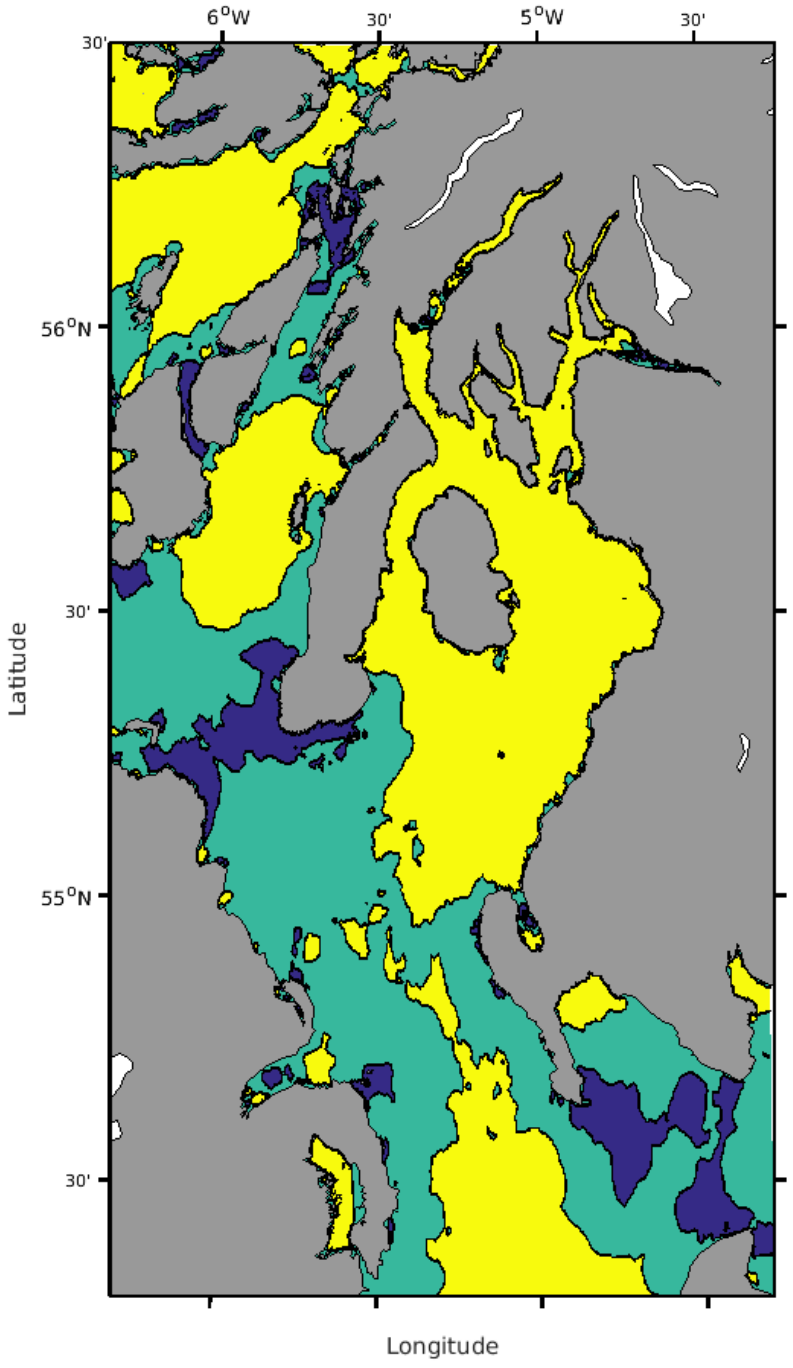

FIGURE 5.26: Computed Simpson-Hunter number $S_{HS} = -\log_{10}(h/u^3)$ for the Clyde Sea and for the North Channel for the month of November 2005, blue is when the value of $S_{SH} > -1$, green areas have an intermediate Simpson-Hunter number between -1 and -2, while yellow areas have values $S_{HS} < -2$

The two figures are very similar, however, due to storms and wind-driven circulation, currents were stronger in November than in August. However, the Simpson-Hunter number is based only on the potential energy of the current to allow the mixing of the water column in summer conditions, but have the limitation that it does not take account of the actual temperature and salinity conditions. In addition, the value reported for the area in study by Pingree and Griffiths (1978) was calculated for summer conditions, when the radiation from the atmosphere is stronger, so it requires more energy to mix the water column. The Simpson-Hunter number was significantly lower for both November and August conditions in the Clyde for the deep areas at the North of the Arran Island, where the currents are weak ($0.4 - 0.6m/s$, Figure 5.1-5.14) and the bathymetry is deeper than 100 m (see Figure 3.1 for the bathymetry): in this case the model was predicting $S_{HS} < -4$ (Figure 5.27-5.28). Those low values were also found for sealochs between the mainland Scotland and the Isle of Bute, as well as the final part of the sealochs, where the current velocities are weaker.

Some areas in the Clyde Sea have large values for the Simpson-Hunter number, since the currents are stronger, such as in the estuary of the Clyde Sea and the mouth of the Loch Fyne. This is mainly due to the combination of strong current due to the fjordic funnelling combined with shallow water. Another area in which the Simpson-Hunter parameter predicts transitional waters is the east coast of the Clyde Sea, close to Ayr, in which the currents are not strong, but the sea is very shallow.

Fully mixed areas are present both in Summer and in Autumn for the areas at the tip of the Kintyre peninsula, where maximum surface currents are well exceeding $5m/s$.

Previous studies in the Clyde Sea (Simpson and Rippeth, 1993; Rippeth and Simpson, 1996) highlighted that the Clyde presents periods of complete vertical mixing during the month of November, due to a lower radiation flux from the atmosphere and to stronger wind and surge conditions.

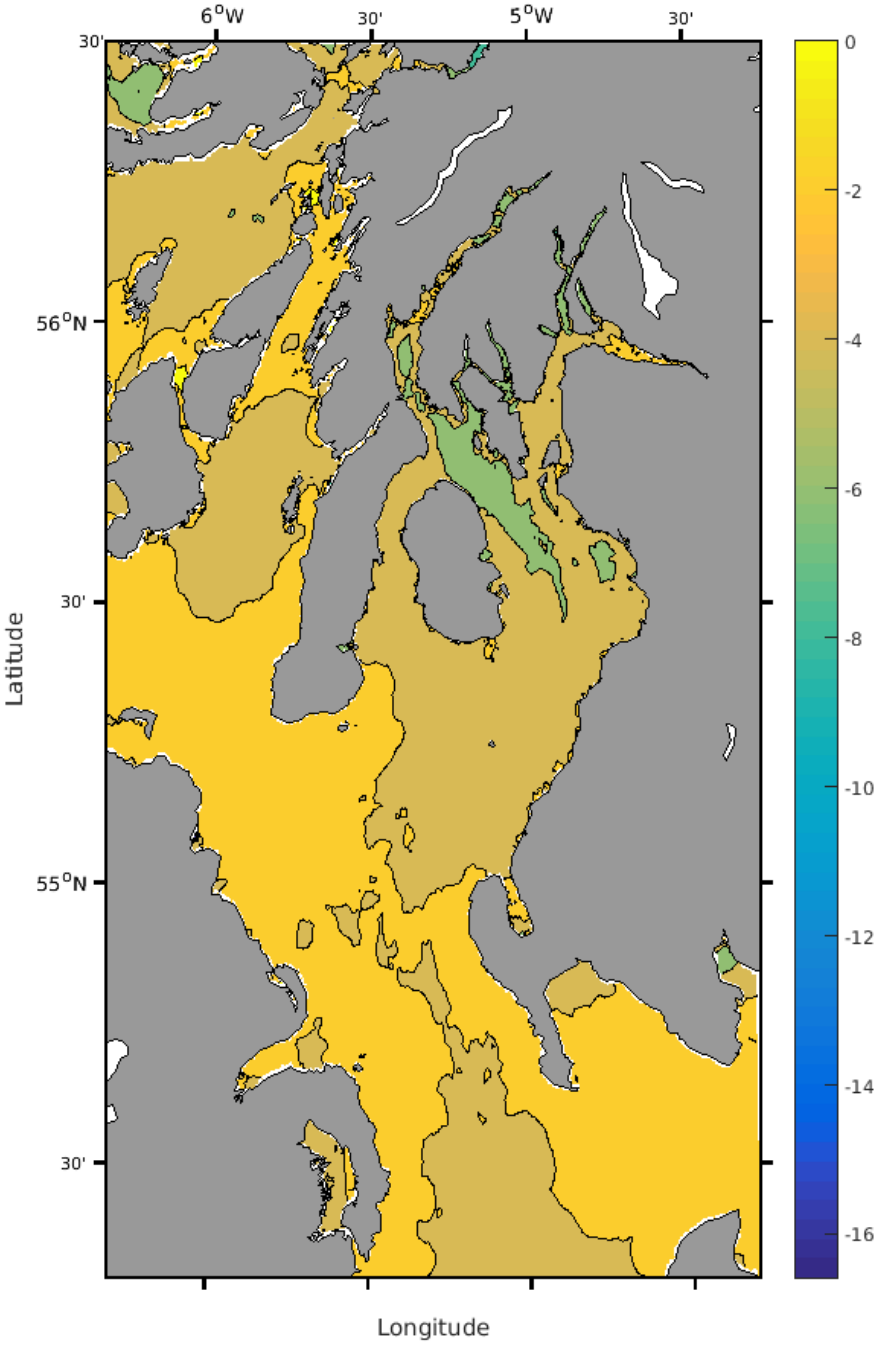

FIGURE 5.27: Computed Simpson-Hunter number $S_{HS} = -\log_{10}(h/u^3)$ for the Clyde Sea and for the North Channel for the month of August 2005

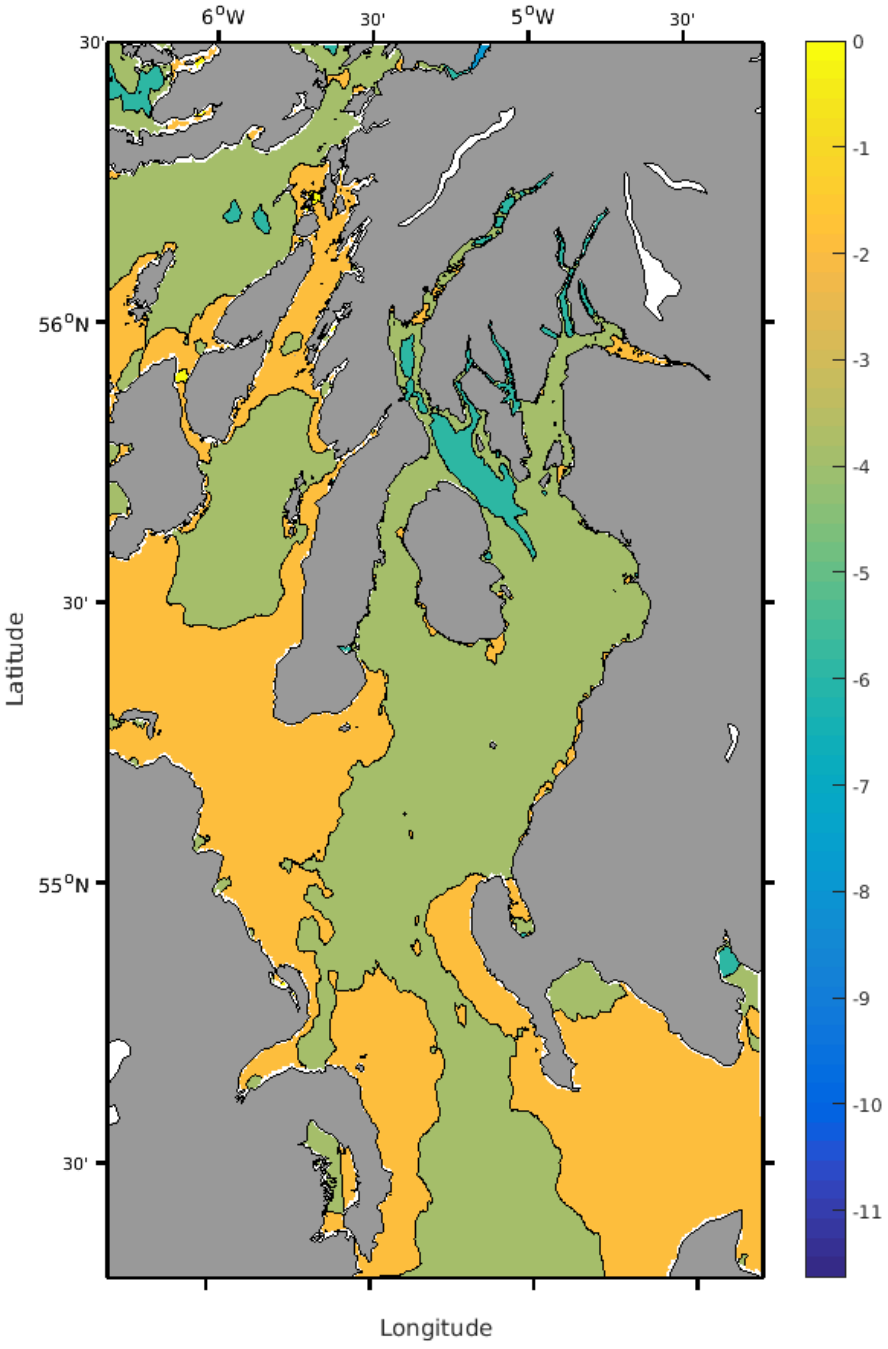

FIGURE 5.28: Computed Simpson-Hunter number $S_{HS} = -\log_{10}(h/u^3)$ for the Clyde Sea and for the North Channel for the month of November 2005

To evaluate the stratification we evaluated a cumulative difference for temperature between the temperature at each layer with the depth-averaged temperature at the same point at the same time:

$$\Delta_T = \frac{\sum_i^N \mid \left(T_i - \bar{T}\right) \cdot d_i \mid}{D} \tag{5.2}$$

where T is the temperature; $\bar{k}$ is the depth-averaged temperature, d_i is the thickness of the layer i, and D is the total depth at the specified location. Joined with the information given by the Simpson-Hunter number, it is possible to see where are the places in the Clyde Sea and in the North Channel where the stratification is present, since the difference in temperature in the water column could also be given by the advection of the temperature by the tidal flow. In Figures 5.29-5.32 the results for the temperature for each season (Winter, Spring, Summer and Autumn respectively) is given.

Highest values, as expected are reported in the Clyde Sea, where also the Simpson-Hunter number was predicting higher possibility for the stratification to occur. Δ_T was higher in magnitude in the Spring and Summer than in the Autumn and Winter months, in particular for the Clyde Sea. These maps are very similar to the Figures 5.25-5.28, however some differences are in the fjordic areas in the Clyde Sea. Since no information was available for river discharges in the Lochs, in particular in Loch Fyne, the model predict a weak stratification in Spring and in Summer, with practically no stratification in Winter and Autumn. This is probably due to the absence of freshwater input in this area, since the freshwater is one of the main causes of the water stratification in the Clyde along with weak currents (Simpson and Rippeth, 1993; Rippeth and Simpson, 1996; Matthews et al., 1999). In Figure 5.34 are reported some profiles of modelled temperature for Winter, Spring, Summer and Autumn for the locations reported in Figure 5.33: results shows that in Summer and Spring the stratification is present in the Clyde Sea and is strong in the central part, while is weak in the fjords such as Loch Fyne, as also noticed in Figures 5.25-5.28. In Autumn, the stratification

is generally weak or totally absent and the surface is generally colder than the bottom layer. The inversion is probably due to the flow of water from the North Channel to the Clyde Sea reported in Simpson and Rippeth (1993); Rippeth and Simpson (1996): the vertical mixing in November can be seen in the last column in the Figure 5.34. In Winter (first column) the situation of temperature is similar to Autumn, with a temperature inversion, with the cold water on top of warm water. However, a thermocline begin to form between the top layer and the bottom layer, while mixed profiles are no longer present except for few locations.

Collectively, the model outputs generally predict the presence of a strong stratification in Spring and in Summer in the Clyde Sea, with a situation in Autumn in which the mixing is present and a return of the stratification during the Winter. In the sealochs, in particular in the Loch Fyne, this cycle is not evident from the model. This is probably due to the fact that no freshwater input is given in those fjords, due to the lack of measurements in the area. The run-off of the freshwater from the land to the sea is one of the key factors on the formation of the stratification, in particular for fjordic areas (Gade and Edwards, 1980; Stigebrandt, 1981).

This is a strong limitation of the model presented here in the Clyde Sea. However, a future development of the model could be to use a hydrological model, such as the Grid-to-Grid model (G2G) (Schellekens, 2010; Clark and Connolly, 2012), to estimate the freshwater input in the area in which this information is missing, since the river are not gauged.

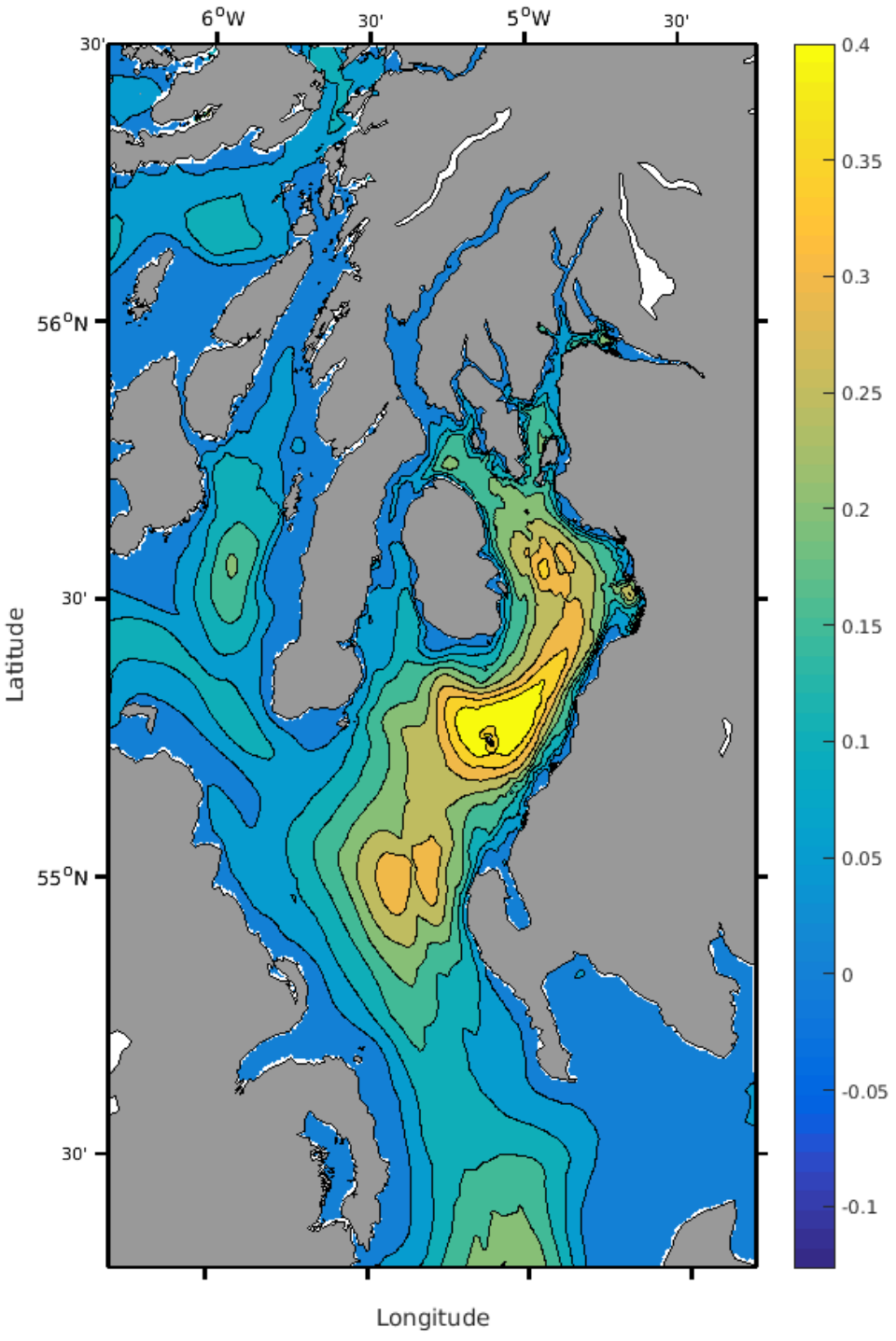

FIGURE 5.29: Modelled average Δ_T for the Winter period

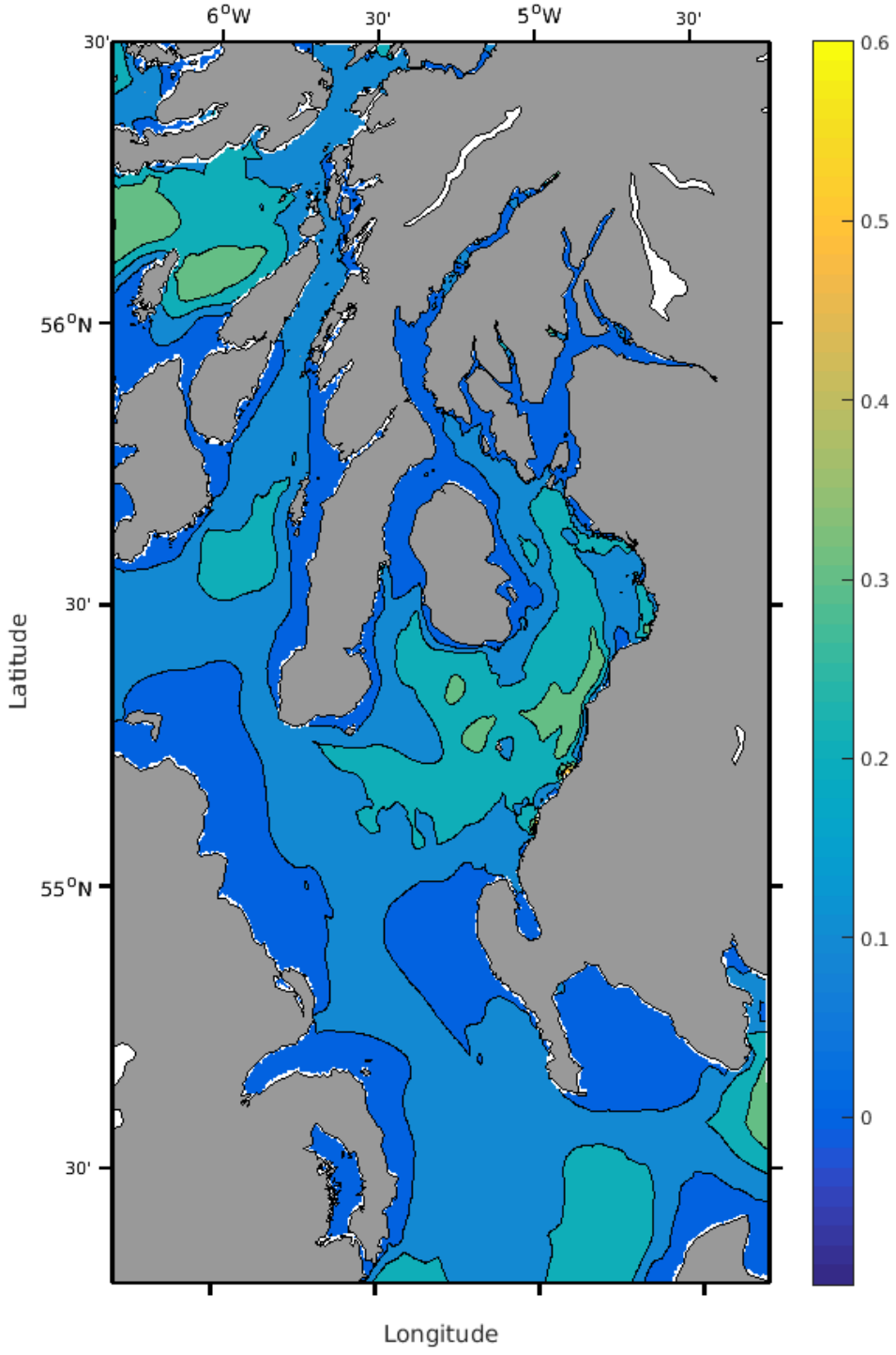

FIGURE 5.30: Modelled average Δ_T for the Spring period

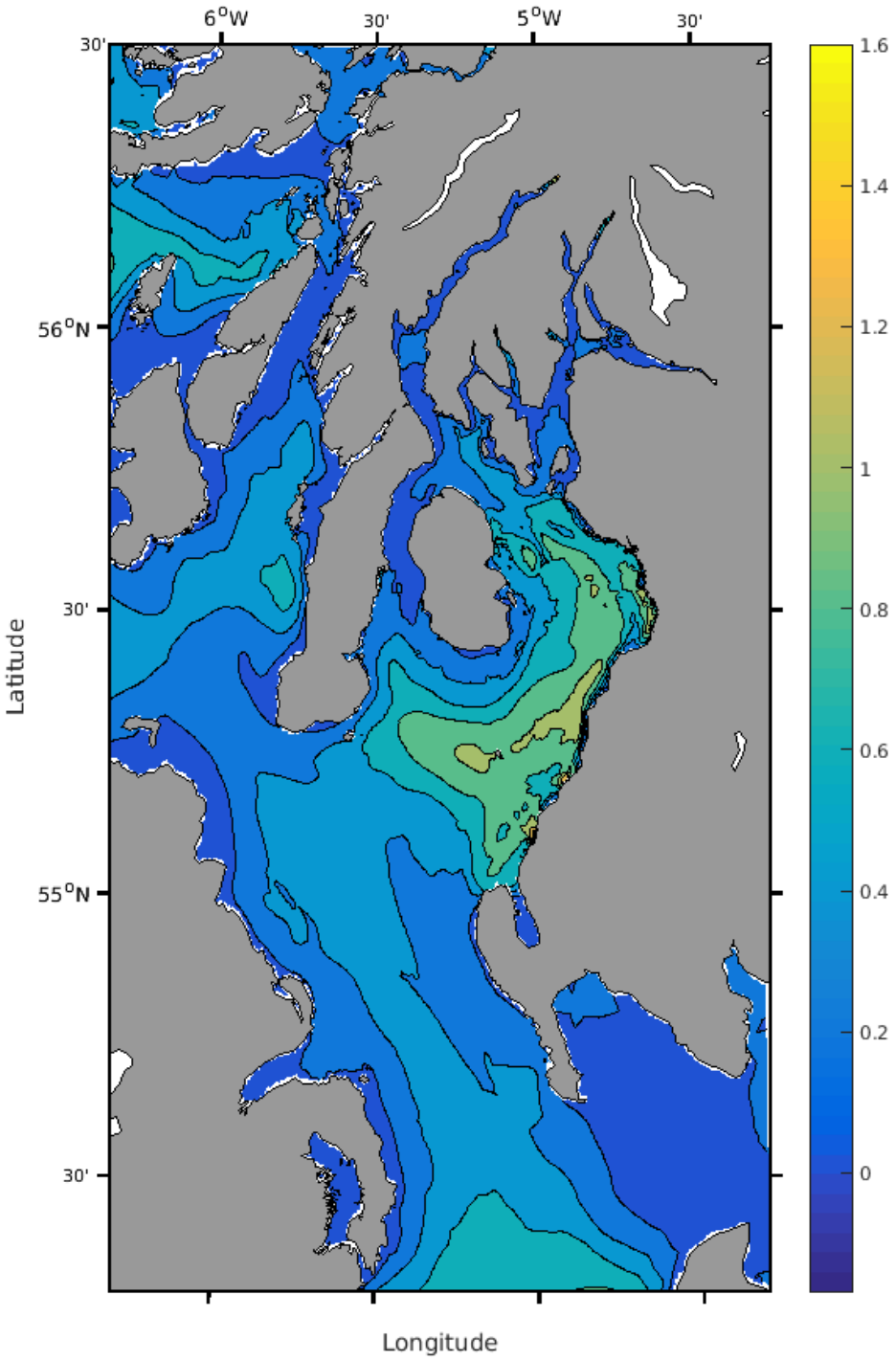

FIGURE 5.31: Modelled average Δ_T for the Summer period

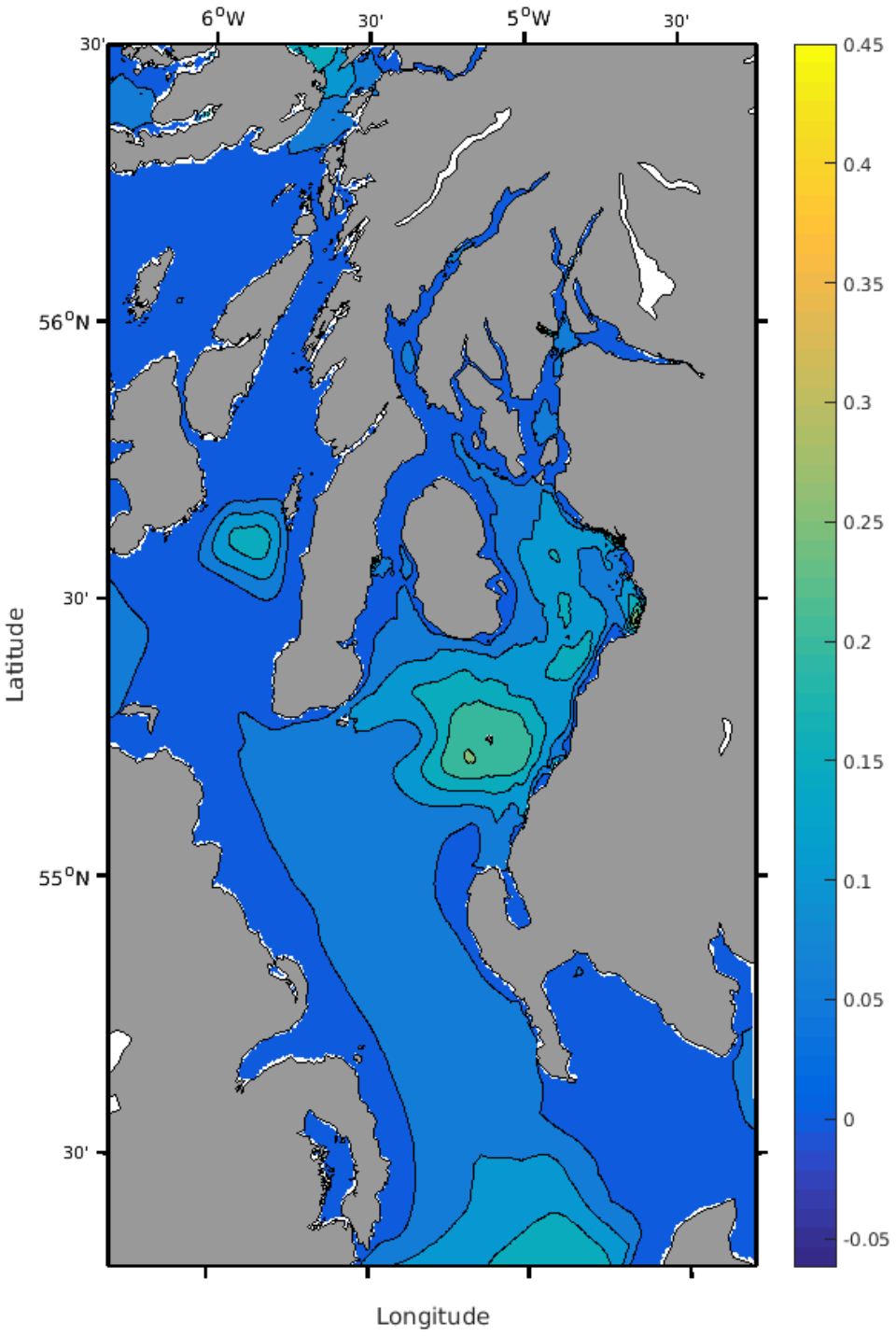

FIGURE 5.32: Modelled average Δ_T for the Autumn period

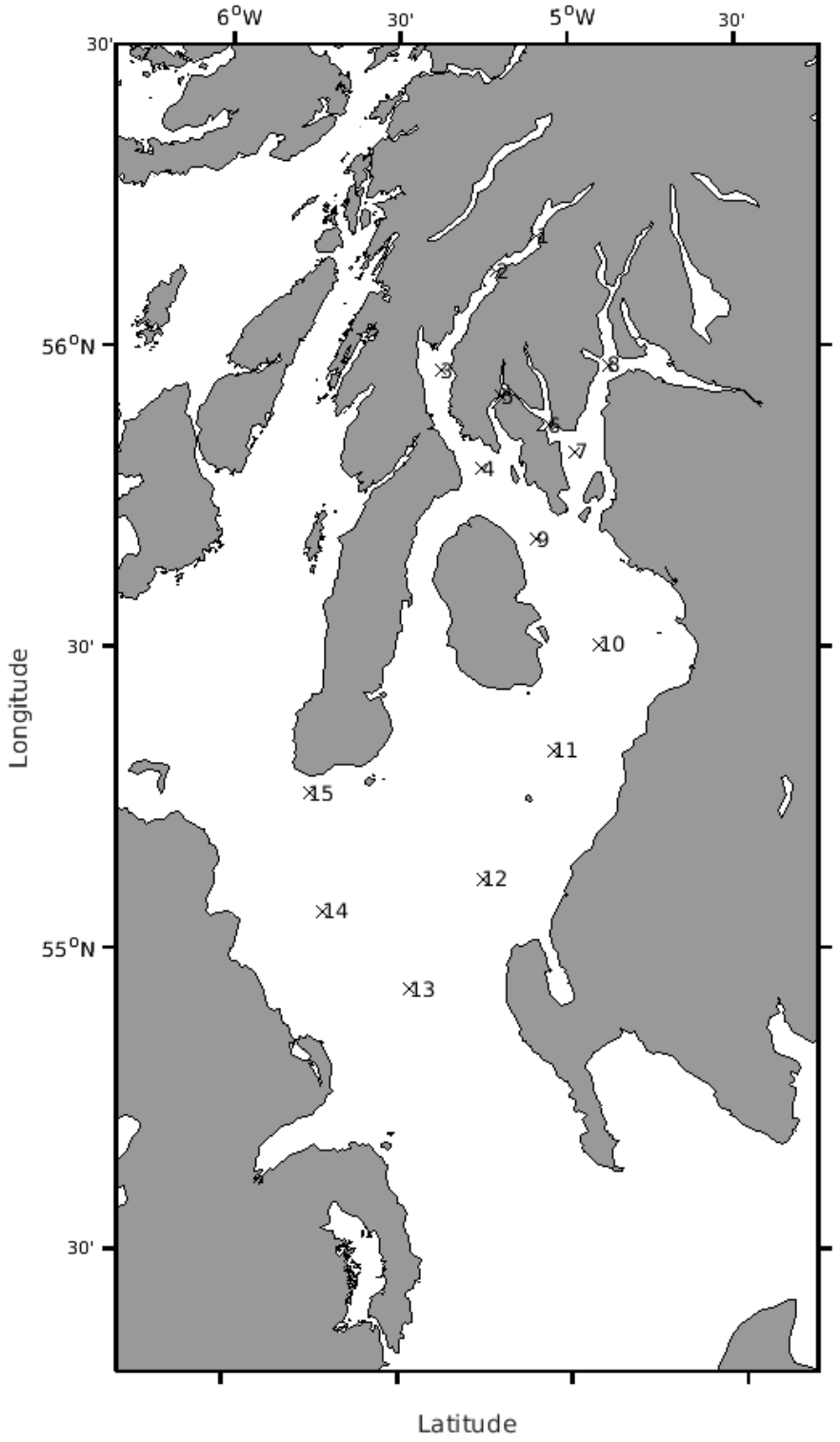

FIGURE 5.33: Position of the points analyzed in the Figure 5.34

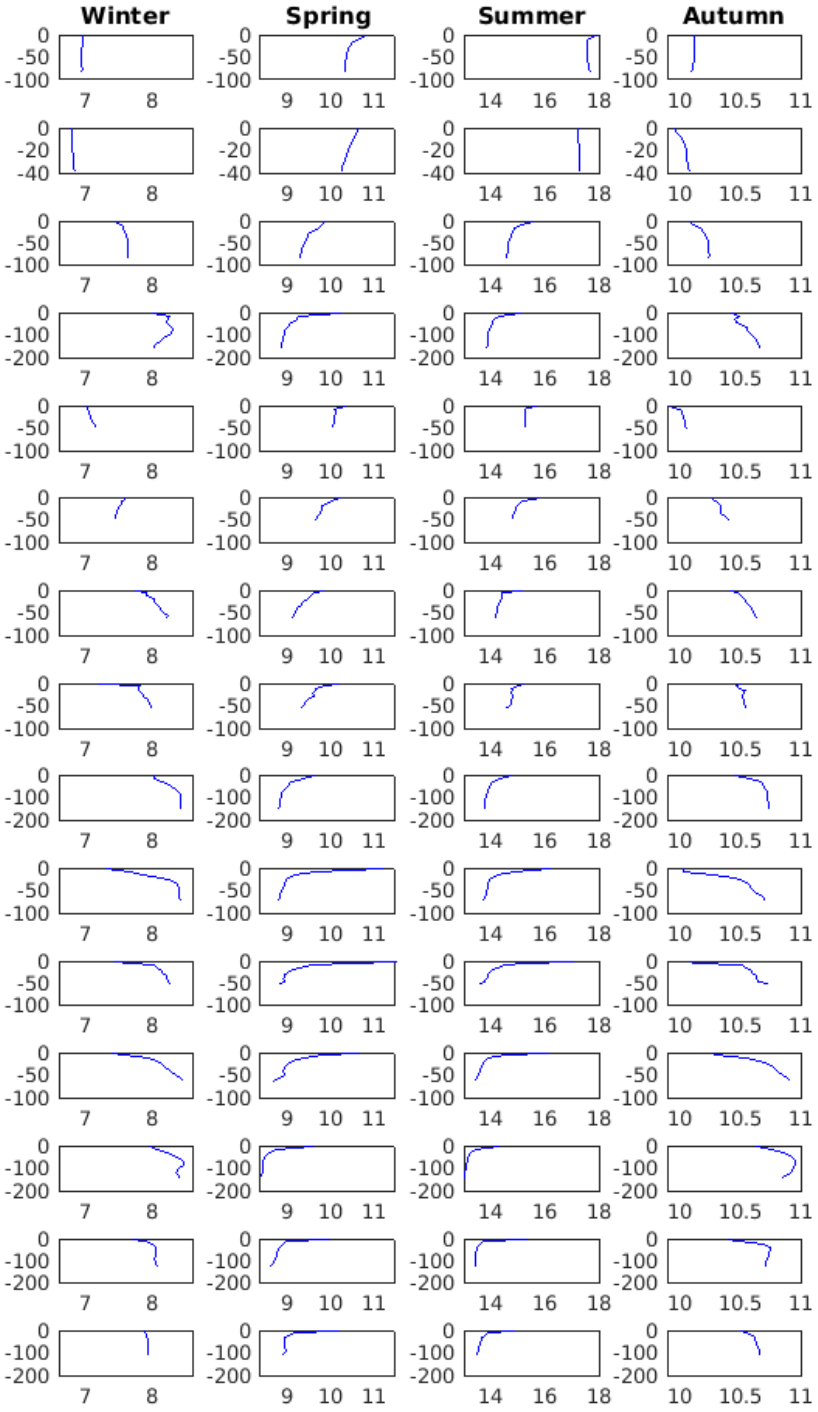

FIGURE 5.34: Model temperature profiles for the points reported in the Figure 5.33: on the x-axis is reported the temperature (in °), while on the y-axis is reported the depth (m). The profiles were taken at the same time for each season: for the Winter the output of the model are from the 15 February 2005 at 15:00 UTC, for the Spring the output of the model are from the 16 May 2005 15:00 UTC, for the Summer are from the 15 August 2005 15:00 UTC, and for the Autumn are from the 15 November 2005 15:00 UTC

5.7 Discussion

The model presented in this chapter managed to describe in a quite accurate way the water circulation of the Clyde Sea, in particular for what concern the barotropic circulation. Baroclinic circulation have not the same degree of accuracy. Some factors could be responsible for this difference between real data and model data: the main reason could be the broad scale data available for this study. The NCEP/NCAR reanalysis, in fact, have a 6 hours time resolution and 1° spatial resolution for the solar heating, making very difficult to have a proper modelling of the temperature and salinity variability, that is strongly dependent by the energy exchange with the solar heating and the atmosphere. In addition, only the surface temperature was available as input from the ocean boundaries, causing a lack of precision in the vertical temperature structure. The uncertainties of the heating, and consequently, of the temperature and saline structure of the Clyde were causing an enhanced error also on the prediction of the tides and on the water level, due to the addition of the term of the temperature and salinity in the primary equation trough also the vertical closure. Vertical closure with course data caused probably the misallignment between the barotropic and the baroclinic model. The larger deviation of salinity in the model were seen in the Clyde Sea, near the estuary of two rivers and also in the North Channel near the estuary of the River Lagan. A possible solution to this would be to couple the FVCOM simulation with an atmospheric model, in order to have a more realistic simulation of the heat exchange and of the freshwater exchange with the atmosphere. In addition, the FVCOM Clyde Sea model should be nested with a broad scale model, in order to simulate the temperature and salinity exchange with the Irish Sea and the Atlantic Ocean, giving a more realistic vertical boundary conditions of the ocean. In order to improve also the salinity performance would be also useful to have salinity values from experimental data near the main rivers of the Clyde. The results from the numerical simulation and from the reanalysis of historical data for the surge show that the origin of the large

storms that affected the Clyde Sea in the last 30 years was usually the North Atlantic Ocean, in particular the areas North to the Clyde Sea, near the Hebridian Islands and the Orkneys. Results also shows that the nonlinear coupling between moderate surge with high spring tides can lead to severe damages to coastal infrastructures. Future development of this model should be the nesting of the model with a large scale shelf model and with a WRF model for the atmosphere. In addition, the development of the FVCOM wave model would be really important for the Clyde Sea model, in order to see which is the effect of the wave-current interactions and the interaction of the waves with the complex bathymetry of the Clyde.

The model was also applied in other projects: one is to simulate the dispersal of shellfish larvae in the Clyde Sea, for which some tests were carried out using the FVCOM lagrangian code by me and Ian Thurlbeck, while some output of the Clyde Sea model were used for a benthic habitat modelling.

Part IV

North Sea

Chapter 6

The physical oceanography of the East Coast of Scotland

The North Sea is one of the most extended shelf seas of the world, with a surface area of 575,300 km^2; is bounded by the the Orkney Islands, by the east coast of Great Britain and by the English channel to the West, by the continental Europe to the South, by the Scandinavian peninsula and the Kattegat and Skagerrak to the East and by the Shetlands and the Norwegian Sea to the North (IHO, 1953).

6.1 Hydrography of the east coast of Scotland

In this thesis we focused our attention in a particular area of the North Sea, the coastal area of the east Scotland. In the figure 6.1 we report the bathymetry of the North Sea and a focus of the bathymetry near the Scottish coastline.
The figure shows the presence of two main estuaries, the Firth of Forth in the S of Scotland and the Moray Firth in the N of Scotland.

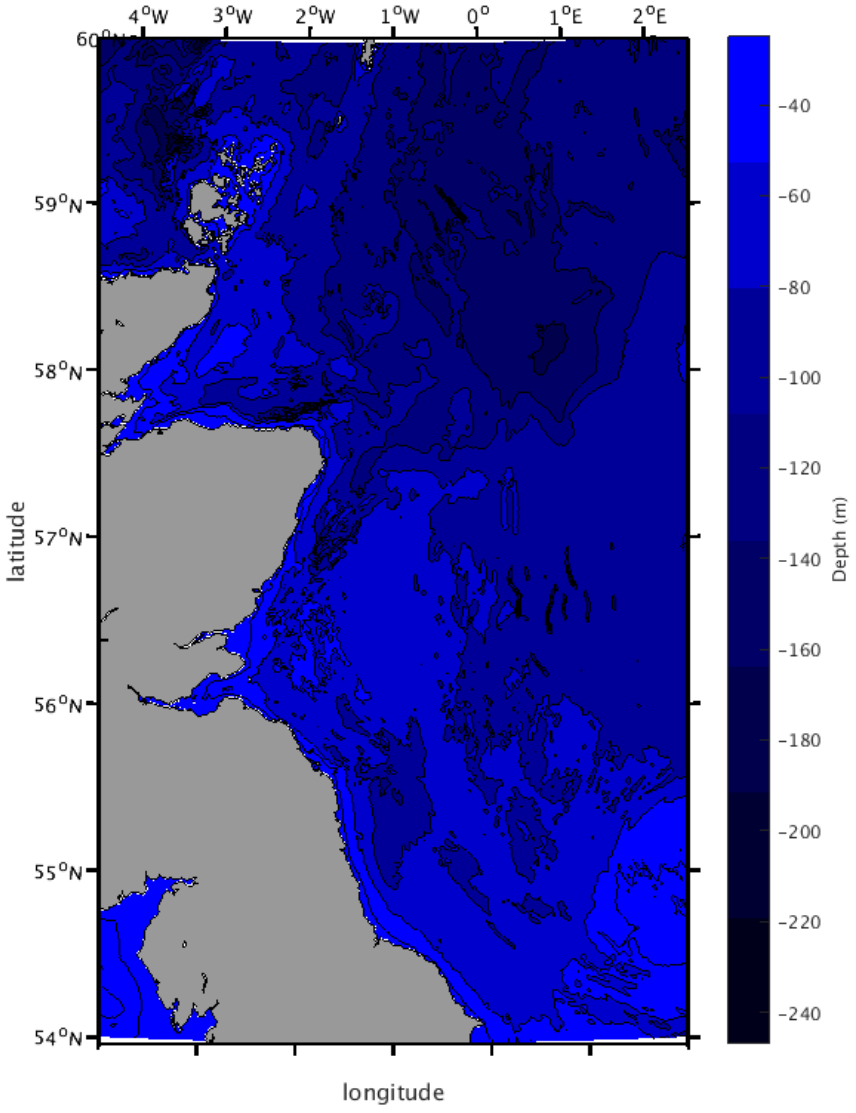

FIGURE 6.1: The bathymetry of the east coast of Scotland (bathymetry from Global Self-consistent, Hierarchical, High-resolution Geography Database (GSHHG), for more information see Wessel and Smith (1996))

The bathymetry is variable in the area, ranging from very shallow area to about -250 m. The water circulation of the east coast is influenced similarly as the Clyde Sea, but tidal currents nearshore are stronger than the Clyde Sea, allowing the mixing of the water column. However, in contrast to the Clyde, the North Sea is exposed to ocean swell waves.

6.2 The Physical oceanography of the North Sea: a brief review

The North Sea has been extensively studied throughout the years, and many reviews have been written. One the most comprehensive and recent review on the physical oceanography of the North Sea was written by Otto et al. (1990). The dominant feature of the water circulation in the North Sea is the tidal motion Otto et al. (1990). The tidal motion of the North Sea is mainly semidiurnal and driven by the M_2 component (Huntley, 1980). In particular, Proudman and Doodson (1924) discovered the presence of three amphidromic points of the M_2 component, that are the main driver of the tidal motion in this area: one in the southern North Sea between the coastline of south-west England and Netherland, one in the central North Sea, close to the shallow sandy area of Dogger Bank and one in the northern North Sea, close to the Norwegian coast.
The combination of these three amphidromes causes tidal range exceeding 5 m at the NE coastline of Scotland, and $>$ 2-3 m in the coastal areas of England, Netherlands and Germany (Huntley, 1980), with tidal currents up to 5 m/s in the Pentland Firth area and $>$ 1 m/s in some areas of the east coast of Scotland (Dietrich, 1950). Stratification in the North Sea is another important factor (Pingree et al., 1978): however, conversely to the Clyde Sea, there are many areas of the North Sea in which the stratification does not occur. In particular the southern North Sea and some coastal areas of the Scotland are not stratified due to the strong tidal currents in the area, that can exceed 1 m/s.

In the central and the northern part of the North Sea, however, the stratification is promoted by low tidal currents combined with larger depths. Wind and pressure perturbations play also an important role in the North Sea: Flather (1987) estimated the maximum depth-averaged storm surge occurring in the North Sea based on a 50 year return period, finding strong maximum surge currents in all the North Sea, exceeding 1 m/s in many locations in both coastal and deep sea. Very large residual currents due to storm surges ($> 1.4m/s$) are reported in the Pentland Firth area (Flather, 1987). Surges are also one of the major threats to coastal communities for the North Sea and the interaction with the tides play an important role in particular for locally generated surge events (Horsburgh and Wilson, 2007).

The water circulation of the North Sea also influences the wave field. The wave pattern and, more in general, the storm pattern in the North Sea is strongly influenced by the North Atlantic ocean (Weisse et al., 2005) and the variability of the wave conditions is closely linked with the North Atlantic Oscillation (NAO) index (Woolf et al., 2002). An increase by 7-18 % of the significant wave height in the North Sea is expected by some numerical models due to the climate change in future years (Grabemann and Weisse, 2008). Wave-current interactions were also studied in a very large scale for the entire North Sea (Tolman, 1991): modulation of the significant wave height and of the mean wave periods were found of the order of 5-10 % of magnitude for those parameters. More significant changes were seen for spectral components. However the model presented by Tolman (1991) had a resolution of 24 km, that is too coarse to see local effects, and in particular, shallow water effects.

A more high-resolution study of the wave-current interactions in the North Sea was made by Osuna and Monbaliu (2004) and by Monbaliu et al. (1998). However, the area in study was more focused to the Southern North Sea and the model domain was very coarse in the east coast of Scotland. The results were very similar to the one found by Tolman (1991), with a modulation due to the currents to the significant wave height and to the mean wave period of about 3 % and 20 % respectively.

Previous studies analyzing real data from the North Sea found that a crossing sea state (see Section 2.5.3 for more details about crossing sea state) occurs about 25 % of the time in both coastal and deep sea (Guedes Soares, 1984, 1991).

Chapter 7

East coast of Scotland model: Materials and Methods

7.1 Introduction

The MIKE by DHI software was chosen for the modelling of the water circulation and wave propagation in the East Coast of Scotland. It was chosen since at the time of the beginning of the project was one of the few models that could model both waves and tides with the same grid, using an unstructured grid approach. In addition it was also chosen because is one of the most widely used in industry and the research project was intended mostly to assess the impact of tidal and wave extraction: with MIKE was also possible to implement tidal arrays turbine and wave energy extractors inside the model.

7.2 MIKE model description

We use the MIKE model, a commercial software distributed by Danish Hydraulics Institute (DHI), for simulating the tidal-, wind-driven circulation and the wave propagation of the east coast of Scotland. The MIKE software is composed of different modules, that can allow the user to simulate different hydrodynamical features at the same time or separately. In addition the MIKE software has a module for the generation of the grid and input files. In particular we used the following modules for simulating the wave propagation:

- The MIKE ZERO modules were used for generating the computational grid and the input files
- The MIKE 3 FM module was used for simulating the tidal- and the wind-driven circulation
- The MIKE 21 SW module was used for modelling the wave propagation.

For the simulation of the wave-current effect we simulated the flow with the MIKE 3 FM and then we use the depth-average current and the water level variation as input for the MIKE 21 SW module. The MIKE by DHI uses, as FVCOM, an unstructured grid approach, but the quality constraints on the grid are less strong than FVCOM for the grid generation.

7.2.1 MIKE 3 Flow Model

MIKE 3FM (Flow Model) is a hydrodynamic model based on the numerical solution of the 3-D incompressible Reynolds averaged Navier-Stokes equations, under the Boussinesq and the hydrostatic pressure approximations (DHI, 2011a). The equations assume this formulation:

$$\frac{\partial u}{\partial t}+\frac{\partial u^2}{\partial x}+\frac{\partial vu}{\partial y}+\frac{\partial wu}{\partial z}-fv=-g\frac{\partial \eta}{\partial x}-\frac{1}{\rho_0}\frac{\partial p_a}{\partial x}-\frac{g}{\rho_0}\int_z^\eta \frac{\partial \rho}{\partial x}dz+F_u+\frac{\partial}{\partial z}\left(K_m\frac{\partial u}{\partial z}\right)+u_sG \tag{7.1}$$

$$\frac{\partial v}{\partial t}+\frac{\partial uv}{\partial x}+\frac{\partial v^2}{\partial y}+\frac{\partial wv}{\partial z}+fu=-g\frac{\partial \eta}{\partial y}-\frac{1}{\rho_0}\frac{\partial p_a}{\partial y}-\frac{g}{\rho_0}\int_z^\eta \frac{\partial \rho}{\partial y}dz+F_v+\frac{\partial}{\partial z}\left(K_m\frac{\partial v}{\partial z}\right)+v_sG \tag{7.2}$$

$$\frac{\partial u}{\partial x}+\frac{\partial v}{\partial y}+\frac{\partial w}{\partial z}=G \tag{7.3}$$

$$\frac{\partial T}{\partial t}+\frac{\partial uT}{\partial x}+\frac{\partial vT}{\partial y}+\frac{\partial wT}{\partial z}=\frac{\partial}{\partial z}(K_h\frac{\partial T}{\partial z})+F_T+\hat{H}+T_sG \tag{7.4}$$

$$\frac{\partial S}{\partial t}+\frac{\partial uS}{\partial x}+\frac{\partial vS}{\partial y}+\frac{\partial wS}{\partial z}=\frac{\partial}{\partial z}(K_h\frac{\partial S}{\partial z})+F_S+S_sG \tag{7.5}$$

In which the diffusion horizontal terms are defined as:

$$(F_T,F_S)=\left[\frac{\partial}{\partial x}\left(K_h\frac{\partial}{\partial}\right)+\frac{\partial}{\partial y}\left(K_h\frac{\partial}{\partial y}\right)\right](T,S) \tag{7.6}$$

The closure of the equations in MIKE 3 for the horizontal momentum diffusion are the same as FVCOM, in particular in MIKE it is also possible to use the Smagorinsky eddy parametrization method (Smagorinsky, 1963).

7.2.2 MIKE 21 Spectral Wave

The MIKE 21 SW (Spectral Wave) is an unstructured grid model for wave prediction and analysis on both regional and small scale (DHI, 2011b). The MIKE 21 SW is based on the wave action conservation equation (Komen et al., 1996; Young, 1999), where the dependent variable is the directional-frequency wave action spectrum.

$$\frac{\partial N}{\partial t}+\nabla\cdot(cN)=\frac{S}{\sigma} \tag{7.7}$$

where S is the energy source term, that depends on the transfer of the wind on the wave field, on the dissipation due to depth induced wave breaking, on the wave-wave interaction, on the dissipation due to bottom friction and on the dissipation caused by the white-capping:

$$S = S_{in} + S_{nl} + S_{ds} + S_{bot} + S_{surf} \tag{7.8}$$

The wave action density spectrum N(σ,θ) is defined as (Bretherton and Garrett, 1968):

$$N(\sigma, \theta) = \frac{E(\sigma, \theta)}{\sigma} \tag{7.9}$$

where E is the wave energy density spectrum, $\sigma = 2\pi f$ is the angular frequency, and θ is the direction of wave propagation. The ∇ operator appearing in the wave-action conservation equation is a four-dimensional operator on x, y, σ and θ. The momentum transfer from the wind to the waves follows the formulation in Komen et al. (1996). The momentum transfer and the drag depend not only on the strength of the wind but also on the wave state itself. The roughness is specified with the Charnock parameter. For the physics of the propagation and breaking of the waves, the MIKE 21 SW uses different parametrizations and formulations, in particular:

- The depth-induced wave breaking is based on the formulation of Battjes and Janssen (1978). The formulation of the depth-induced wave breaking can be written as:

$$S_{surf}(\sigma, \theta) = -\frac{\alpha Q_b \bar{\sigma} H_m^2}{8\pi} \frac{E(\sigma, \theta)}{E_t ot} \tag{7.10}$$

  where $\alpha \approx 1.0$ is a calibration constant, Q_b is the fraction of breaking waves, $\bar{\sigma}$ is the spectrum average frequency, E_{tot} is the total wave energy, that is linked to the wave action density spectrum, and H_m is the estimated maximum wave height, that is defined as $H_m = \gamma d$ (Battjes and Janssen, 1978), in which d is the depth and γ, the free breaking parameter (Battjes, 1974), can be parametrized in different ways: MIKE 21 SW gives three different options to the user. First,

the γ can be specified from the user directly. Kaminsky and Kraus (1993) found experimentally that γ can range between 0.6 and 1.79, Battjes and Stive (1985) proposed a value of $\gamma = 0.73$. MIKE 21 SW also allow the user to choose a variable γ parameter: the Nelson (1987, 1994) formulation that is based on the assumption that γ depends on the local bottom slope, and the Ruessink et al. (2003) where γ is a function of the local wavenumber and the wave depth.

- The bottom friction process, that is fundamental for the interaction between the bottom of the sea with the wave field, particularly in shallow water, can be specified in five different ways and are related to the hydrodynamics as specified in Johnson and Kofoed-Hansen (2000). The five different ways are: 1) No bottom friction, 2) using a friction coefficient C_{fw} (Collins, 1972), 3) the friction factor f_w, 4) the Nikuradse Roughness k_N (Nikuradse, 1933), and 5) the sand grain size $d50$.

- The white capping formulation used by the MIKE 21 SW is the one described in Komen et al. (1996). That considers the energy dissipation of waves, based on the theory of Hasselmann (1974). For the fully spectral formulation, the white capping assumes a form that is dependent on the mean frequency $\bar{\sigma}$ and on the wavenumber k:

$$S_{ds}(\sigma,\theta) = -C_{ds}\left(\bar{k}^2 m_0\right)^2 \left[(1-\delta)\frac{k}{\bar{k}} + \delta\left(\frac{k}{\bar{k}}\right)^2\right]\bar{\sigma}N(\sigma,\theta). \tag{7.11}$$

here the two parameters C_{ds} and δ are the two dissipation coefficients, that control the overall dissipation rate and the strength of dissipation in the energy/action spectrum respectively, and m_0 is the zeroth moment of the overall spectrum.

7.2.3 Wave-current interactions

The wave-current interactions were studied in the east coast of Scotland running the model without and with the currents added to the model and then comparing the results. The coupling between waves and current was a one-way coupling, in which the currents from the MIKE 3 FM model were fed into the MIKE 21 SW model. The WCIs in the spectral wave model affect the propagation of the wavetrains, modifying the wavelengths. In particular the dispersion relation of the waves in the presence of an ambient current is:

$$\sigma = \sqrt{gk\tanh(kd)} = \omega - \overline{k}\cdot\overline{U} \tag{7.12}$$

in which σ is the angular frequency appearing in equations 4.26 and 4.28, k is the wavenumber of the wavetrain, ω is the undisturbed angular frequency and U is the ambient current. From this dispersion relation the formulation of the phase speed is the following:

$$(c_x, c_y) = \overline{c_g} + \overline{U} = \frac{1}{2}\left(1 + \frac{2kd}{\sinh(2kd)}\right)\frac{\sigma}{k} + \overline{U} \tag{7.13}$$

$$c_\sigma = \frac{\partial\sigma}{\partial d}\left[\frac{\partial d}{\partial t} + \overline{U}\cdot\nabla_{\overline{x}}d\right] - c_g\overline{k}\cdot\frac{\partial\overline{U}}{\partial s} \tag{7.14}$$

$$c_\theta = -\frac{1}{k}\left[\frac{\partial\sigma}{\partial d}\frac{\partial d}{\partial m} + \overline{k}\cdot\frac{\partial U}{\partial m}\right] \tag{7.15}$$

Where s is the space coordinate in the wave direction of the propagation, θ and m are the coordinates perpendicular to s, and d is the depth of the sea.

7.2.4 Windsea and swell waves

In the present study the windsea and the swell waves and their interaction are studied. MIKE 21 SW gives the opportunity to separate spectrally the windsea waves and the swell waves. There are two criteria available to make this separation.

The first criterion is based on the difference of the energy between the spectrum and the fully-developed sea condition (Earle, 1984). In this case the threshold frequency is identified as:

$$f_{threshold} = \alpha f_{p,PM} \left(\frac{E_{PM}}{E_{Model}} \right)^{\beta} \tag{7.16}$$

where α = 0.7, β = 0.31, E_{Model} is the total energy at each node point calculated by the MIKE 21 SW model, and the Pierson-Moskowitz peak frequency and the energy are estimated as (see also Chapter 2):

$$f_{PM} = 0.14 \frac{g}{U_{10}} \tag{7.17}$$

$$E_{PM} = \left(\frac{U_{10}}{1.4g} \right)^{4} \tag{7.18}$$

The second method is based on the wave-age criterion (Drennan et al., 2003) from empirical wave measurements in wave tanks and in Lake Ontario field measurements. From Donelan et al. (1985) swell waves are the components fulfilling the following relation:

$$\frac{U_{10}}{c_p} \cos(\theta - \theta_w) < 0.83 \tag{7.19}$$

where U_{10} is the wind speed at 10 m, c_p is the phase speed, θ is the wave propagation direction and θ_w is the direction of the wind.

7.3 Datasets description

7.3.1 Model Forcing

The model forcing data, are summarized here in tables. Table 7.1 list the sources for the east coast of Scotland model for the bathymetry, coastline and physical forcings. In

the next section will be described the procedure used for the set-up of the model using these input data.

Variable	Source	Time res.	Spat. res.	Reference
Bathymetry	GEBCO	N/A	30" x 30"	Fisher et al. (1982)
Bathymetry	Survey	N/A	$< 100m$	Serpetti et al. (2011, 2012)
Coastline	GSHHG	N/A	$< 1km$	Wessel and Smith (1996)
Coastline	Survey	N/A	$< 100m$	Serpetti et al. (2011, 2012)
Tides	OTPS	15 min	2' x 2'	Egbert et al. (2010)
Wind	ERA-Interim ECMWF	3 hs	1/8° x 1/8°	Dee et al. (2011)
Pressure	ERA-Interim ECMWF	3 hs	1/8° x 1/8°	Dee et al. (2011)
Waves	University of Edinburgh	6 hs	$< 1km$	Venugopal and Nemalidinne (2015)

TABLE 7.1: East coast initial conditions and forcings for the MIKE21 and MIKE3 model

7.3.2 Model set-up

This section describes how the models was set-up using the forcing data reported in the table 7.1. Tidal boundary conditions were provided by OSU (Oregon State University) Tidal Prediction Software (OTPS), as the Clyde model Egbert et al. (2010). The tidal predictions are based on water elevations recorded by TOPEX/Poseidon and Jason satellites, adjusted with tidal gauges from ports around the world. The grid and the bathymetry were set-up using the MIKE ZERO toolbox, that was also used to define boundary conditions for the hydrodynamic model and for the wind and pressure forcings. For the bathymetry, the GEBCO bathymetry was used outside the high resolution area, while in the high resolution area near Stonehaven was used an high resolution bathymetry from a survey carried out by Serpetti et al. (2011, 2012). Boundary conditions for waves were provided by Prof. Vengatesan Venugopal (University of Edinburgh) for 2008 and 2010 (Venugopal and Nemalidinne, 2015).

7.3.3 Validation and calibration datasets

Table 7.2 reports the locations for the validation of both the tidal currents and the water level elevations from tidal buoys in the area. In Table 7.3 are reported the details of the wave gauges used for the MIKE 21 SW wave model validation. Satellite observations were also implemented in the validation stage, in order to integrate the three time sequences of waves recorded in the east coast with more data, to have a stronger overall validation. Satellite observations are reported in Table 7.4.

Description	**Coordinates**		**Depth (m)**	**Used for**
	latitude (°)	longitude (°)		
Aberdeen Tide Gauge	57.144	-2.0803	-	water level val/cal
Leith Tide Gauge	55.9898	-3.1682	-	water level validation
Buckie Tide Gauge	57.6667	-2.9667	-	water level validation
BODC 4551 RCM	57.7910	-2.8000	12	current validation
BODC 4561 RCM	57.2320	-1.9680	12	current validation
BODC 4562 RCM	57.2320	-1.9680	27	current validation
BODC 4571 RCM	57.2260	-1.9020	12	current validation
BODC 4572 RCM	57.2260	-1.9020	52	current validation
BODC 4582 RCM	56.9870	-2.1500	23	current validation
BODC 4591 RCM	56.9820	-2.0980	12	current validation
BODC 4592 RCM	56.9820	-2.0980	47	current validation

TABLE 7.2: Location of the validation/calibration instrumentation for the MIKE hydrodynamic model of the east coast of Scotland

Description	**Coordinates**		**Depth (m)**	**Used for**
	longitude (°)	latitude (°)		
Firth of Forth buoy	-2.5038	56.1882	-	waves validation
Moray Firth buoy	-3.3331	57.9663	-	waves val/cal
Aberdeen wave rider	-2.0500	57.1608	-	waves validation

TABLE 7.3: Location of the validation/calibration instrumentation for the MIKE hydrodynamic model of the east coast of Scotland

No	Satellite	Day	Time
1	ers2	01/02/2010	21:46
2	jas1	02/02/2010	15:07
3	jas1	02/02/2010	20:59
4	ers2	02/02/2010	11:27
5	ers2	05/02/2010	11:32
6	ers2	08/02/2010	11:38
7	jas1	08/02/2010	13:31
8	ers2	02/05/2010	11:29
9	jas1	05/05/2010	20:06
10	jas1	08/05/2010	19:17
11	jas1	10/05/2010	01:32
1_{08}	jas1	02/07/2008	12:28
2_{08}	ers2	02/07/2008	21:40
3_{08}	ers2	03/07/2008	11:23
4_{08}	jas1	05/07/2008	11:40
5_{08}	ers2	05/07/2008	21:46
6_{08}	ers2	06/07/2008	11:28
7_{08}	ers2	09/07/2008	11:34
8_{08}	jas1	09/07/2008	17:07
9_{08}	jas1	18/07/2008	08:51
10_{08}	ers2	18/07/2008	21:38
11_{08}	ers2	19/07/2008	11:20
12_{08}	jas1	19/07/2008	15:05
13_{08}	ers2	21/07/2008	21:43
14_{08}	jas1	22/07/2008	08:25
15_{08}	ers2	22/07/2008	11:25
16_{08}	jas1	29/07/2008	13:04

TABLE 7.4: Satellite data for the validation for the MIKE wave model of the east coast of Scotland

For the tidal validation for the East coast of Scotland model, the harmonic components were extracted from the recorded and modelled water level for the tide gauges reported in table above. The methods used were the same as used in 4. Correlation coefficients and RMSE values were used in both the waves and tidal model for the validation. In figure 7.1 a map with the graphic detail of the point used for the validation and calibration of the model is given.

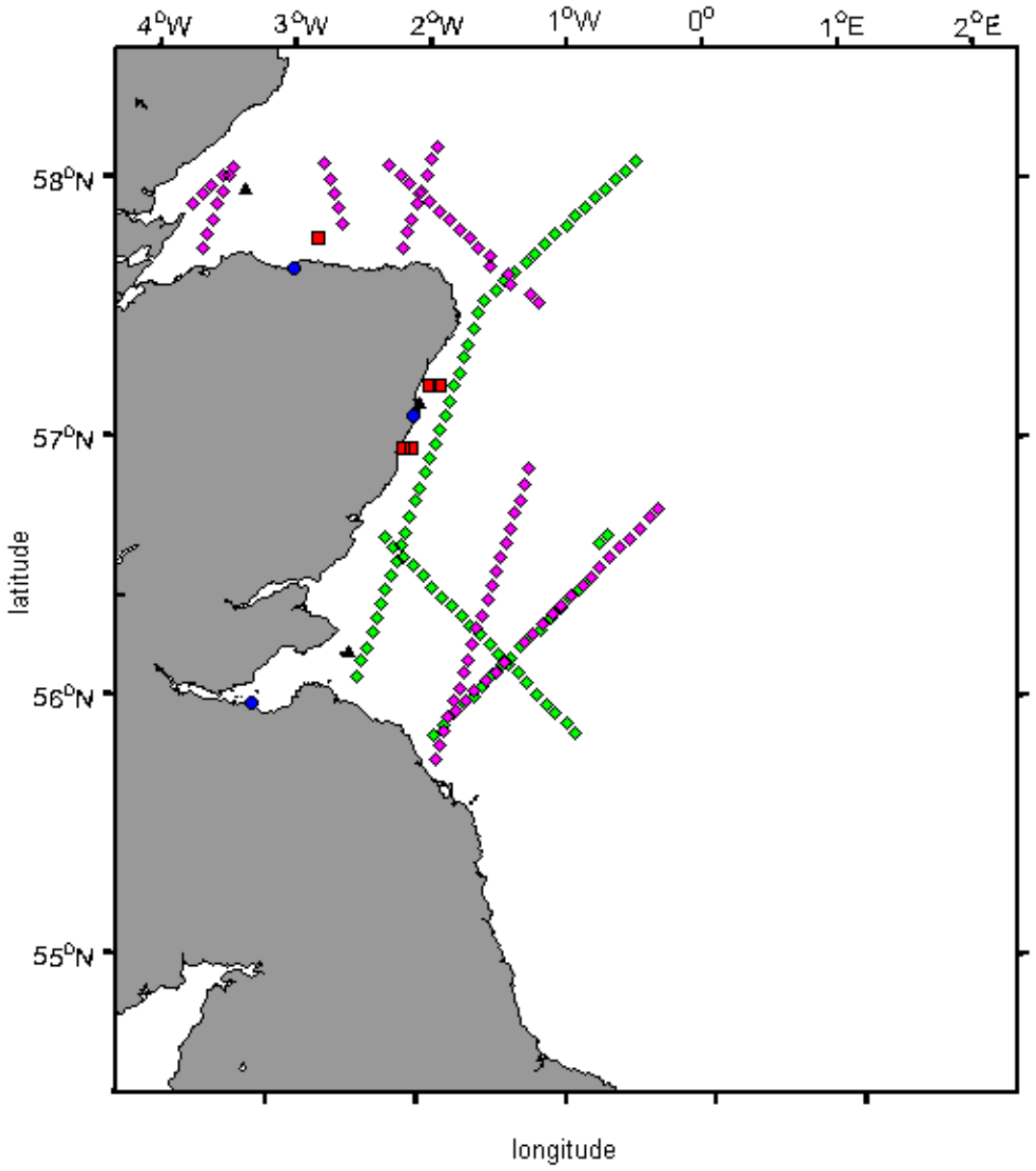

FIGURE 7.1: East coast map with the position of the tide gauge (blue circles), current probes (red squares), wave gauges (black triangles) and satellite observations (green and pink squares for jas and ers2 respectively)

Chapter 8

Results of the North Sea simulations

8.1 Introduction

This chapter report the results of a wave-current one-way coupled model and its calibration and validation using the MIKE hydrodynamic (MIKE 3 FM) and wave (MIKE 21 SW) model described in the Chapter 3. The results of this simulation were used to calibrate and validate a statistical model for the prediction of suspended sediment concentration in the water column.

8.2 Calibration and Validation

8.2.1 Hydrodynamic model

The calibration of the model was carried out for the year 2007 based on the agreement on water level in the Aberdeen tide gauge. The calibration procedure was implemented in order to find the best parameters for the hydrodynamic model, such as the timestep or the bottom roughness coefficients. This procedure was carried out jointly with dr. Chris McCaig. In contrast to the calibration reported in the previous chapter for the FVCOM model, no sponge layer was implemented for the MIKE 3 FM, but the model was calibrated changing the Smagorinsky constant and the drag coefficient. The timestep was fixed to 1 s, after an analysis based on the Courant-Friedrichs-Lewy (CFL) conditions and after some attempt to higher timesteps. Blow-up was recorded for Smagorinsky constant $>$ 0.3, and for low roughness heights. During the calibration it was noticed how the model was performing better using the drag coefficient approach instead of specifying the value of the bottom roughness height for the bottom friction. Compared to the FVCOM Clyde Sea model, the calibration was less time-consuming, since less parameters were present for the calibration and also since the results were quite similar. The final set-up of the hydrodynamic model is reported in Table 8.1.

Variable	Value
Timestep	1 s
Smagorinsky constant	0.2
Horizontal Min Eddy viscosity	$1.8 \cdot 10^{-6}\ m^2/s$
Horizontal Max Eddy viscosity	$10^{10}\ m^2/s$
Vertical Min Eddy viscosity	$10^{-6}\ m^2/s$
Drag coefficient	0.0025
Number of layers	10

TABLE 8.1: Parameters of the model after the calibration procedure

For the second stage, the validation of the hydrodynamic model carried out based on the agreement between the experimental and the model tidal harmonic components

of the water elevation in the three locations reported in Table 7.3. The results of this validation are reported in the Table 8.2

h.c.	**Aberdeen**				**Leith**				**Buckie**			
	h_o	g_o	h_m	g_m	h_o	g_o	h_m	g_m	h_o	g_o	h_m	g_m
M_2	130	24.6	127	23.7	179	55.2	176	54.2	117	338	118	338
S_2	44.1	62.7	45.2	59.9	61.6	95.2	59.9	92.6	40.9	17.5	42.9	12.4
N_2	25.9	2.36	25.5	0.	34.6	32.8	32.6	30.4	23.9	318	24.9	314
O_1	12.5	50.8	12.5	55.8	13.9	64.6	12.6	72.2	11.7	33.8	11.6	36.1
K_1	10.7	207	11.2	200	11.7	220	11.4	219	11.3	155	10.8	179
Q_1	4.40	9.88	3.89	354	3.74	18.7	3.79	7.19	4.24	349	3.73	263

TABLE 8.2: Comparison of the observed and modelled amplitude and phase for dominant semi-diurnal and diurnal tidal components h_0 and g_0 are the observed amplitude in cm and the phase in degrees respectively and h_m and g_m are the modelled amplitude in cm and the phase in degrees

The table shows a good agreement (the maximum difference between the modelled and the observed M_2, that is the dominant component in the area, was 3 cm for the amplitude and 1° for the phase) between the computed and the observed tidal components in the east coast of Scotland, both for the phase and amplitude of main harmonic components. Based on this, we can conclude that the model reproduce well the water level motion due to tides in the area of study. However, in order to study the wave-current interactions and to study the dynamics of the sediments resuspension, it is fundamental also to see how the model performs also on the currents. In the table 7.2 are reported 8 locations in which current measurements, near the Stonehaven Bay and Aberdeen, were available for the year 1992. The output of the model were compared to the observed current components and to the total current magnitude (Table 8.3).

From the results, it is possible to conclude that the model reproduce adequately the current dynamics in the east coast of Scotland, with the error on the total current that does not exceed 15% and the bias does not exceed 0.1 m/s. In general, from the bias it is possible to see that, in general, the model underestimates the current magnitude in the area. This is possibly due to the absence of the residuals at the boundaries, to the wave radiation effect on the current dynamics, and to the absence of the salinity-driven

RCM No	Lat	Lon	RMSE (m/s)	NRMSE	R^2	Bias (m/s)
current						
4551	-2.8	57.791	0.094	0.157	0.17	0.001
4561	-1.968	57.232	0.111	0.124	0.70	-0.03
4562	-1.968	57.232	0.075	0.105	0.75	-0.02
4571	-1.902	57.226	0.223	0.147	0.23	-0.05
4572	-1.902	57.226	0.087	0.112	0.80	-0.02
4582	-2.15	56.987	0.075	0.124	0.80	0.02
4591	-2.098	56.982	0.125	0.132	0.73	-0.062
4592	-2.098	56.982	0.073	0.121	0.82	-0.05
u						
4551	-2.8	57.791	0.098	0.111	0.71	-0.06
4561	-1.968	57.232	0.071	0.088	0.78	-0.007
4562	-1.968	57.232	0.054	0.075	0.9	0.01
4571	-1.902	57.226	0.151	0.133	0.43	-0.028
4572	-1.902	57.226	0.049	0.068	0.84	-0.004
4582	-2.15	56.987	0.041	0.071	0.88	0.006
4591	-2.098	56.982	0.078	0.081	0.76	0.008
4592	-2.098	56.982	0.058	0.085	0.91	0.006
v						
4551	-2.8	57.791	0.099	0.206	0.17	0.08
4561	-1.968	57.232	0.101	0.064	0.92	0.02
4562	-1.968	57.232	0.079	0.062	0.9	-0.01
4571	-1.902	57.226	0.215	0.121	0.71	0.02
4572	-1.902	57.226	0.09	0.061	0.93	0.0122
4582	-2.15	56.987	0.083	0.072	0.91	-0.002
4591	-2.098	56.982	0.116	0.07	0.94	0.035
4592	-2.098	56.982	0.076	0.068	0.92	-0.008

TABLE 8.3: Results from the validation of the currents, showing the difference between the modelled and observed current speeds at the eight locations reported in Table 7.3

and temperature-driven component. The result, however, is still satisfactory: the model manages to reproduce the general dynamics of the area, in which the most important forcing is the tidal motion (Otto et al., 1990).

8.2.2 Wave model

The wave model was calibrated for 2 months (with a spin-up time of 1 month) based on the Firth of Forth wave gauge in order to determine the timestep and the parameters for the validation and the hindcast. The main parameters that were involved in the calibration stage were the breaking parameter γ, and the two dissipation coefficients (C_{Dis},δ) regulating the whitecapping. During the calibration, it was noticed that the γ was the calibration parameter with the stronger effect on the total wave field: the effect of this parameter was assessed in the range 0.6-1, that is the typical range that can be found in literature (Battjes, 1974; Stive, 1985; Battjes and Stive, 1985; Nelson, 1987, 1994; Kaminsky and Kraus, 1993). The final set-up of the model is shown in the Table 8.4:

Variable	Value
Timestep	0.01 - 30 s
Frequencies	25
Directions	16
Charnock coefficient	0.01
γ	0.6
C_{Dis}	2
δ	0.8
k_N	0.01 m

TABLE 8.4: Parameters of the wave model after the calibration procedure

For the validation, the output wave height and period were compared to available experimental measure from wave gauges (see Table 4.10 for more details). This validation was then integrated using satellite data (Table 7.4). This was also important since it was possible to understand the performance of the model spatially. The results of this validation are summarized in the Table 8.5

Results shows that the model performs overall well on wave heights, in particular when the significant wave height is lower than 3 m, while it slightly underestimates the H_s when it is higher. This is evident comparing the performance of the model between winter and summer conditions: in winter, when the wave are higher, the bias between

	Coupled				Uncoupled			
	Bias	RMSE	R	SI	Bias	RMSE	R	SI
Firth of Forth								
H_s	-0.02 m	0.30 m	0.941	0.27	-0.01 m	0.30 m	0.939	0.27
T_m	-0.70 s	1.17 s	0.767	0.25	-0.76 s	1.24 s	0.758	0.27
Moray Firth								
H_s	-0.14 m	0.42 m	0.849	0.38	-0.15 m	0.42 m	0.848	0.39
T_m	-1.18 s	1.75 s	0.668	0.39	-1.23 s	1.83 s	0.656	0.41
Aberdeen								
H_s	-0.07 m	0.21 m	0.836	0.32	-0.07 m	0.22 m	0.831	0.32
T_m	-0.25 s	0.91 s	0.715	0.20	-0.30 s	0.97 s	0.701	0.21
Satellite								
Winter								
H_s	-0.2 m	0.4 m	-	0.25	-0.2 m	0.4 m	-	0.25
T_m	+0 s	0.8 s	-	0.15	+0 s	0.8 s	-	0.15
Spring								
H_s	-0.1 m	0.3 m	-	0.21	-0.1 m	0.3 m	-	0.21
T_m	+0.1 s	1.2 s	-	0.23	+0.1 s	1.2 s	-	0.23

TABLE 8.5: Wave model model performance with experimental data from wave gauges and satellite data: coupled model is referred to the model with wave-currents interactions, while uncoupled is the model without current fields as input

the model and the observations is higher as well as the root-mean square error. On the other hand, the model reproduces better the wave period when the waves are higher, while it overestimates the wave period when the waves are lower. It is important to notice that for satellite measurement the wave period is very difficult to estimate and the uncertainties associated with each measurement are high (Gommenginger et al., 2003). Comparing the Scatter Index (SI) of the wave periods from satellite with the SI based on wave gauges, the two values are of comparable magnitude, but the bias associated with the comparison of model output with satellite data is lower than the wave gauges.

Details of the satellite validation are in Table 12.1-12.2 in the Appendix.

8.3 Wave-Current interaction

Predicted wave fields with and without wave-current interaction were compared during a 7-month period in 2010, covering both winter and summer conditions, for evaluating the importance of WCI on wave features. The results are shown in Figure 8.1. For the comparison between the coupled and the uncoupled model the Root-Mean Square (RMS) between the two runs was computed. Results show some differences between the two runs, in particular, the largest deviations, due to WCI, are found in coastal areas, such as around headlands, bays and in estuaries, in which the currents (mostly driven by tides) are strongest. As expected the highest differences were seen in the proximity of the coastline (Signell et al., 1990): this was because the strength of the currents (mainly tidal-driven) is larger (Dietrich, 1950; Otto et al., 1990). During spring tides, higher values for the current were recorded off Northeast England and near Peterhead and Aberdeen (see Figure 8.1). Wave periods are more affected than wave heights in this coupling, with RMS deviations that can be on average 20 % (absolute value) in shallow-water coastal areas. We also considered the effect of the wave-current interactions on the wave directional spreading, as this is an important variable for the stability of the wave train in deep water and on its evolution (Benjamin and Feir, 1967). The results showed that during the 7-month period the significant wave height was, on average, less affected than directional spreading by wave periods: the difference was of the order of magnitude of 0.1 m near the coastline and less offshore, while the difference in peak spectral wave period (T_p) exceeded 1 s in some of the east coast Firths such as the Moray Firth and the Firth of Forth.

Maximum and minimum variation of the H_s between the coupled and the uncoupled run were also computed (Figure 8.2-6.3): the maximum and the minimum difference was +3 m and -2 m, both occurring during storm events. The larger deviations are modelled for the coastal areas, while they are very little for the open sea.

The magnitude of these values is similar to previous studies in the southern North Sea

(Osuna and Monbaliu, 2004), or in the Adriatic Sea during strong storm conditions (Benetazzo et al., 2013).

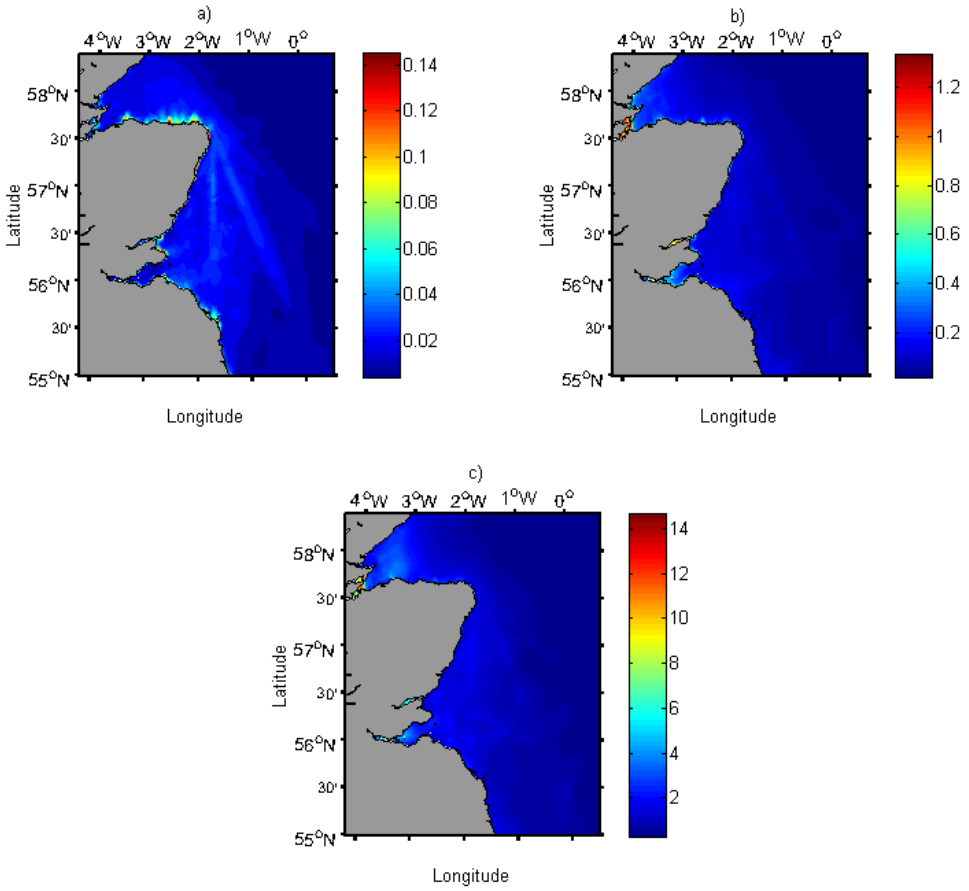

FIGURE 8.1: Root-Mean square difference between the model with wave-currents interactions included and the run without WCIs: a) RMS difference for the H_s (m), b) RMS difference for the T_m (s), c) RMS difference for the directional spreading

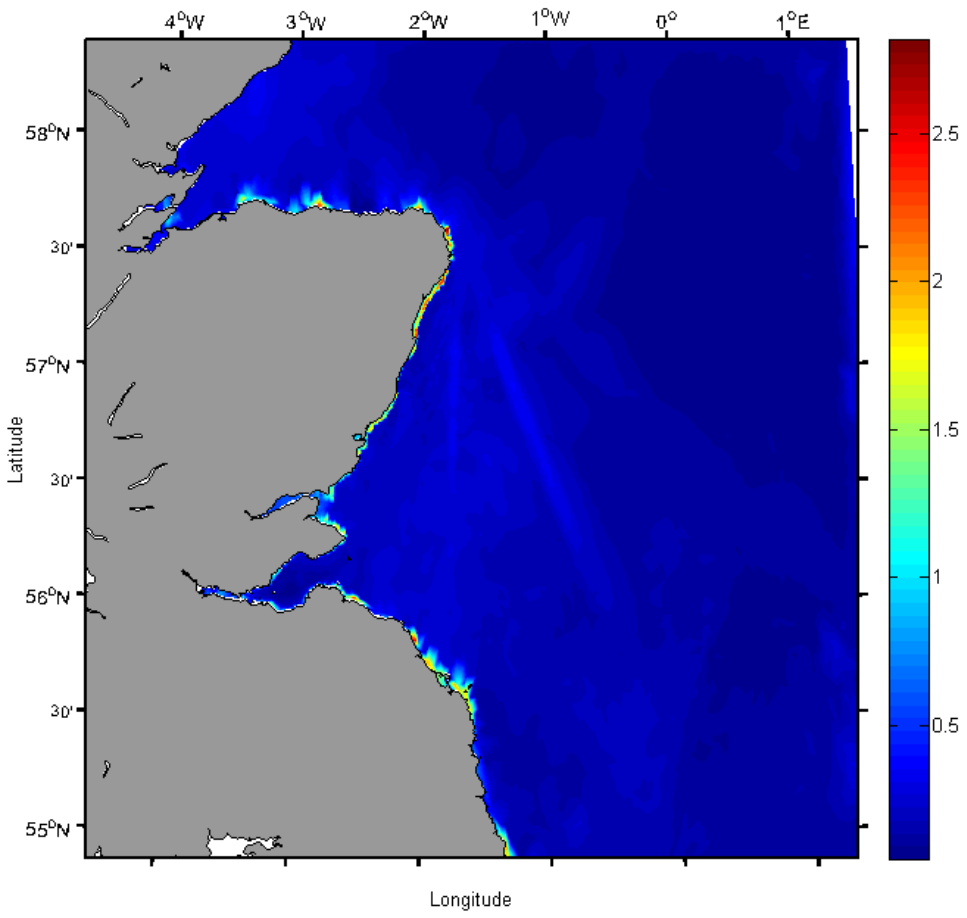

FIGURE 8.2: Maximum positive spatial difference in H_s (m) for the model with and without wave-currents interactions

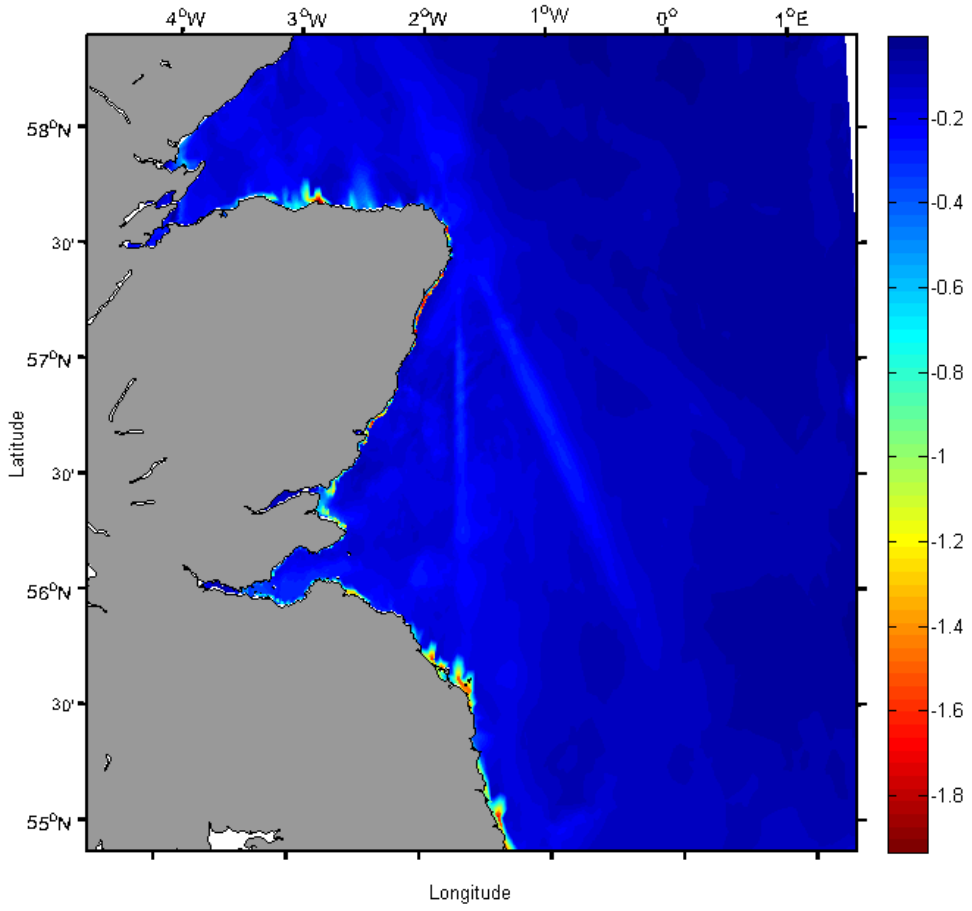

FIGURE 8.3: Maximum negative spatial difference in H_s (m) for the model with and without wave-currents interactions

8.4 Hindcast of storm events

In order to study the importance of the wave-current interactions and the coupling between swell and wind-sea waves off the east coast of Scotland, three storms were considered in the period January-August 2010. Storm events were identified by examining the time series in the Firth of Forth and the Moray Firth in which the highest H_s was recorded. These three storms were selected because they were the three most intense storms during the considered period and originated from different weather conditions.

8.4.1 The 26-27 February 2010 storm

Between the 25-27 February 2010, the UK was affected by a low pressure system, that moved rapidly from west to east. From the afternoon of the 25th to the 26th the centre of the storm was over the North Sea (Figure 8.4). At the same time, another low pressure system (not shown in the map) was over the Norwegian Sea, causing a train of swell moving from N to S. The low pressure over the North Sea caused windsea waves exceeding 4 m.

In Figure 8.5 the situation in the sea is showed at 12:30 of the 26th: swell waves contributed to enhancing the H_s in the centre of the storm, while a train of swell waves was forming from this storm, travelling west to the Moray Firth. Interaction of the windsea and the swell waves caused high waves along the east coast: the maximum H_s recorded by the Firth of Forth wave gauge was 4.8 m. WCI contributed to the enhancement of H_s by up to 1 m in coastal areas, while in the open sea the contribution was very low, up to 0.1 m. In the afternoon of the 26th (Figure 8.6, at 19:00 PM) the storm was near the Firth of Forth. The contribution of the swell waves was significant, increasing the H_s by up to 1 m: model outputs showed that the central part of the storm had a $H_s > 5$ m, while without the swell coming from North the centre of the

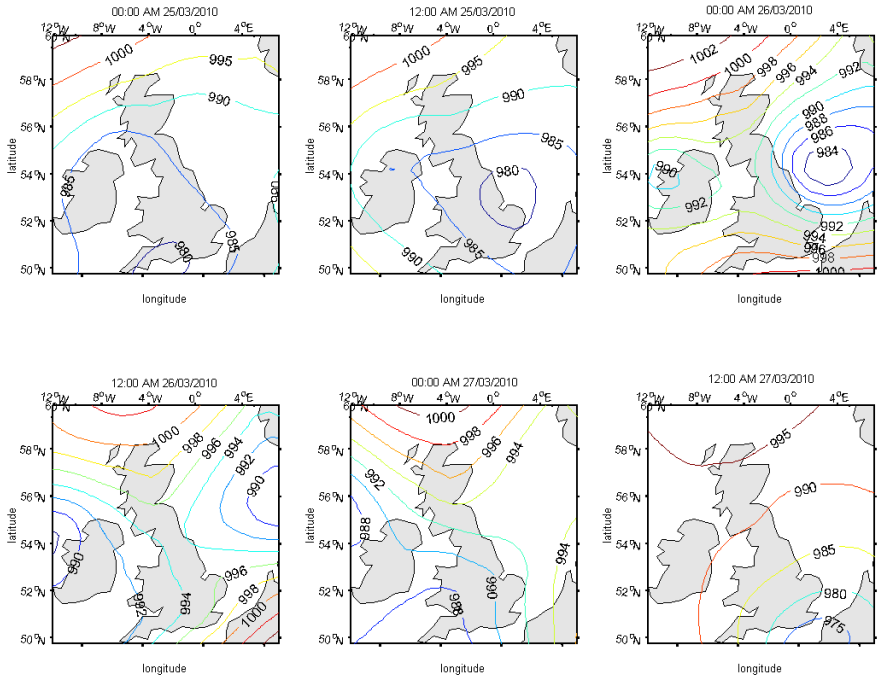

FIGURE 8.4: The mean sea level pressure fields (hPa) before and during the 25-26 February 2010 storm

storm would have been an $H_s < 4.5$ m. To our knowledge no significant damages were recorded for this storm.

8.4.2 The 30-31 March 2010 storm

The larger storm in 2010 occurred during the night of 30 March 2010. Between 29 March 2010 and 01 April 2010 the SE coast of Scotland and the north of England was struck by severe weather and very strong winds. These conditions were caused by a strong depression that originated from a weak minimum near the Azores Islands, in the North Atlantic, in front of the Portuguese coast. This low pressure was ¡990 hPa once over Great Britain and Ireland at midnight of the 30 March 2010 and reached its minimum the day after with a depression of ¡980 hPa over the North of England.

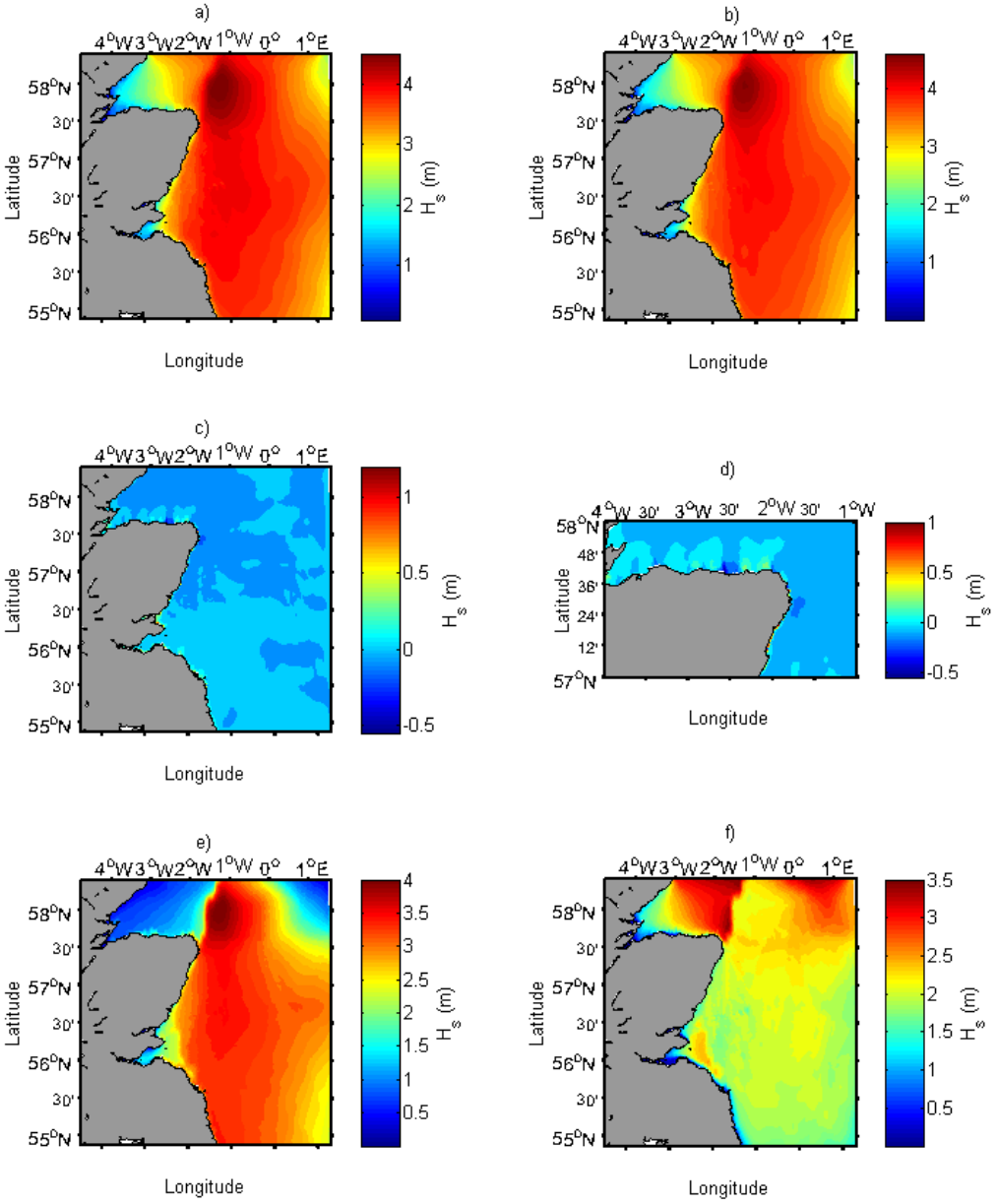

FIGURE 8.5: The modelled H_s in the east coast of Scotland at 12:30 UTC of the 26 February 2010: a) coupled model (WCI on), b) uncoupled model (WCI off), c) difference between coupled and uncoupled, d) difference between coupled and uncoupled in the Moray Firth area, e) wind-sea waves, f) swell waves

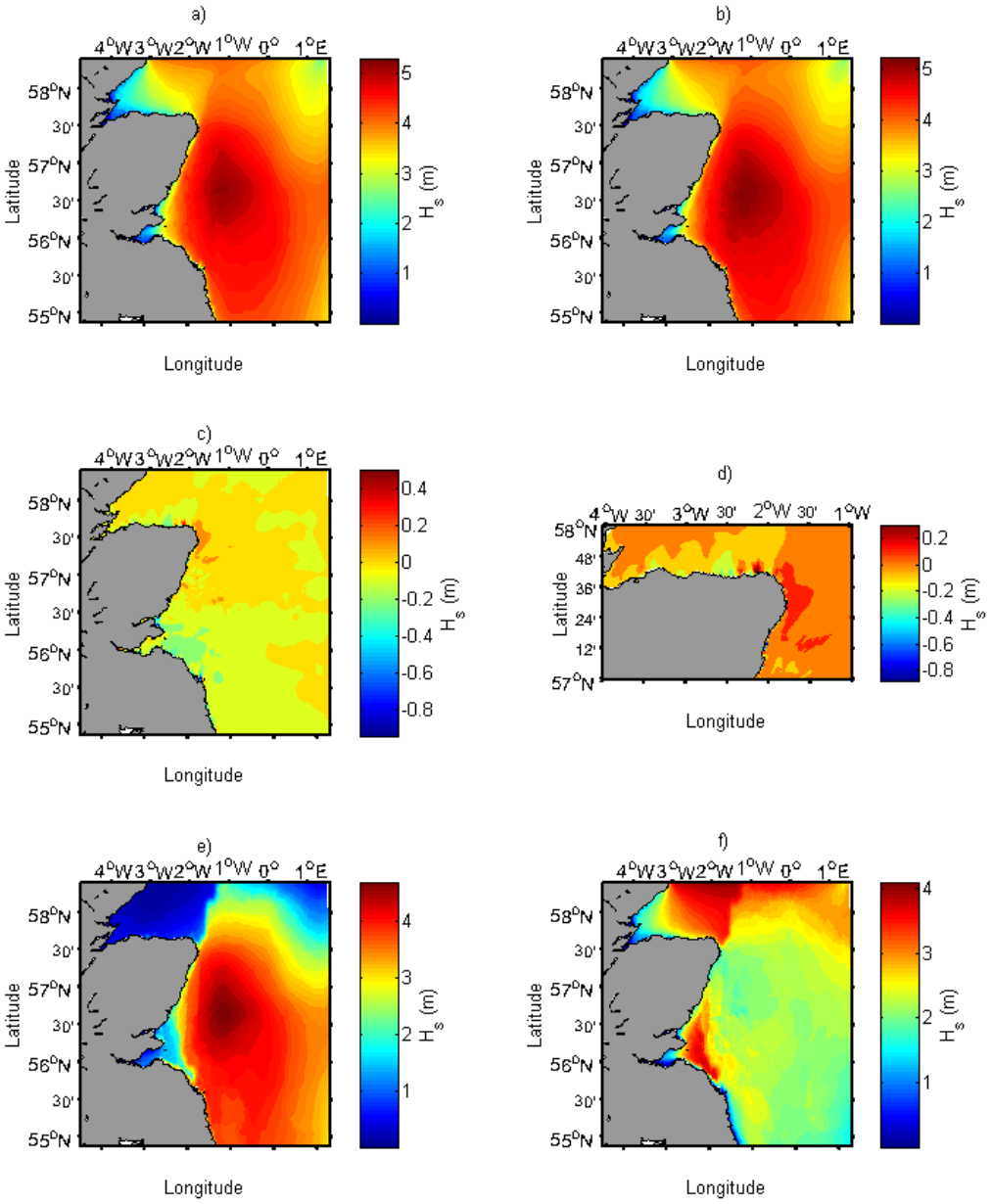

FIGURE 8.6: The modelled H_s in the east coast of Scotland at 19:00 UTC of the 26 February 2010: a) coupled model (WCI on), b) uncoupled model (WCI off), c) difference between coupled and uncoupled, d) difference between coupled and uncoupled in the Moray Firth area, e) wind-sea waves, f) swell waves

The evolution of the storm from surface pressure charts from ECMWF ERA-Interim reanalysis is reported in Figure 8.7 (Dee et al., 2011; Berrisford et al., 2011).

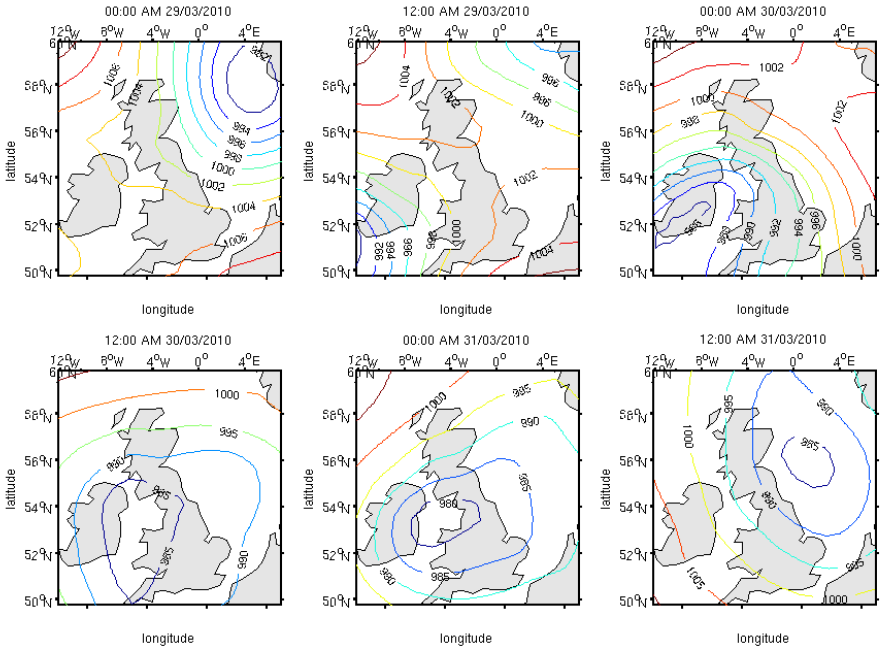

FIGURE 8.7: The mean sea level pressure fields (hPa) before and during the 30-31 March 2010 storm

These figures clearly show that the depression, at its maximum strength, is just above the S of Scotland during the night between the 30-31 March 2010. This depression generated both very high waves (H_s exceeded 6 m, measured in the Firth of Forth) and surge waves exceeding 0.5 m (measured both by Aberdeen and Leith tide gauges). The waves caused significant damages to the coastal defences of cities in the SE of Scotland. In particular the City of Edinburgh council estimated the damages to coastal defences to be about £23,000. Also in Berwick at the southern entrance of the Firth of Forth some damages were caused to the harbour infrastructures. To the east, in Dunbar waves topped the roof of 2-story houses.

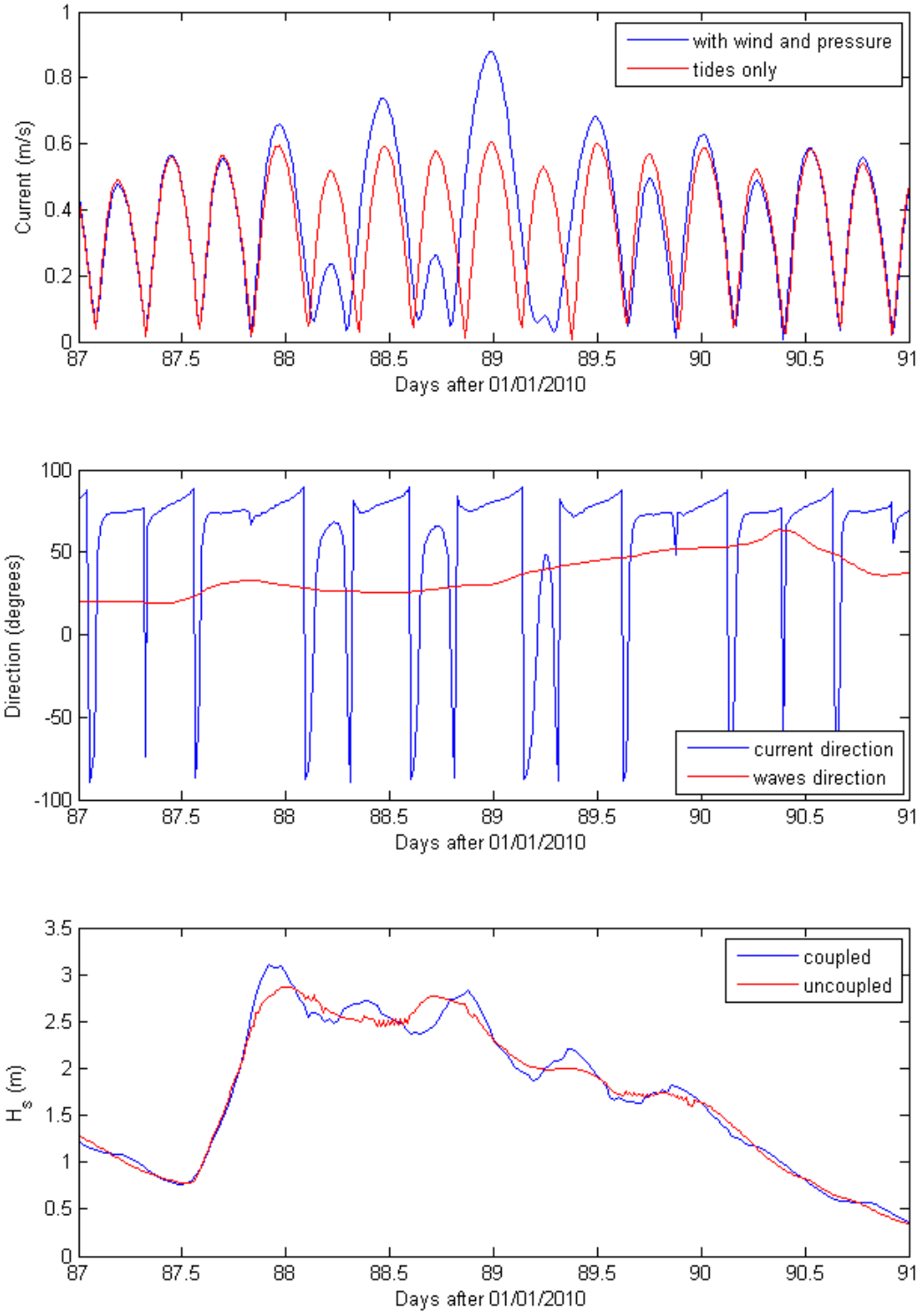

FIGURE 8.8: Modelled currents and waves conditions during the 30-31 March 2010 storm in the location in which the Aberdeen wave buoy was placed

Damaging conditions associated with this storm were caused by a combination of simultaneous factors: (1) tides in the spring period, (2) a surge wave of about 0.5 m generated by local pressure and wind, (3) wind-sea waves generated locally that were interacting with strong currents, (4) a weak, but significant, swell wave field, interacted with the windsea waves.

Figure 8.8 shows the intensity of the current at the Aberdeen wave gauge location and the resulting wave-current interaction. It can be seen that the current was strongly enhanced by the wind, and, consequently the WCI effect was stronger.

At about 00:30 AM on 31 March 2010 the storm was at its maximum causing the wave field to hit the coastline at around the same time as high tide and surge. The different components of the storm were analyzed. First, the surge wave generated by the minimum of pressure above the North Sea was studied. Figure 8.9 shows the difference between the total water level and the water level due to tides at 02:00 UTC on 31 March 2015.

The model predicted a surge wave up to 0.5 m. A comparison between the recorded water level and the model output showed that the model underestimated the surge wave by about 0.1 m. The reason for this underestimation could be because the boundary conditions for the model only included tidal water level and did not include the surge wave from outside the model. The surge wave extended from the Firth of Forth southwards: the water level in those regions was enhanced by about 0.4-0.5 m. In addition to these surge conditions, the H_s of the waves at the same time were exceeding 7 m in the same areas (see Figures 6.10 and 6.11). Figures 6.10 and 6.11 show the wave field at two different times during the storm, at 00:30 AM, and at 02:00 AM respectively. The swell waves effect was very low, but contributed to the enhancement of H_s up to 0.5 m, while on the coastline the contribution of the WCI was very strong. At 02:00 UTC on 31 March 2010 (Figure 8.11), when the storm reaches the coastline, WCI increased H_s by up to 2.5 m in many locations near the Firth of Forth (see figure 12d). Figures 6.10f and 6.11f show a high H_s swell waves at the entrance of the

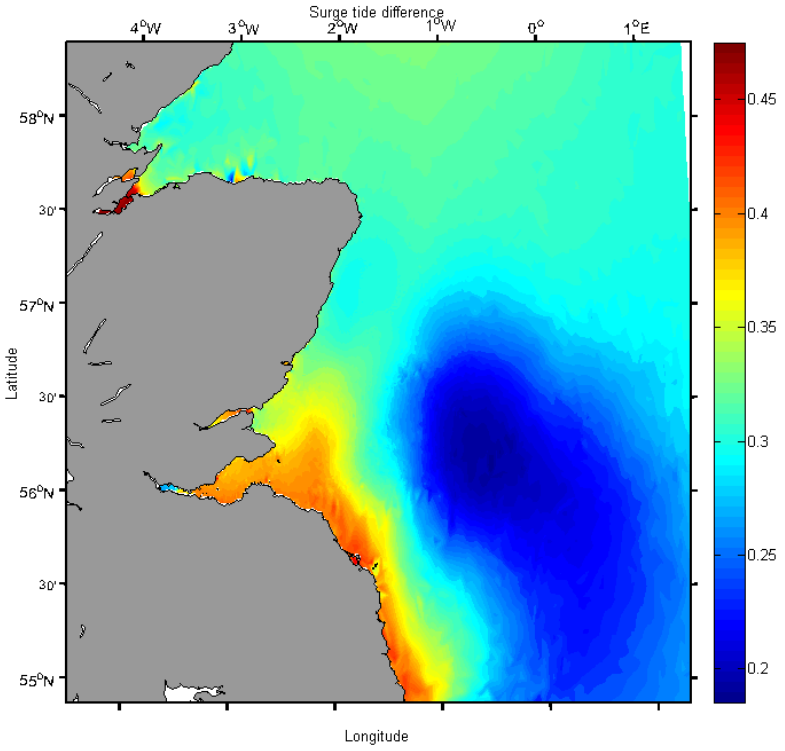

FIGURE 8.9: The modelled surge wave at 02:00 UTC of the 31 March 2010

Firth of Forth. These were waves generated by the large storm shown in figure 6.10e, but no longer influenced by the local wind, which are propagating outside the centre of the windsea waves to the coastline. H_s recorded by the Firth of Forth wave gauge measured a peak of significant wave height of 6.46 m at 0500 UTC on 31 March 2015. The model matched the peak recorded in the wave gauge reasonably well, predicting higher values S of the Firth of Forth, where more damage was caused.

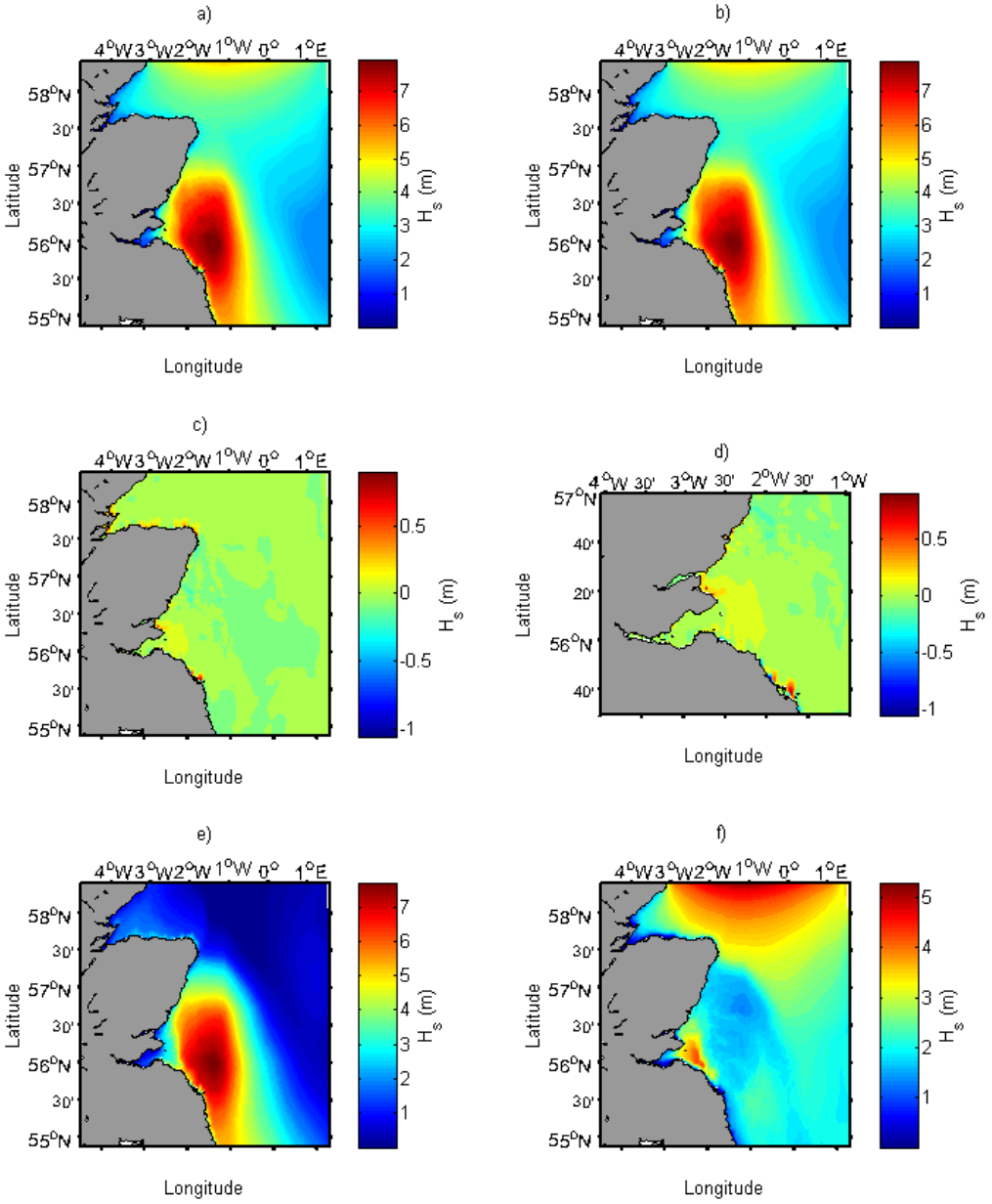

FIGURE 8.10: The modelled H_s in the east coast of Scotland at 00:30 UTC of the 31 March 2010: a) coupled model (WCI on), b) uncoupled model (WCI off), c) difference between coupled and uncoupled, d) difference between coupled and uncoupled in the Firth of Forth area, e) wind-sea waves, f) swell waves

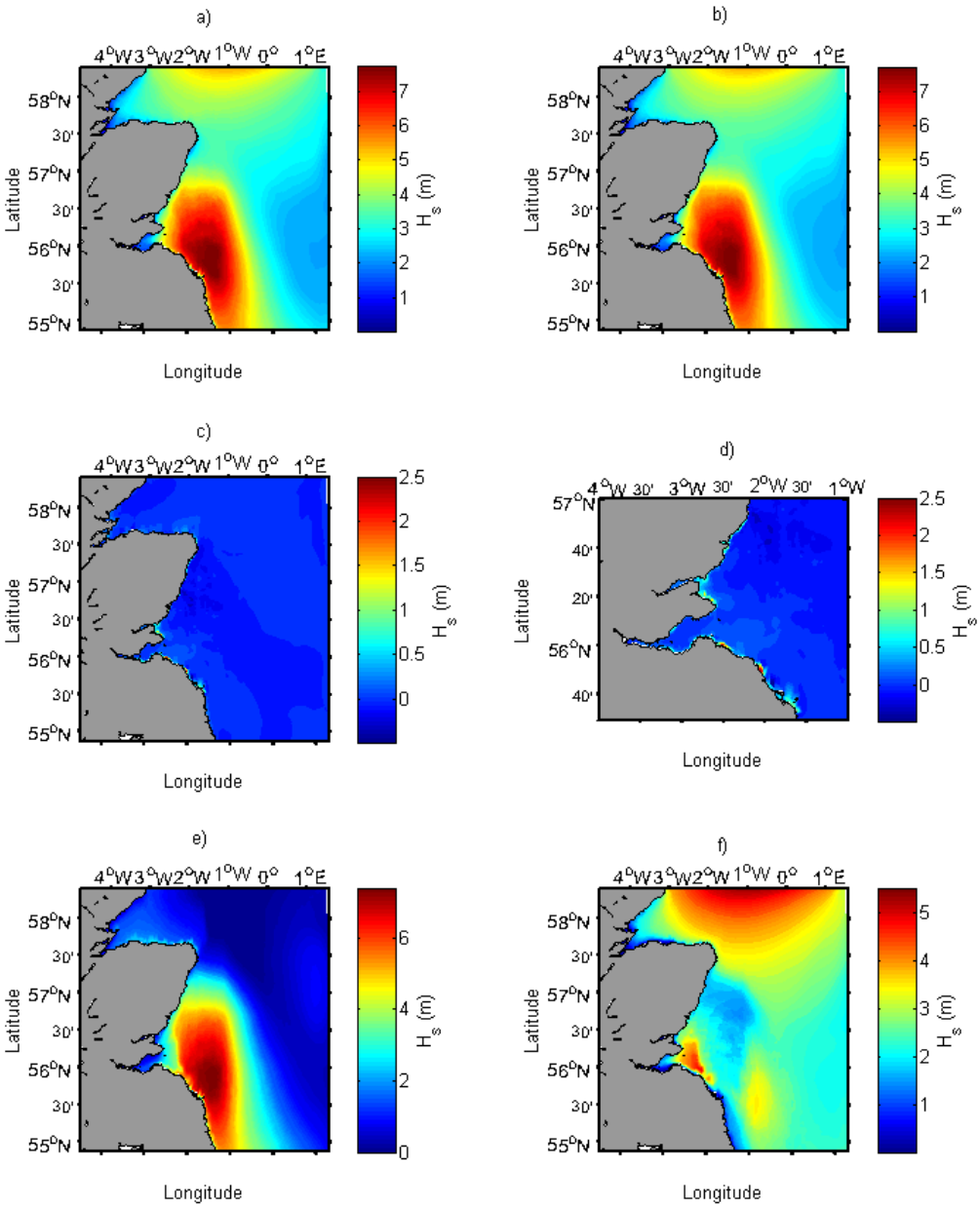

FIGURE 8.11: The modelled H_s in the east coast of Scotland at 02:00 UTC of the 31 March 2010: a) coupled model (WCI on), b) uncoupled model (WCI off), c) difference between coupled and uncoupled, d) difference between coupled and uncoupled in the Firth of Forth area, e) wind-sea waves, f) swell waves

8.4.3 The 19 June 2010 storm

The third storm considered was one that generated high off-shore waves conditions, with swell propagating to the coastline. This is an example of how the coupling of swell and windsea waves could lead to extreme wave conditions, with significant wave height exceeding 6 m offshore and 4-5 m on the coastline. Figure 8.12 shows the pressure conditions between the 18-20 June 2010. On the 17 June 2010 (not shown) a system of low pressure was generated between Greenland and Iceland. This minimum moved quickly to the Scandinavian peninsula, intensifying and remaining in the area of Sweden and Norway for 72 hours. This low pressure caused strong winds in the northern North Sea and consequently the generation of waves in the area between Norway and Scotland. This field of waves arrived at the Scottish coastline at the same time as the low pressure was generating high waves in the bulk of the North Sea, causing two trains of waves to be in the same place at the same time. This condition, known as crossing or bimodal sea, is quite common in the North Sea (Guedes Soares, 1984). The model hindcasted that the storm offshore was at its maximum near 16:00 UTC of the 19 June 2010 (Figure 8.13). At 16:00 UTC on 19 June 2010 the modelled offshore, mid North Sea, windsea generated waves peaked at $H_s \sim 5$ m (Figure 8.13e), whereas the swell waves were a little smaller with $H_s \sim$ 3-4 m (Figure 8.13f). Further north, in the Moray Firth, the swell waves dominated with the swell having $H_s \sim 6$ m and the windsea having $H_s \sim 2$ m. The resulting predicted wave field had $H_s > 6$ m (Figure 8.13b). In the Moray Firth H_s of more than 5 m was recorded. However, at this time, the coupling between currents and waves caused a decrease of the significant wave height at the coastline (Figure 8.13c). In some locations H_s was reduced by more than 0.5 m (see Figure 8.13c/d). 3 hours later (Figure 8.14), the turning tidal currents enhanced the waves by more than 1.5 m in coastal locations. Figure 3 shows that the model matches almost perfectly the water level recorded in the Moray Firth and in the Firth of Forth wave gauges at this time.

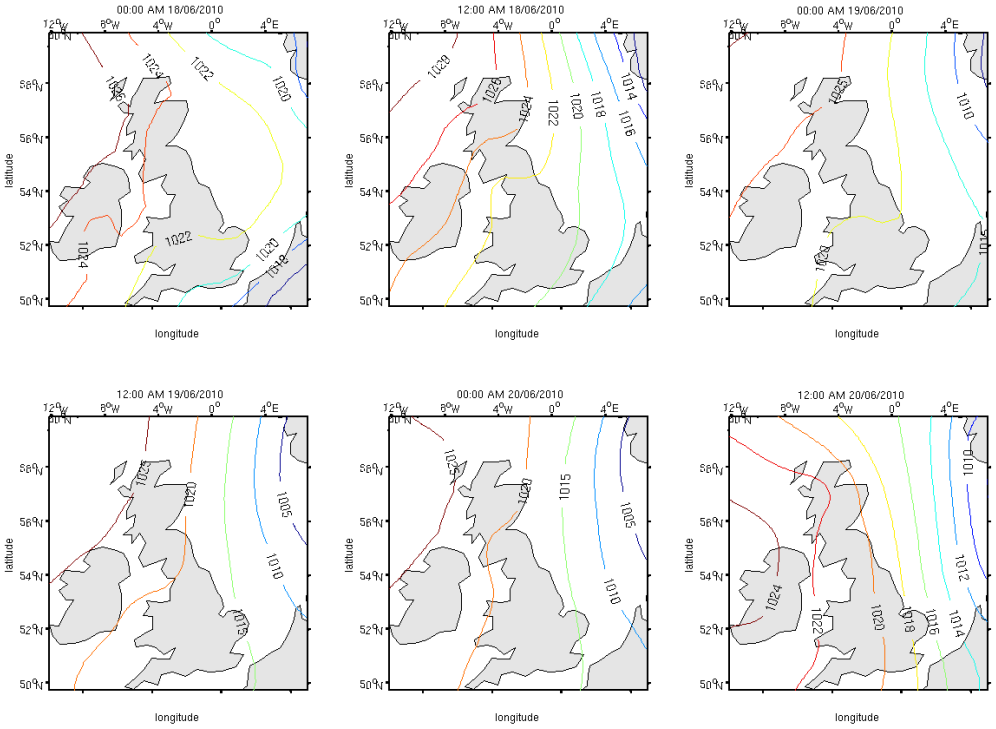

FIGURE 8.12: The mean sea level pressure fields (hPa) before and during the 19 June 2010 storm

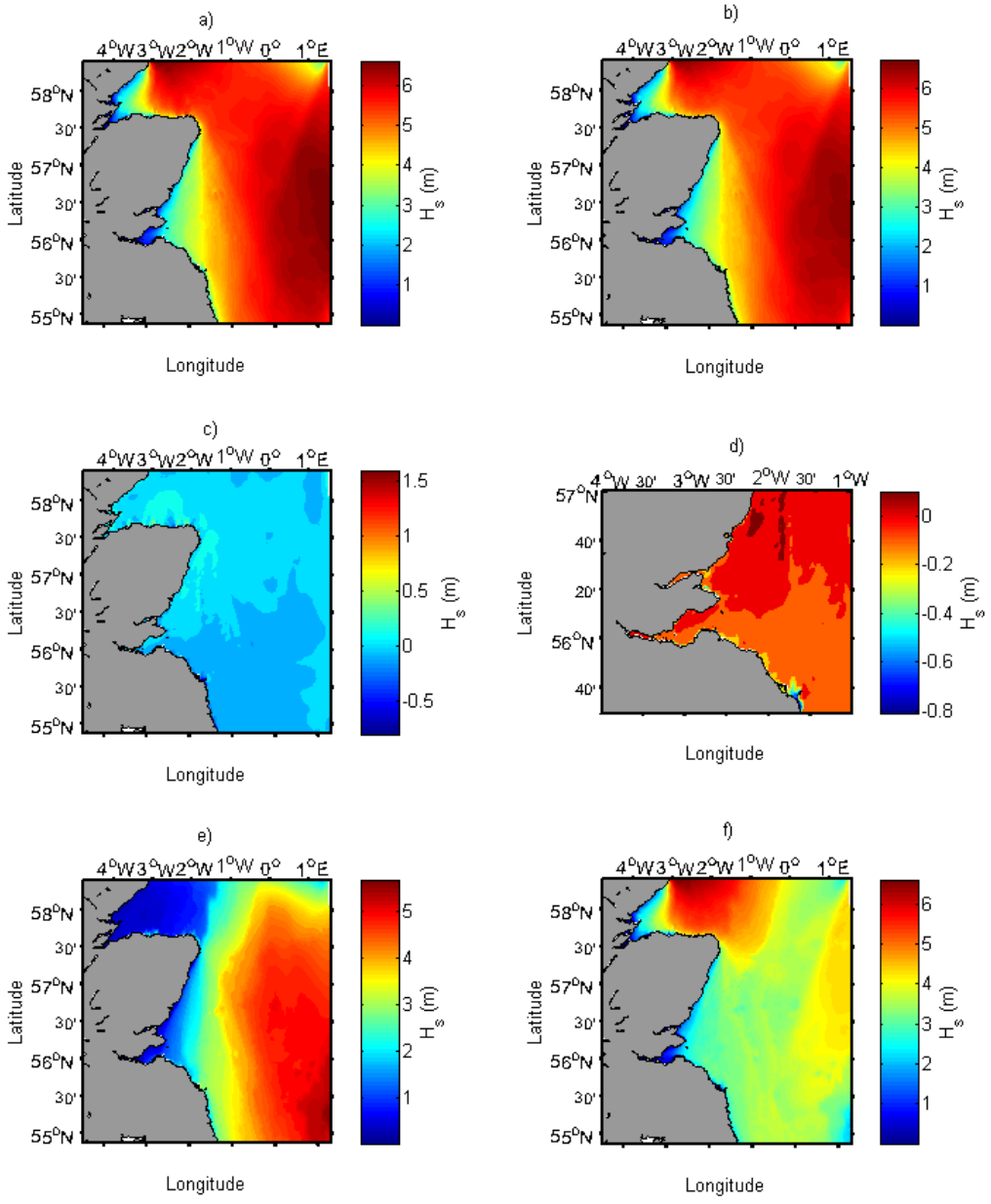

FIGURE 8.13: The modelled H_s in the east coast of Scotland at 16:00 UTC of the 19 June 2010: a) coupled model (WCI on), b) uncoupled model (WCI off), c) difference between coupled and uncoupled, d) difference between coupled and uncoupled in the Firth of Forth area, e) wind-sea waves, f) swell waves

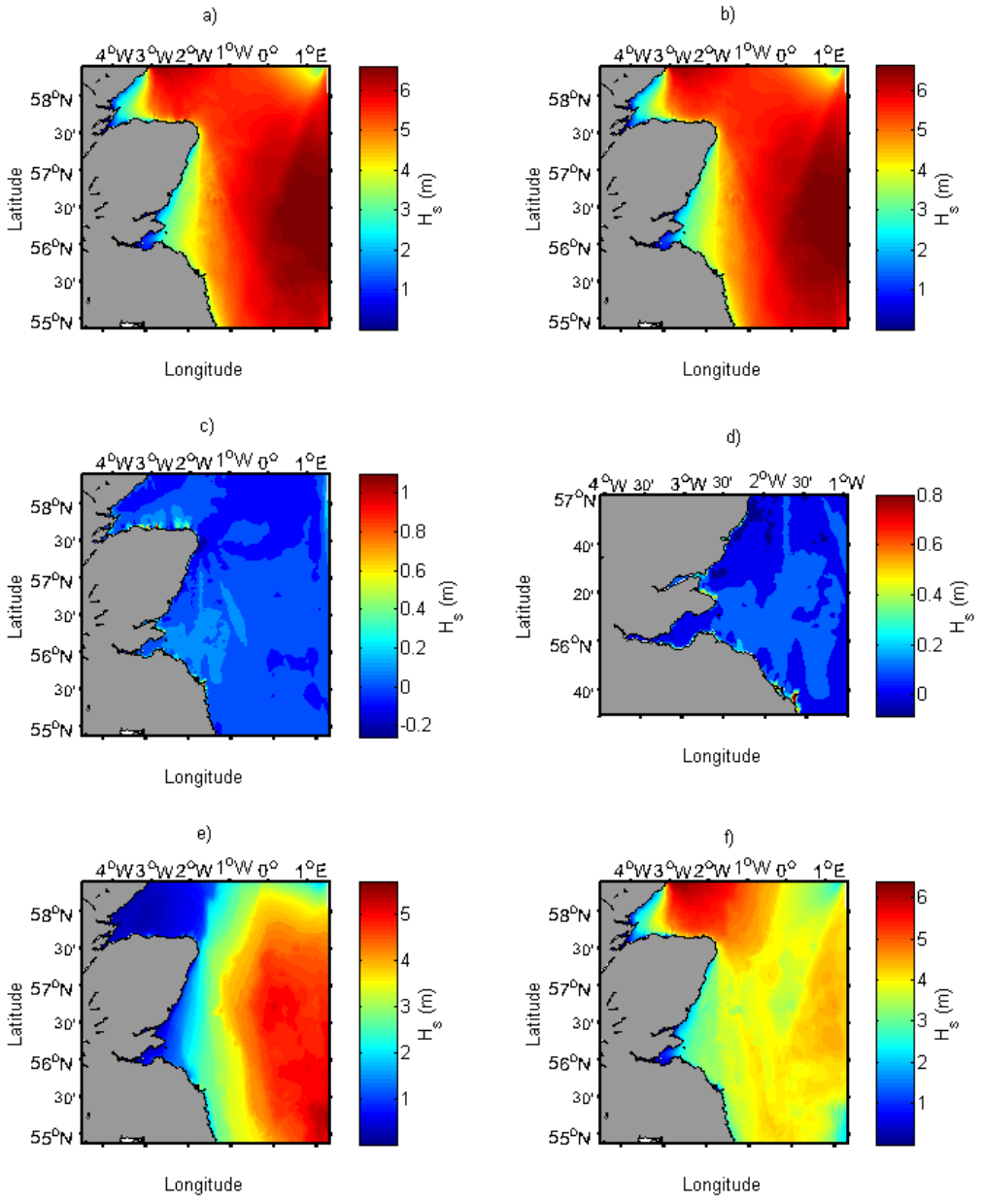

FIGURE 8.14: The modelled H_s in the east coast of Scotland at 19:00 UTC of the 19 June 2010: a) coupled model (WCI on), b) uncoupled model (WCI off), c) difference between coupled and uncoupled, d) difference between coupled and uncoupled in the Firth of Forth area, e) wind-sea waves, f) swell waves

8.4.4 Variation of the spectrum due to WCI

To understand better the effect of the wave-current interactions, the modelled 2D and 1D spectrum were considered. During the 30-31 march, the modelled spectrum was extracted from the locations corresponding to the Firth of Forth wave gauge, Aberdeen wave gauge and Moray Firth wave gauge and the coupled and the uncoupled run were compared. First, the 1D spectrum was analyzed: the results are in Figures 6.15-6.17 for the three considered wave gauges. The spectrum shows no substantial difference between the run with WCIs and the run without wave-currents interactions for the Moray Firth, while some differences can be seen in the Firth of Forth.

Large differences are only recorded for the shallow-water Aberdeen wave gauge: the energy associated with the peak frequency was changing also more than 20%, and also the shift of the peak frequency was recorded.

We, then, analyzed the directional spectrum for the Firth of Forth and for the Aberdeen wave gauge at the same time in Figures 6.15-6.17. The changes are similar in magnitude to the changes recorded in the 1D spectrum. We also showed a difference plot (Figure 8.18-6.19) between the coupled and the uncoupled directional spectrum in the Firth of Forth and at Aberdeen for the same periods. Modelled variations are quite significant for both the directional spectrum and the 1D spectrum, and the variations are both recorded for the spectral peak and for higher frequencies: in particular in the 1D and in the 2D spectrum in Aberdeen for most of the storm two different wavetrains with two different frequencies (windsea waves and swell waves) are presents, and both the peak frequency associated with the windsea and the peak frequency associated with the swell waves are affected by the wave-current interactions.

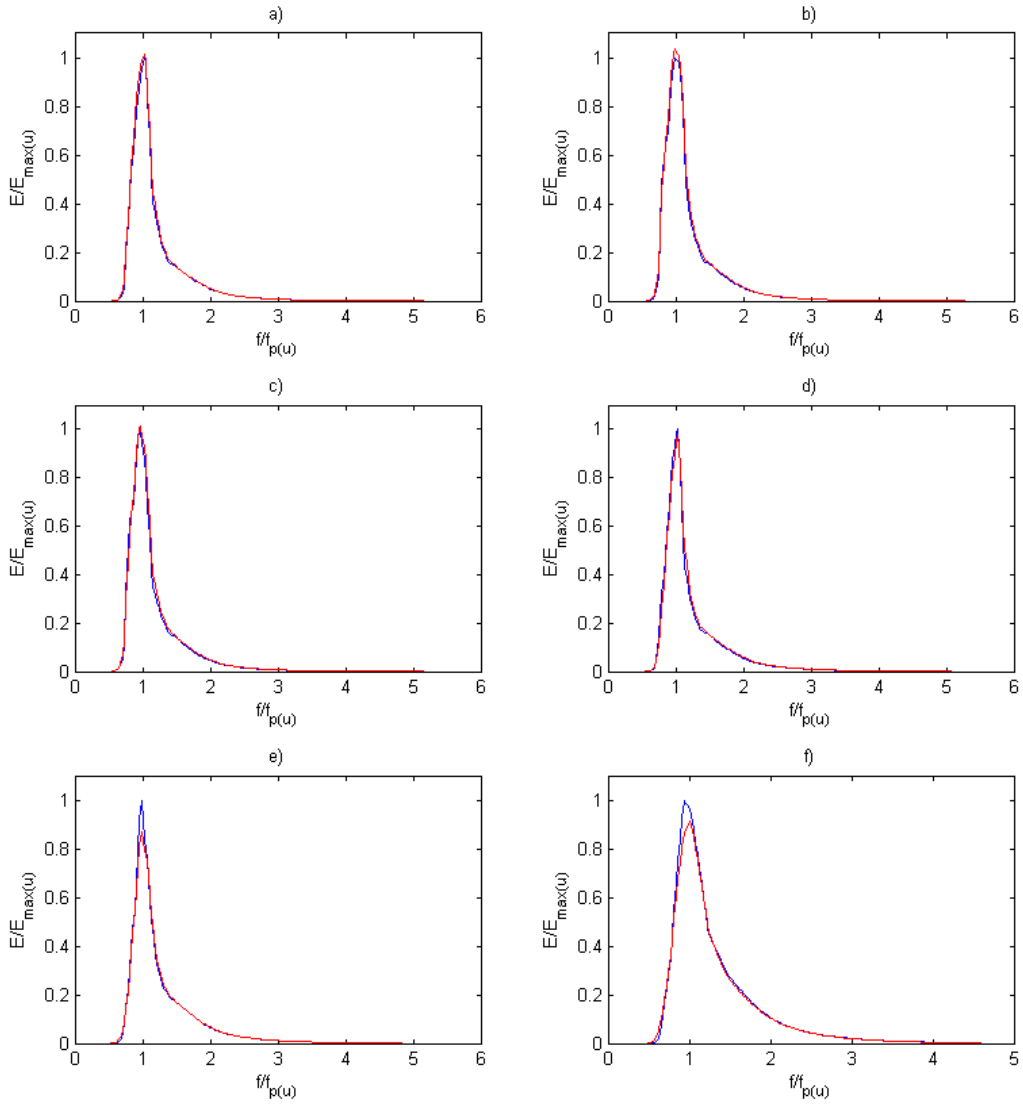

FIGURE 8.15: Modelled 1D spectrum in the Firth of Forth wave gauge, red line is the coupled model (with wave-currents interactions incorporated), while blue line is the uncoupled model: a) 31/03/2010 at 00:30 UTC, b) 31/03/2010 at 01:15 UTC, c) 31/03/2010 at 02:00 UTC, d) 31/03/2010 at 04:15 UTC, e) 31/03/2010 at 06:00 UTC, f) 31/03/2010 at 08:30 UTC

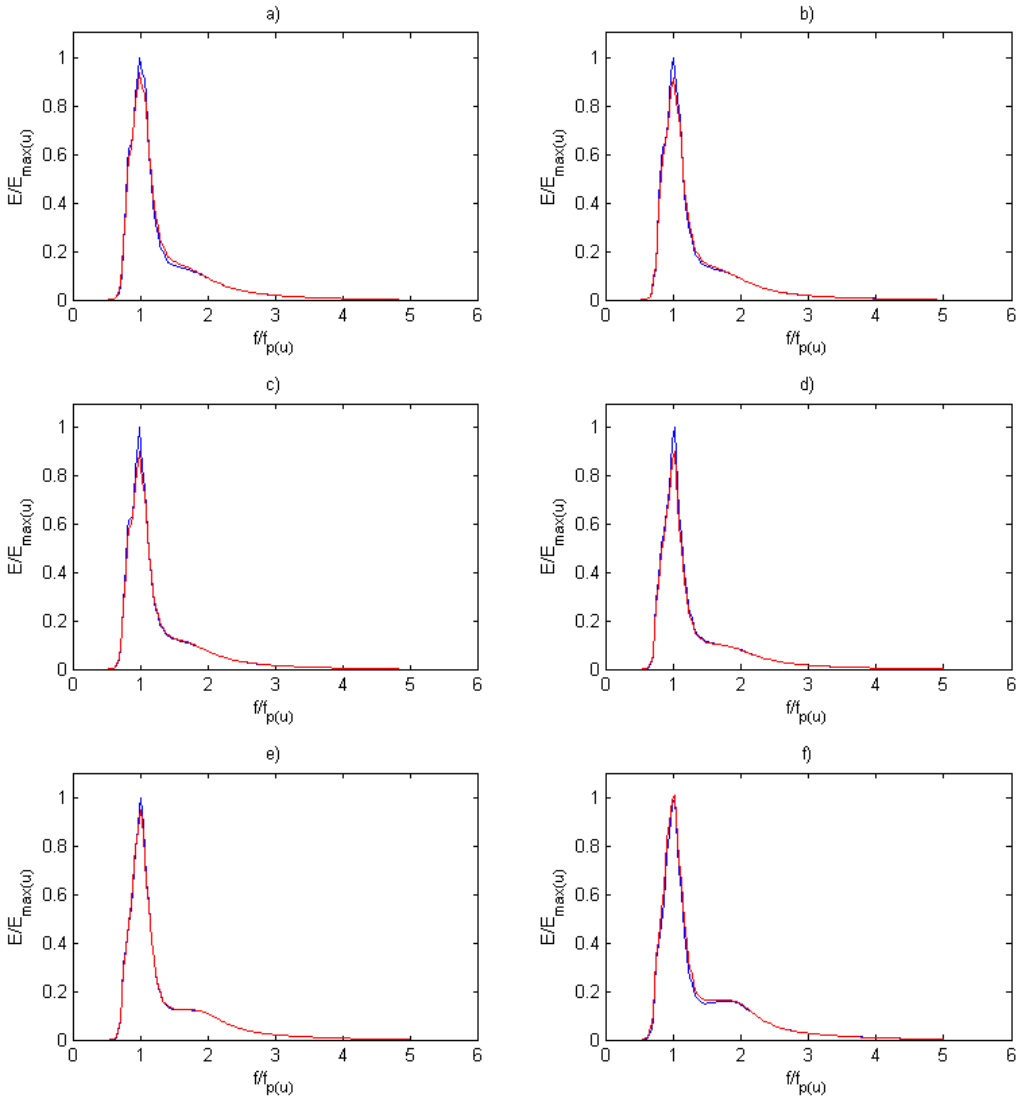

FIGURE 8.16: Modelled 1D spectrum in the Moray Firth wave gauge, red line is the coupled model (with wave-currents interactions incorporated), while blue line is the uncoupled model: a) 31/03/2010 at 00:30 UTC, b) 31/03/2010 at 01:15 UTC, c) 31/03/2010 at 02:00 UTC, d) 31/03/2010 at 04:15 UTC, e) 31/03/2010 at 06:00 UTC, f) 31/03/2010 at 08:30 UTC

8.5 Discussion

The model described in this chapter is capable of hindcasting surge and storms on the east coast of Scotland. The combination of spring tide, strong wind, and high waves

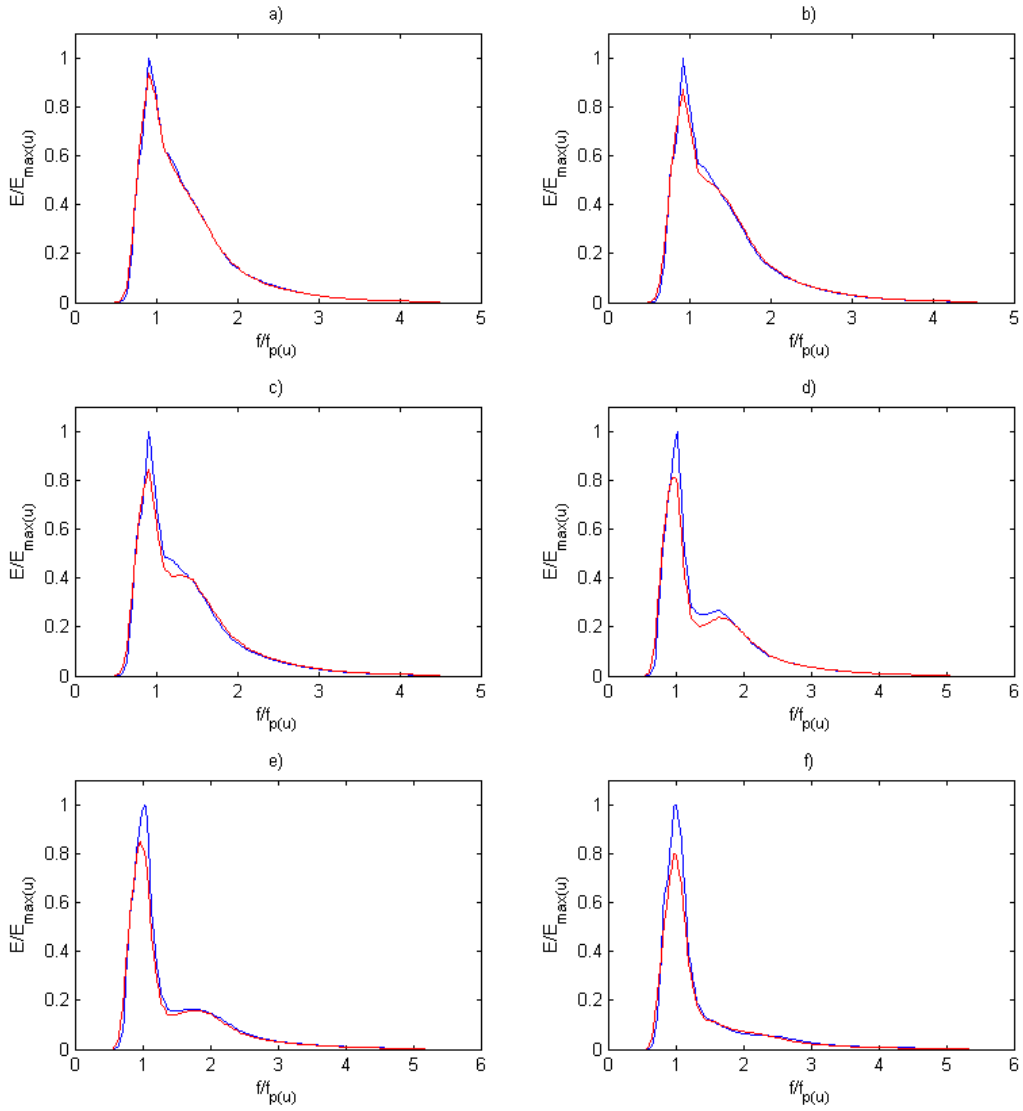

FIGURE 8.17: Modelled 1D spectrum in the Aberdeen wave gauge, red line is the coupled model (with wave-currents interactions incorporated), while blue line is the uncoupled model: a) 31/03/2010 at 00:30 UTC, b) 31/03/2010 at 01:15 UTC, c) 31/03/2010 at 02:00 UTC, d) 31/03/2010 at 04:15 UTC, e) 31/03/2010 at 06:00 UTC, f) 31/03/2010 at 08:30 UTC

can be extremely threatening in coastal areas. The North Sea is one of the areas most affected by this forcings. Storms in North Sea can generate extremely high waves as well as rogue waves (Ponce de León and Guedes Soares, 2014).

The model has also some capabilities of forecasting, coupling it with a larger scale model for waves and currents. However, due to the slowness of the simulation this use is very unlikely: for 1 day of simulation takes about 3-4 hours. A limitation of the model is that the MIKE by DHI software does not allow an online coupling between waves and tides, slowing the simulation process. In fact, currents and waves are simulated by different modules and it is not possible to perform a direct coupling. No temperature and salinity simulation were included in the model, as well as river discharge. Temperature and salinity could affect the stability of the water column and change dramatically the water circulation, while a significant enhancement of the waves could form at the eastuary of the rivers, in which the river flow travel in an opposite direction compared to the waves: this will cause higher waves and the breaking of the waves in the estuary.

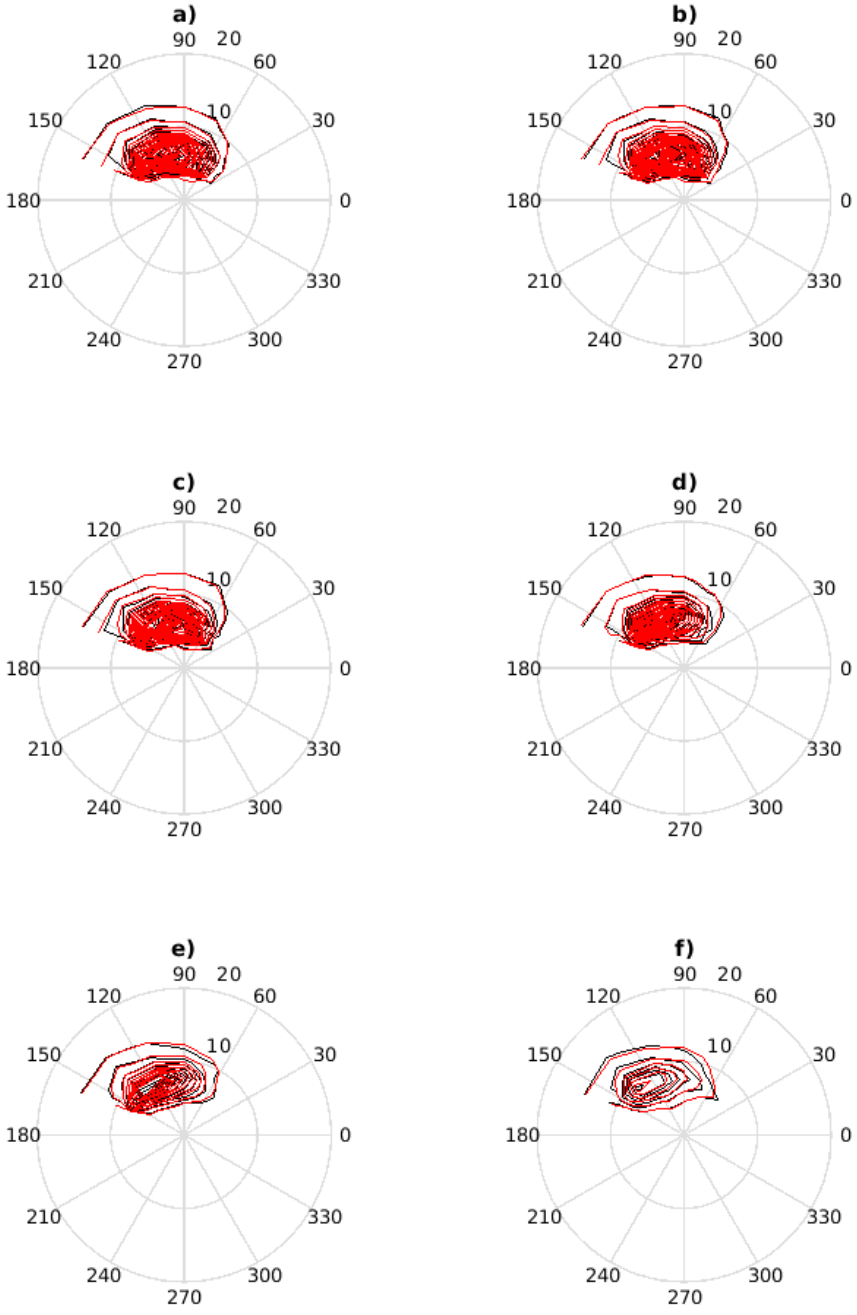

FIGURE 8.18: Polar plot of the modelled 2D directional spectrum (Energy density m^2s/deg) in the Firth of Forth wave gauge, in red is the contour plot of the coupled model spectrum (with wave-currents interactions incorporated), while black is the contour plot of the uncoupled model. Contour lines are plotted every 0.01 m^2s/deg: a) 31/03/2010 at 00:30 UTC, b) 31/03/2010 at 01:15 UTC, c) 31/03/2010 at 02:00 UTC, d) 31/03/2010 at 04:15 UTC, e) 31/03/2010 at 06:00 UTC, f) 31/03/2010 at 08:30 UTC

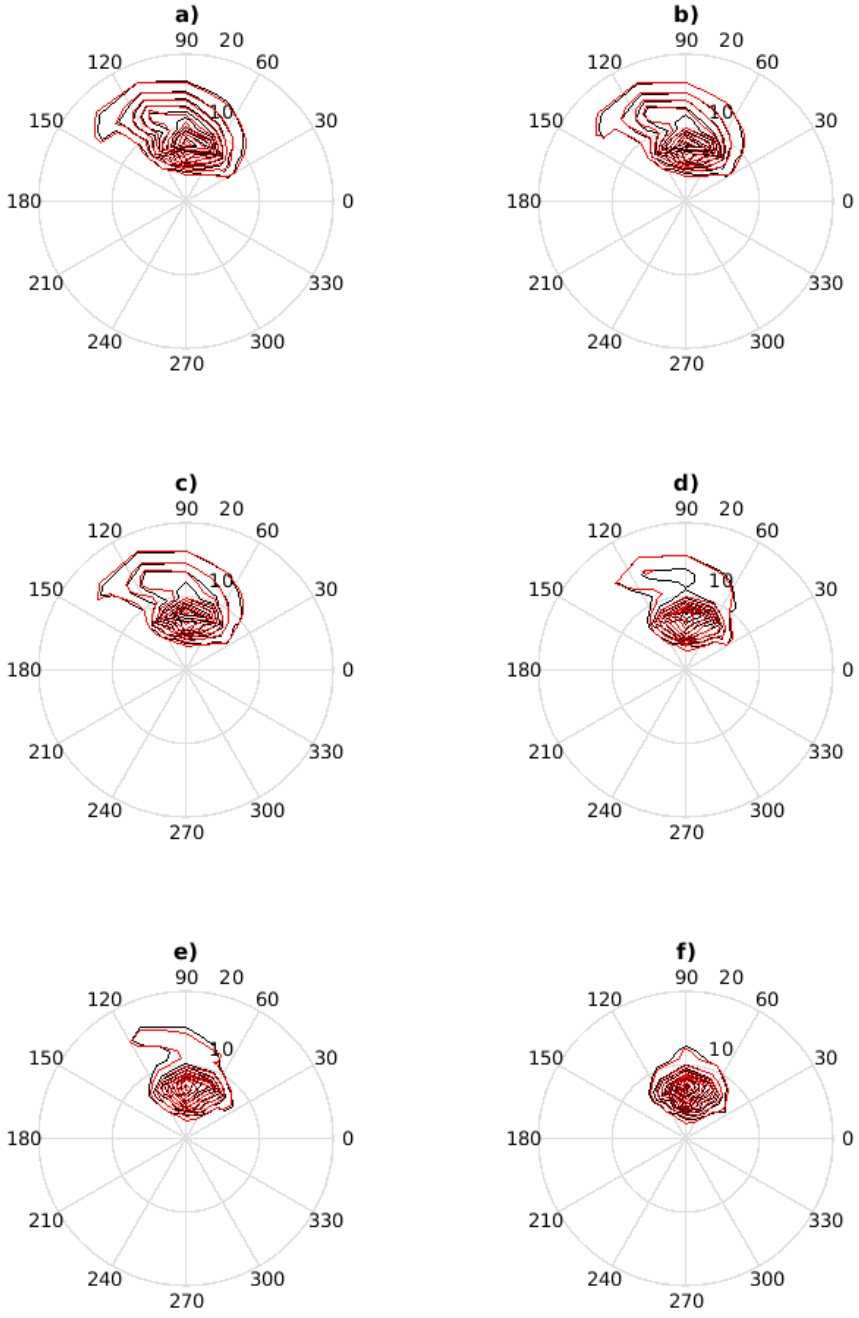

FIGURE 8.19: Polar plot of the modelled 2D directional spectrum (Energy density m^2s/deg) in the Aberdeen wave gauge, in red is the contour plot of the coupled model spectrum (with wave-currents interactions incorporated), while black is the contour plot of the uncoupled model. Contour lines are plotted every 0.01 m^2s/deg: a) 31/03/2010 at 00:30 UTC, b) 31/03/2010 at 01:15 UTC, c) 31/03/2010 at 02:00 UTC, d) 31/03/2010 at 04:15 UTC, e) 31/03/2010 at 06:00 UTC, f) 31/03/2010 at 08:30 UTC

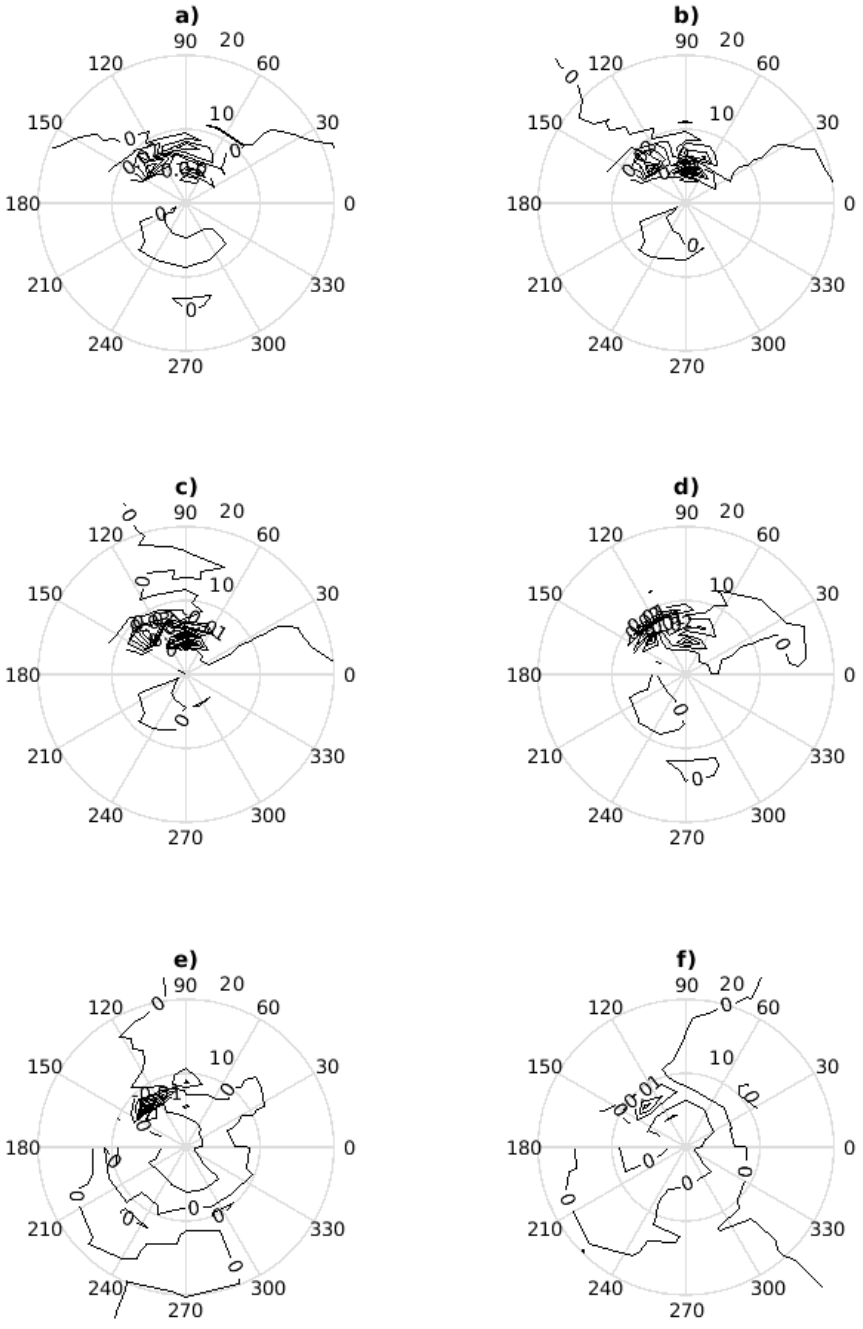

FIGURE 8.20: Polar plot of the modelled difference between coupled and uncoupled 2D directional spectrum (Energy density m^2s/deg) in the Firth of Forth wave gauge, Contour lines are plotted every 0.01 m^2s/deg: a) 31/03/2010 at 00:30 UTC, b) 31/03/2010 at 01:15 UTC, c) 31/03/2010 at 02:00 UTC, d) 31/03/2010 at 04:15 UTC, e) 31/03/2010 at 06:00 UTC, f) 31/03/2010 at 08:30 UTC

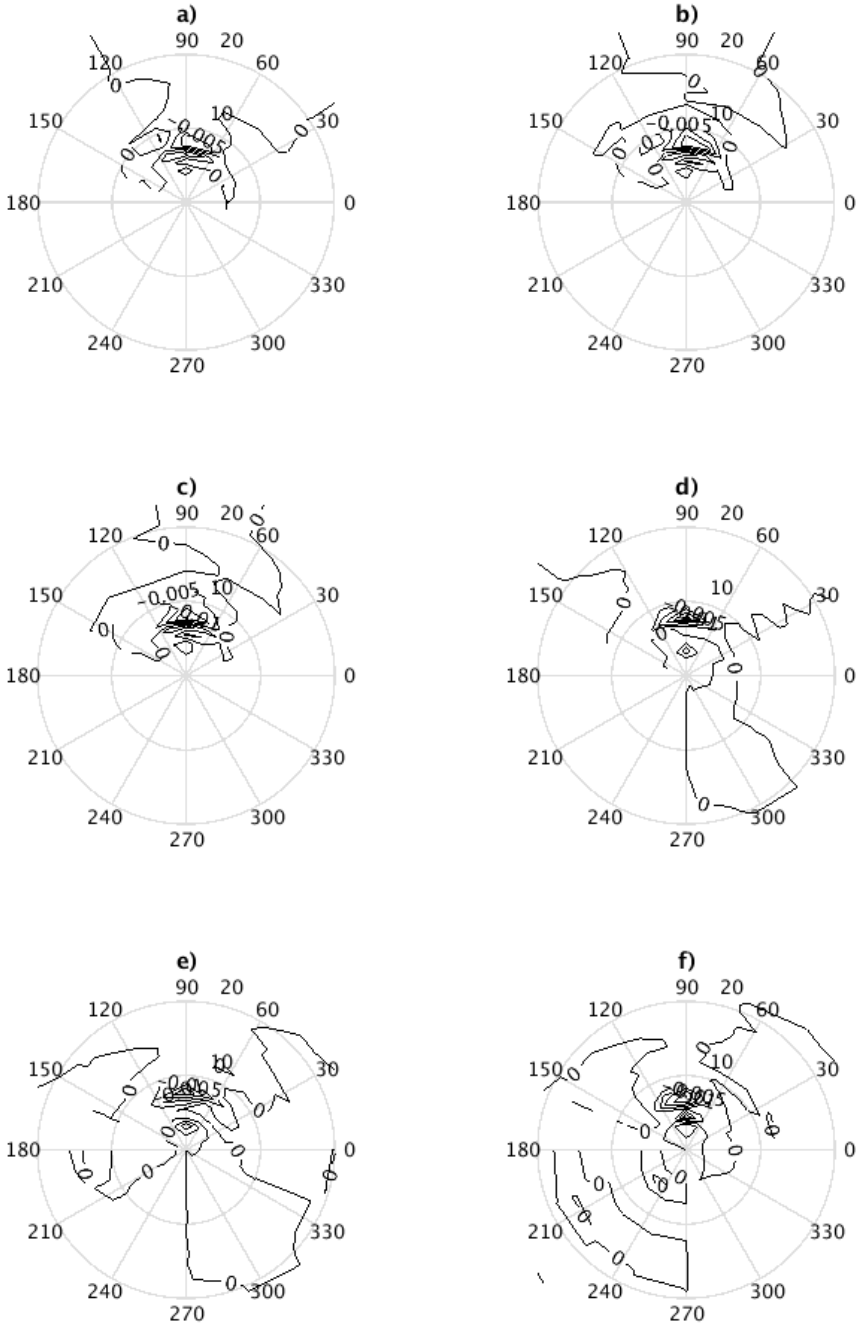

FIGURE 8.21: Polar plot of the modelled difference between coupled and uncoupled 2D directional spectrum (Energy density m^2s/deg) in the Firth of Forth wave gauge, Contour lines are plotted every 0.005 m^2s/deg: a) 31/03/2010 at 00:30 UTC, b) 31/03/2010 at 01:15 UTC, c) 31/03/2010 at 02:00 UTC, d) 31/03/2010 at 04:15 UTC, e) 31/03/2010 at 06:00 UTC, f) 31/03/2010 at 08:30 UTC

Part V

Rogue waves in crossing sea state

Chapter 9

Rogue waves studies review

9.1 Introduction

In this Chapter we will introduce the topic of rogue waves, in particular for the previous studies on the formation of rogue waves in crossing sea state. We will discuss the different mechanism of formation of those abnormal waves and we will explain the experimental set-up of our study. The laboratory experiment was carried out in MARINTEK facility in Trondheim, Norway. The dataset that was used for the statistical analysis of different features of waves in crossing sea was the Toffoli et al. (2011a). In that study, the experimental data were used principally to validate a numerical simulation based on Euler equations and to study the evolution of the kurtosis of the wavetrain during the propagation, that was used in the Toffoli et al. (2011a) as a proxy for the rogue wave probability, as explained also in Chapter 2.

The reason for a reanalysis of this dataset was needed in order to understand better the effect of the angle of crossing sea on other variables than kurtosis, such as the wave heigths distribution, the crests distribution and the maximum height that could occur in crossing sea state. Spectral and spatial distribution were also analyzed in order to

complete the previous study and in order to understand better the mechanism of the Benjamin-Feir instability in crossing sea state.

9.2 Rogue waves and statistical investigation of waves in crossing sea: the experimental set-up

The dataset that was analyzed in this thesis, and in two connected papers, are from an experiment in the MARINTEK wave tank facilities, in Norway. The results reported in the Chapter 7 are a reanalysis a previous publication (Toffoli et al., 2011a), that analyzed the behavior of the kurtosis in the wave tank in crossing sea state conditions, in order to validate a numerical model: in that case no in-depth study about the distribution of other variables was carried out. In Chapter 2 are given more details about the role of kurtosis in rogue wave analysis.

A more thorough analysis was carried out, comparing the distributions of wave heights, crests, troughs and periods to theoretical distributions and comparing those results to previous studies in unidirectional sea state (Onorato et al., 2009). Wave periods of the monochromatic unimodal dataset were also analyzed and compared to crossing sea state results.

The MARINTEK laboratory hosts one of the largest wave tanks in the world: a artificial basin of 70 m x 50 m x 10 m (the depth can be changed). The wave basin is fitted with two sets of wavemakers: the first one is along the short edge and is used for generating long-crested waves and is made by a double flap hydraulically operated unit. The second one, on the 70-m side of the basin, is composed of 144 individual computer-controlled flaps and is used to generate irregular short-crested waves. This is the wavemaker used for generating the waves for this study.

To generate a crossing sea state two identical JONSWAP spectra were generated in the wave tank propagating in two different directions in order to make them interact with

different angles. The following angles were chosen for the studying the interactions in crossing sea state $\Delta\theta$ = 10 °, 20 °, 30 ° and 40 °. Each spectrum has a T_p = 1 s, H_s = 0.068 m and a γ = 6, corresponding to a wave steepness of $k_p a$ = 0.14. The surface elevations were recorded with a frequency of 80 Hz and about 4500 individual waves were recorded for each of the wave probes in the wave tank. Wave gauges were placed every 5 meters from the centre of the longest edge, and in addition arrays of 3 and 8 wave gauges were placed in order to evaluate the directional spectrum of the waves.

9.3 Spectral analysis of the MARINTEK datasets

In order to study both the modulational instability (Benjamin and Feir, 1967) and the behavior of the spectral bandwidth during the propagation of the waves, in particular for the estimation of the theoretical period distributions, the evaluation of the spectrum, and of the spectral moments, is of fundamental importance. The spectra for all the wave gauges and for all the angles were computed using the Maximum Entropy Method (MEM) (Burg, 1967). This spectral analysis, based on a parametric autoregressive analysis was first applied to geophysical problems in the analysis of earthquakes (Bishop and Ulrych, 1975). Seminal works of Holm and Hovem (1979) and Holm (1983) applied this method successfully to the estimation of the ocean waves spectrum.

Rodrı?guez et al. (1999) then analyzed the different methods for the spectral analysis of the ocean waves, such as the Welch periodogram or the MEM, finding that the best overall result was achieved with the MEM, with orders $>$25.

The maximum entropy method was also applied for the estimate of the directional spectrum in this study, in order to study the evolution of the directional spreading during the propagation in the wave tank (Lygre and Krogstad, 1986).

After the evaluation of the spectra and the directional distribution, spectral parameters were evaluated. The first parameter that was evaluated is the peak frequency:

this fundamental parameter is often difficult to estimate and some methods were proposed throughout for a robust evaluation. Young (1995) using Monte-Carlo simulations, found that the most robust estimator of the peak frequency of an experimental spectrum is:

$$\hat{f}_p = \frac{\int_0^\infty f \cdot P^4(f)df}{\int_0^\infty P^4(f)df} \tag{9.1}$$

As reported in Chapter 2, wave period distributions are usually based on the bandwidth, that is a measure of the broadness of the spectral distribution, and is related to the half-width at half-maximum (Serio et al., 2005). Bandwidth parameters are based on the moment of the spectrum, that are defined as:

$$m_i = \int_0^\infty f^i \cdot P(f)df \tag{9.2}$$

We choose to evaluate these spectral moments using the Cavaleri-Simpson's rule (Baxevani and Rychlik, 2006) implemented in the WAFO Matlab toolbox for ocean waves (Brodtkorb et al., 2000). Experimental distributions were compared with theoretical distributions reported in Chapter 2. In order to assess the agreement between the theoretical distributions and the experimental distributions, the χ^2 method was used, while for the correlation coefficients between successive wave heights, crests and periods, a critical comparison was made with values obtained from previous experimental and theoretical studies in literature.

9.4 Statistical analysis of the MARINTEK datasets

Different variables were studied in this experimental study. First of all, the surface elevation was studied statistically, and was compared to the Gaussian distribution and

to the following second-order distribution, that takes into account bound modes in wave steepness or narrow-banded spectrum. We considered for this reason the Socquet-Juglard et al. (2005) distribution, described as:

$$p(\eta) = \frac{1 - 7D_\eta^2 k_p^2}{8\sqrt{2\pi(1 + 3G + 2G^2)}} \exp\left(-\frac{G^2}{2D_\eta^2 k_p}\right) \tag{9.3}$$

$$G = \sqrt{1 + 2D\eta k_p^2} - 1 \tag{9.4}$$

where k_p is the peak wavenumber and D is the standard deviation of the water elevation. Skewness and kurtosis were also evaluated and were compared to theoretical values from Srokosz and Longuet-Higgins (1986):

$$\lambda_3 = 3Dk_p \tag{9.5}$$

$$\lambda_4 = 3 + 18(Dk_p)^2 \tag{9.6}$$

The distribution of the wave heights was studied through comparing the survival probability Rayleigh distribution with the experimental survival probability (Longuet-Higgins, 1952):

$$S(H/H_s > H_0/H_s) = \exp\left[-2(H_0/H_s)^2\right] \tag{9.7}$$

A similar statistical study was carried out for the wave crests distribution, using the second-order survival Tayfun probability for crests, derived in the approximation of narrow-banded spectrum (Tayfun, 1980):

$$S(\eta_c/H_s > \eta_0/H_s) = \exp\left\{-\frac{8}{(k_p H_s)^2}\left[\sqrt{1 + 2\,(k_p H_s)\,\frac{\eta_0}{H_s}} - 1\right]^2\right\} \tag{9.8}$$

If a description of wave crests and heights is usually based on the Rayleigh distribution or to second-order modified Rayleigh distributions, this is not the case for the wave

periods. For this reason, several different theoretical distributions were investigated throughout to describe the periods distribution.

1. The first distribution that is considered in this study is the distribution proposed by Bretschneider (1959), that was derived with the assumption of a wavelength with asymmetry zero and Gaussian kurtosis.

$$p_{BRET}(T) = 2.7\frac{T^3}{\bar{T}^4}\exp\left[-0.675\left(\frac{T}{\bar{T}}\right)^4\right] \tag{9.9}$$

   Where $\bar{T}$ is the mean period evaluated directly from the data and not from the spectral moments.

2. Some years later Longuet-Higgins (1975) proposed a period distribution using the assumption of a narrow-banded spectral density function

$$p_{LH75}(T) = \frac{\nu^2}{2\left[\nu^2 + (\tau^2 - 1)\right]} \tag{9.10}$$

   where ν is the narrowness parameter, introduced by Longuet-Higgins (1975) to measure the spectral bandwidth and is defined as:

$$\nu = \left(\frac{m_0 m_2}{m_1^2} - 1\right)^{1/2} \tag{9.11}$$

   and τ is the normalized period defined as $\tau = T/T_{m01}$, where T_{m01} is the average period evaluated from the spectrum, defined as:

$$T_{m01} = 2\pi\frac{m_0}{m_1} \tag{9.12}$$

3. The year after Cavanie et al. (1976) proposed another theoretical expression for the marginal wave period distribution, that was derived from the joint distribution of wave periods and heigths on the assumption of a spectral Gaussian narrow-banded distribution.

$$p_{CAV}(T) = \frac{\alpha_C^3 \beta_C^2 \tau}{\left[\left(\tau^2 - \alpha_C^2\right)^2 + \alpha_C^4 \beta_C^2\right]^{3/2}} \tag{9.13}$$

where α_C and β_C are two parameters that depends on the broadness parameter ε, that is another spectral bandwidth parameter introduced by Cartwright and Longuet-Higgins (1956):

$$\alpha_C = 1/2\left(1 + \sqrt{1-\varepsilon^2}\right) \tag{9.14}$$

$$\beta_C = \frac{\varepsilon}{\sqrt{1-\varepsilon^2}} \tag{9.15}$$

$$\varepsilon = \left(1 - \frac{m_2^2}{m_0 m_4}\right) \tag{9.16}$$

4. Longuet-Higgins (1983) modified his previous distribution (Longuet-Higgins, 1975), in order to allow the distribution to be asymmetrical and considering the correlation between successive periods as well. The resulting form of the distribution is:

$$p_{LH83}(T) = \left(1 + \frac{\nu^4}{4}\right) \frac{1}{2\nu\tau} \left[1 + \left(1 - \frac{1}{\tau}\right) \frac{1}{\nu^2}\right]^{-3/2} \tag{9.17}$$

5. In the same year, Tayfun (1983) proposed another distribution, derived from the Longuet-Higgins (1975) distribution, using a Taylor partial sum of periods:

$$p_{TAY}(T) = \frac{\left(1+\nu^2\right)^{1/2}}{2\left(1+\eta_T^2\right)^{3/2}} \tag{9.18}$$

where η_T is the centered period normalized with the bandwidth:

$$\eta_T = \frac{\tau - \bar{\tau}}{\nu\bar{\tau}} \tag{9.19}$$

where τ is defined above in Longuet-Higgins (1975).

6. Myrhaug and Rue (1998) proposed a distribution based on a modified Weibull two-parameters distribution:

$$p_{MR98}(T) = \frac{\beta_M t^{\beta_M - 1}}{\alpha_M^{\beta_M}} \exp\left[-\left(\frac{t}{\alpha_M}\right)^{\beta_M}\right] \tag{9.20}$$

where t is defined as $t = T/\zeta$, ζ is the root-mean-square period calculated from the data and α_M and β_M are Weibull parameters $\alpha_M = 1.055$ and $\beta_M = 3.362$. For more detail see Myrhaug and Rue (1998) and Myrhaug et al. (2000).

7. The last and more recent period distribution that was considered in this analysis is the Xu et al. (2004), in which the authors modified the Longuet-Higgins (1983) distribution, introducing a normalization factor in the joint probabilty distribution and then integrating on wave heights. The resulting expression is:

$$p_{XU}(T) = \frac{\pi\left(m_0^2 - m_1 m_2\right)\tau}{m_0^{1/2}\left(m_2\tau - 4\pi m_1\tau + 4\pi^2 m_0\right)^{3/2}} \tag{9.21}$$

In addition to ν and ε, another parameter for evaluating the bandwidth was proposed: the so-called quality factor (Goda, 1970) or peakedness parameter, that is a measure of how much energy is concentrated near the spectral peak, and is the inverse (as meaning) of the broadness parameter:

$$Q_F = \frac{2}{m_0}\int_0^\infty f \cdot P^2(f) df \tag{9.22}$$

A critical comparison on the robustness of the peakedness, the broadness and the narrowness parameters, based on a numerical analysis, was carried out by Rye (1977) and Serio et al. (2005). Results indicates that the peakedness parameter is more reliable and robust than the broadness and the narrowness, because it is less cut-off frequency dependent, while the other two parameters shows a larger variability to the tail of the spectrum. Despite being more stable than the other two, no period distribution was proposed using the quality factor for the measure of the spectral bandwidth.
It is possible also to study jointly the wave periods and the wave heights: many authors proposed a theoretical joint distribution of wave heights and periods, that relates the probability density wave heights with the probability density of the wave periods. It gives the probability of finding a value of the wave period given a determined wave height or vice versa. This distribution is extremely useful for engineering purposes, in order to design coastal and offshore facilities, and is extremely important also for wave renewables, since it gives a prediction of the distribution of joint wave heights and periods. The most common joint distribution, that is widely used is the Longuet-Higgins (1983) joint distribution, that is defined as:

$$p(H_n, T) = \frac{2L(\nu)}{\nu\sqrt{\pi}} \frac{H_n^2}{\tau} \exp\left[-H_n^2 \left(1 + \frac{1 - \left(\frac{1}{\tau}\right)^2}{\nu^2}\right)\right] \tag{9.23}$$

In which H_n is the normalized wave height, defined as $H_n = H/(8m_0)^2$, τ is the normalized period defined above, and $L(\nu)$ is a normalization factor that is defined as:

$$L(\nu) = \frac{2\sqrt{1+\nu^2}}{1+\sqrt{1+\nu^2}} \tag{9.24}$$

When the spectrum is narrow-banded ($\nu \leq 0.6$), like for the experiment that is reported in this thesis, the normalization factor $L(\nu)$ become:

$$L(\nu) \approx 1 + \frac{\nu^4}{2} \approx 1 \tag{9.25}$$

The last parameter considered in the statistical analysis of waves was the correlation between successive wave heights, crests, troughs and periods. This parameter is correlated to the wave group length (Kimura, 1980) and is important since is related to the wave periods and heights distribution and is related to the energy content of the sea state. A wave group is a sequence of waves whose heights exceed a certain threshold and it can represent a threat on marine infrastructures and marine transportation. So from the engineering point of view, predicting its features is fundamental (Rodrı?guez and Soares, 2001). Kimura (1980) formulated a theory on wave group based on the correlation of successive wave heights, based on a two-state Markov chain, these two states are determined by the exceedance or the non-exceedance of a given height threshold H_0, on the assumption that the wave height distribution follow the Rayleigh distribution. Given a wave whose height is H_1, the probability that the following wave will have wave height H_2 is:

$$p(H_1, H_2) = \frac{H_1 H_2}{(1-\kappa^2)\, 16 m_0^2} \exp\left[-\frac{H_1^2 + H_2^2}{(1-\kappa^2)\, 8 m_0^2}\right] I_0\left[-\frac{H_1 H_2 \kappa}{(1-\kappa^2)\, 4 m_0^2}\right] \tag{9.26}$$

where I_0 is the modified Bessel function of order zero and κ is a correlation factor that is given by (Rodrı?guez and Soares, 2001):

$$\kappa = \left[\frac{1}{m_0^2}\left(\left(\int_0^\infty S(f)\cos(2\pi f \tau_1) df\right)^2 + \left(\int_0^\infty S(f)\sin(2\pi f \tau_1) df\right)^2\right)\right]^{1/2} \tag{9.27}$$

with $\tau_1 \approx T_{m02}$, where T_{m02} is:

$$T_{m02} = 2\pi\sqrt{\frac{m_0}{m_2}} \tag{9.28}$$

This correlation factor is related to the correlation coefficient between successive wave heights:

$$R_{HH} = \frac{E(\kappa) - \frac{1}{2}\left(1-\kappa^2\right)K(\kappa) - \frac{\pi}{4}}{1-\frac{\pi}{4}} \approx \frac{\pi}{16-4\pi}\left(\kappa^2 + \frac{\kappa^4}{16} + \frac{\kappa^6}{64}\right) \tag{9.29}$$

where E and K are the the complete Jacobian elliptic integrals of the first and second order respectively. A similar expression was found by Kimura for the successive wave periods, that was related with the rolling of the ships in the sea, but in this case the Markov chain was based on the assumption that the transition probability is based on a two-dimensional Weibull distribution.

$$p(T_i, T_{i+1}) = \frac{n^2}{4\left(\phi^2-\sigma_k^2\right)}\frac{\left[T_i T_{i+1}\right]^{n-1}}{T_r^{2n}}\exp\left[-\frac{\phi}{2\left(\phi^2-\sigma_k^2\right)}\frac{\left(T_i^n + T_{i+1}^n\right)}{T_r^{2n}}\right] I_0\left[\frac{\sigma_k}{\left(\phi^2-\sigma_k^2\right)}\frac{\left(T_i T_{i+1}\right)^{n/2}}{T_r^{2n}}\right] \tag{9.30}$$

In which n is the shape parameter, σ_k is the correlation parameter, T_r is the root-mean square period and ϕ is defined as:

$$\phi = \frac{1}{2}\left[\Gamma\left(\frac{n+2}{n}\right)\right]^{-n/2} \tag{9.31}$$

where Γ is the gamma function. A similar expression to eq. 4.81 can be derived for the successive wave periods, relating the correlation coefficient between successive wave periods with the correlation parameter σ_k, based on both Γ function and hypergeometric function F.

Chapter 10

Crossing sea and rogue waves

This last chapter of this thesis describe a work carried out by myself in collaboration with Prof. Marina Serio of the Department of Physics of the University of Turin (Italy). The analysis reported in this chapter is a reanalysis of an experimental effort published in 2011 (Toffoli et al., 2011a), that led to the first evidence of the excess of kurtosis and of rogue waves in the crossing sea. However, in the previous study only the kurtosis behavior was examined, but no such analysis was carried out for the distribution of heights, crests and periods. For wave periods, successive wave feature correlation, and for the comparison of the bandwidth behavior, also monochromatic sea state data from wave tank were considered, from another experiment, where wave height analysis was reported (Onorato et al., 2009).

10.1 Spectrum and spectral parameters

The spectral density of the recorded waves was estimated using the autoregressive Maximum Entropy Method with an order 30. The spectrum was evaluated at different distances from the wavemaker, in order to see the evolution of the spectrum throughout

the wave tank. In Figure 10.1 the results of this analysis are reported: little changes in the spectral width can be seen, along with a shift of the spectrum to lower frequencies. In the figure 10.2 we report the analysis of the directional spectrum for 10° and 20° (results are the same for the other angles). The results show that the directional spectrum does not change during the propagation, that is consistent with the theory of the wave propagation (Benjamin and Feir, 1967) and with numerical simulation using the Zakharov and the Non-Linear Schrödinger equations (Onorato et al., 2002a; Dysthe et al., 2003).

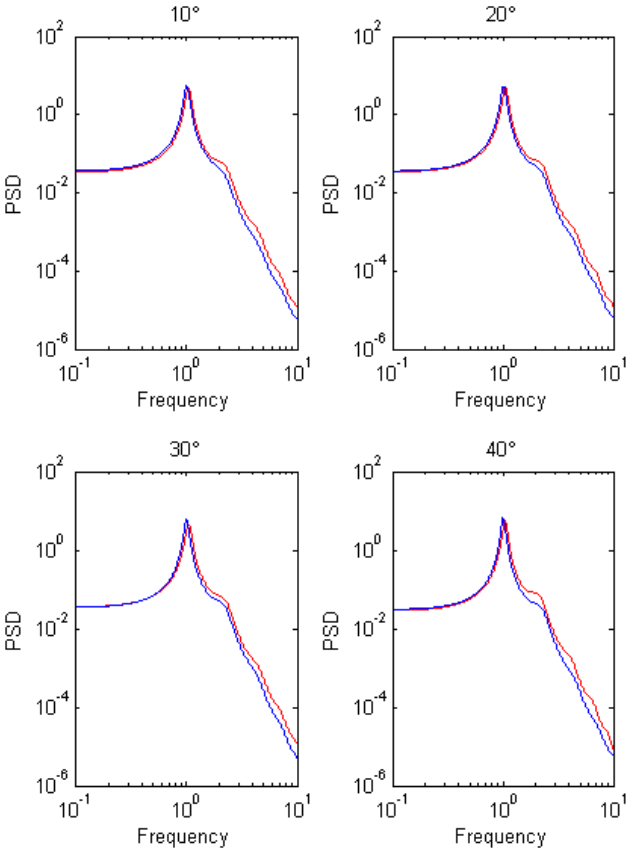

FIGURE 10.1: Spectrum of the data computed with the Burg (1967) method for all the crossing sea angles. Red spectra is $x/L = 3.1$, blue is $x/L = 22.3$

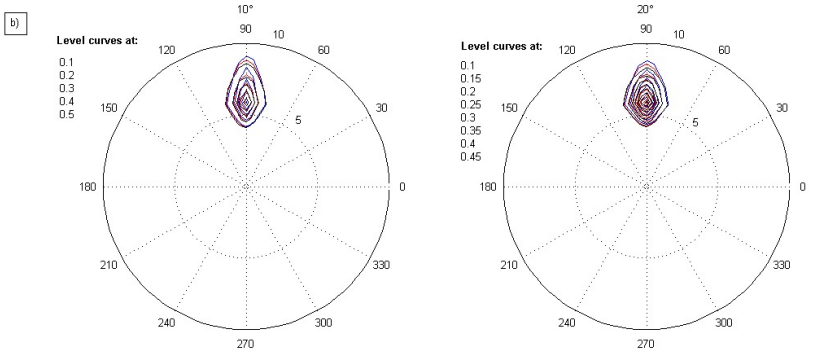

FIGURE 10.2: Directional spectrum of the data for $\beta = 10, 20°$ computed with the Burg (1967) method. Red spectra is $x/L = 3.1$, black is $x/L = 22.3$

To understand better the spectral evolution in the wavetank, the main statistical properties of the spectrum were evaluated: the peak wave period, bandwidth, asymmetry and the kurtosis (Figures 10.3-10.5). Asymmetry and kurtosis were compared with theoretical values reported in Srokosz and Longuet-Higgins (1986). During the evolution of the wavetrain the peak period decreased constantly (Figure 10.3) as expected, but also the bandwidth was decreasing (Figure 10.4): in particular the inverse of the narrowness parameter showed a strong decrease and this was consistent with the Benjamin-Feir instability (Benjamin and Feir, 1967). The decreasing of the bandwidth means that the spectral energy is focusing near the peak frequency, due to non-linear interactions inside the wavetrain. As reported in Chapter 2, the main proxy of the Benjamin-Feir instability in the ocean is the increasing of the kurtosis. For this experiment, the increase of the kurtosis during the propagation in the wavetank is reported in (Toffoli et al., 2011a) and compared with the expected values from Srokosz and Longuet-Higgins (1986) in Figure 10.5.

The decrease of the bandwidth, based on the behavior of the narrowness parameter and of the quality factor in crossing seas was larger for angles $\beta \geq 30°$ and, consistently, the kurtosis increase was larger for the same angles: this is consistent with numerical

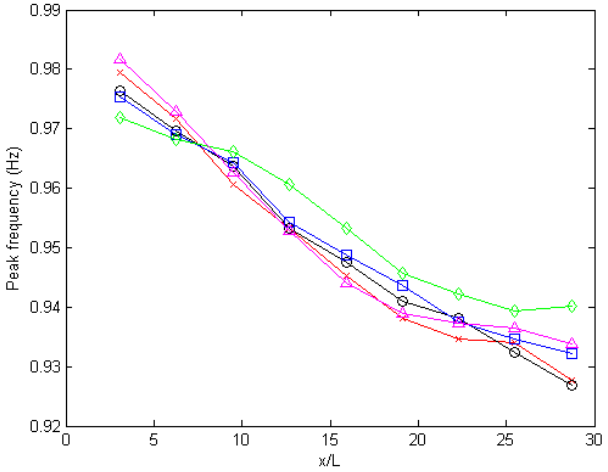

FIGURE 10.3: Evolution as a function of the distance from the wavemaker of the peak frequency (Hz) estimated from Young (1995): red crosses is for 10°, black circles for 20°, blue squares for 30°, green diamonds for 40° and magenta triangles for unidirectional. Adapted from Figure 1b in Sabatino and Serio (2015)

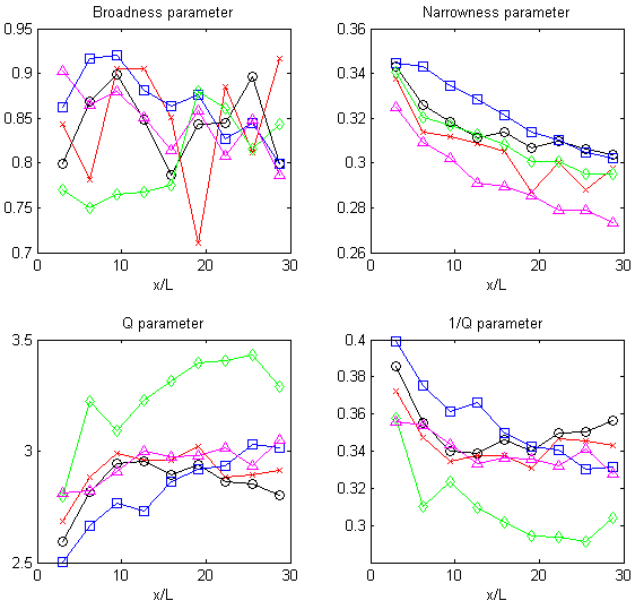

FIGURE 10.4: Evolution as a function of the distance from the wavemaker of the spectral bandwidth: broadness parameter ε (Cartwright and Longuet-Higgins, 1956), narrowness parameter ν (Longuet-Higgins, 1975) and quality factor Q_F (Goda, 1970). Red crosses is for 10°, black circles for 20°, blue squares for 30°, green diamonds for 40° and magenta triangles for unidirectional.

simulations based on the Euler equation (Toffoli et al., 2011a), indicating larger values for the kurtosis for $\beta \leq 30°$. The bandwidth behavior in a crossing sea state was also compared (figure 10.4) with the behavior of the same parameter in monochromatic conditions. The figure shows that increase in monochromatic sea state was comparable with the one recorded for $\beta = 30°, 40°$ in the same spectral conditions. From the spatial behavior of the broadness parameter no clear pattern emerges compared to narrowness and to quality factor. However, the broadness parameter ε is strongly dependent on the 4-th spectral moment (see equation 4.68 (Cartwright and Longuet-Higgins, 1956)), that is more affected than the other moments by the tail of the spectrum and this causes it to be a less reliable estimator for the spectral bandwidth (Rye, 1977; Serio et al., 2005).

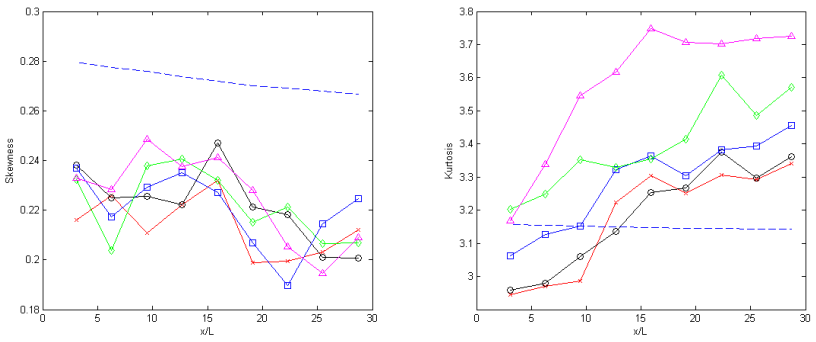

FIGURE 10.5: Evolution as a function of the distance from the wavemaker of the skewness (a) and the kurtosis (b). Dashed lines represent expected values of skewness and kurtosis from Srokosz and Longuet-Higgins (1986), equations 4.57-4.58

Also the increase of the kurtosis was larger for monochromatic conditions as reported in Toffoli et al. (2011a) and in Onorato et al. (2009). These results altogether confirm that the mechanism of the Benjamin-Feir instability is possible also in crossing sea state, but is weaker than the monochromatic sea state, in which only one wavetrain is present. However, is worth noticing that, due to the limitation of the wavetank it was not possible to investigate the behavior of the system for $\beta \leq 40°$. Numerical simulations (Toffoli et al., 2011a) showed that for $40° \leq \beta \leq 60°$ the kurtosis was at its maxima. The surface elevation was also compared with the Gaussian distribution and

the Socquet-Juglard distribution (Figure 10.6): both Socquet-Juglard and Gauss well describe the central part of the distribution, around the peak, while both underestimate the tail of the distribution, in particular when $\eta/\sigma \geq 2$. Also in this case the deviation from the theoretical distributions is larger for $\beta \geq 30°$.

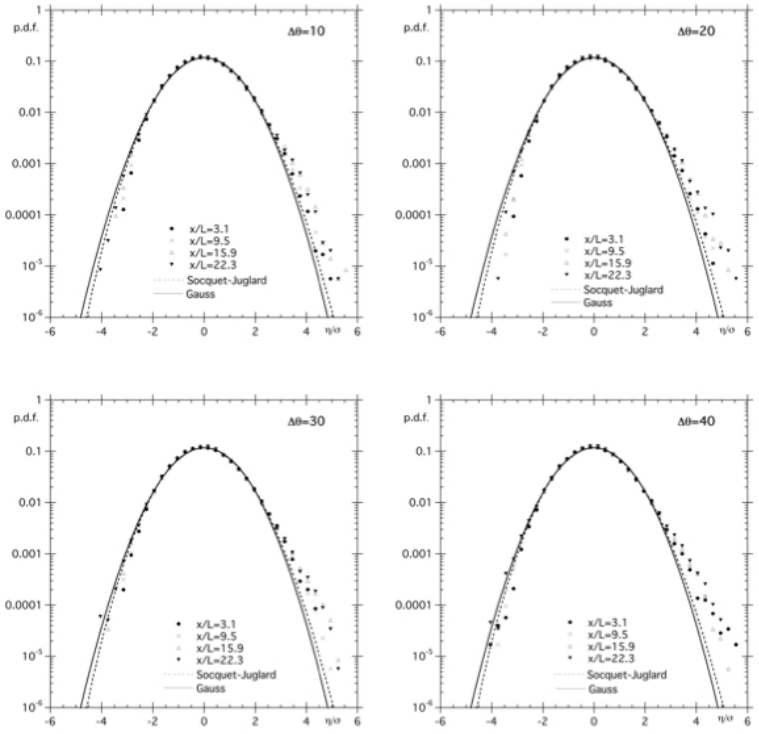

FIGURE 10.6: Probability density function of the surface elevation for the four crossing sea configurations. Dashed line: equations 4.55-4.56 (Socquet-Juglard et al., 2005), Continuous line: Gaussian distribution. The figure is from Sabatino and Serio (2015)

10.2 Wave heights distribution

In Toffoli et al. (2011a) an excess of kurtosis was found in crossing sea states. The excess of kurtosis is an indication for an increased probability of rogue waves formation in the ocean (Janssen, 2003). In this section the wave heights distribution is explored and in particular, the rogue waves probability is assessed and the experimental survival distribution is compared with the theoretical Rayleigh distribution.

In figure 10.7 the wave height survival distribution is shown for all the angles and for four different distances from the wavemaker.

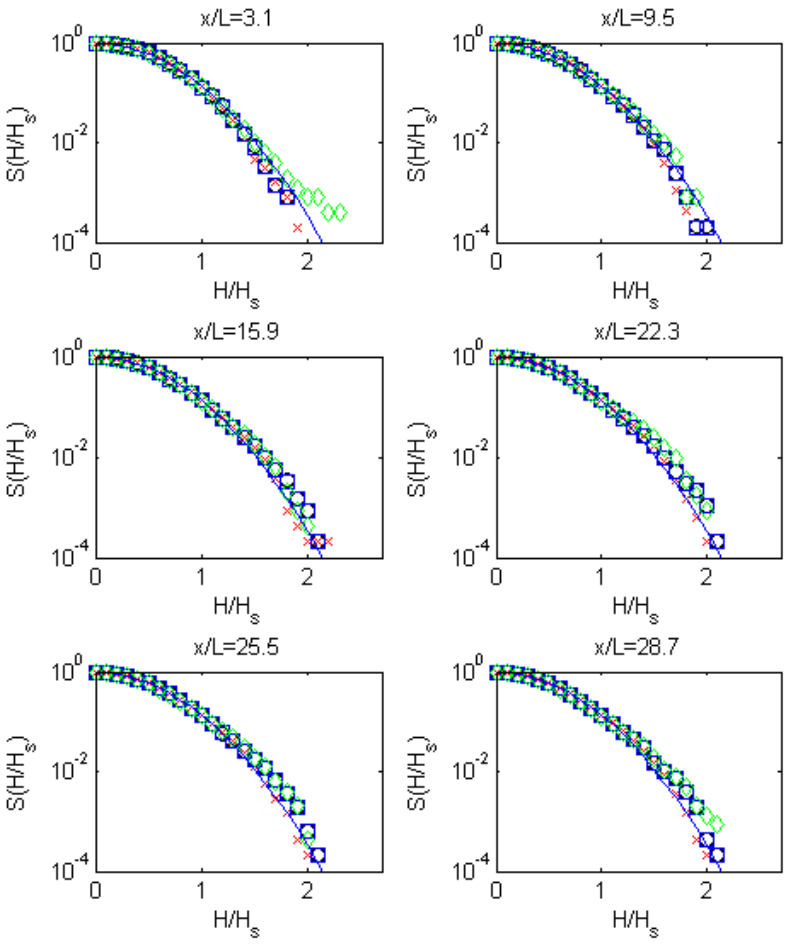

FIGURE 10.7: Wave heights survival probability at six distances from the wavemaker for the four crossing sea configurations. Red crosses is for 10°, black circles for 20°, blue squares for 30°, green diamonds for 40°. Adapted from Sabatino and Serio (2015)

Close to the wavemaker, the experimental survival distribution was lower than theoretical distribution, and from the classification of wave heights distribution in Romans et al. (1995) and in Adcock and Taylor (2014), the experimental distribution found here could be classified as Type 2, where the Rayleigh distribution overestimates the experimental distribution, while for distances $x/L \geq 15.9$, the experimental distribution were

following the Type 1 (Wave heights follow a Rayleigh distribution) and eventually, for $x/L \geq 20$ a Type 3 distribution, in which the experimental survival probability is larger than the Rayleigh distribution and rogue waves have an higher probability to occur than the Rayleigh.

This was both consistent with the findings on the wave spectrum in the previous section, in which the kurtosis was growing with a maximum after $x/L \geq 20$ and with the Benjamin-Feir instability, in which the instabilities of the wavetrain were occurring after 20-30 wave periods (Benjamin and Feir, 1967; Onorato et al., 2002a; Dysthe et al., 2003). The maximum wave height and the probability of rogue waves were also reported in figure 10.8 and results were compared with the monochromatic (unidirectional) experiment: the results for $\beta = 30°, 40°$ were comparable to the unidirectional case, both for the probability of rogue waves as for the maximum wave height, while for smaller angles, both the maximum wave height and the probability of rogue waves was smaller than the unidirectional sea state. The increase of the maximum wave height in the basin was about 12% for the crossing sea state and about 15% for the unidirectional case, that was considered as a baseline in this experiment. The increase of wave height in crossing seas was statistically significant ($p < 10^{-5}$).

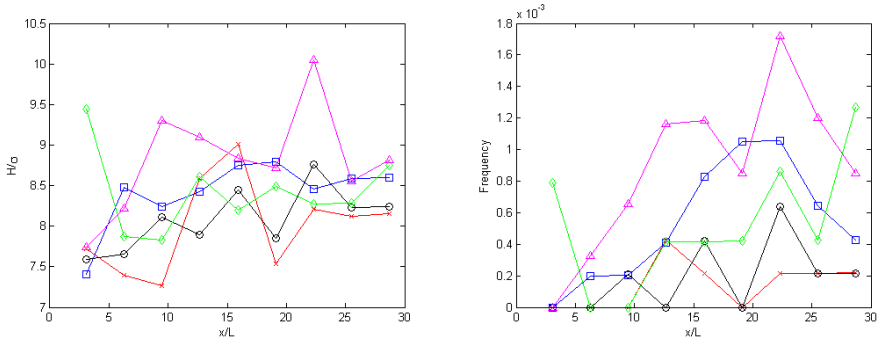

FIGURE 10.8: Evolution as a function of the distance from the wavemaker of the maximum wave height and the rogue wave frequency for all the crossing sea state compared to unidirectional sea state from Onorato et al. (2009) in the same initial spectral conditions. Red crosses is for 10°, black circles for 20°, blue squares for 30°, green diamonds for 40° and magenta triangles for unidirectional. Adapted from Sabatino and Serio (2015)

10.3 Wave crests distribution

A similar procedure was carried out for studying the wave crests survival distribution. In figure 10.9 are reported the survival probability for different distances from the wavemaker for all the crossing sea angles considered, compared with the second-order Tayfun distribution. The results are similar to the wave heights, with the second-order Tayfun distribution providing a good estimate of the experimental distribution for distances $x/L \leq 10$, while for greater distances the Tayfun survival function underestimates the crests larger than $\eta_c/H_s \geq 0.8$. In addition, some waves with $\eta_c/H_s \geq 1.25$, that then can be classified as rogue waves (Dysthe et al., 2008), were recorded, confirming that for those conditions the Benjamin-Feir instability influences not only the wave height distribution but also the wave crests (Onorato et al., 2006b).

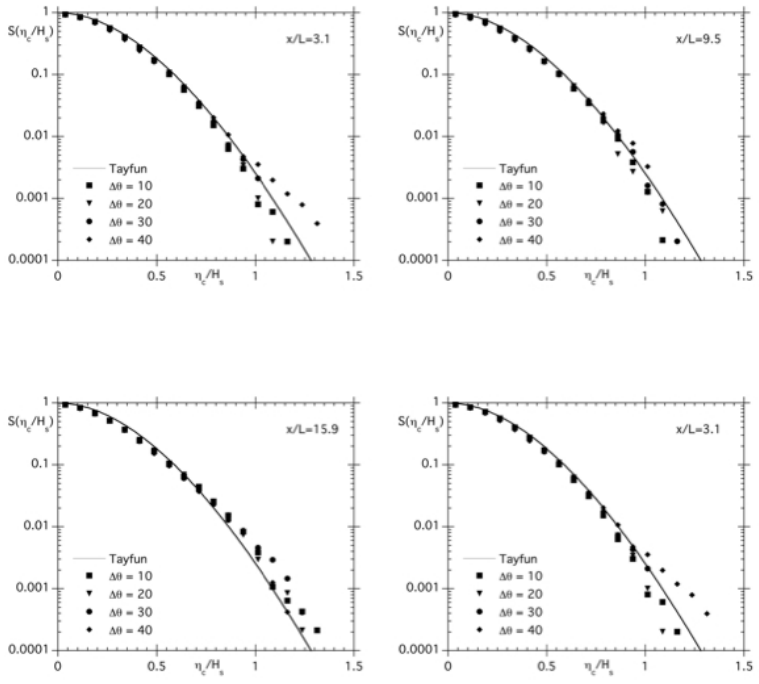

FIGURE 10.9: Wave crests survival probability at four distances from the wavemaker for the four crossing sea configurations compared with the Tayfun (1980) theoretical survival probability. Figure from Sabatino and Serio (2015)

10.4 Wave periods distribution

Experimental wave periods distribution for both crossing and monochromatic sea waves was considered and compared with the existing theoretical models (figure 10.10-7.11). Then the goodness of the fit between theoretical and experimental distribution was evaluated through χ^2 values (Table 10.1).

Distribution	$JONSWAP$	$\beta = 10°$	$\beta = 20°$	$\beta = 30°$	$\beta = 40°$
Bretschneider (1959)	61.0	47.6	45.0	43.3	28.6
Longuet-Higgins (1975)	78.3	69.2	71.9	75.3	36.1
Cavanie et al. (1976)	163.0	130.2	120.7	118.2	62.5
Longuet-Higgins (1983)	51.6	54.0	60.7	66.0	36.4
Tayfun (1983)	32.5	32.9	35.0	36.5	20.0
Myrhaug and Rue (1998)	100.4	78.9	71.9	66.1	40.1
Xu et al. (2004)	102.3	109.5	119.9	122.3	63.6

TABLE 10.1: Reduced χ^2 value for the considered marginal period distributions (spatial average of the wave gauges was applied). Low χ^2 for $\beta = 40°$ are possibly due to the lower number of data recorded for this angle

Results show a poor overall agreement between all the theoretical distributions with the experimental results. The Tayfun distribution is one with the lowest χ^2 between the examined distributions. The Bretschneider and the Longuet-Higgins (1983) shows also a lower χ^2 compared to the others. Qualitatively, the LH83 show a better agreement in the central part of the distribution, around the peak, but fails on the tails of the distribution, while the Tayfun and the Bretschneider presents the opposite behavior.

In general, no theoretical distribution is able to give a satisfactory agreement with the experimental distribution, both in unidirectional and in crossing sea state. The crossing sea angle seems to have a very weak influence on the period distribution. However, is important to notice that all the theoretical distribution are extremely sensitive on the bandwidth estimation and all of them are based on the the broadness and the narrowness parameters, that are not the most robust estimators for the bandwidth (Serio et al., 2005). Secondly those distributions are strongly dependent to the interactions between

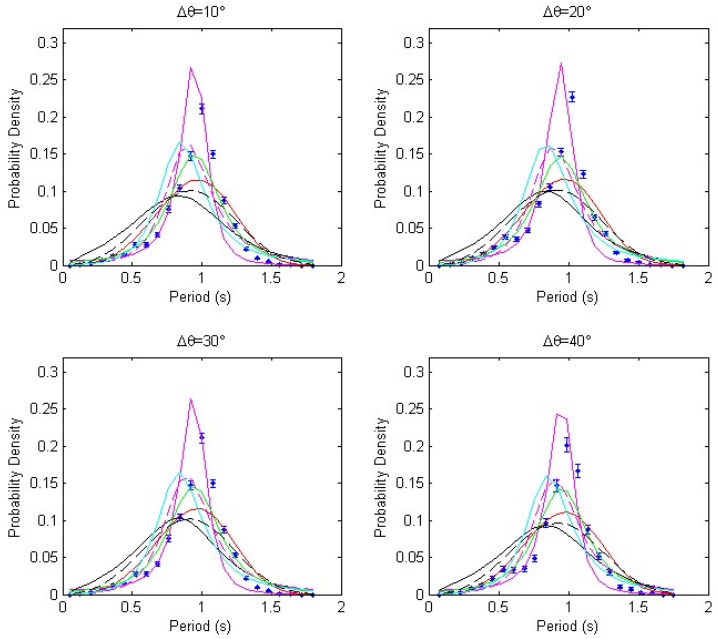

FIGURE 10.10: Wave periods distribution at $x/L = 22.3$ for the four considered crossing sea conditions. Blue points are the experimental values, the magenta line is the Longuet-Higgins (1975), the black continuos line is the Cavanie et al. (1976), dotted magenta line is the Longuet-Higgins (1983), red line is the Bretschneider (1959), green line is the Tayfun (1983), cyan line is the Xu et al. (2004) and the black dotted line is the Myrhaug and Rue (1998)

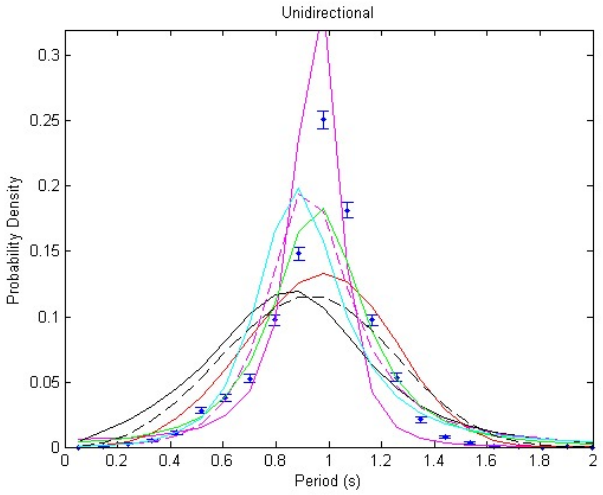

FIGURE 10.11: Wave periods distribution at $x/L = 22.3$ for the four considered crossing sea conditions. The colour are the same in Figure 10.11

waves, that are accounted for in the correlation between successive wave heights and wave periods and on the joint distribution of heights and periods. Those two important features are examined in the following sections.

10.5 Joint wave heights and period distribution

In Figure 10.12-7.13 the experimental joint distribution of wave heigths and periods is studied and compared with the theoretical Longuet-Higgins (1983) distribution for different angles and for different distances to the wavemaker. The theoretical distibution performs reasonably well in describing the density of probability, however shows significant discrepancies in the peak: theoretical and experimental presents a different predicted peak and the LH83 tends to overestimate the density of probability at high periods and low heights, while works well for representing the joint distribution for low periods. Experimental results suggests also that the joint distribution have two or more peaks, that was also observed in previous experimental studies on the joint distribution (Zhang et al., 2013).

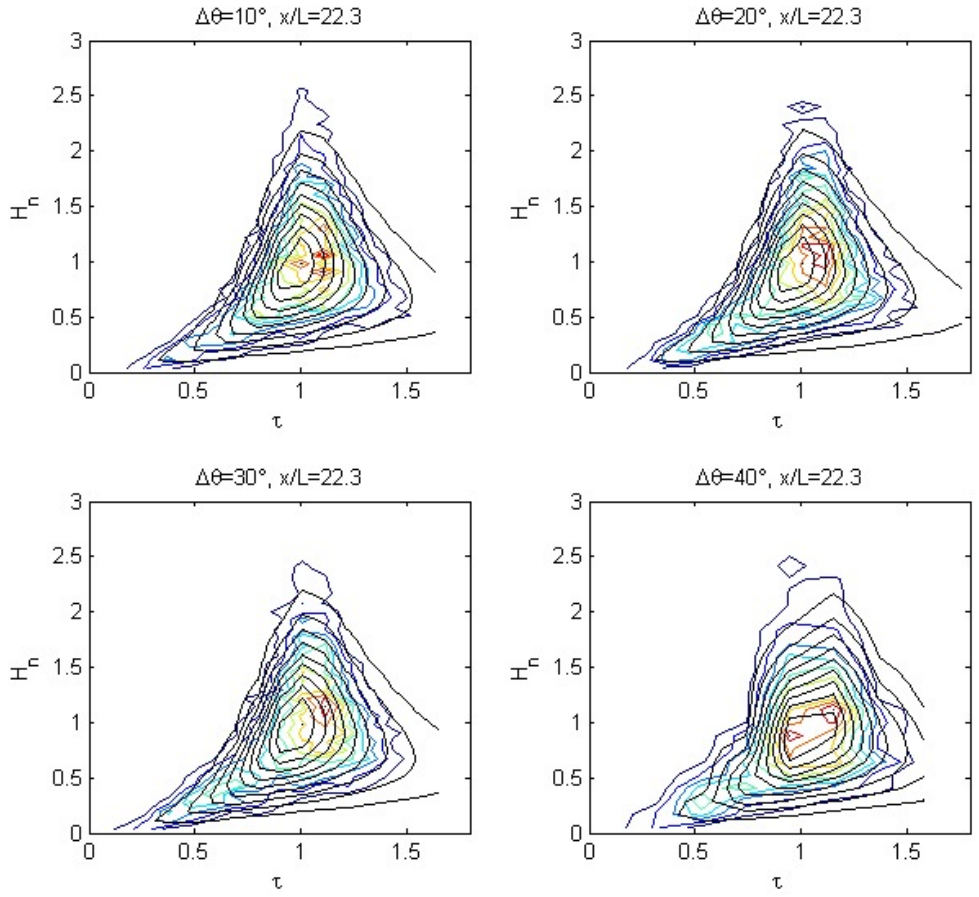

FIGURE 10.12: Joint wave height and period distribution at $x/L = 22.3$ for the four different crossing sea state conditions, theoretical Longuet-Higgins (1975) is in black, experimental values changes color from light blue to dark red depending on the enhanced probability. Contour levels are at (0.9, 0.8, 0.7, 0.6, 0.5, 0.4, 0.3, 0.2, 0.1) x Po,t, the colored lines are the experimental data, while the solid black lines are the theoretical values.

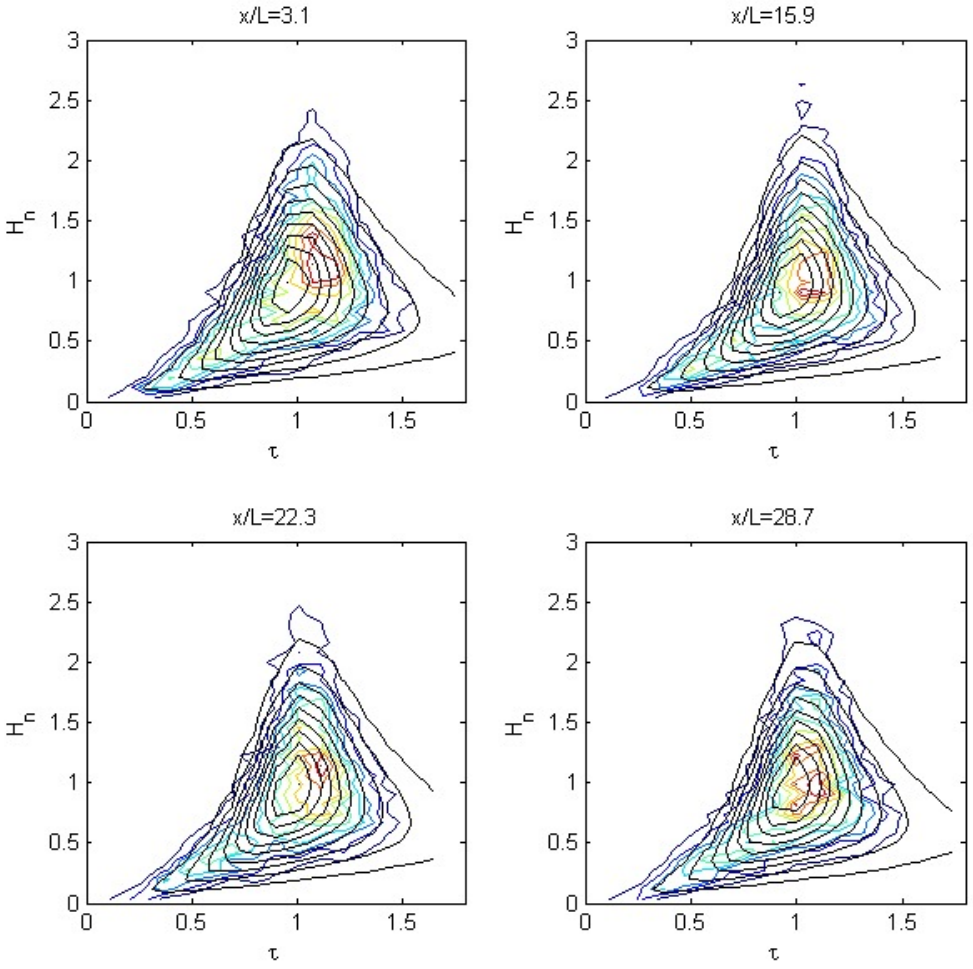

FIGURE 10.13: Joint wave height and period distribution for $\beta = 30°$ at different distances from the wavemaker

10.6 Correlation between successive waves and related distributions

The correlation between successive wave heights was studied in two ways: first the fields of the experimental successive wave heigths distribution is showed for different angles and for different distances from the wavemaker (Figures 7.14-7.15).

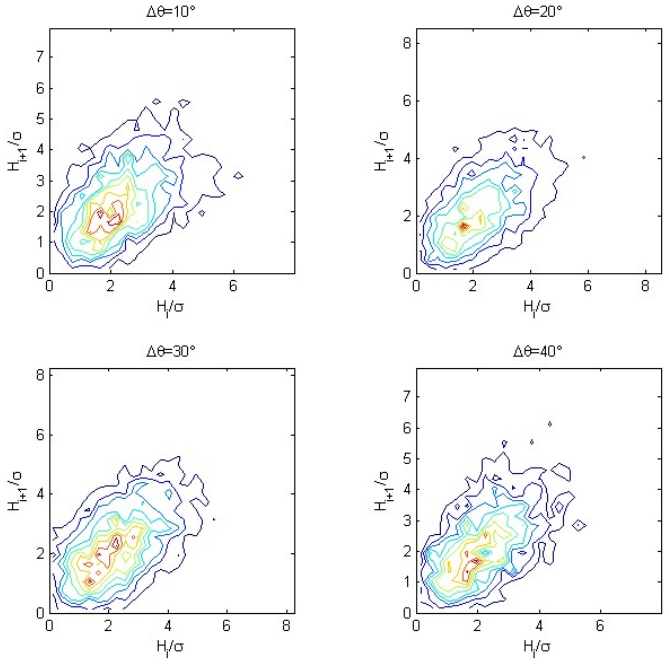

FIGURE 10.14: Successive wave heights distribution for x/L=22.3

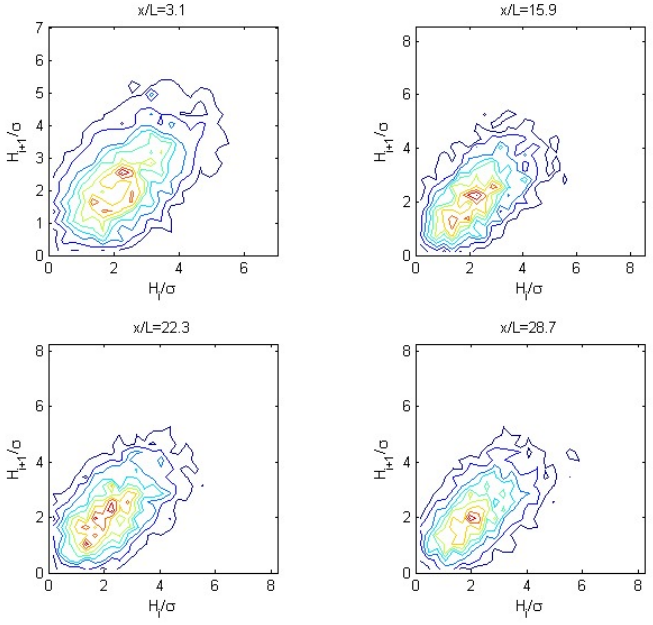

FIGURE 10.15: Evolution of the distribution of successive wave height through the wave tank for $\beta = 30°$

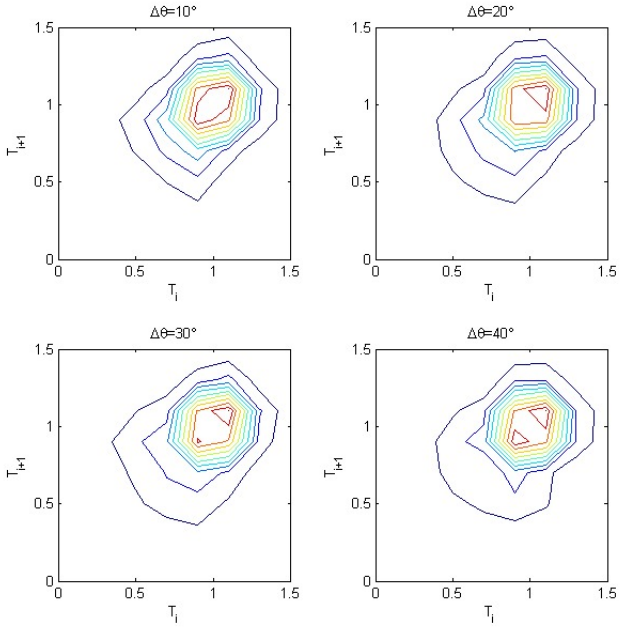

FIGURE 10.16: Successive wave periods distribution for x/L=22.3

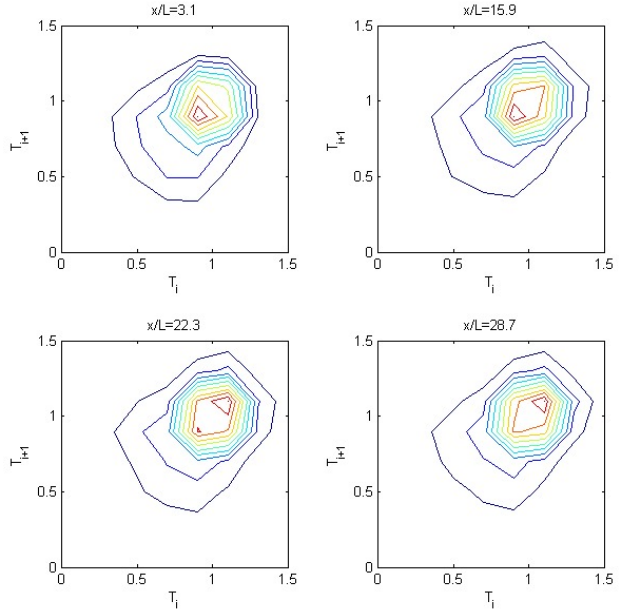

FIGURE 10.17: Evolution of the distribution of successive wave periods through the wave tank for $\beta = 30°$

In addition, the correlation coefficient was calculated, as well as the correlation coefficient between H_i and $H_{i+2}, H_{i+3}, H_{i+4}$ and values found in this study were compared with previous studies in different conditions (Table 10.2). Correlation coefficients between successive wave crests and trought were also evaluated. For wave periods, the procedure was the same as the wave heights: the successive wave periods distribution was evaluated (Figure 10.16-7.17), then the correlation coefficients were calculated and compared with previous studies (Table 10.3).

For the successive wave heights, the value of the correlation coefficient grows with the angle β of crossing sea, having its maxima for $40°$ (however, large angles were not investigated) and was exceeding the monochromatic case, while for $\beta = 10°, 20°$, the correlation coefficient was lower than the unidirectional sea state. The magnitude of the correlation coefficient were similar to previous studies, as well as the magnitude of the second, third and fourth order correlation coefficients. Similar results were found for the wave period, in which the results were comparable to the **?** values in bimodal sea state conditions.

The correlation coefficient for successive wave heights showed, spatially, a small but constant growth in the wavetank. This can be seen in the successive wave height distribution, with the width of the distribution narrowing during the propagation. The main consequence of this narrowing is that, from the Kimura (1980) theory, the wave groups were longer. Kimura (1980) also found that the correlation coefficient between successive wave heights is related to the Goda Quality Factor Q_F: the narrower is the spectrum, the higher will be the correlation coefficient. This is a second and independent proof of the Benjamin-Feir mechanism that is acting in a crossing sea state: in their numerical study, Gramstad and Trulsen (2007) related the length of the wave groups to the BFI in deep water. The longer is the wave group, the higher is the Benjamin-Feir index and so the probability of occurrence of rogue waves.

From these results, it is possible to conclude that it is extremely difficult to determine the correlation coefficient and the distribution between successive wave heights and

periods, since they are strongly affected by the bandwidth of the spectrum and by the conditions of the sea. This experiment, however gave us the opportunity to see how this coefficient and the distribution was varying with the angle and during the propagation of the wave train.

10.7 Discussion

The experimental study presented here highlight how the crossing sea state can cause rogue waves in deep sea. Extending a previous study, and comparing the results with previous researches, the present research shows how the angle between the two trains in very important in the stability of the resulting sea state and in the formation of rogue waves. Even if more energy is present in crossing sea state compared with monochromatic sea, as also indicated by the correlation coefficient calculated for the different configuration. The main limitation of this study is the geometrical limitation to a crossing sea angle $< 40°$. From the previous numerical simulation (Toffoli et al., 2011a), the highest probability for the formation of rogue waves are between $30°$ and $60°$. Further studies should focus on studying the behavior of the spectra and of the variables studied here with different angles and different configurations. In particular the present study consider two identical wavetrain interacting. However in real ocean often the two wavetrains are very different, since one of them is usually a swell wave train, with an higher frequency peak and with a lower energy. Simulating this case would be interesting in order to understand the occurrence of rogue waves caused by wave-wave interactions.

Study	$R_{HH}(i,i+1)$	$R_{HH}(i,i+2)$	$R_{HH}(i,i+3)$	$R_{HH}(i,i+4)$
Rye (1974)				
Wave growth	0.30			
Wave decay	0.20			
Total	0.24	≈ 0	≈ 0	
Dattatri et al. (1977)	0.236			
Arhan and Ezraty (1978)				
North Sea meas.	0.297	0.051	0.036	
JONSWAP	0.298	0.113	< 0.01	
PM spectrum	0.163	0.043	< 0.01	
Kimura (1980)				
Case 1	0.19			
Case 2	0.23			
Case 3	0.29			
Case 4	0.33			
Case 5	0.38			
Su et al. (1982)				
Wave growth	0.374	0.066	0	-0.021
Wave decay	0.34	0.07	0.021	0.013
Total	0.329	0.07	0.003	-0.006
Goda (1983)	0.649	0.351	0.178	0.07
Sobey (1996)				
PM spectrum	0.31			
Mean JONSWAP	0.45			
Sharp JONSWAP	0.571			
Jayewardane (1987)				
Unimodal	0.17	0.091	0.055	
Bimodal	0.165	0.064	-0.041	
?				
Swell-dominated sea (I)	0.311	0.064	0.01	-0.016
Swell-dominated sea (II)	0.520	0.135	0.015	0.012
Swell-dominated sea (III)	0.309	0.154	0.06	0.006
Wind-sea dominated sea (I)	0.549	0.189	0.05	-0.003
Wind-sea dominated sea (II)	0.419	0.148	-0.024	0.000
Wind-sea dominated sea (III)	0.621	0.217	0.061	0.009
Mixed sea state (I)	0.204	0.02	0.012	-0.024
Mixed sea state (II)	0.098	0.125	-0.011	0.011
Mixed sea state (III)	0.194	0.059	0.05	-0.018
PM spectrum	0.263	0.001	0.000	0.039
Rodriguez et al. (2000)	0.444			
Wist et al. (2004)				
Draupner data	0.411	0.126	0.058	
Japan data	0.321	0.077	0.022	
Laboratory	0.516	0.170	0.079	
Present results				
$\beta = 10^\circ$	0.475	0.073	-0.019	-0.020
$\beta = 20^\circ$	0.513	0.140	0.017	-0.012
$\beta = 30^\circ$	0.548	0.187	0.046	-0.009
$\beta = 40^\circ$	0.574	0.195	0.029	-0.026
Unidirectional	0.518	0.108	-0.021	-0.041

TABLE 10.2: Correlation coefficients between successive wave heights compared with previous results, see Sabatino and Serio (2015), Table 1 and **?**, Table 3-4. In Kimura (1980), the case 1 is the broader spectrum, while the case 5 is the narrower spectrum

Study	$R_{TT}(i,i+1)$	$R_{TT}(i,i+2)$	$R_{TT}(i,i+3)$	$R_{TT}(i,i+4)$
?				
Swell-dominated sea (I)	0.282	0.035	-0.006	-0.017
Swell-dominated sea (II)	0.348	0.069	0.023	0.000
Swell-dominated sea (III)	0.301	0.089	0.020	0.007
Wind-sea dominated sea (I)	0.103	0.019	0.049	-0.009
Wind-sea dominated sea (II)	-0.033	0.134	-0.045	0.009
Wind-sea dominated sea (III)	-0.028	0.014	0.069	-0.008
Mixed sea state (I)	0.095	-0.028	0.011	-0.002
Mixed sea state (II)	0.059	0.051	-0.023	-0.001
Mixed sea state (III)	0.050	0.058	0.032	-0.019
PM spectrum	0.161	-0.006	0.012	0.008
Present results				
$\beta = 10°$	0.281	0.084	0.035	0.014
$\beta = 20°$	0.290	0.086	0.029	0.007
$\beta = 30°$	0.302	0.093	0.040	0.018
$\beta = 40°$	0.307	0.084	0.026	0.004
Unidirectional	0.262	0.084	0.034	0.015

TABLE 10.3: Correlation coefficients between successive wave periods compared with previous results

Part VI

Conclusions

Chapter 11

Conclusions

Equipped with his five senses, man explores the universe around him and calls the adventure Science.

Edwin Powell Hubble

11.1 Clyde Sea

The main output of the project for the Clyde Sea is the hydrodynamic model itself: in the literature this is the first fully temperature and salinity resolving high-resolution model built specifically for the Clyde Sea and for their lochs.

The model was mainly used for hindcasting surge events, using historical recorded data from the tide gauges in the Clyde Sea, in particular from Millport. Our analysis of the historical tide gauge data showed that the highest water elevations in the Clyde Sea are recorded when spring astronomical high waters coincide with moderate to severe surge conditions, that usually occur during late Autumn-Winter period. Approximately 90 % of storm surges with residuals > 1 m were generated outside the Clyde Sea. The

storms generating those events usually follow a particular pattern, with the low pressure from the Atlantic moving to the north of mainland Scotland or further north, over the Orkneys or the Fair Isle Channel. Only 8.9% of storm surges exceeding 1 m can be explained by a low pressure over the Clyde or the North Channel.

The surge generation processes in the Clyde Sea contrasts with mechanisms in other semienclosed basins around the world. In the Adriatic Sea, for example, large surges (such as *acqua alta* events in Venice) are internally generated by Bora or Scirocco winds Orlić et al. (1994); Wakelin and Proctor (2002). Similarly, the majority of surges are internally generated in the Baltic Sea Suursaar and Sooäär (2007), and in the Mediterranean Sea itself Ullmann and Moron (2008). Other semienclosed basins, in fact, such as the bays in the west coast of US - are usually protected from surges from outside due to their complex coastline and bathymetry, such as Chesapeake Bay, and only very strong local winds can cause floods and large surges Li et al. (2006). However in all of these cases the extent of the basin is larger than that in the Clyde, the open ocean connecting channel is narrower and/or is oriented in the opposite direction to the climatological wind. The Clyde Sea is also a very particular semienclosed basin, if compared to the classification made by Pickard and Emery Pickard and Emery (1990); Cessi et al. (2014). All of these factors contribute to the peculiar surge climate of the Clyde Sea.

Our high-resolution model of the sealevel dynamics in the Clyde Sea shows that the surge wave from the open boundaries is enhanced by the funnelling effect of the sealochs and estuary in the northern Clyde Sea and by the steep bathymetry at the entrance of the semienclosed basin. In addition, the external surge is often exacerbated by the local field of wind and pressure.

Our results illustrate these phenomena in greater detail than has been possible with previous surge models of the region Townson and Donald (1985); Townson and Collar (1986); Kaya et al. (2005). The hindcasting of the three storms in the Clyde Sea during December 2011 corroborates the experience of coastal flooding patterns. In particular

the 28 December flooding event in the Inner Clyde was due to only a moderate surge wave, with residuals in Millport < 0.6 m, but this coincided with a spring high tide leading to an extreme total sealevel elevation.

A future, discussed, application of the Clyde Sea model presented in this thesis will be the operational stage, in collaboration with the Scottish Environmental Protection Agency. Another possible application could include the nesting of the model with a larger model such as the Scottish Shelf Model. In addition to this, some particle tracking run were carried out: this was in preparation for a larger project involving another Ph.D. student here in Strathclyde that is currently working on model output for studying the shellfish larvae dispersion in the Clyde Sea.

The model was also used for habitat predictions (Elliott et al.): in this case predicted velocities from the model were extracted in the locations were measurement of habitat and fish prevalence were available. Models outputs were then used to predict the habitat composition in the sea south to the Isle of Arran, in the Clyde Sea, giving good results, in particular in predicting seagrass and mud areas around Arran. These results, then, were applied to forecast the gadoid juvenile distribution for three species: Atlantic cod (*Gadus morhua*), haddock (*Melanogrammus aeglefinus*) and whiting (*Merlangius merlangus*).

For the stratification, the Simpson-Hunter number showed that not enough energy from the tides, wind and surge is available for the mixing of the water column in the Clyde Sea. However, the Simpson-Hunter number account only for the potential energy due by currents and not for the actual input given by the atmosphere for the heating. This is only a purely theoretical indication for the area that are likely to be fully mixed, but does not actually tell anything of the real stratification. Considering the distribution through the water column of the temperature and the density, is possible to see that the stratification does exist in all the year, and is stronger in Spring and in Summer. In Autumn, however, in the Clyde Sea, as also reported by previous study (Simpson and Rippeth, 1993; Rippeth and Simpson, 1996; Matthews et al., 1999), the stratification

become weaker and eventually the water column become mixed.

The main limitation of the model is that no gauged river inflow is available from the rivers in the sealochs, such as Loch Fyne. The flow of the freshwater is fundamental for the correct modelling of the stratification, in particular for fjordic areas (Gade and Edwards, 1980; Stigebrandt, 1981). A future development of the model will consider this flow from available hydrographic models that estimates the freshwater inflow from areas in which no river gauges is available.

The second limitation of the model are the waves. FVCOM has a wave module (Qi et al., 2009), that is derived from the SWAN model (Booij et al., 1996, 1999), that is similar to the MIKE 21 SW model for the governing equations and the calibration parameters. Some tests were made using the same grid as the tidal model for the set-up of a wave model for the Clyde Sea. However the model was extremely slow and presented some blows-up: a discussion with Hakeem Johnson (personal communication) from *CH2mHill*, that developed a FVCOM wave model for the Orkneys Island suggested to change the grid and reduce the resolution in order to eliminate the blow-up problem. This will be probably the next step for the development of the Clyde Sea model along with a improved freshwater input.

11.2 East coast of Scotland

The model for the east coast of Scotland was used for studying the wave-currents interactions in the area and the role of this interaction during storms, when both waves and currents are strong. The combination of spring tide, strong wind and high waves can be extremely threatening in coastal areas. The North Sea is one of the areas most affected by such events. Storms in the North Sea can generate extremely high waves as well as rogue waves.

Results indicate that wave-currents and wave-wave interactions play a fundamental role in the wave climate. The validation shows that the model performs reasonably

well during both calm periods and storms for waves, and also performs well for tides and surges.

During severe storms, in particular when the low pressure was over England and Scotland, it was found that the wave-current interactions (WCI) are significant, causing an increase, or decrease, in H_s that can exceed 2 m in some coastal areas, depending on the direction of the wave field compared to the current. A similar result was found for the peak spectral wave period: figure 4 shows that in the time period considered here the largest deviation of wave periods due to WCI is in the estuarine areas of the east coast, with average deviations more of than 1.2 s.

Wave propagation in the Firth of Forth from storms in the mid-North Sea is driven by trains of swell waves detaching from the open-sea storm. During the stormy periods considered here, the windsea waves in the Firth of Forth did not exceeded 3.5 m in the outer area of the estuary and 1 m in the inner part, while the swell field exceeded 5 m at the entrance of the Firth of Forth. In the inner Firth the swell waves have a similar magnitude to the windsea waves. Conversely, the area of the estuary of the Forth is mainly driven by locally generated waves. A similar behavior was noticed in the other two estuarine areas on the east coast: the Tay estuary and the Moray Firth.

The north-east coast of Scotland is more exposed to swell arriving from the North Atlantic and the Norwegian Sea, while the central and the southern part is more exposed to local windsea waves and to storms generated in the bulk of the North Sea.

Modelled 1D and directional 2D spectrum for coupled and uncoupled run were also compared: variations in the energy of the spectral peak were significant in particular for the extracted spectrum in the Aberdeen wave gauge, but also in other locations. In the Aberdeen wave gauge, in particular, the modelled energy density variations in the spectrum due to the wave-currents interactions were exceeding 20% around the peak spectrum frequency and a slight shift of the peak spectrum was also noticed. Some visual changes to the spectral bandwidth are seen in the different modelled spectrum,

in particular for the shallow water sites. Unfortunately, due to the lack of experimental observations of the spectrum, it was not possible to assess the performance of the model on the spectral components.

The model also has forecasting capabilities, in particular when nested with large scale models, such as the North Atlantic model (Venugopal and Nemalidinne, 2015, 2014). A limitation of the model is that the MIKE by DHI software does not allow an online coupling between waves and tides, slowing the simulation process. In fact, currents and waves are simulated by different modules and is not possible to perform a direct coupling. For this work the currents were simulated first and then the output were saved in order to use them as input for the wave model. Another limitation of the model, due to the one-way coupling, is that we cannot study the effect of the wave set-up and set-down on the surge water level (Longuet-Higgins and Stewart, 1962; Bowen et al., 1968). However, this can be implemented in the future, running first the wave model, then using the wave radiation in the hydrodynamic model, to estimate the enhancement of the water level due to waves near the shoreline.

This research also underlines the importance of high-resolution regional scale models for the understanding of sea dynamics and for the forecasting of dangerous sea states: larger models usually have inadequate resolution to estimate the effect of such processes near the coastline. Future work will be focused on the hindcasting of freakish wave state based on the estimation of the kurtosis from the parameters of the model (Janssen, 2003; Tamura et al., 2009; Ponce de León and Guedes Soares, 2014)

The output of the wave model and the current model were used also for building a numerical model for predicting sediment concentration and resuspension in the water column in the area of Stonehaven (Heath et al., 2015), in which data for several years were available (Serpetti et al., 2011, 2012; Serpetti, 2012). The model performed well compared to the observations in the area and accurately replicated the oscillation in concentration of the sediments in the water column in stormy period and also for the seasonal signal. The model then was used to see the effect of the energy extraction

from the water column (both waves and tides) on the sediments. The model predicted, as expected, a reduction of the sediment concentration in the water column when the tidal and the wave extraction was simulated. Results, however, suggested that only a strong reduction (about 50% of the tidal velocity in the area) of the tidal current due to the extraction of energy from the flow would have a significant effect on the sediment concentration, while the effect was less important for the waves. However, this model was only applied for the area of Stonehaven and not for other areas such as the Pentland Firth, in which the construction of tidal and wave devices is planned.

11.3 A critical comparison between MIKE and FVCOM

Two different hydrodynamic models were used for the researches reported in this thesis: the FVCOM, developed by the University of Massachussets-Darmouth and the MIKE developed by the Danish Hydrological Institute (DHI).

Despite both of the models being used to simulate the water and wave circulation in the ocean, these two models are very different for the simulation of the flow but in particular for the interface and for the pre- and post-processing. The FVCOM is a open-source code, written in FORTRAN 90/95. Little or no 'help desk' was available, but the documentation was satisfactory for the basic part (but very few documentation was available for the wave part), while MIKE by DHI had a help desk, that was extremely helpful for technical clarification during the research.

The pre-processing in MIKE was aided by a series of toolbox for the generation of the input files (that have to be in a specified file format): this was an obvious advantage, but was also a limitation, since the input files have to be in a format that is specific to the program. A MatLab toolbox was available also for the generation of the files. The pre-processing of the input file for the model in FVCOM was left to the user, however some files for helping the pre-processing were available from the GitHub of one of the

developers and from Pierre Cazenave, that were extremely useful to generate the netcdf input files required for the version 3.1 of FVCOM. In addition, the FVCOM input files were all in .dat or in netcdf format, that are extremely easy to handle. The same for the post-processing: the output from FVCOM were in netcdf, that is a common format for the geophysics and for the physics in general, and is a format easy to handle with both R and MatLab, both for reading and for writing. However, for the visualization of the output was necessary to develop some MatLab scripts. The MIKE toolbox were extremely useful for the visualization of the output, but the analysis was difficult, since for processing the output in figures, was necessary to pass from MIKE files (with a .dsfu format) to MatLab or R.

From a scientific point of view, FVCOM was easier to understand, since all the scientific documentation was completely available and the main code was available. This was not for MIKE, since the main code was not available. MIKE by DHI was a sort of 'black-box'. However, as shown in Chapter 6, throughout a careful calibration and validation, the results for both the water circulation and the waves were good and comparable to the FVCOM results.

11.4 Rogue waves

The large amount of experimental data collected in the 2011 experiment (Toffoli et al., 2011a), allowed us to do an in-depth investigation on the crossing sea state. In particular we focused on the wave heights, crests and periods statistics and in understanding how and why the previous experiment was seeing the growth of the kurtosis in the wavetank. The growth of the kurtosis during the propagation, for the modulational instability mechanism (Benjamin and Feir, 1967), is one of the most important proxy for the rogue wave presence (Onorato et al., 2002b; Janssen, 2003): the higher the kurtosis, the larger will be the probability of rogue wave occurrence. This theory is

well-known for a monochromatic sea state, when only one train of waves is present, in contrast the basis for crossing seas are more debated: the mechanism of rogue wave formation in crossing sea is not fully understood (Adcock and Taylor, 2014). The previous study on the data (Toffoli et al., 2011a), previous numerical simulations (Onorato et al., 2010) and theoretical studies (Onorato et al., 2006a) indicated that the modulational instability could be the main reason for enhanced rogue wave probability in crossing sea.

The reanalysis indicated that the experimental wave survival probability was higher than the Rayleigh survival probability, in particular for crossing sea angles $\beta > 30^{\circ}$ and effectively the probability of rogue waves exceed the linear theory. However, this probability is lower than the monochromatic case in the same spectral condition (Sabatino and Serio, 2015).

A successive analysis on the spectral bandwidth confirmed that the bandwidth was decreasing during the propagation of the wavetrain, leading the wave spectra to be more focused: this is the main mechanism of the modulational instability and another clue that the modulational instability could be one of the main mechanism for the rogue waves formation in crossing sea conditions in deep water.

The study confirms also that the deviation from linearity and the instabilities become larger for $\beta > 30^{\circ}$. This was also seen for the crests survival probability that was exceeding the second-order theoretical distribution.

The analysis of the period distributions showed no significant differences between angles. However, the main result on wave periods is that all the proposed theoretical distributions fail to predict the experimental distribution, since they overestimate or underestimate the tails of the distribution or the probability density around the peak of the distribution. Future studies should focus on the experimental investigation on angles higher than 40°, in order to find some analytical functional form linking the crossing sea angle and the Benjamim-Feir Index.

Part VII

Appendices

Chapter 12

Appendix

No		Lat	Lon	$H_s(o)$	$T_p(o)$	$H_s(c)$	$T_p(c)$	$H_s(u)$	$T_p(u)$
1W	1	57.85	-2.62	3.4	7.1	1.6	6.2	1.5	6.2
1W	2	57.91	-2.66	1.8	5.4	1.5	6.3	1.5	6.2
1W	3	57.96	-2.69	1.2	4.5	1.5	6.2	1.5	6.2
1W	4	58.02	-2.72	1.4	4.7	1.5	6.2	1.5	6.1
1W	5	58.08	-2.76	1.7	5.2	1.5	6.1	1.5	6.1
2W	6	57.91	-3.72	0.9	4.2	0.5	4.6	0.5	4.7
2W	7	57.95	-3.65	0.9	4.3	0.6	4.7	0.6	4.5
2W	8	57.98	-3.58	1.1	4.7	0.6	5	0.6	4.7
2W	9	58.02	-3.5	1	4.5	0.6	5.1	0.6	4.9
2W	10	58.05	-3.43	0.9	4.2	0.6	5.2	0.6	5.1
3W	11	58.08	-2.29	1.9	5.5	1.7	6.5	1.7	6.4
3W	12	58.04	-2.21	2	5.6	1.6	6.5	1.7	6.4
3W	13	58.01	-2.14	2.2	5.8	1.6	6.5	1.7	6.4
3W	14	57.97	-2.07	2.4	6	1.6	6.4	1.7	6.4
3W	15	57.94	-1.99	2.2	5.8	1.6	6.4	1.6	6.4
3W	16	57.9	-1.92	2.2	5.8	1.5	6.3	1.6	6.4

3W	17	57.87	-1.85	2	5.6	1.6	6.1	1.6	6.3
3W	18	57.83	-1.77	2.3	5.8	1.6	6	1.6	6.2
3W	19	57.8	-1.7	2.3	5.9	1.6	5.9	1.6	6.2
3W	20	57.76	-1.63	2.7	6.3	1.6	5.7	1.5	6
3W	21	57.73	-1.55	2.3	5.8	1.6	5.4	1.6	5.6
3W	22	57.69	-1.55	2.2	5.8	1.6	5.3	1.6	5.5
3W	23	57.66	-1.41	2.2	5.7	1.7	5	1.7	5
3W	24	57.62	-1.4	2.4	6	1.7	4.9	1.7	5
3W	25	57.58	-1.26	2.5	6.2	1.7	4.9	1.7	4.9
3W	26	57.55	-1.19	2.3	5.9	1.7	4.9	1.8	4.9
4W	27	55.78	-1.9	1.3	4.9	1.2	4.2	1.2	4.2
4W	28	55.84	-1.87	1.3	4.9	1.3	4.2	1.3	4.3
4W	29	55.89	-1.84	1.1	4.4	1.4	4.2	1.4	4.3
4W	30	55.95	-1.81	1.4	4.8	1.4	4.2	1.5	4.2
4W	31	56.01	-1.78	1.3	4.6	1.4	4.2	1.5	4.3
4W	32	56.06	-1.74	1.7	5.4	1.5	4.2	1.5	4.3
4W	33	56.12	-1.71	1.4	4.8	1.5	4.3	1.5	4.4
4W	34	56.17	-1.68	1.7	5.3	1.5	4.3	1.5	4.4
4W	35	56.23	-1.65	1.8	5.5	1.5	4.3	1.6	4.4
4W	36	56.29	-1.62	1.4	5	1.5	4.3	1.6	4.4
4W	37	56.34	-1.59	1.7	5.3	1.5	4.4	1.6	4.4
4W	38	56.4	-1.55	1.4	4.8	1.5	4.4	1.6	4.4
4W	39	56.46	-1.52	1.8	5.5	1.5	4.4	1.6	4.4
4W	40	56.51	-1.49	1.5	4.9	1.6	4.4	1.6	4.4
4W	41	56.57	-1.46	1.7	5.2	1.6	4.4	1.6	4.4
4W	42	56.62	-1.42	1.8	5.3	1.6	4.4	1.6	4.4
4W	43	56.68	-1.39	1.9	5.5	1.6	4.3	1.6	4.4
4W	44	56.74	-1.36	1.9	5.4	1.6	4.4	1.6	4.3

4W	45	56.79	-1.32	1.9	5.4	1.6	4.4	1.6	4.3
4W	46	56.85	-1.29	1.8	5.3	1.6	4.4	1.6	4.3
4W	47	56.91	-1.26	1.8	5.4	1.6	4.4	1.6	4.4
5W	48	57.76	-2.18	1.1	4.4	1.1	5.5	1.2	5.7
5W	49	57.82	-2.15	1.7	5.5	1.5	5.9	1.5	6.1
5W	50	57.87	-2.12	2	5.9	1.7	6.3	1.7	6.5
5W	51	57.93	-2.08	1.9	5.6	1.9	6.6	1.9	6.7
5W	52	57.98	-2.05	2.3	6.1	2	6.8	2	6.9
5W	53	58.04	-2.01	2.7	6.7	2.1	6.9	2.1	7
5W	54	58.1	-1.98	2.5	6.3	2.1	7	2.1	7.1
5W	55	58.15	-1.94	2.6	6.3	2.2	7	2.2	7.1
6W	56	57.74	-3.63	0.9	4.2	1	4.8	1	4.8
6W	57	57.79	-3.6	0.9	4.1	1.2	5.1	1.1	5.1
6W	58	57.85	-3.56	1.1	4.4	1.2	5.2	1.2	5.3
6W	59	57.91	-3.53	0.8	3.8	1.2	5.3	1.2	5.3
6W	60	57.96	-3.49	0.8	3.8	1.2	5.3	1.2	5.4
6W	61	58.02	-3.46	1	4.2	1.2	5.3	1.2	5.3
7W	62	55.97	-1.76	1.6	5.3	1.5	5.2	1.5	5.2
7W	63	56.01	-1.69	1.3	4.9	1.6	5.3	1.6	5.2
7W	64	56.05	-1.63	1.5	5.2	1.6	5.3	1.6	5.3
7W	65	56.09	-1.56	1.3	4.9	1.6	5.3	1.7	5.3
7W	66	56.12	-1.49	1.6	5.4	1.6	5.3	1.7	5.3
7W	67	56.16	-1.43	1.3	4.9	1.7	5.3	1.7	5.3
7W	68	56.24	-1.29	1.4	5.1	1.7	5.2	1.7	5.2
7W	69	56.27	-1.23	2	5.8	1.7	5.2	1.7	5.3
7W	70	56.31	-1.16	2.1	6	1.7	5.2	1.7	5.3
7W	71	56.35	-1.09	2	5.8	1.7	5.2	1.7	5.3
7W	72	56.38	-1.03	2.2	6.2	1.7	5.2	1.7	5.3

7W	73	56.42	-0.96	2.1	6	1.7	5.3	1.7	5.3
7W	74	56.46	-0.88	1.8	5.6	1.7	5.3	1.8	5.3
7W	75	56.49	-0.82	1.6	5.3	1.8	5.4	1.8	5.4
7W	76	56.53	-0.76	1.9	5.7	1.8	5.4	1.8	5.4
7W	77	56.57	-0.69	1.5	5.1	1.8	5.4	1.8	5.5
7W	78	56.61	-0.62	1.5	5.2	1.8	5.4	1.8	5.5
7W	79	56.64	-0.55	2.2	6	1.8	5.4	1.8	5.5
7W	80	56.68	-0.48	2.6	6.6	1.8	5.4	1.8	5.4
7W	81	56.72	-0.41	1.5	5.1	1.8	5.4	1.8	5.4
7W	82	56.75	-0.35	1.5	5.2	1.8	5.4	1.8	5.4

TABLE 12.1: Winter satellite validation: (o) are the observed data, (c) is the coupled model, (u) is the uncoupled model and No corresponds to the observation reported in Table S2

No		Lat	Lon	$H_s(o)$	$T_p(o)$	$H_s(c)$	$T_p(c)$	$H_s(u)$	$T_p(u)$
1S	1	56.1	-2.45	0.8	4	1	5.3	1.1	5.5
1S	2	56.16	-2.42	1	4.5	1.1	5.3	1.2	5.5
1S	3	56.21	-2.39	0.8	4	1.1	5.3	1.2	5.4
1S	4	56.27	-2.35	1.1	4.6	1.1	5.2	1.2	5.4
1S	5	56.33	-2.32	1	4.6	1.1	5.2	1.2	5.4
1S	6	56.38	-2.29	0.9	4.3	1.1	5.2	1.2	5.4
1S	7	56.44	-2.26	0.9	4.3	1.1	5.2	1.2	5.4
1S	8	56.49	-2.23	0.8	3.9	1.2	5.2	1.2	5.4
1S	9	56.55	-2.19	0.8	4	1.2	5.3	1.2	5.4
1S	10	56.61	-2.16	0.8	4.1	1.2	5.3	1.2	5.4
1S	11	56.66	-2.13	0.9	4.1	1.2	5.4	1.2	5.5
1S	12	56.72	-2.1	0.9	4.1	1.2	5.4	1.2	5.5
1S	13	56.78	-2.06	1	4.4	1.3	5.3	1.2	5.4
1S	14	56.83	-2.03	1.1	4.6	1.3	5.3	1.2	5.4

1S	15	56.89	-2	1	4.3	1.2	5.3	1.2	5.4
1S	16	56.95	-1.96	1.3	4.9	1.2	5.3	1.2	5.3
1S	17	57	-1.93	1.3	5	1.3	5.4	1.2	5.3
1S	18	57.06	-1.9	1.2	4.7	1.3	5.4	1.2	5.3
1S	19	57.11	-1.86	1.1	4.7	1.3	5.4	1.2	5.3
1S	20	57.17	-1.83	1.2	4.8	1.3	5.4	1.2	5.3
1S	21	57.23	-1.8	1.3	4.9	1.3	5.3	1.2	5.3
1S	22	57.28	-1.76	1.3	5	1.4	5.4	1.3	5.4
1S	23	57.34	-1.73	1.3	5	1.5	5.6	1.4	5.5
1S	24	57.39	-1.7	1.7	5.7	1.5	5.7	1.4	5.7
1S	25	57.45	-1.66	1.2	4.8	1.6	5.9	1.5	5.8
1S	26	57.51	-1.63	1.6	5.5	1.7	6	1.6	6
1S	27	57.56	-1.59	1.4	5.2	1.8	6.1	1.7	6.1
2S	28	57.6	-1.51	0.8	4	0.9	6.7	0.9	6.7
2S	29	57.64	-1.44	0.8	4	0.9	6.7	0.9	6.7
2S	30	57.67	-1.37	1	4.5	0.9	6.6	0.9	6.6
2S	31	57.71	-1.29	1.1	4.8	0.9	6.6	0.9	6.6
2S	32	57.74	-1.22	1.5	5.5	0.9	6.6	0.9	6.6
2S	33	57.78	-1.15	1	4.4	0.9	6.6	0.9	6.6
2S	34	57.82	-1.08	1	4.6	0.9	6.6	0.9	6.6
2S	35	57.85	-1	1.2	4.9	0.9	6.6	0.9	6.5
2S	36	57.89	-0.93	1.2	4.9	0.9	6.5	0.9	6.5
2S	37	57.92	-0.86	1.4	5.3	0.9	6.5	0.9	6.5
2S	38	57.96	-0.78	1.2	4.8	0.8	6.5	0.8	6.5
2S	39	57.99	-0.71	1.3	5	0.8	6.5	0.8	6.4
2S	40	58.03	-0.64	1.1	4.6	0.8	6.4	0.8	6.4
2S	41	58.06	-0.56	1.4	5.2	0.8	6.4	0.8	6.4
2S	42	58.1	-0.49	1.2	4.9	0.8	6.4	0.8	6.4

3S	43	55.88	-1.91	1.8	5.7	1.5	5.3	1.5	5.3
3S	44	55.92	-1.84	1.5	5.3	1.5	5.2	1.5	5.2
3S	45	55.96	-1.77	1.7	5.6	1.5	5.1	1.5	5.2
3S	46	56	-1.71	1.9	6	1.5	5.1	1.5	5.2
3S	47	56.03	-1.64	1.7	5.6	1.5	5.1	1.6	5.2
3S	48	56.07	-1.58	1.8	5.8	1.6	5.1	1.6	5.1
3S	49	56.11	-1.51	2	6	1.6	5.1	1.6	5.1
3S	50	56.15	-1.44	1.8	5.7	1.6	5.1	1.6	5.1
3S	51	56.18	-1.38	1.7	5.5	1.6	5.1	1.6	5.1
3S	52	56.22	-1.31	2	6	1.6	5.1	1.6	5.1
3S	53	56.26	-1.25	1.7	5.6	1.6	5.1	1.6	5.1
3S	54	56.29	-1.18	1.9	5.9	1.6	5.1	1.6	5.1
3S	55	56.33	-1.11	1.6	5.5	1.6	5	1.6	5.1
3S	56	56.37	-1.04	1.9	5.9	1.6	5	1.6	5
3S	57	56.41	-0.98	1.6	5.4	1.6	5	1.6	5
3S	58	56.44	-0.91	1.7	5.6	1.6	5	1.6	5
3S	59	56.48	-0.84	1.6	5.4	1.6	5	1.6	5
3S	60	56.62	-0.77	1.5	5.3	1.6	5	1.6	4.9
3S	61	56.65	-0.71	1.6	5.4	1.6	5	1.6	4.9
4S	62	56.64	-2.27	1.4	5.1	1	4	1	4
4S	63	56.6	-2.21	1.4	5.2	1	4	1	4
4S	64	56.56	-2.14	1.6	5.4	1.1	4	1.1	4
4S	65	56.53	-2.07	1.4	5.1	1.1	4	1.1	4
4S	66	56.49	-2	1.6	5.3	1.2	4	1.2	4
4S	67	56.45	-1.94	1.6	5.3	1.2	4.1	1.2	4
4S	68	56.41	-1.87	1.5	5.2	1.2	4.1	1.2	4.1
4S	69	56.38	-1.8	1.9	5.8	1.3	4.2	1.3	4.1
4S	70	56.34	-1.73	1.9	5.8	1.4	4.3	1.4	4.3

4S	71	56.3	-1.67	1.7	5.4	1.4	4.3	1.4	4.3
4S	72	56.27	-1.6	2	5.9	1.5	4.3	1.5	4.3
4S	73	56.23	-1.53	1.8	5.6	1.5	4.4	1.5	4.4
4S	74	56.19	-1.47	2	6	1.5	4.4	1.5	4.4
4S	75	56.15	-1.4	2.1	6.1	1.5	4.4	1.5	4.4
4S	76	56.12	-1.33	2.1	6	1.5	4.4	1.5	4.4
4S	77	56.08	-1.27	1.8	5.6	1.5	4.4	1.5	4.4
4S	78	56.04	-1.2	1.9	5.8	1.6	4.4	1.5	4.4
4S	79	56	-1.13	1.8	5.7	1.6	4.4	1.6	4.4
4S	80	55.97	-1.07	2.1	6	1.6	4.5	1.6	4.4
4S	81	55.93	-1	1.6	5.3	1.6	4.5	1.6	4.4
4S	82	55.89	-0.94	1.7	5.5	1.6	4.5	1.6	4.4

TABLE 12.2: Spring satellite validation: (o) are the observed data, (c) is the coupled model, (u) is the uncoupled model and No corresponds to the observation reported in Table S2

Date	Description
05/12/1985	Low pressure minimum over Central, North, West Scotland coastline
20/03/1986	Low pressure minimum over Central, North, West Scotland coastline
30/10/1986	Low pressure minimum west Orkneys, over Orkneys or over Fair Isle Channel
22/11/1986	Low pressure minimum west Orkneys, over Orkneys or over Fair Isle Channel
12/12/1986	Low pressure minimum in the North Atlantic open sea
15/12/1986	Low pressure minimum in the North Atlantic open sea

27/03/1987	Low pressure minimum over Ireland, North Channel, Clyde sea or South of Scotland
12/01/1988	Low pressure minimum in the North Atlantic open sea
01/02/1988	Low pressure minimum over Ireland, North Channel, Clyde sea or South of Scotland
09/02/1988	Low pressure minimum over Central, North, West Scotland coastline
25/07/1988	Low pressure minimum west Orkneys, over Orkneys or over Fair Isle Channel
10/08/1988	Low pressure minimum in the North Atlantic open sea
16/12/1989	Low pressure minimum over Ireland, North Channel, Clyde sea or South of Scotland
24/12/1989	Low pressure minimum in the North Atlantic open sea
25/12/1990	Low pressure minimum west Orkneys, over Orkneys or over Fair Isle Channel
01/01/1991	Low pressure minimum in the North Atlantic open sea
05/01/1991	Low pressure minimum over Central, North, West Scotland coastline
12/11/1991	Low pressure minimum in the North Atlantic open sea
18/12/1992	Low pressure minimum west Orkneys, over Orkneys or over Fair Isle Channel
10/01/1993	Low pressure minimum in the North Atlantic open sea

10/01/1993	Low pressure minimum west Orkneys, over Orkneys or over Fair Isle Channel
21-22/01/1993	Low pressure minimum west Orkneys, over Orkneys or over Fair Isle Channel
23/01/1993	Low pressure minimum west Orkneys, over Orkneys or over Fair Isle Channel
18/05/1993	Low pressure minimum over Ireland, North Channel, Clyde sea or South of Scotland
30/03/1994	Low pressure minimum in the North Atlantic open sea
07/12/1994	Low pressure minimum west Orkneys, over Orkneys or over Fair Isle Channel
08/12/1994	Low pressure minimum in the North Atlantic open sea
17/01/1995	Low pressure minimum in the North Atlantic open sea
18/01/1995	Low pressure minimum over Central, North, West Scotland coastline
21/01/1995	Low pressure minimum over Central, North, West Scotland coastline
30/07/1996	Low pressure minimum in the North Atlantic open sea
06/11/1996	Low pressure minimum over Central, North, West Scotland coastline
18/02/1997	Low pressure minimum in the North Atlantic open sea
19/02/1997	Low pressure minimum in the North Atlantic open sea

24/02/1997	Low pressure minimum over Central, North, West Scotland coastline
24/12/1997	Low pressure minimum over Central, North, West Scotland coastline
09/11/1998	Low pressure minimum over Central, North, West Scotland coastline
26/12/1998	Low pressure minimum west Orkneys, over Orkneys or over Fair Isle Channel
30/12/1998	Low pressure minimum in the North Atlantic open sea
15/01/1999	Low pressure minimum west Orkneys, over Orkneys or over Fair Isle Channel
08/12/1999	Low pressure minimum over Central, North, West Scotland coastline
23/12/1999	Low pressure minimum in the North Atlantic open sea
25/12/1999	Low pressure minimum west Orkneys, over Orkneys or over Fair Isle Channel
06/02/2000	Low pressure minimum in the North Atlantic open sea
10/02/2000	Low pressure minimum in the North Atlantic open sea
28/10/2000	Low pressure minimum west Orkneys, over Orkneys or over Fair Isle Channel
29/11/2000	Low pressure minimum west Orkneys, over Orkneys or over Fair Isle Channel
31/12/2000	Low pressure minimum in the North Atlantic open sea

06/02/2001	Low pressure minimum over Ireland, North Channel, Clyde sea or South of Scotland
28/01/2002	Low pressure minimum over Central, North, West Scotland coastline
01/02/2002	Low pressure minimum in the North Atlantic open sea
03/02/2002	Low pressure minimum west Orkneys, over Orkneys or over Fair Isle Channel
10/03/2002	Low pressure minimum west Orkneys, over Orkneys or over Fair Isle Channel
01/01/2004	Low pressure minimum west Orkneys, over Orkneys or over Fair Isle Channel
08/01/2005	Low pressure minimum over Ireland, North Channel, Clyde sea or South of Scotland
11/01/2005	Low pressure minimum west Orkneys, over Orkneys or over Fair Isle Channel
07/11/2005	Low pressure minimum west Orkneys, over Orkneys or over Fair Isle Channel
11/11/2005	Low pressure minimum west Orkneys, over Orkneys or over Fair Isle Channel
19/11/2006	Low pressure minimum west Orkneys, over Orkneys or over Fair Isle Channel
27/11/2006	Low pressure minimum in the North Atlantic open sea
30/11/2006	Low pressure minimum in the North Atlantic open sea
03/12/2006	Low pressure minimum west Orkneys, over Orkneys or over Fair Isle Channel

29/12/2006	Low pressure minimum in the North Atlantic open sea
31/12/2006	Low pressure minimum over North Sea
11/01/2007	Low pressure minimum west Orkneys, over Orkneys or over Fair Isle Channel
18/01/2007	Low pressure minimum west Orkneys, over Orkneys or over Fair Isle Channel
05/03/2007	Low pressure minimum west Orkneys, over Orkneys or over Fair Isle Channel
08-09/01/2008	Low pressure minimum over Central, North, West Scotland coastline
17/01/2009	Low pressure minimum west Orkneys, over Orkneys or over Fair Isle Channel
22/11/2009	Low pressure minimum over Central, North, West Scotland coastline
25/11/2009	Low pressure minimum west Orkneys, over Orkneys or over Fair Isle Channel
11/11/2010	Low pressure minimum over North Sea
11/11/2010	Low pressure minimum over Central, North, West Scotland coastline
23/05/2011	Low pressure minimum west Orkneys, over Orkneys or over Fair Isle Channel
12/09/2011	Low pressure minimum in the North Atlantic open sea
28/11/2011	Low pressure minimum in the North Atlantic open sea
08-09/12/2011	Low pressure minimum west Orkneys, over Orkneys or over Fair Isle Channel

13/12/2011	Low pressure minimum over Central, North, West Scotland coastline
16/12/2011	Low pressure minimum over Central, North, West Scotland coastline
03/01/2012	Low pressure minimum over Central, North, West Scotland coastline
31/01/2013	Low pressure minimum over Central, North, West Scotland coastline
19/12/2013	Low pressure minimum west Orkneys, over Orkneys or over Fair Isle Channel
24/12/2013	Low pressure minimum over Central, North, West Scotland coastline
24-25/12/2013	Low pressure minimum west Orkneys, over Orkneys or over Fair Isle Channel
27/12/2013	Low pressure minimum over Ireland, North Channel, Clyde sea or South of Scotland
03/01/2014	Low pressure minimum over Central, North, West Scotland coastline
26/01/2014	Low pressure minimum over Central, North, West Scotland coastline
08/02/2014	Low pressure minimum over Ireland, North Channel, Clyde sea or South of Scotland
12/02/2014	Low pressure minimum west Orkneys, over Orkneys or over Fair Isle Channel
02/03/2014	Low pressure minimum over Central, North, West Scotland coastline
02/07/2014	Low pressure minimum in the North Atlantic open sea

06/10/2014	Low pressure minimum over Central, North, West Scotland coastline

TABLE 12.3: Storm surges considered in the statistical analysis

Bibliography

T. A. Adcock and P. H. Taylor. The physics of anomalous (rogue) ocean waves. *Reports on Progress in Physics*, 77(10):105901, 2014.

G. Airy. Article tides and waves? *Encyclopaedia metropolitana*, 1845.

O. Andersen. Shallow water tidal determination from altimetry-the M 4 constituent. *Bollettino di Geofisica Teorica ed Applicata*, 40(3-4):427–437, 1999.

O. B. Andersen. The M4 shallow water tidal constituent from altimetry and tide gauges. In *Satellite altimetry for geodesy, geophysics and oceanography*, pages 231–235. Springer, 2004.

D. Andrews and M. McIntyre. On wave-action and its relatives. *J. Fluid Mech*, 89(04): 647–664, 1978.

M. Arhan and R. Ezraty. Statistical relations between successive wave heights. *Oceanol. Acta*, 1:151–158, 1978.

T. Ball, A. Edwards, and A. Werritty. Coastal flooding in Scotland: towards national-level hazard assessment. *Natural hazards*, 70(2):1133–1152, 2014.

J. Battjes. Surf similarity. *Coastal Engineering Proceedings*, 1(14), 1974.

J. Battjes and J. Janssen. Energy loss and set-up due to breaking of random waves. *Coastal Engineering Proceedings*, 1(16), 1978.

J. Battjes and M. Stive. Calibration and verification of a dissipation model for random breaking waves. *Journal of Geophysical Research: Oceans (1978–2012)*, 90(C5): 9159–9167, 1985.

A. Baxevani and I. Rychlik. Maxima for gaussian seas. *Ocean Engineering*, 33(7):895–911, 2006.

P. J. Baxter. The east coast big flood, 31 january–1 february 1953: a summary of the human disaster. *Philosophical Transactions of the Royal Society of London A: Mathematical, Physical and Engineering Sciences*, 363(1831):1293–1312, 2005.

A. Benetazzo, S. Carniel, M. Sclavo, and A. Bergamasco. Wave–current interaction: Effect on the wave field in a semi-enclosed basin. *Ocean Modelling*, 70:152–165, 2013.

T. B. Benjamin. Internal waves of permanent form in fluids of great depth. *Journal of Fluid Mechanics*, 29(03):559–592, 1967.

T. B. Benjamin and J. Feir. The disintegration of wave trains on deep water part 1. theory. *Journal of Fluid Mechanics*, 27(03):417–430, 1967.

P. Berrisford, P. Kållberg, S. Kobayashi, D. Dee, S. Uppala, A. Simmons, P. Poli, and H. Sato. Atmospheric conservation properties in era-interim. *Quarterly Journal of the Royal Meteorological Society*, 137(659):1381–1399, 2011.

T. Bishop and T. Ulrych. Maximum entropy spectral analysis and autoregressive decomposition. *Rev. geophys. space Phys*, 13:183–200, 1975.

N. Booij, L. Holthuijsen, and R. Ris. The" swan" wave model for shallow water. *Coastal Engineering Proceedings*, 1(25), 1996.

N. Booij, R. Ris, and L. H. Holthuijsen. A third-generation wave model for coastal regions: 1. model description and validation. *Journal of geophysical research: Oceans*, 104(C4):7649–7666, 1999.

J. D. Boon. *Secrets of the tide: tide and tidal current analysis and predictions, storm surges and sea level trends*. Elsevier, 2013.

A. J. Bowen, D. L. Inman, and V. P. Simmons. Wave set-down and set-up. *Journal of Geophysical Research*, 73(8):2569–2577, 1968. ISSN 2156-2202. doi: 10.1029/JB073i008p02569. URL `http://dx.doi.org/10.1029/JB073i008p02569`.

D. Bowers, R. Macdonald, D. McKee, W. Nimmo-Smith, and G. Graham. On the formation of tide-produced seiches and double high waters in coastal seas. *Estuarine, Coastal and Shelf Science*, 134:108–116, 2013.

F. P. Bretherton and C. J. Garrett. Wavetrains in inhomogeneous moving media. *Proceedings of the Royal Society of London. Series A. Mathematical and Physical Sciences*, 302(1471):529–554, 1968.

C. L. Bretschneider. Wave variability and wave spectra for wind-generated gravity waves. Technical report, DTIC Document, 1959.

P. A. Brodtkorb, P. Johannesson, G. Lindgren, I. Rychlik, J. Rydén, E. Sjö, et al. WAFO-a Matlab toolbox for analysis of random waves and loads. In *The Tenth International Offshore and Polar Engineering Conference*. International Society of Offshore and Polar Engineers, 2000.

J. P. Burg. Maximum entropy spectral analysis. In *37th Annual International Meeting*. Society of Exploration Geophysics, 1967.

A. Callaway, R. Quinn, C. J. Brown, M. Service, and S. Benetti. Trace metal contamination of Beauforts Dyke, North Channel, Irish Sea: A legacy of ordnance disposal. *Marine pollution bulletin*, 62(11):2345–2355, 2011a.

A. Callaway, R. Quinn, C. J. Brown, M. Service, D. Long, and S. Benetti. The formation and evolution of an isolated submarine valley in the North Channel, Irish Sea: an investigation of Beaufort's Dyke. *Journal of Quaternary Science*, 26(4):362–373, 2011b.

D. Cartwright and A. C. Edden. Corrected tables of tidal harmonics. *Geophysical Journal International*, 33(3):253–264, 1973.

D. Cartwright and M. S. Longuet-Higgins. The statistical distribution of the maxima of a random function. In *Proceedings of the Royal Society of London A: Mathematical, Physical and Engineering Sciences*, volume 237, pages 212–232. The Royal Society, 1956.

D. Cartwright and R. Tayler. New computations of the tide-generating potential. *Geophysical Journal International*, 23(1):45–73, 1971.

L. Cavaleri, L. Bertotti, L. Torrisi, E. Bitner-Gregersen, M. Serio, and M. Onorato. Rogue waves in crossing seas: the louis majesty accident. *Journal of Geophysical Research: Oceans (1978–2012)*, 117(C11), 2012.

A. Cavanie, X. Arhan, and X. Ezraty. A statistical relationship between individual heights and periods of storm waves. 1976.

P. Cessi, N. Pinardi, and V. Lyubartsev. Energetics of semienclosed basins with two-layer flows at the strait. *Journal of Physical Oceanography*, 44(3):967–979, 2014.

C. Chen, H. Liu, and R. C. Beardsley. An unstructured grid, finite-volume, three-dimensional, primitive equations ocean model: application to coastal ocean and estuaries. *Journal of atmospheric and oceanic technology*, 20(1):159–186, 2003.

C. Chen, R. C. Beardsley, and G. Cowles. An unstructured grid, finite-volume coastal ocean model (FVCOM) system. *OCEANOGRAPHY-WASHINGTON DC-OCEANOGRAPHY SOCIETY-*, 19(1):78, 2006a.

C. Chen, G. Cowles, and R. Beardsley. An unstructured grid, finite-volume coastal ocean model: FVCOM user manual. *SMAST/UMASSD*, 2006b.

P. Clark and E. Connolly. Operational use of a grid-based model for flood forecasting. *Proceedings of the Institution of Civil Engineers*, 165(2):65, 2012.

D. L. Codiga. *Unified tidal analysis and prediction using the UTide Matlab functions*. Graduate School of Oceanography, University of Rhode Island Narragansett, RI, 2011.

J. I. Collins. Prediction of shallow-water spectra. *Journal of Geophysical Research*, 77 (15):2693–2707, 1972.

F. Cottier, M. Inall, and C. Griffiths. Seasonal variations in internal wave energy in a Scottish sea loch. *Ocean Dynamics*, 54(3-4):340–347, 2004.

G. W. Cowles. Parallelization of the FVCOM coastal ocean model. *International Journal of High Performance Computing Applications*, 22(2):177–193, 2008.

G. H. Darwin. On the secular changes in the elements of the orbit of a satellite revolving about a tidally distorted planet. *Philosophical Transactions of the Royal Society of London*, 171:713–891, 1880.

J. Dattatri, H. Raman, and N. Jothishankar. Wave groups: analysis of run and run length. In *Proceedings of the 6th Australasian Hydraulics Fluid Mechanics Conference, Adelaide*, pages 64–67, 1977.

A. M. Davies and P. Hall. The sensitivity of tidal current profiles in the North Channel of the Irish Sea to the parameterization of momentum diffusion. *Continental shelf research*, 18(2):357–404, 1998.

A. M. Davies and P. Hall. The response of the north channel of the irish sea and clyde sea to wind forcing. *Continental Shelf Research*, 20(8):897–940, 2000.

A. M. Davies, P. Hall, M. J. Howarth, P. Knight, and R. Player. A detailed comparison of measured and modeled wind-driven currents in the North Channel of the Irish Sea. *Journal of Geophysical Research: Oceans (1978–2012)*, 106(C9):19683–19713, 2001a.

A. M. Davies, P. Hall, M. J. Howarth, P. J. Knight, and R. J. Player. Comparison of observed (hf radar and adcp measurements) and computed tides in the north channel of the irish sea. *Journal of physical oceanography*, 31(7):1764–1785, 2001b.

A. M. Davies, P. Hall, M. J. Howarth, P. J. Knight, and R. J. Player. Tidal currents, energy flux and bottom boundary layer thickness in the Clyde Sea and North Channel of the Irish Sea. *Ocean Dynamics*, 54(2):108–125, 2004.

R. E. Davis and A. Acrivos. Solitary internal waves in deep water. *Journal of Fluid Mechanics*, 29(03):593–607, 1967.

D. Dee, S. Uppala, A. Simmons, P. Berrisford, P. Poli, S. Kobayashi, U. Andrae, M. Balmaseda, G. Balsamo, P. Bauer, et al. The ERA-Interim reanalysis: Configuration and performance of the data assimilation system. *Quarterly Journal of the Royal Meteorological Society*, 137(656):553–597, 2011.

DHI. *MIKE 3 Hydrodynamics User Manual*, volume 1. 2011a.

DHI. *MIKE 21 Wave modelling User Manual*, volume 1. 2011b.

G. Dietrich. Die natürlichen Regionen von Nord-und Ostsee auf hydrographischer Grundlage. *Kieler Meeresforsch*, 7(2):35–69, 1950.

M. A. Donelan, J. Hamilton, and W. Hui. Directional spectra of wind-generated waves. *Philosophical Transactions of the Royal Society of London A: Mathematical, Physical and Engineering Sciences*, 315(1534):509–562, 1985.

A. T. Doodson. The harmonic development of the tide-generating potential. *Proceedings of the Royal Society of London. Series A, Containing Papers of a Mathematical and Physical Character*, pages 305–329, 1921.

A. T. Doodson and H. D. Warburg. *Admiralty manual of tides*. HM Stationery Office, 1941.

H. Dooley. Factors influencing water movements in the Firth of Clyde. *Estuarine and Coastal Marine Science*, 9(5):631–641, 1979.

L. Draper. Freak ocean waves. *Weather*, 21(1):2–4, 1966.

W. M. Drennan, H. C. Graber, D. Hauser, and C. Quentin. On the wave age dependence of wind stress over pure wind seas. *Journal of Geophysical Research: Oceans (1978–2012)*, 108(C3), 2003.

K. Dysthe, H. E. Krogstad, and P. Müller. Oceanic rogue waves. *Annu. Rev. Fluid Mech.*, 40:287–310, 2008.

K. B. Dysthe, K. Trulsen, H. E. Krogstad, and H. Socquet-Juglard. Evolution of a narrow-band spectrum of random surface gravity waves. *Journal of Fluid Mechanics*, 478: 1–10, 2003.

M. Earle. Development of algorithms for separation of sea and swell. *National Data Buoy Center Tech Rep MEC-87-1, Hancock County*, 53, 1984.

A. Edwards, M. Baxter, D. Ellett, J. Martin, D. Meldrum, and C. Griffiths. Clyde sea hydrography. *Proceedings of the Royal Society of Edinburgh. Section B. Biological Sciences*, 90:67–83, 1986.

K. Edwards, R. Barciela, and M. Butenschon. Validation of the nemo-ersem operational ecosystem model for the north west european continental shelf. *Ocean Science*, 8: 983–1000, 2012.

G. D. Egbert, S. Y. Erofeeva, and R. D. Ray. Assimilation of altimetry data for non-linear shallow-water tides: Quarter-diurnal tides of the Northwest European Shelf. *Continental Shelf Research*, 30(6):668–679, 2010.

V. W. Ekman. *Om jordrotationens inverkan på vindströmmar i hafvet...* Centraltryck, 1902.

B. Eliasson and P. K. Shukla. Numerical investigation of the instability and nonlinear evolution of narrow-band directional ocean waves. *Physical review letters*, 105(1): 014501, 2010.

S. A. Elliott, A. D. Sabatino, M. R. Heath, W. R. Turrell, and D. M. Bailey. Predictive substratum modelling for juvenile gadoid distribution and abundance.

K. C. Ewans. Observations of the directional spectrum of fetch-limited waves. *Journal of Physical Oceanography*, 28(3):495–512, 1998.

C. L. Fefferman. Existence and smoothness of the navier-stokes equation. *The millennium prize problems*, pages 57–67, 2000.

J. H. Ferziger and M. Perić. *Computational methods for fluid dynamics*, volume 3. Springer Berlin, 2002.

R. Fisher, M. Jantsch, R. Comer, et al. General Bathymetric chart of the Oceans (GEBCO). *Canadian Hydrographic Service, Ottawa, Canada*, 1982.

R. Flather. Estimates of extreme conditions of tide and surge using a numerical model of the north-west European continental shelf. *Estuarine, Coastal and Shelf Science*, 24 (1):69–93, 1987.

R. A. Flather. A numerical model investigation of the storm surge of 31 january and 1 february 1953 in the north sea. *Quarterly Journal of the Royal Meteorological Society*, 110(465):591–612, 1984.

M. G. G. Foreman. *Manual for tidal heights analysis and prediction*. Institute of Ocean Sciences, Patricia Bay, 1979.

G. Forristall. On the statistical distribution of wave heights in a storm. *Journal of Geophysical Research: Oceans (1978–2012)*, 83(C5):2353–2358, 1978.

H. Gade and A. Edwards. Deep water renewal in fjords. In *Fjord oceanography*, pages 453–489. Springer, 1980.

B. Galperin, L. Kantha, S. Hassid, and A. Rosati. A quasi-equilibrium turbulent energy model for geophysical flows. *Journal of the Atmospheric Sciences*, 45(1):55–62, 1988.

C. Garrett and W. Munk. Space-time scales of internal waves. *Geophysical & Astrophysical Fluid Dynamics*, 3(1):225–264, 1972.

C. Garrett and W. Munk. Space-time scales of internal waves: A progress report. *Journal of Geophysical Research*, 80(3):291–297, 1975.

C. Garrett, J. Keeley, and D. Greenberg. Tidal mixing versus thermal stratification in the Bay of Fundy and Gulf of Maine. *Atmosphere-Ocean*, 16(4):403–423, 1978.

H. Gerritsen. What happened in 1953? the big flood in the netherlands in retrospect. *Philosophical Transactions of the Royal Society of London A: Mathematical, Physical and Engineering Sciences*, 363(1831):1271–1291, 2005.

B. Gjevik and T. Straume. Model simulations of the M2 and the K1 tide in the Nordic Seas and the Arctic Ocean. *Tellus A*, 41(1):73–96, 1989.

Y. Goda. Numerical experiments on wave statistics with spectral simulation. *Report of the Port and Harbour Research Institute*, 9(3):3–57, 1970.

Y. Goda. Analysis of wave grouping and spectra of long-travelled swell. *Rep. Port Harbour Res. Inst*, 22(1):3–41, 1983.

E. Gold. Lewis fry richardson. 1881-1953. *Obituary Notices of Fellows of the Royal Society*, pages 217–235, 1954.

C. Gommenginger, M. Srokosz, P. Challenor, and P. Cotton. Measuring ocean wave period with satellite altimeters: A simple empirical model. *Geophysical Research Letters*, 30(22), 2003.

I. Grabemann and R. Weisse. Climate change impact on extreme wave conditions in the north sea: an ensemble study. *Ocean Dynamics*, 58(3-4):199–212, 2008.

O. Gramstad and K. Trulsen. Influence of crest and group length on the occurrence of freak waves. *Journal of Fluid Mechanics*, 582:463–472, 2007.

W. D. Grant and O. S. Madsen. The continental-shelf bottom boundary layer. *Annual Review of Fluid Mechanics*, 18(1):265–305, 1986.

C. Guedes Soares. Representation of double-peaked sea wave spectra. *Ocean Engineering*, 11(2):185–207, 1984.

C. Guedes Soares. On the occurence of double peaked wave spectra. *Ocean Engineering*, 18(1):167–171, 1991.

R. Halliday. Rare fishes from the Clyde sea area. *Journal of Natural History*, 3(3): 309–320, 1969.

R. Haring, A. Osborne, and L. Spencer. Extreme wave parameters based on continental shelf storm wave records. *Coastal Engineering Proceedings*, 1(15), 1976.

R. J. Harper and M. L. Dock. Underwater olfaction for real-time detection of submerged unexploded ordnance. In *Defense and Security Symposium*, pages 65400V–65400V. International Society for Optics and Photonics, 2007.

K. Hasselmann. On the spectral dissipation of ocean waves due to white capping. *Boundary-Layer Meteorology*, 6(1-2):107–127, 1974.

K. Hasselmann, T. Barnett, E. Bouws, H. Carlson, D. Cartwright, K. Enke, J. Ewing, H. Gienapp, D. Hasselmann, P. Kruseman, A. Meerburg, P. Müller, D. Olbers, K. Richter, W. Sell, and H. Walden. Measurements of wind-wave growth and swell decay during the joint north sea wave project (jonswap). Technical report, Deutches Hydrographisches Institut, 1973.

S. Haver. A possible freak wave event measured at the draupner jacket january 1 1995. *Rogue waves 2004*, pages 1–8, 2004.

N. Heaps. Storm surges, 1967–1982. *Geophysical Journal International*, 74(1):331–376, 1983.

M. R. Heath, A. D. Sabatino, N. Serpetti, and R. O'Hara Murray. Scoping the impact tidal and wave energy extraction on suspended sediment concentrations and underwater light climate. *TeraWatt Position Papers, MASTS*, 2015.

J. Hinkel, C. Jaeger, R. J. Nicholls, J. Lowe, O. Renn, and S. Peijun. Sea-level rise scenarios and coastal risk management. *Nature Climate Change*, 5(3):188–190, 2015.

K. B. Hjelmervik and K. Trulsen. Freak wave statistics on collinear currents. *Journal of Fluid Mechanics*, 637:267–284, 2009.

S. Holm. Spectral moment matching in the maximum entropy spectral analysis method. *IEEE Transactions on Information Theory*, 29(2):311–313, 1983.

S. Holm and J. M. Hovem. Estimation of scalar ocean wave spectra by the maximum entropy method. *Oceanic Engineering, IEEE Journal of*, 4(3):76–83, 1979.

L. H. Holthuijsen. *Waves in oceanic and coastal waters*. Cambridge University Press, 2007.

K. Horsburgh and C. Wilson. Tide-surge interaction and its role in the distribution of surge residuals in the north sea. *Journal of Geophysical Research: Oceans (1978–2012)*, 112(C8), 2007.

T. Howard, A. Pardaens, J. Lowe, J. Ridley, R. Hurkmans, J. Bamber, G. Spada, and D. Vaughan. Sources of 21st century regional sea level rise along the coast of North-West Europe. *Ocean Science*, 10(3):473–483, 2014.

D. Huntley. Tides on the north-west European continental shelf. *The North-West European Shelf Seas, Oceanogr. Ser*, 24:301–351, 1980.

IHO. *Limits of Oceans and Seas*, volume 28. International Hydrographic Organization, 1953.

M. E. Inall and T. P. Rippeth. Dissipation of tidal energy and associated mixing in a wide fjord. *Environmental Fluid Mechanics*, 2(3):219–240, 2002.

D. Irvine and D. Tilley. Ocean wave directional spectra and wave-current interaction in the agulhas from the shuttle imaging radar-b synthetic aperture radar. *Journal of Geophysical Research: Oceans (1978–2012)*, 93(C12):15389–15401, 1988.

J. Jackson and A. Elliott. Internal waves in the Clyde Sea. *Estuarine, Coastal and Shelf Science*, 54(1):51–64, 2002.

P. A. Janssen. Nonlinear four-wave interactions and freak waves. *Journal of Physical Oceanography*, 33(4):863–884, 2003.

I. Jayewardane. Analysis of some bimodal spectra and the reproduction of these spectra in thelaboratory. In *Proceedings of the 2nd International Conference on Coastal and Port Engineering inDeveloping Countries, Beijing, China. COPEDEC*, pages 2046–2056, 1987.

H. K. Johnson and H. Kofoed-Hansen. Influence of bottom friction on sea surface roughness and its impact on shallow water wind wave modeling. *Journal of physical oceanography*, 30(7):1743–1756, 2000.

E. Kalnay, M. Kanamitsu, R. Kistler, W. Collins, D. Deaven, L. Gandin, M. Iredell, S. Saha, G. White, J. Woollen, et al. The NCEP/NCAR 40-year reanalysis project. *Bulletin of the American meteorological Society*, 77(3):437–471, 1996.

G. M. Kaminsky and N. C. Kraus. Evaluation of depth-limited wave breaking criteria. In *Ocean Wave Measurement and Analysis (1993)*, pages 180–193. ASCE, 1993.

L. H. Kantha and C. A. Clayson. An improved mixed layer model for geophysical applications. *Journal of Geophysical Research: Oceans*, 99(C12):25235–25266, 1994.

T. W. Kao, F.-S. Pan, and D. Renouard. Internal solitons on the pycnocline: generation, propagation, and shoaling and breaking over a slope. *Journal of Fluid Mechanics*, 159:19–53, 1985.

H. Karunarathna. Modelling the long-term morphological evolution of the clyde estuary, scotland, uk. *Journal of Coastal Conservation*, 15(4):499–507, 2011.

A. Kasai, T. Rippeth, and J. Simpson. Density and flow structure in the Clyde Sea front. *Continental Shelf Research*, 19(14):1833–1848, 1999.

Y. Kaya, M. Stewart, and M. Becker. Flood forecasting and flood warning in the Firth of Clyde, UK. *Natural hazards*, 36(1-2):257–271, 2005.

C. Kharif and E. Pelinovsky. Physical mechanisms of the rogue wave phenomenon. *European Journal of Mechanics-B/Fluids*, 22(6):603–634, 2003.

A. Kimura. Statistical properties of random wave groups. *Coastal Engineering Proceedings*, 1(17), 1980.

G. Kinahan. The Beaufort's Dyke, off the Coast of the Mull of Galloway. In *Proceedings of the Royal Irish Academy*, pages 26–828. JSTOR, 1900.

P. Knight and M. Howarth. The flow through the North Channel of the Irish Sea. *Continental Shelf Research*, 19(5):693–716, 1999.

G. Komen, K. Hasselmann, and K. Hasselmann. On the existence of a fully developed wind-sea spectrum. *Journal of physical oceanography*, 14(8):1271–1285, 1984.

G. J. Komen, L. Cavaleri, M. Donelan, K. Hasselmann, S. Hasselmann, and P. Janssen. *Dynamics and modelling of ocean waves*. Cambridge university press, 1996.

T. W. Körner. *The pleasures of counting*. Cambridge University Press, 1996.

H. Lamb. Climatic fluctuations in historical times and their connexion with transgressions of the sea, storm floods and other coastal changes. *Verhulst en Gottschalk*, 1980.

I. Lavrenov. The wave energy concentration at the agulhas current off south africa. *Natural hazards*, 17(2):117–127, 1998.

Y.-D. Lenn and T. K. Chereskin. Observations of ekman currents in the southern ocean. *Journal of Physical Oceanography*, 39(3):768–779, 2009.

M. Li, L. Zhong, W. C. Boicourt, S. Zhang, and D.-L. Zhang. Hurricane-induced storm surges, currents and destratification in a semi-enclosed bay. *Geophysical Research Letters*, 33(2), 2006.

J. W. Loder and D. A. Greenberg. Predicted positions of tidal fronts in the Gulf of Maine region. *Continental Shelf Research*, 6(3):397–414, 1986.

M. Longuet-Higgins. On the joint distribution of the periods and amplitudes of sea waves. *Journal of Geophysical Research*, 80(18):2688–2694, 1975.

M. S. Longuet-Higgins. On the statistical distributions of sea waves. *J. mar. Res.*, 11(3): 245–265, 1952.

M. S. Longuet-Higgins. On the joint distribution of wave periods and amplitudes in a random wave field. In *Proceedings of the Royal Society of London A: Mathematical, Physical and Engineering Sciences*, volume 389, pages 241–258. The Royal Society, 1983.

M. S. Longuet-Higgins and R. W. Stewart. Radiation stress and mass transport in gravity waves, with application to surf beats. *Journal of Fluid Mechanics*, 13: 481–504, 8 1962. ISSN 1469-7645. doi: 10.1017/S0022112062000877. URL `http://journals.cambridge.org/article_S0022112062000877`.

A. Lygre and H. E. Krogstad. Maximum entropy estimation of the directional distribution in ocean wave spectra. *Journal of Physical Oceanography*, 16(12):2052–2060, 1986.

P. Lynch. *The emergence of numerical weather prediction: Richardson's dream*. Cambridge University Press, 2006.

P. Lynch. The origins of computer weather prediction and climate modeling. *Journal of Computational Physics*, 227(7):3431–3444, 2008.

J. K. Mallory. Abnormal waves on the southeast coast of south africa. *International hydrographic review*, 1974.

J. Matthews, F. Buchholz, R. Saborowski, G. Tarling, S. Dallot, and J. Labat. On the physical oceanography of the Kattegat and Clyde Sea area, 1996–98, as background to ecophysiological studies on the planktonic crustacean, Meganyctiphanes norvegica (Euphausiacea). *Helgoland Marine Research*, 53(1):70–84, 1999.

T. J. McDougall. Neutral surfaces. *Journal of Physical Oceanography*, 17(11):1950–1964, 1987.

G. Mellor and A. Blumberg. Wave breaking and ocean surface layer thermal response. *Journal of physical oceanography*, 34(3):693–698, 2004.

G. L. Mellor and T. Yamada. Development of a turbulence closure model for geophysical fluid problems. *Reviews of Geophysics*, 20(4):851–875, 1982.

R. Midgley, J. Simpson, P. Hyder, and T. Rippeth. Seasonal cycle of vertical structure and deep water renewal in the Clyde Sea. *Estuarine, Coastal and Shelf Science*, 53(6): 813–823, 2001.

J. W. Miles. Kelvin waves on oceanic boundaries. *Journal of Fluid Mechanics*, 55(01): 113–127, 1972.

H. Mitsuyasu, F. Tasai, T. Suhara, S. Mizuno, M. Ohkusu, T. Honda, and K. Rikiishi. Observations of the directional spectrum of ocean wavesusing a cloverleaf buoy. *Journal of Physical Oceanography*, 5(4):750–760, 1975.

J. Monbaliu, C. Yu, and P. Osuna. Sensitivity of wind wave simulation to coupling with a tide/surge model with application to the southern north sea. *Coastal Engineering Proceedings*, 1(26), 1998.

L. Moskowitz. Estimates of the power spectrums for fully developed seas for wind speeds of 20 to 40 knots. *Journal of geophysical research*, 69(24):5161–5179, 1964.

P. Müller, C. Garrett, and A. Osborne. Rogue waves. *Oceanography*, 18(3):66, 2005.

W. Munk, F. Snodgrass, and M. Wimbush. Tides off-shore: Transition from california coastal to deep-sea waters. *Geophysical and Astrophysical Fluid Dynamics*, 1(1-2): 161–235, 1970.

W. H. Munk. On the wind-driven ocean circulation. *Journal of meteorology*, 7(2):80–93, 1950.

W. H. Munk and E. R. Anderson. Notes on the theory of the thermocline. *J. Mar. Res.*, 3:276–295, 1948.

T. S. Murty. *Storm surges: meteorological ocean tides*, volume 212. Department of Fisheries and Oceans Ottawa, 1984.

D. Myrhaug and H. Rue. Joint distribution of successive wave periods revisited. *Journal of ship research*, 42(3):199–206, 1998.

D. Myrhaug, E. A. Dahle, H. RUE, and O. H. Slaattelid. Statistics of successive wave periods with application to rolling of ships. *International shipbuilding progress*, 47 (451):253–266, 2000.

R. C. Nelson. Design wave heights on very mild slopesan experimental study. *Transactions of the Institution of Engineers, Australia. Civil engineering*, 29(3):157–161, 1987.

R. C. Nelson. Depth limited design wave heights in very flat regions. *Coastal Engineering*, 23(1):43–59, 1994.

R. J. Nicholls, S. E. Hanson, J. A. Lowe, R. A. Warrick, X. Lu, and A. J. Long. Sea-level scenarios for evaluating coastal impacts. *Wiley Interdisciplinary Reviews: Climate Change*, 5(1):129–150, 2014.

J. Nikuradse. Str {ö} mungsgestze in rauhen Rohren. 1933.

A. I. Olbert and M. Hartnett. Storms and surges in irish coastal waters. *Ocean Modelling*, 34(1):50–62, 2010.

M. Onorato, A. R. Osborne, M. Serio, and S. Bertone. Freak waves in random oceanic sea states. *Physical Review Letters*, 86(25):5831, 2001.

M. Onorato, A. Osborne, M. a. a. Serio, D. Resio, A. Pushkarev, V. E. Zakharov, and C. Brandini. Freely decaying weak turbulence for sea surface gravity waves. *Physical review letters*, 89(14):144501, 2002a.

M. Onorato, A. R. Osborne, and M. Serio. Extreme wave events in directional, random oceanic sea states. *Physics of Fluids (1994-present)*, 14(4):L25–L28, 2002b.

M. Onorato, A. Osborne, and M. Serio. Modulational instability in crossing sea states: A possible mechanism for the formation of freak waves. *Physical review letters*, 96 (1):014503, 2006a.

M. Onorato, A. Osborne, M. Serio, L. Cavaleri, C. Brandini, and C. Stansberg. Extreme waves, modulational instability and second order theory: wave flume experiments on irregular waves. *European Journal of Mechanics-B/Fluids*, 25(5):586–601, 2006b.

M. Onorato, T. Waseda, A. Toffoli, L. Cavaleri, O. Gramstad, P. Janssen, T. Kinoshita, J. Monbaliu, N. Mori, A. Osborne, et al. Statistical properties of directional ocean waves: the role of the modulational instability in the formation of extreme events. *Physical Review Letters*, 102(11):114502, 2009.

M. Onorato, D. Proment, and A. Toffoli. Freak waves in crossing seas. *The European Physical Journal Special Topics*, 185(1):45–55, 2010.

M. Onorato, D. Proment, and A. Toffoli. Triggering rogue waves in opposing currents. *Physical review letters*, 107(18):184502, 2011.

M. Orlić, M. Kuzmić, and Z. Pasarić. Response of the Adriatic Sea to the bora and sirocco forcing. *Continental Shelf Research*, 14(1):91–116, 1994.

A. Osborne and T. Burch. Internal solitons in the Andaman Sea. *Science*, 208(4443): 451–460, 1980.

A. R. Osborne, M. Onorato, and M. Serio. The nonlinear dynamics of rogue waves and holes in deep-water gravity wave trains. *Physics Letters A*, 275(5):386–393, 2000.

P. Osuna and J. Monbaliu. Wave–current interaction in the southern north sea. *Journal of marine systems*, 52(1):65–87, 2004.

L. Otto, J. Zimmerman, G. Furnes, M. Mork, R. Saetre, and G. Becker. Review of the physical oceanography of the north sea. *Netherlands Journal of Sea Research*, 26(24): 161 – 238, 1990. ISSN 0077-7579.

P. G. Petrova, M. A. Tayfun, and C. G. Soares. The effect of third-order nonlinearities on the statistical distributions of wave heights, crests and troughs in bimodal crossing seas. *Journal of Offshore Mechanics and Arctic Engineering*, 135(2):021801, 2013.

O. Phillips. The dynamics of the upper ocean, cambridge univ. *Press, Cambridge*, 1977.

G. L. Pickard and W. J. Emery. *Descriptive physical oceanography: an introduction*. Elsevier, 1990.

W. J. Pierson. The interpretation of wave spectrums in terms of the wind profile instead of the wind measured at a constant height. *Journal of geophysical research*, 69(24): 5191–5203, 1964.

W. J. J. Pierson and L. Moskowitz. A proposed spectral form for fully developed wind seas based on the similarity theory of sa kitaigorodskii. Technical report, DTIC Document, 1963.

R. Pingree and D. Griffiths. Tidal fronts on the shelf seas around the british isles. *Journal of Geophysical Research: Oceans*, 83(C9):4615–4622, 1978.

R. Pingree and D. Griffiths. Sand transport paths around the British Isles resulting from M 2 and M 4 tidal interactions. *Journal of the Marine Biological Association of the United Kingdom*, 59(02):497–513, 1979.

R. Pingree and D. Griffiths. The N 2 tide and semidiurnal amphidromes around the British Isles. *Journal of the Marine Biological Association of the United Kingdom*, 61 (03):617–625, 1981a.

R. Pingree and D. Griffiths. S 2 tidal simulations on the North-West European Shelf. *Journal of the Marine Biological Association of the United Kingdom*, 61(03):609–616, 1981b.

R. Pingree, P. Holligan, and G. Mardell. The effects of vertical stability on phytoplankton distributions in the summer on the northwest European Shelf. *Deep Sea Research*, 25 (11):1011–1028, 1978.

S. Ponce de León and C. Guedes Soares. Extreme wave parameters under North Atlantic extratropical cyclones. *Ocean Modelling*, 81:78–88, Aug. 2014. ISSN 14635003. doi: 10.1016/j.ocemod.2014.07.005. URL `http://www.sciencedirect.com/science/article/pii/S146350031400095X`.

T. Poodle. Freshwater inflows to the Firth of Clyde. *Proceedings of the Royal Society of Edinburgh*, 90:55–66, 1986.

J. F. Price, R. A. Weller, and R. R. Schudlich. Wind-driven ocean currents and ekman transport. *Science*, 238(4833):1534–1538, 1987.

J. Proudman. The tides of the atlantic ocean (george darwin lecture). *Monthly Notices of the Royal Astronomical Society*, 104:244, 1944.

J. Proudman and A. T. Doodson. The principal constituent of the tides of the North Sea. *Philosophical Transactions of the Royal Society of London. Series A, Containing Papers of a Mathematical or Physical Character*, pages 185–219, 1924.

D. T. Pugh. *Tides, surges and mean sea-level (reprinted with corrections)*. John Wiley & Sons Ltd, 1996.

J. Qi, C. Chen, R. C. Beardsley, W. Perrie, G. W. Cowles, and Z. Lai. An unstructured-grid finite-volume surface wave model (fvcom-swave): implementation, validations and applications. *Ocean Modelling*, 28(1):153–166, 2009.

J. Rego and C. Li. On the receding of storm surge along Louisiana's low-lying coast. *Journal of Coastal Research*, pages 1045–1049, 2009a.

J. L. Rego and C. Li. On the importance of the forward speed of hurricanes in storm surge forecasting: A numerical study. *Geophysical Research Letters*, 36(7), 2009b.

J. L. Rego and C. Li. Nonlinear terms in storm surge predictions: Effect of tide and shelf geometry with case study from Hurricane Rita. *Journal of Geophysical Research: Oceans (1978–2012)*, 115(C6), 2010a.

J. L. Rego and C. Li. Storm surge propagation in Galveston Bay during Hurricane Ike. *Journal of Marine Systems*, 82(4):265–279, 2010b.

L. F. Richardson. *Weather prediction by numerical process*. Cambridge University Press, 2007.

T. Rippeth and J. Simpson. The frequency and duration of episodes of complete vertical mixing in the Clyde Sea. *Continental Shelf Research*, 16(7):933–947, 1996.

C. J. Roach, H. E. Phillips, N. L. Bindoff, and S. R. Rintoul. Detecting and characterizing ekman currents in the southern ocean. *Journal of Physical Oceanography*, 45(5): 1205–1223, 2015.

G. Rodrı?guez, C. G. Soares, and U. Machado. Uncertainty of the sea state parameters resulting from the methods of spectral estimation. *Ocean Engineering*, 26(10):991–1002, 1999.

G. R. Rodrı?guez and C. G. Soares. Correlation between successive wave heights and periods in mixed sea states. *Ocean Engineering*, 28(8):1009–1030, 2001.

G. R. Rodriguez, C. G. Soares, and L. Ferrer. Wave group statistics of numerically simulated mixed sea states. *Journal of Offshore Mechanics and Arctic Engineering*, 122(4):282–288, 2000.

P. S. Romans, L. Vandersohuren, et al. Response based design conditions in the north sea: Application of a new method. In *Offshore Technology Conference*. Offshore Technology Conference, 1995.

B. Ruessink, D. Walstra, and H. Southgate. Calibration and verification of a parametric wave model on barred beaches. *Coastal Engineering*, 48(3):139–149, 2003.

H. Rye. Wave group formation among storm waves. *Coastal Engineering Proceedings*, 1 (14), 1974.

H. Rye. The stability of some currently used wave parameters. *Coastal Engineering*, 1: 17–30, 1977.

A. Sabatino, C. McCaig, R. O. Murray, and M. Heath. Modelling wave–current interactions off the east coast of scotland. *Ocean Science Discussions*, pages 3099–3142, 2015.

A. D. Sabatino and M. Serio. Experimental investigation on statistical properties of wave heights and crests in crossing sea conditions. *Ocean Dynamics*, 65(5):707–720, 2015.

S. E. Sand, N. O. Hansen, P. Klinting, O. T. Gudmestad, and M. J. Sterndorff. Freak wave kinematics. In *Water Wave Kinematics*, pages 535–549. Springer, 1990.

J. Schellekens. *Hydrological Modelling Using Convective Scale Rainfall Modelling: Phase 3*. Environment Agency, 2010.

P. Schureman. *Manual of harmonic analysis and prediction of tides*. Number 98. US Government Printing Office, 1958.

M. Serio, M. Onorato, A. Osborne, and P. Janssen. On the computation of the Benjamin-Feir Index. *Nuovo Cimento*, 2:0, 2005.

N. Serpetti. *Modelling and mapping the physical and biogeochemical properties of sediments on the North Sea coastal waters*. PhD thesis, University of Aberdeen, 2012.

N. Serpetti, M. Heath, E. Armstrong, and U. Witte. Blending single beam RoxAnn and multi-beam swathe QTC hydro-acoustic discrimination techniques for the Stonehaven area, Scotland, UK. *Journal of Sea Research*, 65(4):442–455, 2011.

N. Serpetti, M. Heath, M. Rose, and U. Witte. High resolution mapping of sediment organic matter from acoustic reflectance data. *Hydrobiologia*, 680(1):265–284, 2012.

R. P. Signell, R. C. Beardsley, H. C. Graber, and A. Capotondi. Effect of Wave Current Interaction on Wind Driven Circulation In Narrow Shallow Embayments. *Journal of Geophysical Research*, 95(6):9671–9678, 1990.

J. Simpson and J. Hunter. Fronts in the irish sea. *Nature*, 250:404–406, 1974.

J. Simpson and T. Rippeth. The Clyde Sea: a model of the seasonal cycle of stratification and mixing. *Estuarine, Coastal and Shelf Science*, 37(2):129–144, 1993.

J. Smagorinsky. General circulation experiments with the primitive equations: I. The basic experiment*. *Monthly weather review*, 91(3):99–164, 1963.

R. J. Sobey. Correlation between individual waves in a real sea state. *Coastal Engineering*, 27(3):223–242, 1996.

H. Socquet-Juglard, K. Dysthe, K. Trulsen, H. E. Krogstad, and J. Liu. Probability distributions of surface gravity waves during spectral changes. *Journal of Fluid Mechanics*, 542:195–216, 2005.

R. L. Soulsby. The bottom boundary layer of shelf seas. *Elsevier oceanography series*, 35: 189–266, 1983.

A. J. Souza, H. Burchard, C. Eden, C. Pattiaratchi, H. van Haren, P. Craig, and N. Huang. Coastal ocean turbulence and mixing.

M. Srokosz and M. Longuet-Higgins. On the skewness of sea-surface elevation. *Journal of Fluid Mechanics*, 164:487–497, 1986.

A. Stigebrandt. A mechanism governing the estuarine circulation in deep, strongly stratified fjords. *Estuarine, Coastal and Shelf Science*, 13(2):197–211, 1981.

A. Stigebrandt. A note on the locus of a shelf front. *Tellus A*, 40(5):439–442, 1988.

M. Stive. A scale comparison of waves breaking on a beach. *Coastal engineering*, 9(2): 151–158, 1985.

G. G. Stokes. On the theory of oscillatory waves. *Trans Cambridge Philos Soc*, 8:441–473, 1847.

H. Stommel. The westward intensification of wind-driven ocean currents. *Eos, Transactions American Geophysical Union*, 29(2):202–206, 1948.

M. Su, M. Bergin, and S. Bales. Characteristics of wave groups in storm seas. In *Proc. Ocean Structural Dynamics Symposium*, volume 82, pages 118–132. ASCE New York, 1982.

Ü. Suursaar and J. Sooäär. Decadal variations in mean and extreme sea level values along the Estonian coast of the Baltic Sea. *Tellus A*, 59(2):249–260, 2007.

H. U. Sverdrup. Wind-driven currents in a baroclinic ocean; with application to the equatorial currents of the eastern pacific. *Proceedings of the National Academy of Sciences*, 33(11):318–326, 1947.

H. Tamura, T. Waseda, and Y. Miyazawa. Freakish sea state and swell-windsea coupling: Numerical study of the suwa-maru incident. *Geophysical Research Letters*, 36 (1), 2009.

M. A. Tayfun. Narrow-band nonlinear sea waves. *Journal of Geophysical Research: Oceans (1978–2012)*, 85(C3):1548–1552, 1980.

M. A. Tayfun. Effects of spectrum band width on the distribution of wave heights and periods. *Ocean Engineering*, 10(2):107–118, 1983.

G. I. Taylor. Tidal oscillations in gulfs and rectangular basins. *Proceedings of the London Mathematical Society*, 2(1):148–181, 1922.

A. Toffoli, O. Gramstad, K. Trulsen, J. Monbaliu, E. Bitner-Gregersen, and M. Onorato. Evolution of weakly nonlinear random directional waves: laboratory experiments and numerical simulations. *Journal of Fluid Mechanics*, 664:313–336, 2010.

A. Toffoli, E. Bitner-Gregersen, A. Osborne, M. Serio, J. Monbaliu, and M. Onorato. Extreme waves in random crossing seas: Laboratory experiments and numerical simulations. *Geophysical Research Letters*, 38(6), 2011a.

A. Toffoli, L. Cavaleri, A. Babanin, M. Benoit, E. Bitner-Gregersen, J. Monbaliu, M. Onorato, A. Osborne, and C. Stansberg. Occurrence of extreme waves in three-dimensional mechanically generated wave fields propagating over an oblique current. *Natural Hazards and Earth System Science*, 11(3):895–903, 2011b.

A. Toffoli, T. Waseda, H. Houtani, T. Kinoshita, K. Collins, D. Proment, and M. Onorato. Excitation of rogue waves in a variable medium: An experimental study on the interaction of water waves and currents. *Physical Review E*, 87(5):051201, 2013.

A. Toffoli, T. Waseda, H. Houtani, L. Cavaleri, D. Greaves, and M. Onorato. Rogue waves in opposing currents: an experimental study on deterministic and stochastic wave trains. *Journal of Fluid Mechanics*, 769:277–297, 2015.

H. L. Tolman. Effects of tides and storm surges on north sea wind waves. *Journal of physical oceanography*, 21(6):766–781, 1991.

J. Townson and A. Donald. Numerical Modelling of Storm Surges in the Clyde Sea Area. In *ICE Proceedings*, volume 79, pages 637–655. Thomas Telford, 1985.

J. M. Townson and R. H. Collar. Water movement and the simulation of storm surges in the Firth of Clyde. *The environment of the estuary and firth of Clyde, Proc. Roy. Soc. Edinburgh B*, 90:87–96, 1986.

A. Ullmann and V. Moron. Weather regimes and sea surge variations over the Gulf of Lions (French Mediterranean coast) during the 20th century. *International Journal of Climatology*, 28(2):159, 2008.

V. Venugopal and R. Nemalidinne. Marine energy resource assessment for orkney and pentland waters with a coupled wave and tidal flow model. In *ASME 2014 33rd International Conference on Ocean, Offshore and Arctic Engineering*, pages V09BT09A010–V09BT09A010. American Society of Mechanical Engineers, 2014.

V. Venugopal and R. Nemalidinne. Wave resource assessment for Scottish waters using a large scale North Atlantic spectral wave model. *Renewable Energy*, 76:503–525, 2015.

S. Wakelin and R. Proctor. The impact of meteorology on modelling storm surges in the Adriatic Sea. *Global and Planetary Change*, 34(1):97–119, 2002.

R. H. Weisberg and L. Zheng. Hurricane storm surge simulations comparing three-dimensional with two-dimensional formulations based on an Ivan-like storm over the Tampa Bay, Florida region. *Journal of Geophysical Research: Oceans (1978–2012)*, 113(C12), 2008.

R. Weisse, H. von Storch, and F. Feser. Northeast atlantic and north sea storminess as simulated by a regional climate model during 1958-2001 and comparison with observations. *Journal of Climate*, 18(3):465–479, 2005.

S. R. Werner, R. C. Beardsley, S. J. Lentz, D. L. Hebert, and N. S. Oakey. Observations and modeling of the tidal bottom boundary layer on the southern flank of Georges Bank. *Journal of Geophysical Research: Oceans (1978–2012)*, 108(C11), 2003.

P. Wessel and W. H. Smith. A global, self-consistent, hierarchical, high-resolution shoreline database. *Journal of Geophysical Research: Solid Earth (1978–2012)*, 101(B4): 8741–8743, 1996.

H. T. Wist, D. Myrhaug, and H. Rue. Statistical properties of successive wave heights and successive wave periods. *Applied Ocean Research*, 26(3):114–136, 2004.

J. Wolf and R. Flather. Modelling waves and surges during the 1953 storm. *Philosophical Transactions of the Royal Society of London A: Mathematical, Physical and Engineering Sciences*, 363(1831):1359–1375, 2005.

D. K. Woolf, P. Challenor, and P. Cotton. Variability and predictability of the north atlantic wave climate. *Journal of Geophysical Research: Oceans (1978–2012)*, 107 (C10):9–1, 2002.

D. Xu, X. Li, L. Zhang, N. Xu, and H. Lu. On the distributions of wave periods, wavelengths, and amplitudes in a random wave field. *Journal of Geophysical Research: Oceans (1978–2012)*, 109(C5), 2004.

I. Young. The determination of confidence limits associated with estimates of the spectral peak frequency. *Ocean engineering*, 22(7):669–686, 1995.

I. R. Young. *Wind generated ocean waves*, volume 2. Elsevier, 1999.

H. Zhang, Z. Cherneva, and C. G. Soares. Joint distributions of wave height and period in laboratory generated nonlinear sea states. *Ocean Engineering*, 74:72–80, 2013.